Constraining Antarctic polynya formation and sea ice and snow evolution using autonomous observations and modeling

Ethan Chen Campbell

A dissertation
submitted in partial fulfillment of the
requirements for the degree of

Doctor of Philosophy

University of Washington

2025

Reading Committee:

Stephen C. Riser, Chair

Georgy E. Manucharyan

Eric A. D'Asaro

Program Authorized to Offer Degree:
School of Oceanography

University of Washington

Abstract

Constraining Antarctic polynya formation and sea ice and snow evolution
using autonomous observations and modeling

Ethan Chen Campbell

Chair of the Supervisory Committee:
Professor Stephen C. Riser
School of Oceanography

This dissertation focuses on resolving key uncertainties in Southern Ocean sea ice and snow processes using under-ice autonomous ocean observations and modeling techniques in a Lagrangian, or flow-following, framework. After an introduction to the region and relevant processes (**Chapter 1**), the first portion of this work (**Chapter 2**) investigates the periodic appearance of large sea ice openings offshore of Antarctica, known as open-ocean polynyas. The rarity of these intermittent events in the 50-year satellite record has prevented oceanographers from pinpointing the factors that initiate polynyas and fully characterizing the vigorous cycle of ocean mixing and heat exchange believed to sustain them. Fortuitously, two Argo profiling floats, which are free-drifting robotic instruments that can collect ocean measurements beneath sea ice, were present during unexpected polynya events that occurred over Maud Rise in the Weddell Sea in 2016 and 2017. By placing their ocean measurements in context of meteorological data and past hydrographic and satellite records, we conclude that these sea ice openings were preconditioned by reduced upper-ocean salinity stratification and triggered by storms. Identifying links between these conditions and fluctuations in the primary mode of Southern Hemisphere climate variability, the Southern Annular Mode, yields a robust explanation for why polynyas have appeared at this location in some years but not others. These first in situ ocean

observations also confirm that the anomalous openings were maintained by deep convective mixing, as long suspected.

Antarctic sea ice thickness and overlying snow depth are important climate variables due to their strong influence on freshwater fluxes, ocean-atmosphere heat exchange, and momentum transfer. Yet monitoring their evolution from satellites has proven challenging, partly due to a sparsity of in situ measurements for validation purposes. The next portion of this work (**Chapter 3**) presents a newly developed numerical model that reconstructs the daily evolution of snow deposited on Antarctic sea ice along satellite-observed Lagrangian ice drift trajectories. Atmospheric reanalysis input data and parameterizations of key snow accumulation, erosion, and transformation processes are calibrated using autonomous snow buoy measurements. The resulting model reconstruction from 2003 to 2024 offers constraints on the annual mass budget of snow intercepted by sea ice in the Southern Ocean, including the magnitude and timing of freshwater release to the ocean. This represents a substantially larger flux than previously diagnosed, with implications for water mass transformation and vertical mixing. Snow-ice formation is inferred by comparing the simulated snow accumulation with satellite-observed snow depths, and trends in the reconstruction estimates are assessed.

In the third portion of this work (**Chapter 4**), Antarctic sea ice formation and melt rates are directly estimated by calculating mixed layer salinity budgets along the wintertime drift trajectories of over 300 under-ice Argo profiling floats in the Southern Ocean. All except one budget term can be constrained using the float measurements and auxiliary data sources, leaving sea ice-induced fluxes from brine rejection during ice formation and freshwater release during ice melt to be inferred as the large budget residual. The seasonal cycle of sea ice exhibits a pronounced asymmetry with a prolonged net growth phase that slows in mid-winter before the initiation of rapid melt in fall. A circumpolar climatology of sea ice growth and melt rates within the Antarctic seasonal ice zone show net annual sea ice production near the Antarctic continent that switches to net annual melt at around 65°S. However, sea ice freezing and melt rates estimated from the

float observations are found to be highly sensitive to uncertainties in the magnitude and timing of freshwater fluxes from snow. This float-based methodology highlights the potential to reconstruct climatological Antarctic sea ice thickness using autonomous ocean measurements.

The final portion of this dissertation (**Chapter 5**) highlights a retrospective study on an undergraduate Python programming and ocean data analysis course that was co-developed and taught remotely in 2020 with another graduate student. Our teaching integrated evidence-based teaching practices—a flipped structure, activities infused with active learning, an individualized final research project, and efforts to center accessibility. A mixed-methods approach is used to evaluate the efficacy of the instructional design using data from surveys, online teaching platforms, student work, assessments, and a focus group. We find that the course elements bolstered student engagement and learning, allowing students with less or no prior coding experience to achieve similar success as peers with more experience.

TABLE OF CONTENTS

LIST OF FIGURES

LIST OF TABLES

ACKNOWLEDGMENTS

I extend my profound gratitude to my advisor, Steve Riser, for his thoughtful and patient mentorship over the past 10 years, starting from a summer research internship in 2014 when I was an undergraduate student. I also thank my other committee members—Mikelle Nuwer, Eric D'Asaro, Georgy Manucharyan, and Cecilia Bitz, as well as a former committee member, Curtis Deutsch—for their guidance and steadfast encouragement. I am greatly appreciative of all the members of the Riser/Gray, Deutsch, and Thompson research groups, as well as the rest of the 2016 graduate cohort, for their camaraderie and support throughout my time in the department. I am also deeply thankful to those who introduced me to oceanographic research and inspired me to remain in this amazing community—especially Jorge Sarmiento, Joseph Majkut, and Danny Sigman, whose mentorship left a lasting impact. I also wish to thank Linda Damianides and Marcia Kozelka of Emerson Middle School for showing me the joy of math and writing, a gift that continues to shape my life.

I thank my family for providing the foundation for this work and for being my champions throughout this journey. In particular, I honor my late grandma, my po-po, who sacrificed her doctoral ambitions after becoming a mother—a decision for which I owe an enduring debt of gratitude. This endeavor would not have been possible without the support of my partner, Pin-An, who I thank for her unwavering care, compassion, and exuberance. Special thanks also go to those who have formed my community in Seattle—especially in this department, Ampersand Bikes Club, the Greenways coalition, and Whose Streets Our Streets. Lastly, I extend my thanks to Kohaku, my cat, for his unconditional love and companionship.

For Chapter 2, I wish to thank Annie Wong, Robert Drucker, Josh Plant, Tanya Maurer, and Ken Johnson for assistance with float data calibration, and all others involved in float and sensor design, construction, calibration, and deployment for their contributions. Data were collected and

made freely available by the Southern Ocean Carbon and Climate Observations and Modeling (SOCCOM) Project, which is funded by the U.S. National Science Foundation, Division of Polar Programs, supplemented by NASA, and by the International Argo Program and the NOAA programs that contribute to it.

For Chapters 3 and 4, I offer my thanks to David Darr and Georgy Manucharyan for their computational support. I also acknowledge Alek Petty, Eric D'Asaro, and Cecilia Bitz for their useful feedback on these projects and the participants of the Physical Oceanography Dissertation Symposium (PODS) XIII for insightful discussions. I extend my appreciation to those involved in the Alfred Wegener Institute's snow buoy program and the RV *Polarstern* cruises on which snow buoys were deployed, which enabled the calibration of the model reconstruction in Chapter 3.

For Chapter 5, I wish to recognize my incredible collaborator and co-first author, Katy Christensen, who contributed equally to this work, as well as our teaching mentor, Mikelle Nuwer. We are grateful to all the undergraduate students who we taught in OCEAN 215 for their participation, patience, and feedback during the course. We thank Kathy Newell for her assistance with obtaining data and Rick Keil for believing in our vision for the course, as well as the three anonymous reviewers and the journal editors whose helpful comments substantially improved the quality and clarity of our study.

My graduate work was made possible by generous fellowship support from the University of Washington Program on Climate Change, the Office of Naval Research through the National Defense Science & Engineering Graduate Fellowship (NDSEG) Program, and the ARCS Foundation–Seattle Chapter, as well as funding from the University of Washington School of Oceanography and the National Science Foundation's Southern Ocean Carbon and Climate Observations and Modeling (SOCCOM) and Global Ocean Biogeochemistry Array (GO-BGC) projects.

DEDICATION

To my family, for making it possible for me to walk this path
and instilling in me the curiosity that brought this work to life.

Chapter 1:

INTRODUCTION

Sea ice in the Southern Ocean forms a thin yet dynamic layer of frozen seawater that encircles the Antarctic continent. Its outer boundary, known as the sea ice extent, exhibits a broad seasonal cycle spurred by new ice formation and predominantly northward, wind-driven drift every fall and winter, followed by melt-back in the spring and summer months (P. R. Holland & Kwok, 2012; Eayrs et al., 2019). As many explorers, mariners, and researchers have learned over the years—most famously, perhaps, Sir Ernest Shackleton, whose recently-discovered ship *Endurance* became trapped in Weddell Sea pack ice in 1915 (Dowdeswell et al., 2020)—Antarctic sea ice presents a formidable barrier to navigation. For much of the year, it obscures the underlying ocean located within the Antarctic seasonal ice zone (SIZ), largely preventing direct ("in situ") or satellite-based measurements from unraveling its secrets.

The significance of Antarctic sea ice extends far beyond the inconvenience it poses to intrepid researchers. Sea ice cover serves an important role in Earth's climate system by reflecting solar radiation, which modifies the planetary energy budget and dampens the rise of global temperature (Riihelä et al., 2021). Ice formation along the Antarctic continent also drives the global overturning circulation (Orsi et al., 1999, 2001), the "conveyer belt" current whose strength has been tied to the ocean's release and storage of heat and carbon over millennia (Stephens & Keeling, 2000; Sigman et al., 2010). Furthermore, sea ice serves as a protective buffer for Antarctic ice sheets, while its absence can contribute to ice shelf disintegration (Massom et al., 2018). Antarctic sea ice is crucial for marine habitats, with its declines in recent years linked to a collapse of emperor penguin colonies (Fretwell et al., 2023) and believed to endanger krill, the

keystone species of the Southern Ocean (Swadling et al., 2023) whose population health is essential for sustainable Antarctic commercial fisheries. Lastly, the influence of sea ice on maritime navigability means that its future trajectory could either limit or facilitate tourism to the Antarctic continent, already rapidly increasing (Liggett et al., 2024), as well as elevate interest in resource extraction or geopolitical threats to governance through the Antarctic Treaty System (Rintoul et al., 2018). Anticipating these societal impacts requires a stronger grasp on the physical science of sea ice-ocean-atmosphere interactions, which this dissertation seeks to contribute to.

Illuminating this complex physical system has become even more urgent as the sea ice-covered Southern Ocean appears to be on the cusp of rapid change. After 40 years of slowly increasing Antarctic sea ice extent (Parkinson, 2019)—in contrast to accelerating declines in Arctic sea ice—the Antarctic abruptly revealed its capacity for startling shifts. A record low sea ice minimum was observed in February 2022 (Raphael & Handcock, 2022; Turner et al., 2022) followed by a record low seasonal maximum in September 2023 (Roach & Meier, 2024), reductions that appear to stem from the emergence of a new regime around 2016 (Purich & Doddridge, 2023).

Subsurface ocean warming has been implicated as a potential cause of the sea ice drop (Meehl et al., 2019; Eayrs et al., 2021; L. Zhang et al., 2022; J. Wang et al., 2024), but the precise mechanisms at play are not yet clear. The processes through which warm subsurface water can be entrained into the surface ocean layer, where its heat will affect sea ice, are highly sensitive to the strength of its vertical density layering, which is controlled by the upper-ocean freshwater balance (Gordon & Huber, 1984; de Lavergne et al., 2014; Kjellsson et al., 2015; Bronselaer et al., 2018), and perturbations like turbulent ocean mixing from intense storms (McPhee et al., 1996, 1999; J. Zhang et al., 2013; Graham, Itkin, et al., 2019). Seminal work by Martinson (1990) and subsequent study by Wilson et al. (2019) highlighted how a powerful internal ice–ocean system feedback can determine the resiliency of Antarctic sea ice to perturbations from storms. This key negative feedback to ice growth occurs when brine rejection leads to ocean mixed-layer deepening,

entraining warmer deep water and thus moderating or sometimes fully counteracting further ice growth. It is within this theoretical framework that **Chapter 2** of this dissertation, published as Campbell et al. (2019) in *Nature*, endeavors to explain the sudden loss of sea ice within large offshore openings known as open-ocean polynyas, whose appearance in the Weddell Sea has been an enduring mystery in polar oceanography.

Compared to Arctic sea ice, the relatively thin Antarctic sea ice cover is more strongly affected by the overlying snow layer, which motivates study of this element of the coupled system. Yet limited observations exist to verify the role of snow deposited on sea ice in shaping thermodynamic ice growth and the freshwater balance of the upper ocean. Due to its insulating effect, snow cover in the Antarctic is understood to exert a profound influence on the rate of basal ice growth and consequent brine rejection into the ocean (Maykut, 1986). Furthermore, snow-ice formation—the freezing of snow and seawater following flooding of an ice floe due to its depression below the ocean surface—is prevalent across much of the Southern Ocean (Massom et al., 2001; Maksym & Markus, 2008; Arndt et al., 2024), unlike the Arctic Ocean, complicating the interpretation of satellite retrievals. These challenges and uncertainties heighten the need for renewed efforts to constrain the snow mass balance on Antarctic sea ice—such as the Lagrangian reconstruction model presented in **Chapter 3** of this dissertation.

Significant gaps remain in our understanding of how the Southern Ocean, its sea ice and overlying snow cover, and the atmosphere interact with each other. The persistent challenge of obtaining seasonally and regionally diverse observations of sea ice has translated to a limited ability for researchers to identify the role that ice–ocean freshwater exchange has played, if any, in the regime shift that has taken place in recent years. Yet it is known that water mass transformation in the Southern Ocean is closely tied to freshwater fluxes around Antarctica, which are controlled by the balance of brine rejection from the formation of sea ice and freshwater input primarily from the melt of ice and snow (Abernathey et al., 2016; Haumann et al., 2016b; Pellichero et al., 2018; Nissen et al., 2022). The need to better quantify these freshwater fluxes

through direct ocean observations serves as the primary motivation for **Chapter 4** of this dissertation.

Lastly, the final portion of this dissertation presents a retrospective assessment of an undergraduate introductory Python programming and ocean data analysis course, which was co-developed and co-taught remotely in 2020 with another graduate student, Katy Christensen. Our resulting mixed-methods study examines the challenges and merits of implementing evidence-based teaching practices and fostering a supportive learning environment in an undergraduate course—as well as the value of embedding scientific computing skills into a geoscience curriculum. This collaborative work, published as Campbell and Christensen et al. (2024) in *Journal of Geoscience Education*, comprises **Chapter 5** of this dissertation.

Chapter 2:

ANTARCTIC OFFSHORE POLYNYAS LINKED TO SOUTHERN HEMISPHERE CLIMATE ANOMALIES

This chapter is reproduced from:

Campbell, E.C., Wilson, E.A., Moore, G.W.K., Riser, S.C., Brayton, C.E., Mazloff, M.R., Talley, L.D. (2019). Antarctic offshore polynyas linked to Southern Hemisphere climate anomalies. *Nature*, 570(7761), 319-325. doi:10.1038/s41586-019-1294-0.

2.1 Abstract

Offshore Antarctic polynyas—large openings in the winter sea ice cover—are thought to be maintained by a rapid ventilation of deep-ocean heat through convective mixing. These rare phenomena may alter abyssal properties and circulation, yet their formation mechanisms are not well understood. Here we demonstrate that concurrent upper-ocean preconditioning and meteorological perturbations are responsible for the appearance of polynyas in the Weddell Sea region of the Southern Ocean. Autonomous profiling float observations—collected in 2016 and 2017 during the largest polynyas to form near the Maud Rise seamount since 1976—reveal that the polynyas were initiated and modulated by the passage of severe storms, and that intense heat loss drove deep overturning within them. Wind-driven upwelling of record strength weakened haline stratification in the upper ocean, thus favoring destabilization in 2016 and 2017. We show that previous Weddell polynyas probably developed under similarly anomalous conditions, which are associated with a mode of Southern Hemisphere climate variability that is predicted to strengthen as a result of anthropogenic climate change.

2.2 Introduction

The blanket of sea ice that develops around Antarctica each winter reduces interaction between the ocean and the atmosphere. By eliminating this barrier, large offshore openings in the sea ice pack—sometimes referred to as "open-ocean" or "sensible heat" polynyas—expose the ocean surface to heat extraction by the frigid atmosphere above. The resultant loss of surface buoyancy may drive convective overturning, maintaining ice-free conditions by liberating vast amounts of heat stored precariously just below the cold surface layer (Gordon, 1978; Martinson et al., 1981; Martinson, 1990). These deep mixing events may rapidly modify the ocean interior, with far-reaching implications for abyssal properties (Zanowski et al., 2015), large-scale ocean circulation (Martin et al., 2013; Cheon et al., 2014; C. Heuzé et al., 2015; Behrens et al., 2016; Pedro et al., 2016; L. Zhang et al., 2019), and carbon sequestration (Bernardello et al., 2014; Resplandy et al., 2015). Further, heat ventilation during offshore polynya events can be expected to affect the regional atmospheric state (Moore et al., 2002; Pedro et al., 2016; Weijer et al., 2017) and possibly global climate patterns through atmospheric teleconnections (Cabré et al., 2017).

The Antarctic Bottom Water that fills the global abyss today originates from the Antarctic continental margin (Amblas & Dowdeswell, 2018). However, in past glacial climates (J. A. Smith et al., 2010; Amblas & Dowdeswell, 2018)—when grounded ice sheets restricted formation at present-day sites—and perhaps even pre-industrial times (Broecker et al., 1999; de Lavergne et al., 2014), it may have been formed predominantly in offshore polynyas. This offshore deep water formation pathway is spuriously prevalent in many present-generation climate models, and introduces biases into the present and future Southern Ocean properties, circulation, and sea ice area (C. Heuzé et al., 2013; Kjellsson et al., 2015; Behrens et al., 2016; Reintges et al., 2017). In contrast to climate models, the modern satellite record (1972–present) shows only intermittent occurrence of offshore polynyas, the largest of which have appeared in the Weddell Sea region near the Maud Rise seamount and in the Cosmonaut Sea offshore of East Antarctica (Comiso & Gordon, 1987). In the most prominent example, early satellite observations revealed massive,

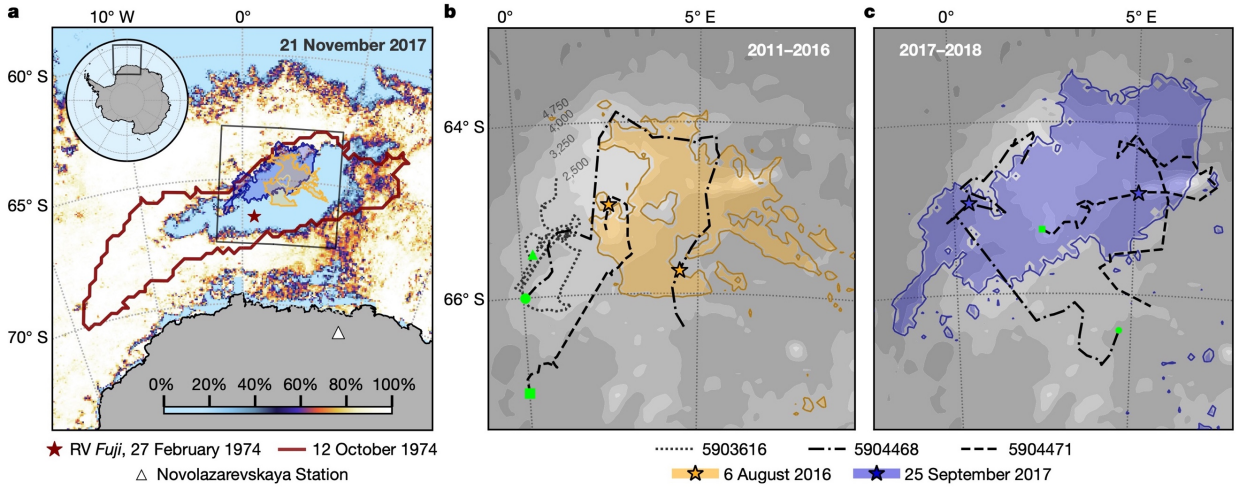

Figure 2.1: Polynyas of 1974, 2016, and 2017 in relation to profiling float trajectories near Maud Rise. (a) Sea ice concentration in the eastern Weddell sector of the Southern Ocean on 21 November 2017 from AMSR2-ASI, overlaid with 50% SIC contours showing polynya extent on 27 February 1974 (from Nimbus-5 ESMR; red contour) as well as on 6 August 2016 and 25 September 2017 (from AMSR2-ASI; orange and blue shading). The gray box encompasses the area shown in **(b)** and **(c)**. The red star identifies the MLS measurement obtained by research vessel (RV) *Fuji* on 27 February 1974 (shown in Figure 2.2b; Motoi et al., 1987), and the white triangle marks Novolazarevskaya Station, Queen Maud Land (see pressure record in Figure 2.5c). **(b)**, Bathymetry around Maud Rise (depth contours labeled in meters) with polynya extent from 2016 shaded as in **(a)**. Trajectories of floats 5903616 (December 2011 to June 2016), 5904468 (January 2015 to December 2016), and 5904471 (December 2014 to December 2016) begin at deployment locations (green) and include estimated locations during the 2016 polynya (orange stars). **(c)** Bathymetry as in **(b)** with polynya extent from 2017 shaded as in **(a)**. Trajectories of floats 5904468 (January 2017 to May 2018) and 5904471 (January 2017 to June 2018) begin at marked locations (green) and include estimated locations during the 2017 polynya (blue stars). See Supplementary Figure 2.7, Supplementary Figure 2.13 for full evolution of SIC during the 2016 and 2017 polynyas with float locations.

persistent Weddell polynyas over three consecutive winters from 1974 to 1976 (Carsey, 1980) (Figure 2.1a). Despite an absence of in situ ocean measurements during these events, bottom-reaching mixing within the polynyas was inferred from a hydrographic survey in 1977, which discovered erosion of normal temperature and salinity layering in one location (Gordon, 1978).

Shorter-lived, smaller openings have recurred near Maud Rise (Comiso & Gordon, 1987; Lindsay et al., 2004), with the largest reappearances in 2016 and 2017 (Swart et al., 2018; L. Zhang et al., 2019; Figure 2.1). Notably, the 2016–2017 polynyas accompanied a reversal of the positive trend in Antarctic sea ice extent that has been observed over the past three decades (G. Wang et al., 2019; Meehl et al., 2019), which raises the possibility that the Maud Rise events may reflect a

larger climate signal (L. Zhang et al., 2019). The tendency of polynyas to emerge near the seamount is not a coincidence. Theory, model simulations, and sparse observations suggest that topography–flow interactions at Maud Rise enhance upward heat fluxes and generate eddies that transmit divergent strain to the ice cover (Gordon & Huber, 1990; D. M. Holland, 2001; Lindsay et al., 2004; de Steur et al., 2007; see Kurtakoti et al. [2018] for a comprehensive discussion of related mechanisms). However, the intermittency of openings remains unexplained. More generally, the absence of detailed measurements of an offshore polynya has afforded little opportunity to validate the local processes and climate influences that have been put forward to explain how destabilization, polynya formation, and possibly deep overturning may occur within the ice-covered gyres of the Southern Ocean.

Here we present the first comprehensive analysis of the ocean, ice, and atmosphere during an offshore Antarctic polynya event. Passive microwave sea ice concentration (SIC) data and ERA-Interim (ERA-I) reanalysis fields depict the evolution of ice and atmosphere in 2016 and 2017 (Figure 2.2a, Figure 2.3a–b), whereas three under-ice profiling floats—purposefully trapped in the rotating Taylor column circulation over Maud Rise (de Steur et al., 2007) (Figure 2.1b–c)—together provide a continuous record from 2011–2018 (Figure 2.4). Two of these floats, deployed as part of the Southern Ocean Carbon and Climate Observations and Modeling (SOCCOM) Project, were present during the 2016–2017 polynya events. A synthesis of almost 4,000 past hydrographic observations from floats, ships, and instrumented seals near Maud Rise provides year-round climatological baselines, against which 2016 and 2017 may be compared (Supplementary Figure 2.6; Methods section “Hydrographic climatologies”). Lastly, a new record of past offshore polynyas reveals connections to large-scale climate fluctuations (Figure 2.5).

2.3 Methods

2.3.1 Regions

Various gridded fields were averaged within the Maud Rise region (63°–67°S, 0°–10°E), which loosely encompasses the 4,000 m isobath around the seamount (Figure 2.1b–c) and the area of polynya formation in 2016 and 2017. Other metrics were calculated within an area that we designate the eastern Weddell region (62°–68°S, 15°W–20°E), which spans the eastern Weddell, Lazarev, and western Riiser-Larsen seas. This larger area increases signal strength for records with spatial uncertainty or sparsity, such as discrete polynya events, storm statistics, and precipitation.

In the context of hydrographic observations, the Maud Rise region instead refers to a radius of 250 km from Maud Rise (65°S, 3°E; see Supplementary Figure 2.6). This encloses the "halo" of elevated subsurface heat content identified over the seamount (Muench et al., 2001; de Steur et al., 2007). Here the eastern Weddell region refers to hydrographic observations collected within 500 km of Maud Rise.

2.3.2 Sea ice

2.3.2.1 Sea ice concentration data

Satellite observations of Antarctic sea ice before 1972 are presently limited to a visible-band composite of September 1964 from the NASA Nimbus I mission, which showed a possible offshore polynya in the Weddell Sea (Meier et al., 2013). The quality of the imagery prevents conclusive identification. The modern passive microwave SIC era began in 1972 with the single-channel Nimbus-5 Electrically Scanning Microwave Radiometer (ESMR) (Carsey, 1980). We use daily SIC from December 1972 to May 1977 from the NSIDC Nimbus-5 ESMR v1 product on a 25-km polar stereographic grid, the result of heavy reprocessing (Parkinson et al., 2004). Gaps of weeks to months are present.

A series of more reliable multi-channel sensors followed. We use the merged NASA Goddard Space Flight Center v3 25-km product distributed by NSIDC from November 1978 to December 2017 (Meier, Fetterer, Savoie, et al., 2017). The merged Goddard product is nearly identical to the NOAA/NSIDC Climate Data Record (CDR), which is based on two well-validated SIC algorithms, with two main differences: additional manual quality control and inclusion of the period from 1978–1987, for which SIC data are available every other day (Meier et al., 2014; Meier, Fetterer, Savoie, et al., 2017). From January 2018 to February 2019, we use the NOAA/NSIDC Near-Real-Time (NRT) CDR v1 product (Meier, Fetterer, & Windnagel, 2017). The combined "NSIDC Merged" record from 1978–2019 was used for SIC climatology (Figure 2.2a) and polynya identification (Figure 2.5a). Nimbus-5 ESMR was included in the polynya record to highlight the 1974–1976 events, although precise quantitative comparison with NSIDC Merged is not possible. For more qualitative analyses, we use higher-resolution daily SIC data from the Advanced Microwave Scanning Radiometer (AMSR) sensors (see Figure 2.2a for comparison with NSIDC Merged). We use the University of Bremen v5 AMSR-E (2002–2011) and AMSR2 (2012–2019) products, derived using the ARTIST Sea Ice (ASI) algorithm at a resolution of 6.25 km (Spreen et al., 2008; Beitsch et al., 2014).

SIC climatology (Figure 2.2a) includes days with valid data from at least 75% of grid cells in the Maud Rise region. Median and 25%–75% IQR time series were generated by compositing over day-of-year, then filtering with a 7-day centered running mean. Along-trajectory SIC (Figure 2.4) represents the average SIC from AMSR2-ASI (from 4 July 2012 onwards) or NSIDC Merged (from 19 December 2011 to 3 July 2012) within a moving 1° latitude × 2° longitude box centered on the given or estimated location for each float profile.

2.3.2.2 Polynya identification

A polynya is defined as any nonlinear-shaped opening within sea ice that contains open water, brash ice, new ice, nilas, and/or young ice (World Meteorological Organization, 2014). Passive

microwave sensing generally underestimates SIC for new, thin ice, aiding the detection of polynyas (Comiso et al., 1997; Comiso & Steffen, 2001). Following past studies identifying polynyas in the Cosmonaut Sea (Comiso & Gordon, 1996; Arbetter et al., 2004), we define "polynya extent" as the sum of connected pixels (allowing diagonal connections) with SIC beneath some threshold. We excluded areas connected to the open ocean (that is, embayments), common during transitional freeze and melt periods, and calculated the centroid of individual openings. Patches of ice within connected open regions were negated using a binary dilation algorithm to ensure that polynya extent, rather than area, was quantified.

Figure 2.5a highlights midwinter openings that appear from closed ice cover, as occurred in 2016 and 2017 (Supplementary Figure 2.7, Supplementary Figure 2.13). These differ from early-winter embayments that later became enclosed, such as occurred in 1974 (Carsey, 1980). The latter probably reflects ocean preconditioning strong enough to permit overturning from slight amounts of ice growth or even cooling alone (a "thermal mode" of stratification; Martinson et al., 1981; Motoi et al., 1987; Gordon, 1991; Timmermann et al., 1999). This mode does not require perturbations such as storms, which we identify as critical for midwinter openings. For comparison, we included the 1974–1976 polynyas in our record despite their different mode of formation.

We consider the period of closed ice cover over Maud Rise to be delimited each winter by one week after the first date of 90% average SIC and one week before the last date of 90% SIC, consistent with climatological SIC (Lindsay et al., 2004). The one-week buffers account for gradual ice advance and retreat, during which small, brief openings frequently form via enclosure and climatological melt (Comiso & Gordon, 1987). Fixed start and/or end dates of 1 July and 31 October, consistent with climatology (Figure 2.2a), were used for freeze and/or melt seasons with already-established polynyas (1974–1976, 2017) or some gaps in SIC data (1973). Other winters with major data gaps (1972, 1977, 1978, 1987) were omitted from the record. The summed daily extent of polynyas with centroids in the eastern Weddell region was calculated using SIC

thresholds of 40%, 50%, and 60% for comparison, because grid connectivity is sensitive to SIC threshold. These thresholds reflect the dynamic mix of open water and new ice within polynyas (Comiso & Steffen, 2001), and lie between the low (for example, 15%) thresholds used to define the seasonal ice edge and high (for example, 80%) thresholds previously used to identify Antarctic offshore polynyas (Comiso & Gordon, 1996; Arbetter et al., 2004). Dates with non-zero total polynya extent at the 60% threshold, chosen to maximally differentiate years from one another, were designated "polynya days." As an approximation, polynya day counts from 1979–1986 were doubled because SIC data are available every other day. Our average SIC threshold of 50% was used in Figure 2.1a, which depicts the largest polynya identified within the Maud Rise region on each date, and Figure 2.2a, Figure 2.3a, which track the summed extent of polynyas with centroids in the eastern Weddell region.

The accuracy of our methodology was checked by visually inspecting SIC images. Our assessment is consistent with previous reports of Maud Rise polynyas in 1973 (Martinson et al., 1981; Comiso & Gordon, 1987), 1980 (Comiso & Gordon, 1987), 1994 (D. M. Holland, 2001; Muench et al., 2001; Venegas & Drinkwater, 2001), and 2005 (de Steur et al., 2007). A previous analysis for the Maud Rise region of total days with average SIC under 92% from 1979–2004 (Gordon et al., 2007) is qualitatively similar to our polynya record. Given the association of deep convection with coherent openings (Gordon, 1978), however, we focus on discrete polynya events, rather than slight reductions in SIC. We note that a small opening outside the detection parameters of our algorithm (and therefore absent in Figure 2.5a) appeared above Maud Rise in late October 2018, just before climatological melt.

2.3.3 Hydrography

2.3.3.1 Hydrographic data

Argo profiling floats drift at a depth of around 1,000 m and sample every 7–10 days, profiling on ascent (Riser et al., 2016). Sampling intervals are generally 2 dbar above 1,000 m and 100 dbar

below 1,000 m (Riser et al., 2018). Measurements are rated to accuracies of at least 0.005°C, 0.01 psu, and 2.5 dbar (Riser et al., 2016). An ice-avoidance algorithm monitors median temperature between 50 and 20 m, aborting ascent if near the freezing point, which indicates ice cover (Klatt et al., 2007; Wong & Riser, 2011; Riser et al., 2018). Under-ice profiles are stored without position fixes and transmitted upon spring ice melt. A rare exception is when a float surfaces within a polynya, as occurred in 2017 with SOCCOM floats 5904468 and 5904471 (Supplementary Figure 2.13). Because the algorithm requires three consecutive ice-free determinations (Riser et al., 2018), both floats inferred warm conditions in or near the polynya over about 21 days before surfacing.

All Argo temperature and salinity measurements (Supplementary Figure 2.6) south of 55°S and between 70°W and 50°E through 1 October 2018 were downloaded from the US-GODAE Global Data Assembly Center (GDAC) (Carval et al., 2017). We rejected profiles without timestamps, consecutive under-ice profiles with timestamps erroneously reflecting transmission upon ice melt, and data from floats affected by position and date jumps and other quality control issues.

Under-ice or missing positions (quality control flags “8” or “9”) were linearly interpolated, using profile timestamps to assign distances along great circle routes between known GPS fixes. Advanced methods, such as interpolation along contours of planetary potential vorticity, could reduce position uncertainty over some areas of the Weddell Sea; however, this may not be the case near Maud Rise, particularly to the southwest and northeast of the seamount (Chamberlain et al., 2018). Given the tendency of floats to remain trapped over Maud Rise (Figure 2.1b,c) owing to Taylor column dynamics (Muench et al., 2001; de Steur et al., 2007; Meredith et al., 2015), it is unlikely that floats 5903616, 5904468, and 5904471 deviated away from the seamount during the winters of 2012 through to 2017. SOCCOM float deployments were conducted with this phenomenon in mind (Talley et al., 2019).

Both real-time ("R") and delayed-mode ("D") data were obtained. Although both have passed automatic quality control checks, only delayed-mode data have undergone detailed quality control inspection, although sensor drift calibrations often extend automatically to real-time profiles (Carval et al., 2017). If a profile was available on delayed-mode, we used its adjusted parameters. The first cast within a profile file was selected if multiple were available. Only depths at which all three quality control flags for pressure, temperature, and salinity were good ("1") or probably good ("2") were extracted.

Float 5904468 represents an exception to this procedure. Drift in its salinity sensor, a Sea-Bird SBE-41CP conductivity cell, began in early 2016 at a rate of approximately 0.07 psu per year, constant with depth and linear in time. This drift was corrected through 13 May 2017 (profile #83) by the GDAC using standard procedures (weighted least-squares fit to deep climatology based on nearby Argo data). We extended this correction from 23 May 2017 (profile 84) to 8 May 2018 (profile 118) by subtracting the linear trend of 1,600–1,700 m average salinity, calculated from profiles linearly interpolated to 1-m spacing. Corrected 1,600–1,700 m average salinity agrees with that measured by the nearby float 5904471 over 2015–2018 (see Figure 2.1b–c) to within about 0.01 psu except for periods of mixing during the 2017 polynya. Profiles from 119 onwards were not used.

Salinity measurements are provided by the GDAC with a precision of 0.001 psu. The combination of weak vertical salinity gradient in the Weddell Sea and fine sampling interval (2 dbar) creates artificial 0.001 psu steps, generating spurious static instabilities. We applied a mild quadratic smoothing spline (*UnivariateSpline* from SciPy with smoothing factor s = 0.00015) to all float salinity profiles, attenuating these jumps while preserving integrity of the profile. This procedure essentially downsamples the salinity measurements to allow buoyancy frequency to be accurately resolved at all depths.

Dissolved oxygen measurements from floats 5904468 and 5904471 were downloaded from the SOCCOM quality-controlled archive (Johnson et al., 2019). Dissolved oxygen data from the

non-SOCCOM float 5903616 were obtained from the University of Washington (UW) Calibrated O_2 package, v1.1 (Drucker & Riser, 2016), with updated profiles provided by R. Drucker (personal communication). The sampling interval of dissolved oxygen is coarser than for CTD data, ranging from about 5 dbar above 100 m to about 100 dbar below 1,000 m (Riser et al., 2018). Dissolved oxygen optodes onboard most SOCCOM floats collect in-air samples for direct calibration, allowing for accuracy of about 1% of near-surface values (around 325 μmol kg^{-1}), or 3 μmol kg^{-1} (Johnson et al., 2017). The optode on 5903616 lacks this capability and instead has been calibrated to deep reference data, with an accuracy of about 2%, or 7 μmol kg^{-1} (Drucker & Riser, 2016). Comparison of UW-calibrated dissolved oxygen from 5903616 with SOCCOM-calibrated dissolved oxygen from 5904468 and 5904471—performed in surface-referenced potential density space—revealed a positive bias of about 6.0 μmol kg^{-1}, uniform in depth, during their overlap period at Maud Rise (2015–2016). We subtracted this offset from all UW-O_2 profiles by float 5903616.

Shipboard CTD and bottle data and instrumented elephant seal profiles (Supplementary Figure 2.6) featuring both temperature and salinity were obtained at original depth levels from the World Ocean Database 2018 prerelease (Boyer et al., 2018) with August 2018 additions. Depth levels were retained only if global quality control flags for depth, temperature, and salinity profiles as well as the three quality control flags at that depth were marked good ("0").

Instrumented elephant seals typically dive to about 600 m while foraging, although dives to 2,000 m occasionally occur (Roquet et al., 2014). CTD measurements begin at the deepest point of a dive and continue during ascent; data may be collected on as many as four dives per day (Boehme et al., 2009). Owing to data transfer and energy constraints, casts are transmitted in compressed form. A "broken-stick" algorithm selects 10–25 depths that best represent the profile; thus, resolution may be coarse for deeper profiles (Boehme et al., 2009; Roquet et al., 2014). The filters we apply when creating hydrographic climatologies account for this possibility (see below).

Measurement accuracy is estimated at 0.04°C and 0.03 psu (Siegelman et al., 2019), lower than for floats; satellite fixes are accurate to about 5 km (Roquet et al., 2014).

2.3.3.2 Derived oceanographic quantities

The Python implementation of the Gibbs SeaWater Oceanographic Toolbox of TEOS-10 (https://teos-10.github.io/GSW-Python/) was used to compute profiles of depth or pressure, potential temperature, surface-referenced potential density, and buoyancy (Brunt-Väisälä) frequency squared (N^2). We interpolated N^2 profiles to 1-m spacing, then applied a 50-m centered running mean. This filtering reduces noise and spikes, allowing patches of consistently low N^2 to be visible in Figure 2.4d and Supplementary Figure 2.11d despite the compressed vertical axis.

Mixed-layer depths (MLD; Figure 2.4, Supplementary Figure 2.8c, Supplementary Figure 2.11) were determined as the depth at which surface-referenced potential density exceeds its value at z_{ref} = 10 m, estimated using interpolation or nearest-neighbor extrapolation, by a threshold of $\Delta\sigma_\theta$ = 0.03 kg m^{-3} (de Boyer Montégut et al., 2004; Dong et al., 2008). Mixed-layer temperature (MLT) and mixed-layer salinity (MLS) were averaged from profiles interpolated to 0.1-m spacing and extrapolated to the surface. We note that MLDs sometimes shoaled sharply during the 2016 and 2017 polynyas, rather than deepening (Supplementary Figure 2.8c). This reflects the development of shallow fresh layers from ice melt (Figure 2.2b), as seen in idealized ice–ocean model experiments with storm perturbations (E. A. Wilson et al., 2019). The two profiling floats, sampling coarsely in time and space, did not observe active overturning, which probably occurred within plumes of horizontal scale O(100 m) occupying a fraction of the convection region (J. Marshall & Schott, 1999; Margirier et al., 2017; Testor et al., 2018) at locations with a weaker melt layer or pycnocline. The observed interior mixed layers (Supplementary Figure 2.11) may have been formed by nearby deep convection, communicated laterally through efficient mixing due to baroclinic instability.

Upper-ocean freshwater anomaly (Supplementary Figure 2.8e), or "salt deficit" (Martinson, 1990; Martinson & Iannuzzi, 1998; E. A. Wilson et al., 2019), was integrated from 0–250 m, encompassing MLDs in all seasons (see Supplementary Figure 2.8c) and salinity variability an order of magnitude greater than below 250 m. The metric was computed as in Wilson et al. (2019), in terms of the freshwater provided by melt of an equivalent sea ice thickness (units of meters):

$$\eta(250\text{ m}) = \frac{1}{\Delta S_i}\int_{0\text{ m}}^{250\text{ m}} [S(250\text{ m}) - S(z)]\, dz \qquad (2.1)$$

where S is salinity and ΔS_i is the approximate salinity difference between ocean and sea ice (about 30 psu; Martinson & Iannuzzi, 1998). Trapezoidal integration was applied to profiles interpolated and extrapolated as above.

To interpret the climatological 0–250 m freshwater anomaly (gray shading in Supplementary Figure 2.8e), we assume that brine rejection approximately balances ice melt from local and nonlocal sources, because Maud Rise is near the circumpolar line of zero annual net freshwater flux associated with sea ice (Haumann et al., 2016b), and that salt fluxes from geostrophic advection are relatively small. This implies that positive salt fluxes from Ekman upwelling (due to cyclonic wind stress curl; see Figure 2.5e) approximately balance precipitation and evaporation on an annual net basis. We thus interpret the seasonal cycle of climatological 0–250 m freshwater anomaly as predominantly reflecting brine rejection and ice melt. A similar approach has been used to estimate ice formation rates from instrumented seal profiles offshore of East Antarctica (Charrassin et al., 2008).

Convection resistance (CR) represents the buoyancy loss required for overturning to reach a given depth, H:

$$\mathrm{CR}(H) = \frac{g}{\rho_0}\int_{0\text{ m}}^{H} [\sigma_\theta(H) - \sigma_\theta(z)]\, dz \qquad (2.2)$$

where g is acceleration due to gravity, ρ_0 is a seawater reference density (1,027.8 kg m^{-3}), and σ_θ is surface-referenced potential density (Bailey et al., 2005; de Lavergne et al., 2014; Frajka-Williams et al., 2014). Depth sections of convection resistance illustrate that low interior

stratification combined with a weakened winter halocline, as occurred in 2016 and 2017, may permit deep-reaching convection near Maud Rise (Supplementary Figure 2.11e).

2.3.3.3 Composites of float time series

Data from floats 5903616 (active only until 2 June 2016), 5904468, and 5904471 were combined to create time series of MLS, MLD, MLT, and 0–250 m freshwater anomaly in 2016 and 2017 (Figure 2.2b, Supplementary Figure 2.8c–e). Float measurements were linearly interpolated to daily resolution, and the daily means (for MLT and MLD), maxima (for MLS), or minima (for freshwater anomaly) were calculated. MLS and MLT agree between the three floats to within 0.05 psu and 0.25°C, except in the 2–3 months after ice melt. Freshwater anomaly and MLD are more variable, but fluctuations generally occur synchronously. Maximum MLS and minimum freshwater anomaly were chosen to highlight the most extreme preconditioning observed near Maud Rise, motivated by the notion that overturning will preferentially occur where stratification is weakest. Given the substantial spatial inhomogeneity around Maud Rise (de Steur et al., 2007; Kurtakoti et al., 2018), sampling by 2–3 floats probably underestimates the most extreme preconditioning that occurred in 2016–2017.

The red line in Figure 2.2b represents the MLS required to eliminate stratification between the mixed layer and 250 m, at which point initiation of deep convection would be trivial (Martinson, 1990). This "overturning limit" is fresher than salinity at 250 m owing to the destabilizing warmth of the thermocline (E. A. Wilson et al., 2019). Its value was determined as the MLS at which surface density, computed using composite (average) MLT, would exceed composite surface-referenced potential density at 250 m. The use of surface density neglects the development of thermobaric instabilities, which could hasten overturning near this limit of zero stratification (McPhee, 2000).

2.3.3.4 Salinity fluxes from upwelling

Upwelling due to divergence of Ekman transport can cause heat and salt fluxes into the mixed layer (Timmermann et al., 1999; Pellichero et al., 2017; Meehl et al., 2019). Vertical velocity w_{Ek} at the base of the Ekman layer is related to wind stress curl (Talley, 2011) in the absence of ice cover:

$$w_{\mathrm{Ek}} = \nabla \cdot \boldsymbol{U}_{\mathrm{Ek}} = \boldsymbol{k} \cdot \nabla \times \frac{\boldsymbol{\tau}}{\rho_0 f} \tag{2.3}$$

where $\boldsymbol{U}_{\mathrm{Ek}}$ is the horizontal vector Ekman transport, $\boldsymbol{k}$ is the vertical unit vector, $\boldsymbol{\tau}$ is the vector surface wind stress, ρ_0 is a seawater reference density (about 1027.8 kg m^{-3}), and f is the Coriolis parameter.

Upwelling prevails over Maud Rise because wind stress curl is consistently negative (Figure 2.5e). We estimated, in back-of-the-envelope fashion, the anomalous mixed-layer salt flux resulting from record cyclonic wind stress curl over Maud Rise in the ice-free months of 2015 and 2016—before the 2016 polynya—compared to a typical previous year (Figure 2.5e; Methods section "Atmospheric reanalysis"). The average wind stress curl from ERA-I over 1979–2014 was -2.06×10^{-7} N m^{-3}, while the averages for January–May 2015 and 2016 were -2.90×10^{-7} N m^{-3} and -3.08×10^{-7} N m^{-3}, respectively, increasing upwelling by 8.0 m and 9.8 m.

To estimate the corresponding mixed-layer salt flux, salinity gradients across the base of the mixed layer were measured using observations from floats 5903616, 5904468, and 5904471 over January–May 2015 and 2016. MLD during these periods averaged 41.3 m and 56.2 m, respectively. MLS averaged 33.90 psu and 34.22 psu, while the average salinities of depth levels between the time-varying MLD and 7.8 m or 9.6 m below the MLD were 34.09 psu and 34.34 psu, respectively. Expected MLS elevation was computed using these values:

$$\Delta S_{\mathrm{ml}} = \frac{h_{\mathrm{up}} S_{\mathrm{up}} + \left(h_{\mathrm{ml}} - h_{\mathrm{up}}\right) S_{\mathrm{ml}}}{h_{\mathrm{ml}}} - S_{\mathrm{ml}} \tag{2.4}$$

where S_{ml} and S_{up} are MLS and sub-mixed-layer salinity, and h_{ml} and h_{up} represent MLD and thickness of the upwelled layer. We determine that additional Ekman upwelling elevated MLS by

at least 0.04 psu in 2015 and 0.02 psu in 2016, for a total of at least 0.06 psu. These are lower bounds because upwelling continues in winter, although the absence of ice–ocean stress data precludes the estimation of upwelling during ice-covered months. Statistically propagating the Argo salinity measurement accuracy of ±0.01 psu yields a ΔS_{ml} uncertainty of just ±0.002 psu; however, additional contributions from the exclusion of ice-covered months, coarseness of sampling, spatial inhomogeneity, and time averaging are less easily quantified.

2.3.3.5 Hydrographic climatologies

Float, shipboard, and instrumented seal measurements were used to create climatologies of average MLS, MLD, MLT, and 0–250 m freshwater anomaly near Maud Rise (R < 250 km) and away from Maud Rise (250 km < R < 500 km; Figure 2.2b, Supplementary Figure 2.8c–e). Profiles with a shallowest measurement below 30 m, deepest measurement above 250 m, or MLD greater than 250 m were excluded, ensuring that the mixed layer and upper seasonal pycnocline were captured. These filters yielded 1,035 float profiles from 50 floats, 265 shipboard casts, and 124 seal profiles near Maud Rise, and 1,523 float profiles from 79 floats, 510 shipboard casts, and 445 seal profiles away from Maud Rise (Supplementary Figure 2.6). Mean and median years of the compiled observations are 2008 and 2012 for Maud Rise and 2006 and 2008 away from Maud Rise. Fewer than 1% of these observations were collected before 1970.

Calculated metrics were composited by day-of-year within 365 overlapping 21-day bins, looping from December to January. Median and 25%–75% IQR were computed for each bin instead of mean and standard deviation to reduce sensitivity to outliers and reflect skewness in spatial and temporal variability. Lastly, a 21-day centered running mean was applied. We note that the absence of abrupt changes in these metrics—for example, sharp increases in MLS during ice formation—is an artifact of the compositing method. Years featuring early and late ice formation are combined, for example, resulting in gradual changes.

2.3.3.6 Sub-pycnocline temperature records

Supplementary Figure 2.14d–e depicts 15.5 years (2002–2017) of 258-m temperature anomalies from climatology within the eastern Weddell region (R < 500 km from Maud Rise) based on 2,445 float, 151 shipboard, and 407 seal profiles, and 250–1,000 m average temperature anomalies based on 2,421 float and 133 shipboard profiles and one seal profile. We compare observations with a gridded 1/4° monthly climatology, the 2018 WOCE/Argo Global Hydrographic Climatology (WAGHC; Gouretski, 2018).

We included profiles with a shallowest measurement above 30 m and a deepest measurement below the depth(s) of interest. Temperatures at 258 m or at the 14 WAGHC levels from 218–1,050 m were estimated from each profile using linear interpolation. Observations were co-located in space with WAGHC fields using nearest-neighbor interpolation, then the climatological value on a given day-of-year was estimated using linear interpolation over values assigned to the 15th of each month. The average 250–1,000 m anomaly was computed after linearly interpolating anomalies at the 14 depths (218–1,050 m) to 1-m spacing. Lastly, the anomalies were binned biannually, with at least five samples required in each bin. Supplementary Figure 2.14d–e displays median and 25%–75% IQR values in addition to violin plots, which represent a kernel density distribution of the binned data.

Decadal changes in Weddell gyre heat content are probably closely related to Circumpolar Deep Water inflow variability (Fahrbach et al., 2011; Ryan et al., 2016), but uncertainty remains regarding the importance of internal processes such as offshore polynyas (Smedsrud, 2005; Fahrbach et al., 2006). Ventilation during the 1974–1976 openings cooled depths from 200–2,700 m by 0.4°C within the polynya area (Gordon, 1982), a signal that propagated into deep and abyssal waters away from the Weddell Sea through advective transport and wave mechanisms (Zanowski et al., 2015; Zanowski & Hallberg, 2017). Nonetheless, local rebound in heat content near Maud Rise had occurred by 1984 (Smedsrud, 2005). The absence of polynya activity in the

latter half of the 1980s (Figure 2.5a) is thus further evidence against a recurrence timescale governed exclusively by deep heat recharge.

2.3.3.7 Polynya heat flux estimates

Gradual deep cooling and freshening observed by both floats from 2015 to early 2016 (Supplementary Figure 2.11a–b) probably reflects movement of floats from the warm "halo" encircling Maud Rise into its overlying Taylor column regime (Figure 2.1b). However, subsequent deep anomalies are inconsistent with hydrographic surveys conducted in 1994 (Muench et al., 2001) and 2005 (de Steur et al., 2007), despite conditions coincidentally also favoring polynya formation in those years (Figure 2.5a). We thus attribute these abrupt decreases in heat content primarily to ventilation during the 2016 polynya. We difference sub-mixed-layer potential temperature profiles for each float immediately before 27 July 2016 with those over the five succeeding months until 1 January 2017 to estimate the rate of convective heat loss (Q, in W m^{-2}):

$$Q = \frac{\rho_0 c_p}{\Delta t} \int_{1650\ \mathrm{m}}^{200\ \mathrm{m}} \Delta\theta(z)\,dz \qquad (2.5)$$

where ρ_0 is a seawater reference density (1,027.8 kg m^{-3}), c_p is the specific heat of seawater (3,850 J kg^{-1} °C^{-1}), Δt is the polynya duration (21 days), and $\Delta\theta(z)$ is the change in potential temperature at depth z. The median heat flux is 208 W m^{-2} from 31 profiles, 74% of which yield estimates between 0 W m^{-2} and the average ocean–atmosphere turbulent heat flux during the polynya, 252 W m^{-2} (Figure 2.3c, Supplementary Figure 2.12). Estimates outside this range may reflect lateral mixing or float displacement.

2.3.4 Atmosphere

2.3.4.1 Southern Annular Mode

In its positive phase, SAM is characterized by lower pressure over Antarctica than over mid-latitudes, associated with poleward displacement of the mid-latitude westerly jet (Thompson et

al., 2011). We use a monthly index of SAM from 1972–2019 (G. J. Marshall, 2003). The index is filtered using a two-year centered running mean in Figure 2.5b to highlight lower-frequency fluctuations.

2.3.4.2 Atmospheric reanalysis

Six-hourly and monthly-mean 0.75°-resolution surface-level analysis and forecast fields from ERA-Interim (ERA-I), a third-generation global reanalysis product (Dee et al., 2011), were obtained from January 1979 to December 2018. Forecast output was de-accumulated, and climatologies were constructed by compositing over day-of-year, calculating mean and 25%–75% IQR values, and filtering using a seven-day centered running mean.

10-m wind speed (Figure 2.3b, Supplementary Figure 2.9) was calculated as:

$$|\boldsymbol{u}| = \sqrt{u^2 + v^2}\,. \tag{2.6}$$

Wind stress curl (Figure 2.5e) was computed using second-order-accurate central differencing:

$$\nabla \times \boldsymbol{\tau} = \frac{\Delta \tau_y}{\Delta x} - \frac{\Delta \tau_x}{\Delta y}\,. \tag{2.7}$$

Given the uncertainty of ice motion products near ice–ocean boundaries and in areas of low SIC (Sumata et al., 2014), we instead estimate wind-forced ice drift velocities (u_i and v_i) from ERA-I using a "rule-of-thumb" for thin Weddell Sea pack ice that suggests drift is around 3% of wind speed at a turning angle of around 23° to the left of winds (Martinson & Wamser, 1990). Others have used a scaling of 2% and turning angle of 30° (Zhaomin Wang et al., 2015); our results are not sensitive to the choice of these parameters. Potential ice divergence due to wind forcing (Supplementary Figure 2.10) was inferred from these drift velocities:

$$\nabla \cdot \boldsymbol{u}_i = \frac{\Delta u_i}{\Delta x} + \frac{\Delta v_i}{\Delta y}\,. \tag{2.8}$$

Because geostrophic winds are nondivergent, the response of a spatially uniform ice cover will also be nondivergent despite the turning angle (Kottmeier & Sellmann, 1996). Ice divergence

therefore requires deviations from geostrophy, such as sub-geostrophic speeds associated with gradient winds in an intense cyclone, or spatially inhomogeneous ice properties. Supplementary Figure 2.10 highlights potential ice divergence associated with the former. Divergence during storm episodes probably also occurs owing to ice deformation on shorter spatial scales than those resolved by ERA-I (Itkin et al., 2017).

Under weak winds, ocean heat loss within a polynya may warm the lower atmosphere enough to generate a persistent low-pressure anomaly, cyclonic wind field, and ice divergence, thus maintaining the opening (Martinson et al., 1981; Timmermann et al., 1999). This positive feedback is not apparent in ERA-I in 2016 (Supplementary Figure 2.10) or 2017 (not shown), perhaps because anomalies are quickly advected downstream by background winds and transient storms.

Ocean-atmosphere turbulent heat fluxes were estimated from ERA-I fields using the COARE 2.0 bulk flux algorithm (Fairall et al., 1996), as described in Renfrew et al. (2002). Calculated open-water heat fluxes for each grid cell were scaled by open water fraction (1 – SIC) from ERA-I and averaged within the Maud Rise region. Dividing by the mean open water fraction yields the average heat flux within the 2016 polynya (Figure 2.3c).

2.3.4.3 Weddell Low

We designate the Weddell Low as the climatological low mean sea-level pressure (MSLP) center over the Riiser-Larsen Sea, around which a large-scale geostrophic wind field circulates (P. R. Holland & Kwok, 2012). The curl of this wind field has a leading role in controlling the strength of the Weddell gyre (Jullion et al., 2010; Meijers et al., 2016; Armitage et al., 2018). By analogy to the Amundsen Sea Low (Fogt et al., 2012), the Weddell Low may be expected to modulate cyclone central pressures and spatial density across the Weddell Sea region. We characterize the Weddell Low as the region ±1σ in latitude and longitude around the minimum ERA-I monthly mean MSLP identified within 60°–70°S, 60°W–60°E. The average minimum occurs at 64.4°S, 16.7°E,

resulting in an area bounded by 61.9°–66.8°S, 12.5°W–45.8°E. The Weddell Low index represents monthly mean MSLP within this region, filtered using a two-year centered running mean as above (Figure 2.5c).

2.3.4.4 Meteorological station records

To complement and extend the reanalysis record, Figure 2.5c also includes MSLP data from Novolazarevskaya Station on the Queen Maud Land coast of Antarctica (71°S, 12°E; location marked in Figure 2.1a; data available from 1972–2019). Monthly means were obtained from the Reference Antarctic Data for Environmental Research (READER) archive (Turner et al., 2004). For comparison, Supplementary Figure 2.14b shows monthly mean MSLP from the nearby Neumayer (71°S, 8°W; 1981–2019) and Syowa (69°S, 40°E; 1957–2019) Stations from the READER archive and from Maitri Station (71°S, 12°E; 1990–2019), South African National Antarctic Expedition Station (SANAE; 70°S, 2°W; 1973–1994), and SANAE-Automatic Weather Station (SANAE-AWS; 72°S, 3°W; 1997–2019), obtained as subdaily records from the NOAA-NCEI Integrated Surface Database (ISD; A. Smith et al., 2011). The first two years of the Neumayer and SANAE-AWS records were dropped owing to sparse data and quality issues. As above, two-year centered running means are presented. We observe consistent fluctuations between the station records. Strong correlation between Novolazarevskaya and the Weddell Low (r = 0.84; see Supplementary Table 2.1) suggests that the former is a useful proxy for the latter during the pre-ERA-I period.

2.3.4.5 Storm identification

A high degree of similarity between six-hourly MSLP from SANAE-AWS, south of Maud Rise, and the nearest ERA-I grid cell from 1997–2019 (r = 0.93; mean absolute deviation = 2.2 hPa; mean bias = 0.8 hPa) suggests that ERA-I skillfully represents variability near Maud Rise associated with synoptic-scale weather systems. Validation with independent pressure data from drifting ice buoys in the Bellingshausen Sea also suggests that ERA-I is skilled at capturing individual storms

in the Southern Ocean, particularly relative to other available reanalyses(Bracegirdle, 2013). We identify the passage of particularly intense cyclones within the Maud Rise (Figure 2.2a, Figure 2.3a) and eastern Weddell (Figure 2.5d) regions. Previous work indicates that storms with a central pressure below 950 hPa represent the most extreme 5% of individually tracked cyclones at a latitude of 65°S (Patoux et al., 2009). Adopting this pressure threshold, we find (coincidentally) that 5.3% of ERA-I six-hourly MSLP fields feature one or more grid cells below 950 hPa within the eastern Weddell region. Statistically, this corresponds to a wind speed threshold of about 20 m s^{-1}, which is exceeded in 5.8% of instantaneous six-hourly fields. Days on which either criteria are met are designated “storm days” (see Supplementary Figure 2.9). These are denoted by vertical bars in Figure 2.2a, Figure 2.3a, Supplementary Figure 2.8a and counted annually during ice-covered winter (May to October) in Figure 2.5d. In plots spanning 2016 and 2017, sequences of storm days separated by a single non-storm day are aggregated for ease of visualization.

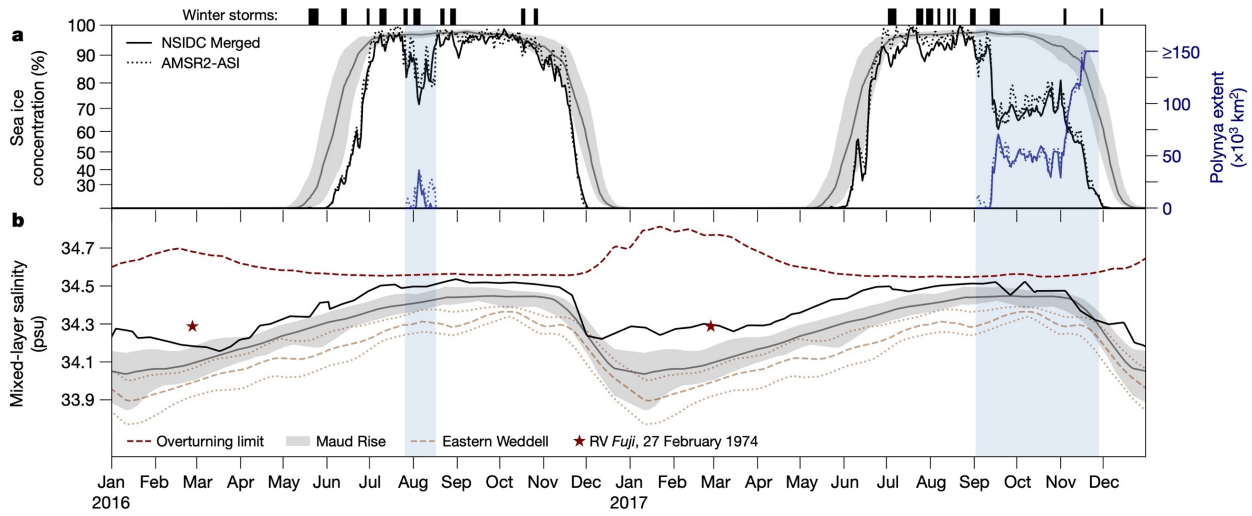

Figure 2.2: Storms, sea ice concentration, and mixed-layer salinity at Maud Rise in 2016 and 2017. Marked at the top are intense winter storm events near Maud Rise (also see Supplementary Figure 2.9 and Methods section "Storm identification"). **(a)** Average daily SIC within the Maud Rise region (63°–67°S, 0°–10°E) from NSIDC Merged (solid black line) and AMSR2-ASI (dashed black line) in 2016 and 2017. SIC climatology from NSIDC Merged (1978–2019) is shown as median (gray line) and 25%–75% interquartile range (IQR; gray shading). Note the stretched *y* axis. Polynya extent is quantified (blue lines) during the 2016 and 2017 events (vertical blue shading). **(b)** Composite of the highest mixed-layer average salinity (MLS) measured by floats 5903616, 5904468, and 5904471 in 2016 and 2017 (black line; see Methods sections "Derived oceanographic quantities" and "Composites of float time series"). MLS climatology for the Maud Rise region (R < 250 km from 65°S, 3°E) is shown as median (gray line) and IQR (gray shading); climatology for the eastern Weddell region away from Maud Rise (250 < R < 500 km) is presented for comparison (light brown dashed and dotted lines for median and IQR, respectively; see Methods section "Hydrographic climatologies"). Red stars indicate the MLS measured by RV *Fuji* on 27 February 1974 at 66.5°S, 1.2°E, near Maud Rise (Motoi et al., 1987; see red star in Figure 2.1a). The MLS required to eliminate 0–250 m stratification, the "overturning limit," is shown in red (see Methods section "Composites of float time series").

2.4 Results and discussion

2.4.1 Polynya formation in 2016

On 27 July 2016, a month after ice formed over Maud Rise, a sliver of open water appeared above its northeast flank (Figure 2.2a, Supplementary Figure 2.7), which is a location that is predisposed for reduced SIC (D. M. Holland, 2001; Lindsay et al., 2004; Kurtakoti et al., 2018). Despite below-freezing air temperatures, the polynya eventually expanded to 33,000 km² (Figure 2.3a and Supplementary Figure 2.8b), making it the largest opening from full ice cover since 1976 (Figure

2.5a). The polynya closed 21 days later, on 17 August 2016 (Figure 2.3a, Supplementary Figure 2.7). An exceptionally rapid melt season across all Antarctic sectors followed in November. Although most explanations for this unprecedented sea ice retreat have focused on the variability in atmospheric circulation associated with tropically forced teleconnections (G. Wang et al., 2019; Meehl et al., 2019; and references therein), wind-driven upwelling of warm subsurface water may have also contributed in some regions (Meehl et al., 2019).

Profiling float data near Maud Rise show that a late freeze in 2016 (Figure 2.2a) followed 4–5 months of increased mixed-layer temperature (Supplementary Figure 2.8d) and mixed-layer salinity (MLS; Figure 2.2b). These anomalies are consistent with strengthened upwelling and entrainment of Weddell Deep Water, which is warmer and saltier than the overlying upper ocean (Figure 2.4a–b). Abnormal ocean conditions persisted into the period of ice formation. Early July featured the two highest MLS measurements in our eastern Weddell record for that month, which correspond to a maximum elevation of MLS above the Maud Rise climatology of +0.12 psu (Figure 2.2b).

We attribute the 2016 polynya primarily to preconditioning from these salinity anomalies. Under sea ice, stratification is governed by fluctuations in MLS. The special vulnerability of the Maud Rise water column to overturning is in part due to its high climatological MLS relative to that of the surrounding region (Gordon & Huber, 1990; Figure 2.2b). In a normal winter, brine rejection from ice growth over Maud Rise brings the pycnocline to the brink of erosion (E. A. Wilson et al., 2019). Complete destabilization, however, is averted through entrainment of warm thermocline water as the mixed layer deepens. Ventilation of this "thermal barrier" into the mixed layer suppresses ice growth, providing a negative feedback that preserves stratification (Martinson, 1990; Martinson & Iannuzzi, 1998; Timmermann et al., 1999; McPhee, 2000; E. A. Wilson et al., 2019). However, by mid-July 2016, an increase in MLS of just 0.05 psu would have eliminated stratification and triggered deep convection (red line in Figure 2.2b), less than a third of that required in a normal year.

In this precarious state, we infer that intense storms overrode the stabilizing negative feedback and initiated deep convection by providing two sudden perturbations: ice divergence and enhanced turbulent mixing. Divergence may occur across a continuum of spatial scales owing to ice deformation and drift (Itkin et al., 2017), and enables rapid ice growth and brine rejection while preventing immediate stabilization from ice melt. Wind-driven turbulent mixing entrains heat and salt into the mixed layer (Martinson & Iannuzzi, 1998), a response that is amplified under weak stratification (E. A. Wilson et al., 2019). The heat may melt ice, as idealized model experiments with storm perturbations have demonstrated for the Maud Rise ice–ocean system (E. A. Wilson et al., 2019). Although ice may reform, negating the stabilizing buoyancy input of melt, entrained salt will linger and will reduce stability (Martinson, 1990; Martinson & Iannuzzi, 1998; Timmermann et al., 1999). These perturbations have been observed to co-occur: during a 1994 winter field campaign over Maud Rise, two violent storms elevated mixed-layer temperature by 0.3°C above freezing and opened leads that forced an evacuation of the researchers' ice camp (McPhee et al., 1996). Young, possibly thinner ice in July 2016 would have been particularly susceptible to wind forcing (Itkin et al., 2017), which would enhance both mechanisms.

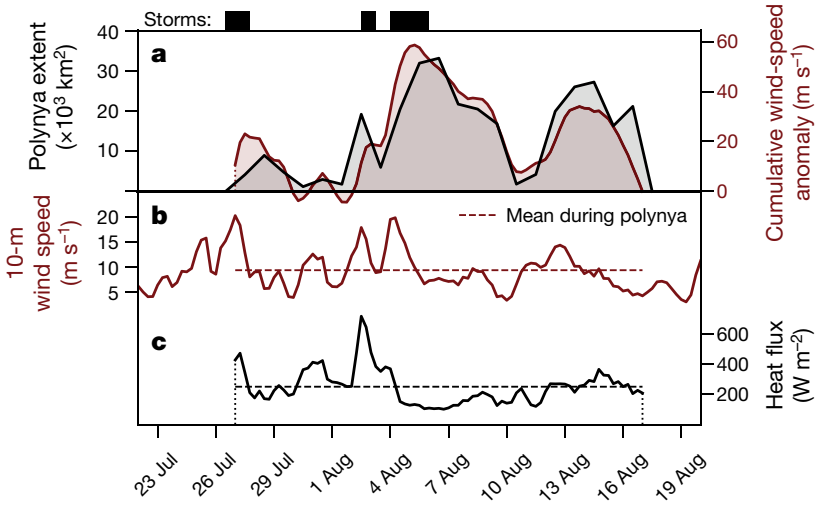

Figure 2.3: Local meteorology and heat loss during the 2016 polynya. Intense winter storm events near Maud Rise are identified at the top, as in Figure 2.2. **(a)** Daily polynya extent from AMSR2-ASI (see Methods section "Polynya identification") is shaded in black. Overlaid in red is the cumulative sum of the anomaly of 10-m wind speed (as shown in **[b]**) from its mean value during the 2016 polynya. **(b)** Average six-hourly 10-m wind speed from ERA-I reanalysis within the Maud Rise region (63°–67°S, 0°–10°E). c, Average six-hourly ocean-atmosphere turbulent heat flux within the polynya (see Methods section "Atmospheric reanalysis"). Dashed lines indicate mean values during the polynya event.

Using atmospheric reanalysis, we identify the passage of the most severe cyclones near Maud Rise (see Methods section "Storm identification"). Most storms coincide with marked reductions in average SIC (Figure 2.2a, Supplementary Figure 2.9). Indeed, the 2016 polynya opened during a storm that featured 10-m wind speeds of up to 25 m s^{-1} and surface pressures as low as 947 hPa (Figure 2.3a, Supplementary Figure 2.9a). We find a surprising correspondence (r = 0.81) between the evolution of the extent of the polynya in 2016 and the cumulative wind-speed anomaly from a baseline value (Figure 2.3a), which indicates that the polynya grew with strong winds from storms and shrank during quiescent periods. Along its ice-covered perimeter, high winds may have triggered ice loss and destabilization through turbulent mixing. Within its interior, heat extraction and salty turbulent entrainment from high winds would have driven convection, preventing ice from reforming. During a storm on 2 August, the polynya expanded concurrently with ocean–atmosphere turbulent heat fluxes of up to 718 W m^{-2} (Figure 2.3b–c) and possible ice divergence (Supplementary Figure 2.10). A lapse in storm activity and a reduction

in heat flux apparently enabled the polynya to close (Figure 2.3a,c). Nonetheless, MLS remained near the overturning limit throughout the winter (Figure 2.2b). A storm on 28–30 August caused substantial SIC reduction and warm entrainment (Supplementary Figure 2.8d, Supplementary Figure 2.9a), and in late October—following two storms (Figure 2.2a)—a distinct polynya appeared south of Maud Rise, and eventually grew during climatological melt to encompass much of the eastern Weddell (Supplementary Figure 2.7).

2.4.2 Deep mixing and resultant preconditioning

We observe an abrupt appearance of anomalies in the ocean interior after the opening of the 2016 polynya: cooling of 0.2°C, freshening of 0.025 psu, and an increase in dissolved oxygen of 10 μmol kg^{-1} at a depth of around 650 m (Figure 2.4a–c, Supplementary Figure 2.11). Co-located with these modified patches are bands of near-zero buoyancy frequency (N), which indicate nearly absent stratification (Figure 2.4d). These properties reflect recent mixing with winter surface water, as observed during open-ocean convection in the subpolar North Atlantic (Våge et al., 2009). The apparent strengthening and deepening of interior mixed layers after the polynya—observed by both floats (Supplementary Figure 2.11)—suggest lateral mixing and homogenization of remnant convective plumes, which probably evolved on scales missed by the coarse sampling in space and time (see Methods section “Derived oceanographic quantities”). The isolated intrusion from 500 m to 800 m, which is embedded within displaced isotherms and isohalines (Figure 2.4a–b), resembles the submesoscale coherent vortices that are frequently observed after open-ocean convection, such as in the Mediterranean Sea (Testor et al., 2018). Together these fingerprints identify the altered water mass as the product of deep-reaching convective mixing.

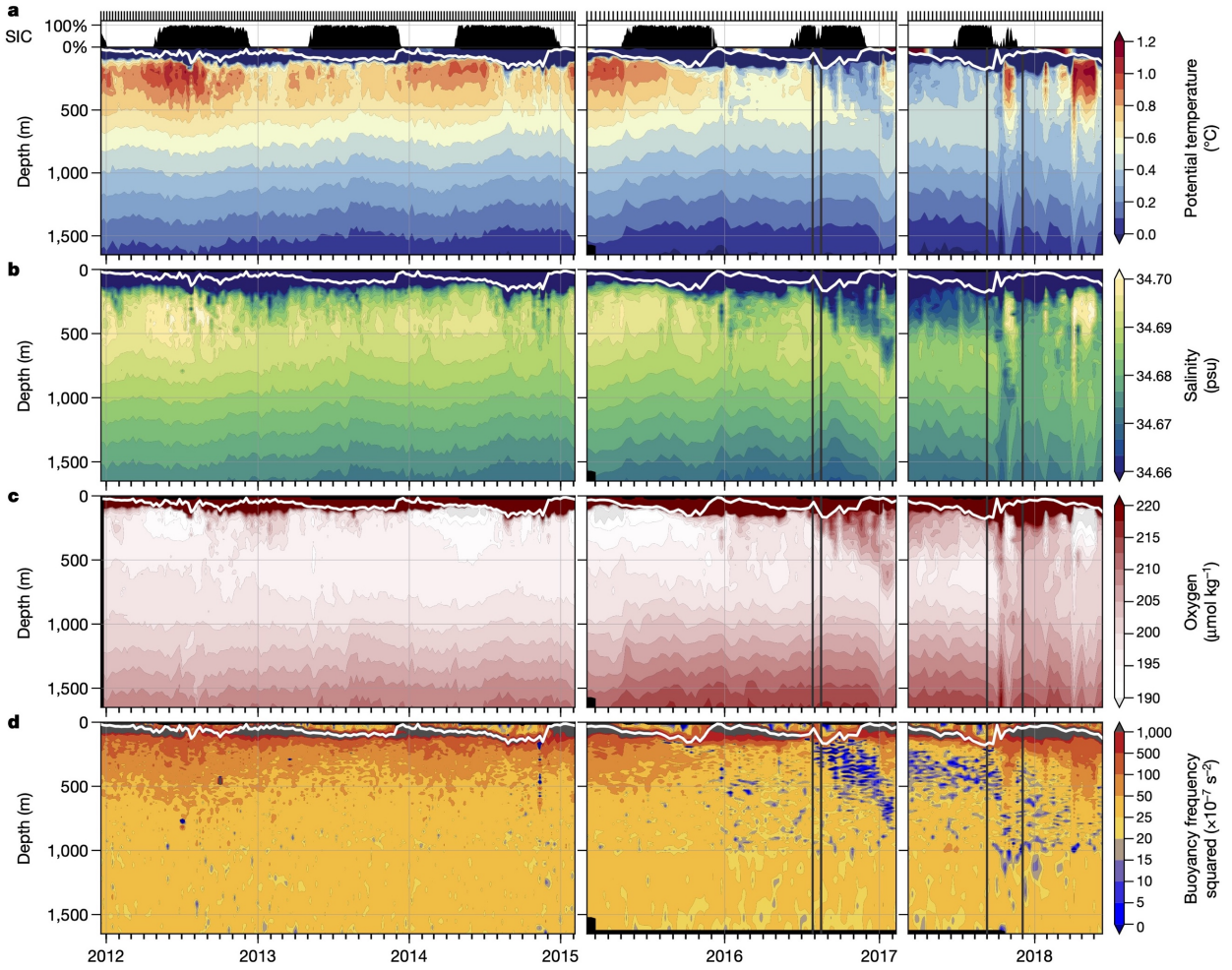

Figure 2.4: Hydrographic observations from Maud Rise from 2011–2018. (a–d) Continuous-time depth sections of potential temperature **(a)**, salinity **(b)**, dissolved oxygen **(c)**, and buoyancy frequency squared (N^2) **(d)** assembled using observations from profiling floats 5903616 (left), 5904468 (center), and 5904471 (right). Individual profiles are marked at the top (black ticks). Mixed-layer depth is indicated in white. Vertical lines in each panel mark the start and end dates of the 2016 and 2017 polynyas. Along-trajectory SIC, primarily from AMSR2-ASI, is shaded at the top in black (see Methods section "Sea ice concentration data"). See Supplementary Figure 2.11 for the complete time range of data from each float.

Analysis of the reduced deep heat content in post-polynya profiles yields estimated ventilation rates (Methods section "Polynya heat flux estimates") that approach the average ocean–atmosphere turbulent heat flux during the 2016 polynya (252 W m^{-2}; Figure 2.3c, Supplementary Figure 2.12). This close correspondence suggests that deep convection was driven primarily by a continuous loss of surface buoyancy, rather than by the interior thermobaric mixing that has been invoked to explain overturning near Maud Rise (McPhee, 2000). Persistent above-

freezing mixed-layer temperature provides additional evidence for continuous thermal convection (Supplementary Figure 2.8d). Nonetheless, thermobaricity may have modulated the depth of mixing by supplying additional kinetic energy to plumes descending across the pycnocline.

Crucially, the deep freshening that accompanied heat loss in 2016 implies a net upwards mixing of salt (Motoi et al., 1987), thus reducing stability in 2017. This upwards transfer is corroborated by an increase in total salt content from 0 m to 250 m—equivalent to the effect of brine rejection from 0.46 m of ice formation (Supplementary Figure 2.8e)—as well as an average MLS elevation of 0.15 psu over the ice-free months of 2017 (Figure 2.2b). This extreme degree of preconditioning is comparable to that observed near Maud Rise before the 1974 polynya (Motoi et al., 1987; red stars in Figure 2.1a, Figure 2.2b).

2.4.3 Polynya recurrence in 2017

Low upper-ocean stability in early 2017 preconditioned the region for the emergence of a larger polynya than that formed in 2016 (Figure 2.1). In July and August, SIC and upper-ocean salt content were highly variable (Figure 2.2a, Supplementary Figure 2.8e), indicating cycles of melt and refreeze consistent with a strengthened negative feedback to ice growth and a weakly stabilizing buffer from thin ice. Indeed, we estimate that net in situ ice growth in 2017 was half of that experienced in a normal winter (Supplementary Figure 2.8e). On 27 July, after four days of storm activity, numerous scattered, short-lived polynyas appeared southwest of Maud Rise. Later, on 3 September, two larger openings emerged above the seamount during a brief storm; they then merged and rapidly grew after storms from 13 to 18 September, which featured the highest wind speeds seen in reanalysis that winter (Figure 2.2a, Supplementary Figure 2.9b, Supplementary Figure 2.13). Within this expanding polynya, both floats inferred ice-free conditions from prolonged warm near-surface temperatures and surfaced to transmit data—a highly unusual occurrence (Supplementary Figure 2.13; see Methods section “Hydrographic data”). A 1.5-month

lull in storm activity saw the extent of the polynya stabilize at around 50,000 km², before seasonal ice melt and coalescence with the open ocean occurred in November (Figure 2.1a,c, 2a, Supplementary Figure 2.13).

In October 2017, a near-homogeneous cold, fresh, and high-oxygen coherent structure, spanning depths from around 200 m to 1,700 m, was detected from within the polynya. The development of such a structure indicates deeper and more vigorous convection than in 2016 (Figure 2.4a–c). As with the remnant "chimney" observed in 1977 (Gordon, 1978), normal ocean layering was absent. Whether mixing extended below 1,700 m in 2017 cannot be determined from the float data, but we note that the low interior stratification offers little resistance to convection (Supplementary Figure 2.11e). This raises the possibility that smaller, shorter-lived polynyas may introduce modification to a similar depth as the 1974–1976 events. However, mixing within transient polynyas near Maud Rise need not be bottom-reaching to affect the properties of the abyssal world ocean. Counterintuitively, bottom water masses remain mostly topographically confined to the Weddell Basin, whereas deep and intermediate layers outflow and spread northwards as Antarctic Bottom Water (Mantyla & Reid, 1983; Jullion et al., 2014; and references therein). Even brief polynyas may have an outsized effect. Total heat loss during the 21-day opening in 2016 was approximately equal to that which occurs during a normal ice-covered winter (Gordon & Huber, 1990), thus accelerating the transformation of circumpolar-derived Weddell Deep Water on its slow transit through the Weddell gyre (Jullion et al., 2014).

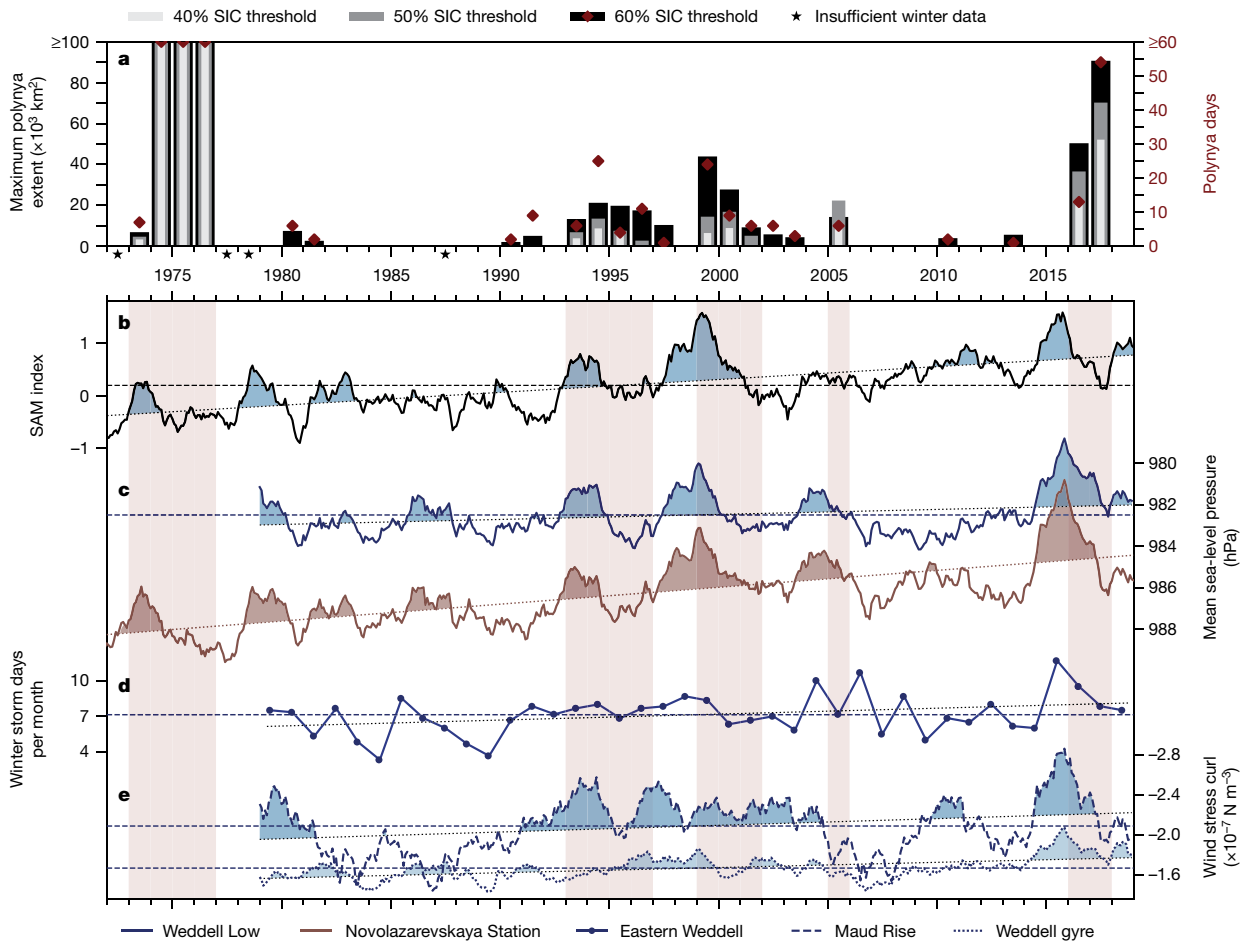

Figure 2.5: Relationships between past polynyas near Maud Rise and climate forcing from 1972–2018. (a) Annual maximum polynya extent (bars) and number of polynya days (red diamonds; see Methods section "Polynya identification"). Maximum polynya extent is calculated for three SIC thresholds representing increasingly strict polynya definitions: 60%, 50%, and 40%. Polynya days are quantified using the 60% threshold. Stars indicate years with incomplete or absent SIC records. **(b)** SAM index for the years 1972–2018. **(c)** Mean sea-level pressure from ERA-I reanalysis, for 1979–2018, within the Weddell Low region (blue; see Methods section "Weddell Low"), and from Novolazarevskaya Station, Queen Maud Land, for 1972–2018 (brown; see white triangle in Figure 2.1a and Methods section "Meteorological station records"). Note the reversed *y* axis. **(d)** Eastern Weddell region (62°–68°S, 15°W–20°E) winter (May–October) mean storm days per month (see Methods section "Storm identification"). **(e)** Average wind stress curl from ERA-I over Maud Rise (63°–67°S, 0°–10°E; dashed) and the entire Weddell gyre (60°S to the Antarctic continent, 60°W–45°E; dotted). Time series in **(b)**, **(c)**, and **(e)** are filtered using a two-year centered running mean and shaded above their linear trends to highlight longer-term fluctuations. See Supplementary Table 2.1 for trends and significance for **(b–e)**. Horizontal dashed lines are mean values. Years with polynya activity at the 50% threshold are shaded vertically in red in **(b–e)**.

2.4.4 Role of climate variability

Although 2016 and 2017 were exceptional, transient polynyas near Maud Rise have also occurred in clusters of years from 1993–1996 and 1999–2001, as well as in 2005 (Figure 2.5a). This is in line with sequences of polynya years found in a high-resolution model simulation of the region (Kurtakoti et al., 2018). We have shown that the recurrence of polynyas may be explained by upward salt transfer from convective mixing. However, what controls the intermittency of initial openings is still unknown. By examining climate records from 1972–2018 to identify a common mechanism, we find that the Southern Annular Mode (SAM)—the leading mode of variability in the Southern Hemisphere (Thompson et al., 2011)—fluctuates in lockstep (Figure 2.5b,c, Supplementary Table 2.1) with indices of mean sea-level pressure for the Weddell Low, the climatological low surface pressure center east of Maud Rise (r = −0.71; see Methods section "Weddell Low"), and from Novolazarevskaya Station, south of Maud Rise (r = −0.82; see white triangle in Figure 2.1a). In turn, the curls of wind stress over both the entire Weddell gyre and Maud Rise are correlated with the Weddell Low (r = 0.61 and 0.48, respectively; Figure 2.5c,e). Also correlated with the Weddell Low is the frequency of severe winter storms within the eastern Weddell region (r = −0.55; Figure 2.5d). These relationships are analogous to those associated with variability of the Amundsen Sea Low (Fogt et al., 2012).

Figure 2.5 illustrates that past transient polynyas near Maud Rise were preceded by synchronous deviations in these indices: positive SAM, deeper Weddell Low, strengthened cyclonic wind stress curl, and frequent winter storm activity. Notably, there were more than twice as many winter storms in 2015 and 2016 as occurred in the least stormy years (Figure 2.5d). We have suggested that intense storms facilitate ice loss through turbulent mixing and ice divergence. The other large-scale anomalies provide the preconditioning necessary to permit a polynya in the first place (Martinson et al., 1981). Local wind stress curl is a proxy for ocean upwelling velocity due to the Ekman relation, and modeling and theoretical studies indicate that enhanced upwelling favors polynya development by concentrating warm, salty Weddell Deep Water closer to the

surface (Martinson et al., 1981; Timmermann et al., 1999; Cheon et al., 2014, 2015; Kurtakoti et al., 2018; E. A. Wilson et al., 2019). Perhaps more important, however, are the salinity fluxes into the mixed layer that are associated with upwelling. Record-strong wind stress curl in 2015 and 2016 (Figure 2.5e) increased MLS near Maud Rise by at least 0.06 psu (Methods section "Salinity fluxes from upwelling"), which reduced upper-ocean stability (Motoi et al., 1987) and preconditioned the 2016 opening. Spin-up of the barotropic Weddell gyre circulation due to strengthened wind stress curl (see Methods section "Weddell Low") may have also enhanced topography- or eddy-related upwelling (Gordon & Huber, 1990; de Steur et al., 2007) and possibly topographic mixing as faster flow impinged on Maud Rise. Either could have intensified upward heat fluxes in 2016, contributing to the delayed freeze and presumably thinner ice in July. Ultimately, these upwelling- and storm-induced offshore polynyas are linked to positive fluctuations in SAM, which represent large-scale anomalies in the climate of the Southern Hemisphere.

The exceptional 1974–1976 Weddell polynyas, which were larger than the 2016–2017 openings (Figure 2.1a), do not conform perfectly to this explanation. The 1974 event occurred under similar circumstances to the 2017 polynya, in that it was preceded by a positive deviation in SAM (Figure 2.5b) and lower mean sea-level pressure (Figure 2.5c), as well as delayed ice formation in 1973 (not shown) and a brief "precursor" polynya that year (Martinson et al., 1981; Comiso & Gordon, 1987; Figure 2.5a). But these anomalies were modest. The degree and spatial extent of preconditioning in 1974 were probably augmented by previously proposed mechanisms: a generally saltier Southern Ocean surface (de Lavergne et al., 2014) and below-average precipitation over the preceding decade associated with prolonged negative SAM (Gordon et al., 2007). Reduced precipitation, however, cannot explain the 2016 opening, which followed six years of higher-than-average precipitation (Supplementary Figure 2.14c).

2.4.5 Comparison with climate models

Accurate modeling of the Southern Ocean requires realistic simulation of deep water formation and ventilation processes (C. Heuzé et al., 2013). This remains an urgent challenge. In many climate models that are included in the fifth Coupled Model Intercomparison Project (CMIP5), large Weddell polynyas featuring open-ocean deep convection recur on widely varying timescales (de Lavergne et al., 2014; Behrens et al., 2016). In these models and others, heat steadily accumulates in Weddell Deep Water over multiple years or decades (Martin et al., 2013; Dufour et al., 2017; Reintges et al., 2017; L. Zhang et al., 2019), possibly owing to freshwater forcing biases and insufficient vertical mixing (C. Heuzé et al., 2015; Kjellsson et al., 2015). This build-up eventually erodes stratification in an episode of spontaneous ventilation; cycles of recharge and discharge of heat then follow, associated with Weddell polynyas (Martin et al., 2013; Behrens et al., 2016; Dufour et al., 2017; Reintges et al., 2017; L. Zhang et al., 2019). Observational records of ocean and sea ice are insufficiently long to assess whether these convective cycles, which create a global mode of internal variability (Martin et al., 2013; Resplandy et al., 2015; Behrens et al., 2016; Pedro et al., 2016; Cabré et al., 2017; L. Zhang et al., 2019), are natural or spurious. This is concerning, because some models suggest that recent Southern Ocean sea surface temperature and sea ice trends may simply reflect this cycle—that is, represent a rebound from ventilation during the 1974–1976 Weddell polynyas (L. Zhang et al., 2019).

The 2016–2017 events offer an opportunity to assess whether destratification from mid-depth heat accumulation, which is prevalent in models, contributes to polynya formation in reality. The preceding decade-long hiatus in polynya activity is presumably long enough to discern trends in subsurface heat (Figure 2.5a). However, we do not find marked heat accumulation before 2016 in records compiled from about 3,000 sub-pycnocline temperature measurements within the eastern Weddell region (Supplementary Figure 2.14d,e, Supplementary Table 2.1; Methods section “Sub-pycnocline temperature records”). Although the presence of warm Weddell Deep Water is required to sustain overturning, an increase in local heat content is probably not

the immediate cause of polynyas near Maud Rise. This suggests that model results involving Weddell polynyas should be interpreted with greater caution, even when the simulated features resemble observed polynyas in size and location.

Similarly, although deep convection in simulated Weddell polynyas often proceeds until the subsurface heat reservoir is depleted (Martin et al., 2013; Behrens et al., 2016; Dufour et al., 2017; L. Zhang et al., 2019), the observed cooling after the 1974–1976 and 2016–2017 polynyas of up to 1.0°C (Gordon, 1978; see Methods section "Sub-pycnocline temperature records") and 0.3°C (Figure 2.4a), respectively, is probably not severe enough to explain the lack of major openings in 1977 (Carsey, 1980) and 2018 (Figure 2.5a). Instead, reductions in upwelling (Figure 2.5e) and storm frequency (Figure 2.5d), combined with westward advection of upper-ocean salinity anomalies away from Maud Rise (Martinson et al., 1981; Kurtakoti et al., 2018), probably terminate multiyear polynya sequences.

2.5 Future implications

Progress in simulating and predicting offshore Antarctic polynyas will require a more precise understanding of how storms cause sea ice destruction and how upwelling affects haline stratification. New insight into these relationships may also inform long-standing questions on how Southern Ocean stratification modulates deep ventilation on glacial–interglacial timescales (Sigman et al., 2010); here, the possible role of offshore polynyas is poorly understood (J. A. Smith et al., 2010; Amblas & Dowdeswell, 2018). Although observations of additional offshore polynyas would be valuable in clarifying these mechanisms, climate models predict that their formation may soon be prohibited by the Southern Ocean surface freshening trend of about 0.01 psu per decade, which is associated with anthropogenic climate change (de Lavergne et al., 2014). However, this simulated non-convective regime has evidently not yet been reached. At present, we observe that the Maud Rise region experiences interannual variability in upper-ocean

salinity—and thus also stability—that is an order of magnitude higher than this slow decadal freshening rate. This may enable intermittent openings similar to those in 2016 and 2017 for decades to come. Moreover, we identify statistically significant positive multidecadal trends in polynya-favorable conditions: the strengthening of SAM, Weddell Low, cyclonic wind stress curl, and winter storm activity (Supplementary Table 2.1). These reflect poleward shifts in Southern Hemisphere westerly winds and storm tracks, which are expected to continue under anthropogenic forcing (Thompson et al., 2011; Chang et al., 2012). We propose that these changes may bring enhanced upwelling and a more frequently disturbed sea ice cover to the Weddell Sea region, conceivably signaling a greater future role for transient offshore polynyas in opening a window to the abyssal ocean.

2.6 Code and data availability

Analytical scripts used to generate the figures in this paper are available at https://github.com/ethan-campbell. The data analyzed in this chapter are all publicly available, with the exception of updates to the UW Calibrated O_2 package, described below:

1. Ocean bathymetry data were obtained from the ETOPO1 1 Arc-Minute Global Relief Model (Amante & Eakins, 2009) at http://dx.doi.org/10.7289/V5C8276M (accessed February 2017).
2. Sea ice concentration data were obtained for the period 1972–1977 from the NSIDC Nimbus-5 ESMR v1 product (Parkinson et al., 2004) at http://dx.doi.org/10.5067/W2PKTWMTY0TP (accessed February 2017); for the period 1978–2017 from the merged NASA Goddard v3 product (Meier, Fetterer, Savoie, et al., 2017) at http://dx.doi.org/10.7265/N59P2ZTG (accessed October 2018); for January 2018–February 2019 from the NOAA/NSIDC Near-Real-Time CDR v1 product (Meier, Fetterer, & Windnagel, 2017) at http://dx.doi.org/10.7265/N5FF3QJ6 (accessed February 2019); and for the period 2002–2019 from the University of Bremen ASI AMSR-E and AMSR2 v5 products (Spreen et al., 2008; Beitsch et al., 2014) at https://seaice.uni-bremen.de/sea-ice-concentration/ (accessed February 2019).
3. Profiling float temperature and salinity measurements were obtained from the US-GODAE GDAC (Carval et al., 2017; accessed October 2018; server no longer available, see http://www.argo.ucsd.edu instead). Dissolved oxygen measurements for floats 5904468 and 5904471 were obtained from the SOCCOM quality-controlled archive (Johnson et al., 2019) at http://dx.doi.org/10.6075/J02J6968 (accessed January 2019) and for float 5903616 from the UW Calibrated O_2 package, v1.1 (Drucker & Riser, 2016; accessed August 2016; public link no longer available—contact for access to data), with updated dissolved oxygen profiles provided by R. Drucker (personal communication, August 2017).

4. Shipboard and elephant seal temperature and salinity measurements were obtained from the World Ocean Database 2018 prerelease (Boyer et al., 2018) with August 2018 additions at http://www.nodc.noaa.gov/OC5/SELECT/dbsearch/dbsearch.html (accessed October 2018).
5. Gridded climatological ocean temperature fields were obtained from the 2018 WAGHC (Gouretski, 2018), now at https://www.cen.uni-hamburg.de/en/icdc/data/ocean/waghc.html (previous link accessed January 2018).
6. The monthly SAM index (G. J. Marshall, 2003) was obtained for the period 1972–2019 at http://legacy.bas.ac.uk/met/gjma/sam.html (accessed February 2019).
7. Monthly and daily ERA-I atmospheric reanalysis fields (Dee et al., 2011) were obtained for the period 1979–2018 using the Python MARS API, described at https://confluence.ecmwf.int/display/WEBAPI/ (accessed February 2019).
8. Queen Maud Land pressure records (see Methods section “Meteorological station records”) were obtained from the READER archive (Turner et al., 2004) at http://legacy.bas.ac.uk/met/READER (accessed February 2019) and the NOAA-NCEI ISD (A. Smith et al., 2011), now at https://www.ncei.noaa.gov/products/land-based-station/integrated-surface-database (previous link accessed February 2019).

2.7 Supplementary figures

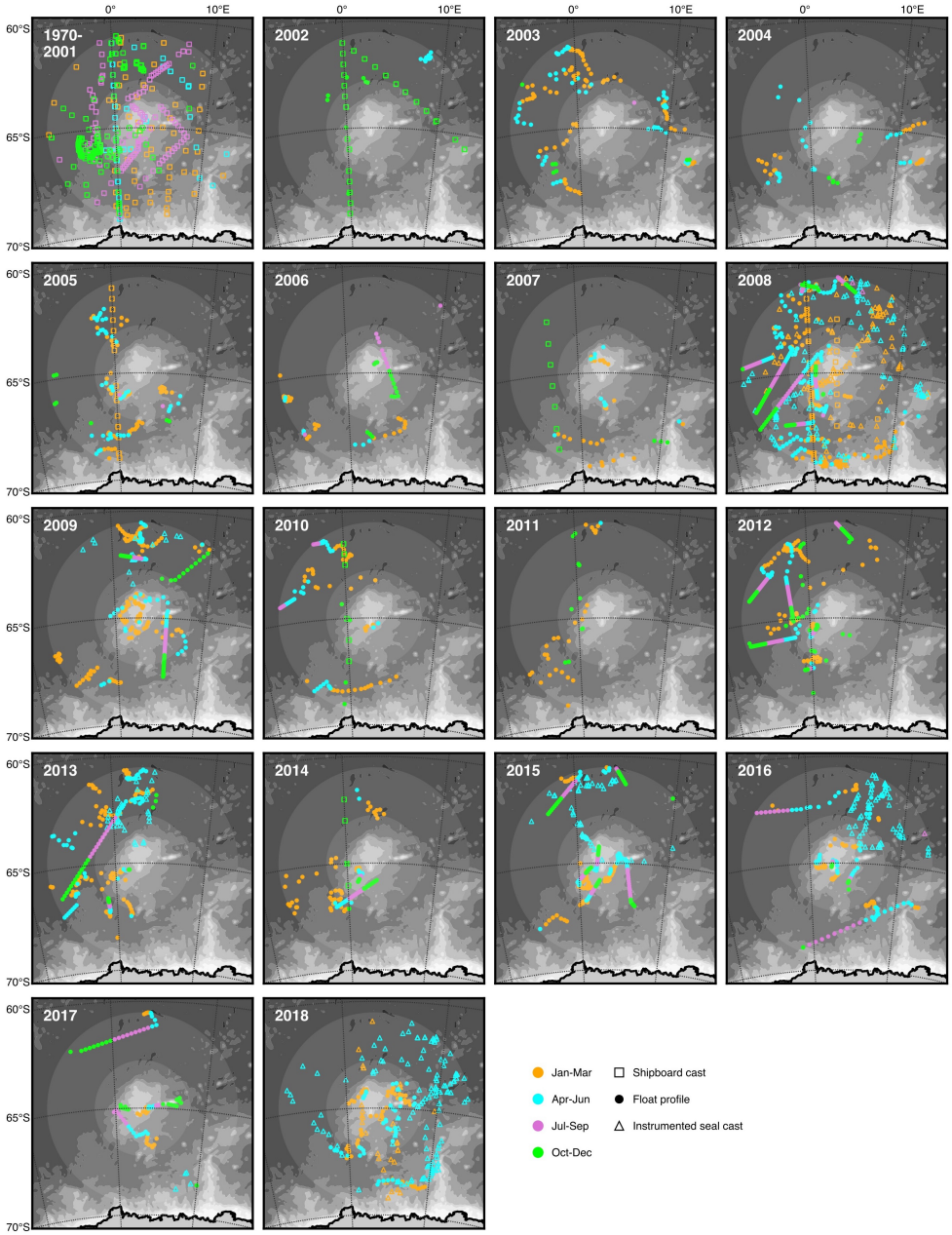

Supplementary Figure 2.6: Locations of observations used to construct hydrographic climatologies for the Maud Rise and eastern Weddell regions. Observations from 1970 to 2001 are shown together (top left); observations from 2002 to 2018 are represented by one panel per year. Included are float profiles from the Argo GDAC (filled circles) as well as shipboard (open squares) and instrumented seal (open triangles) casts from the World Ocean Database (see Methods section "Hydrographic data"). Colors indicate seasons. Bathymetric contours (intervals of 750 m) highlight Maud Rise and the Antarctic continental shelf. Concentric circles represent radii of 250 km and 500 km from Maud Rise, encompassing the Maud Rise and eastern Weddell regions, respectively (see Methods section "Regions").

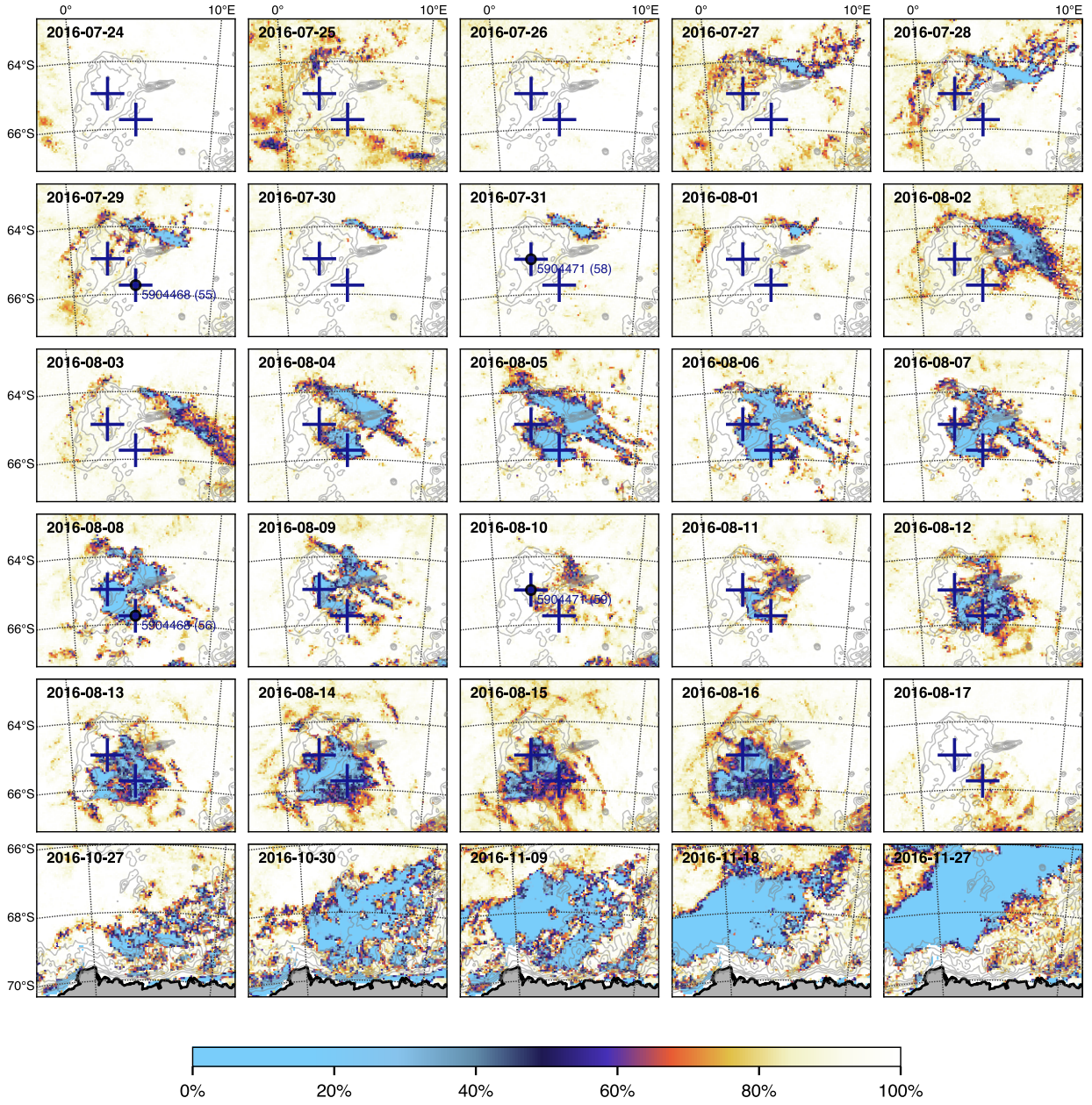

Supplementary Figure 2.7: Sea ice concentration during the 2016 polynya. Daily SIC from AMSR2-ASI around Maud Rise from 24 July to 17 August 2016, encompassing the main polynya event, followed by selected SIC fields from AMSR2-ASI during the late-winter 2016 polynya south of Maud Rise (bottom row; note different map area). Estimated locations of SOCCOM profiling floats 5904471 and 5904468 (see Methods section "Hydrographic data") are marked in blue; a circle marker and profile number indicate that a hydrographic profile was obtained on that date. Bathymetry shallower than 3,500 m is contoured at intervals of 500 m to highlight Maud Rise (center of July–August images) as well as Astrid Ridge (bottom right of October–November images), an extension of the Antarctic continental shelf.

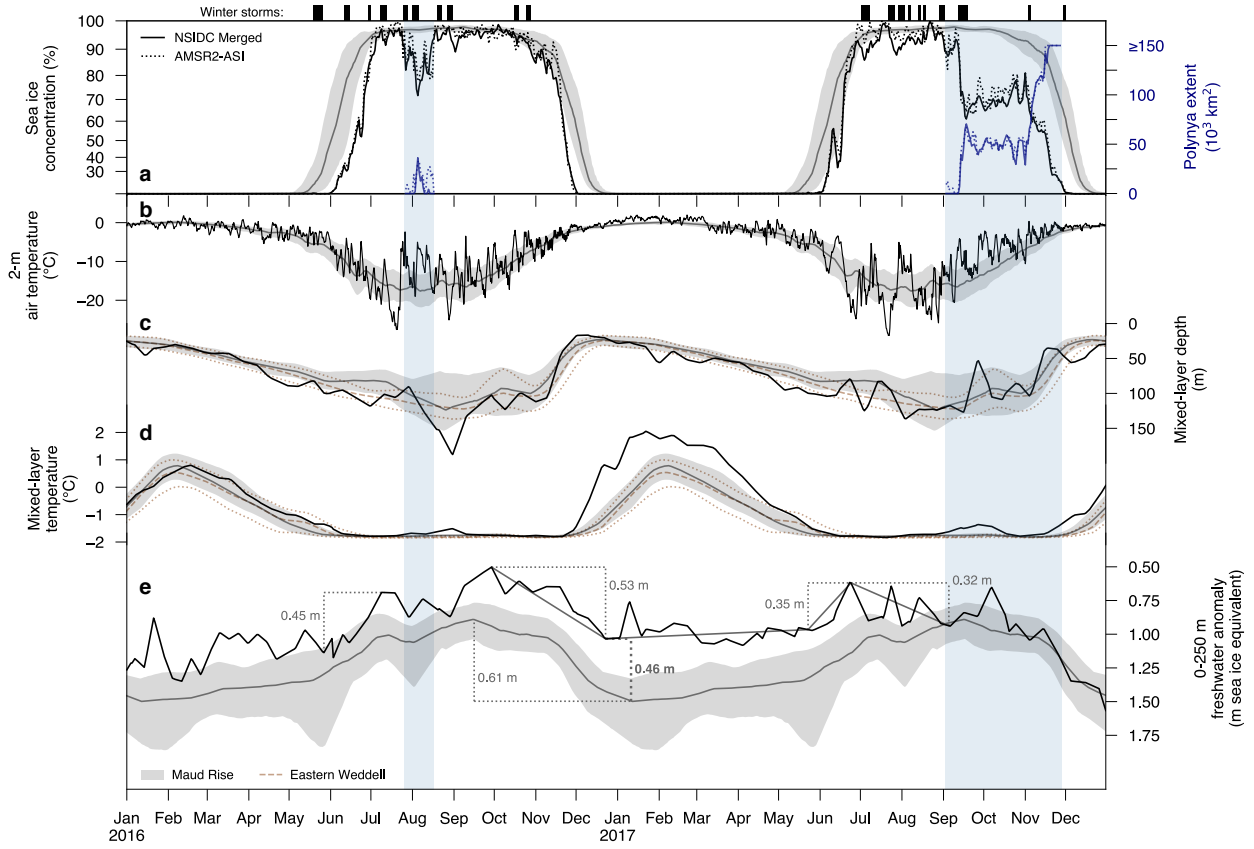

Supplementary Figure 2.8: Evolution of sea ice concentration, air temperature, and upper ocean properties at Maud Rise in 2016 and 2017. Marked at the top are intense winter storm events near Maud Rise, as in Figure 2.2 (also see Supplementary Figure 2.9 and Methods section "Storm identification"). **(a)** Average daily SIC within the Maud Rise region (63°–67°S, 0°–10°E) from NSIDC Merged (solid black line) and AMSR2-ASI (dashed black line) in 2016 and 2017, as in Figure 2.2a. SIC climatology from NSIDC Merged (1978–2019) is shown as median (gray line) and 25%–75% interquartile range (IQR; gray shading). Note the stretched *y* axis. Polynya extent is quantified (blue lines) during the 2016 and 2017 events (vertical blue shading). **(b)** Six-hourly 2-m air temperature around Maud Rise (within 63°–67°S, 0°–10°E) from ERA-I reanalysis (black line). Climatology for 1979–2018 is shown as mean (gray line) and IQR (gray shading). **(c)** Composite of average MLD in 2016 and 2017 measured by floats 5903616, 5904468, and 5904471 (black line; see Methods sections "Derived oceanographic quantities" and "Composites of float time series"). MLD climatology for the Maud Rise region (R < 250 km from 65°S, 3°E) is shown as median (gray line) and IQR (gray shading); climatology for the eastern Weddell region away from Maud Rise (250 < R < 500 km) is presented for comparison (light brown dashed and dotted lines for median and IQR, respectively; see Methods section "Hydrographic climatologies"). **(d)** Composite of average mixed-layer potential temperature (MLT) and MLT climatology presented as in **(c)**. **(e)** Composite of the lowest observed upper-250-m freshwater anomaly (or "salt deficit"; see Methods sections "Derived oceanographic quantities" and "Composites of float time series") and freshwater anomaly climatology for the Maud Rise region presented as in **(c)**. Note the reversed *y* axis. Key changes quantified, from left to right, are 2016 freeze, climatological melt, 2016 melt, anomaly from climatology in January 2017, 2017 freeze, and change between 2017 freeze and 2017 polynya appearance. Note the reversed *y* axis.

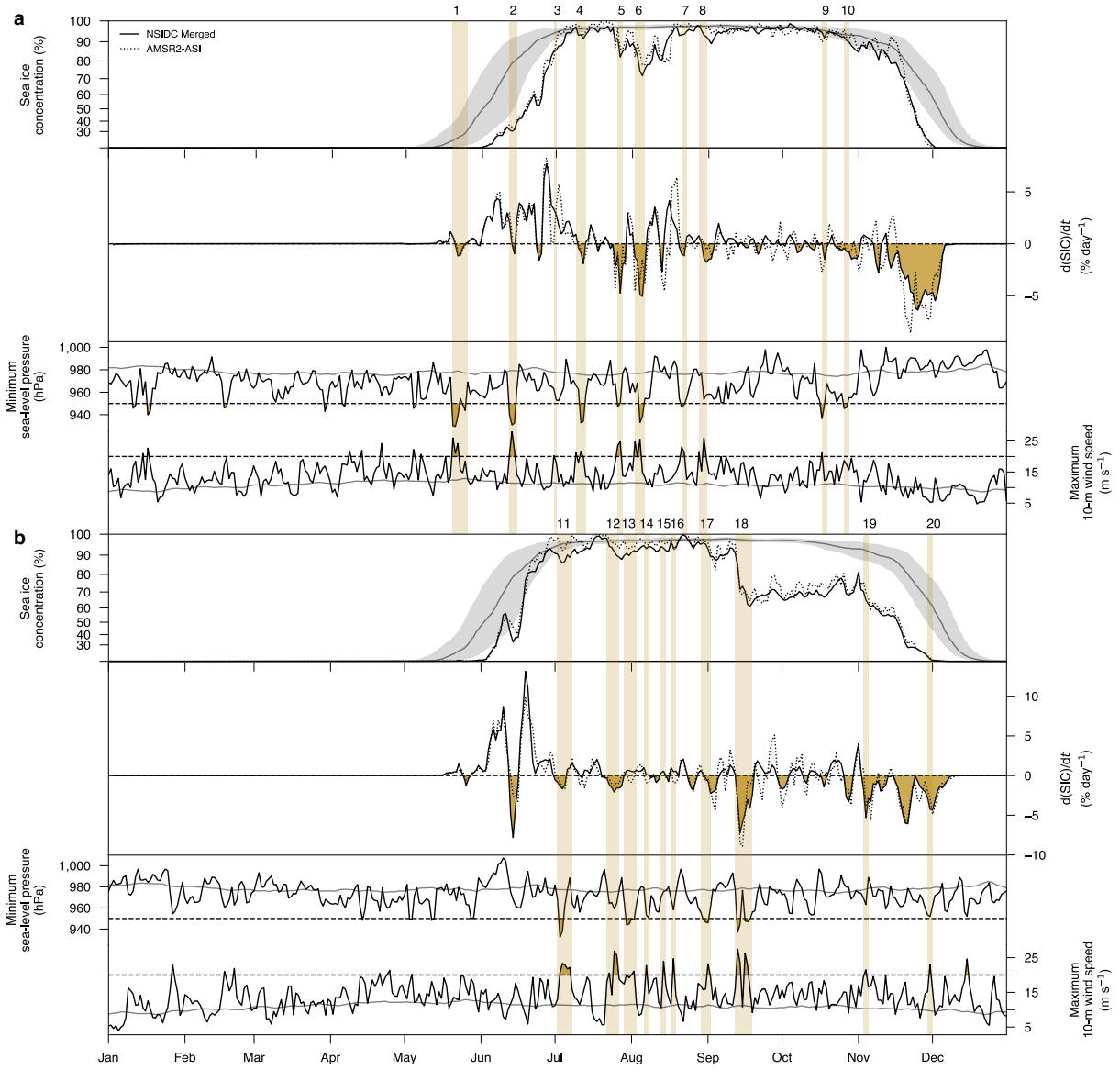

Supplementary Figure 2.9: Correspondence of sea ice loss episodes and major storms near Maud Rise. (a–b) Time series are shown for 2016 (**a**) and 2017 (**b**). Average daily SIC within the Maud Rise region (63°–67°S, 0°–10°E) from NSIDC Merged (solid black line) and AMSR2-ASI (dashed black line) is presented at the top for each year, as in Figure 2.2a. SIC climatology from NSIDC Merged (1978–2019) is shown as median (gray line) and 25%–75% interquartile range (gray shading). Note the stretched *y* axis. Daily changes in SIC are presented in the center for each year, with negative changes in NSIDC Merged highlighted (dark yellow shading); both NSIDC Merged and AMSR2-ASI time series are smoothed using a 3-day right-edge running-mean filter. At the bottom for each year are the minimum daily sea-level pressure and maximum daily 10-m wind speed near Maud Rise (within 63°S–67°S, 0°–10°E) from ERA-I reanalysis. Mean climatological values of these minimum/maximum metrics are shown (gray lines) to highlight the lack of a pronounced seasonal cycle. The most intense winter polar lows, as shown in Figure 2.2, Figure 2.3, Supplementary Figure 2.8, are identified here using pressure and wind speed thresholds (dark yellow shading from dashed lines), and aggregated "storm days" are numbered at the top and marked with vertical yellow bars (see Methods section "Storm identification").

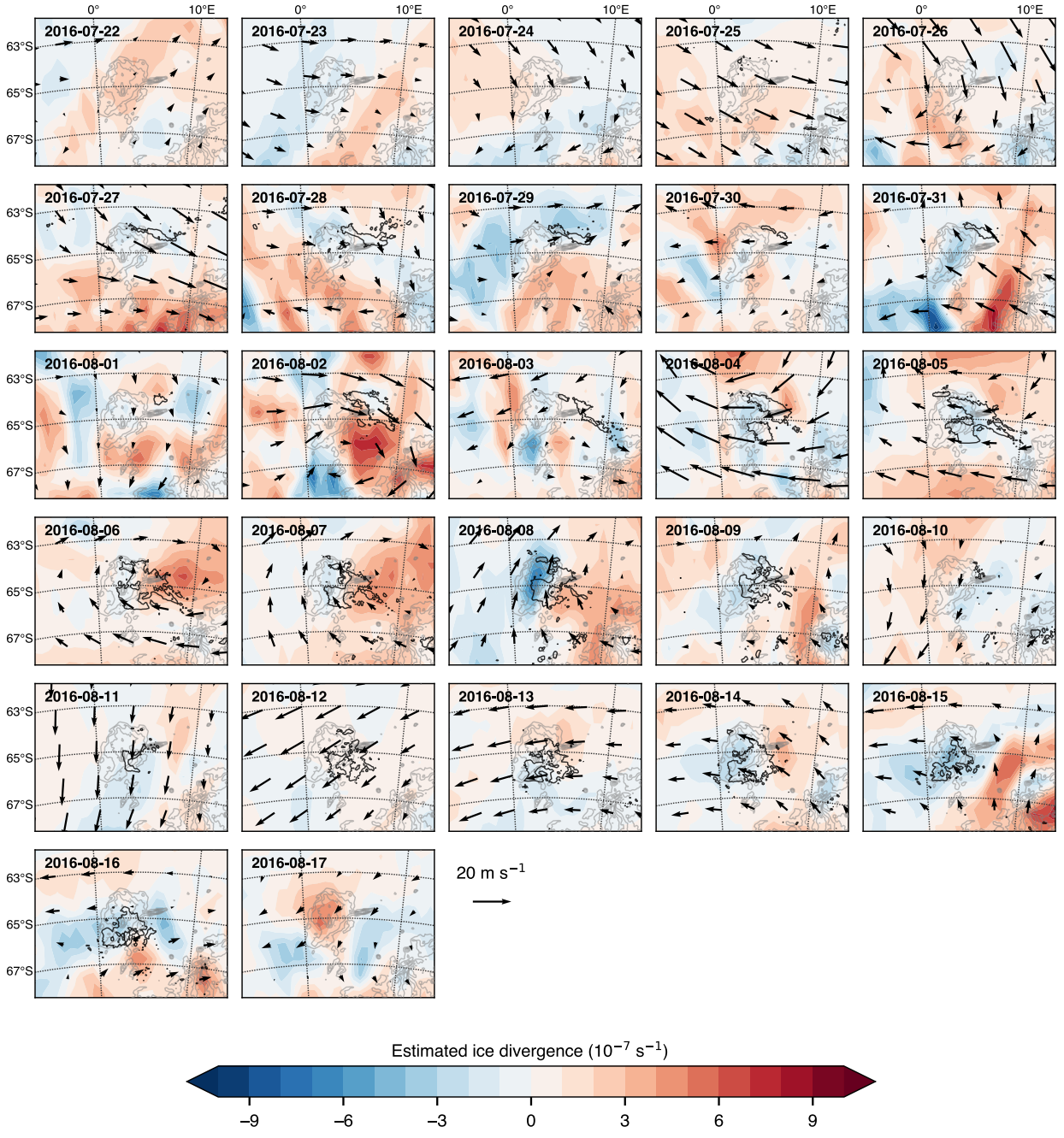

Supplementary Figure 2.10: Winds and wind-induced sea ice divergence during the 2016 polynya. 50% SIC contours (black) from AMSR2-ASI show the daily polynya evolution from 22 July to 17 August, 2016. Bathymetry shallower than 3,500 m is contoured at intervals of 500 m (light gray) to highlight Maud Rise (center). Daily mean 10-m wind vectors from ERA-I reanalysis, subsampled as every fifth *u*-wind and every second *v*-wind vector, are plotted with a 20 m s^{-1} key as reference. Estimated daily mean wind-induced sea ice divergence (see Methods section "Atmospheric reanalysis") is shaded such that red represents divergence and blue represents convergence.

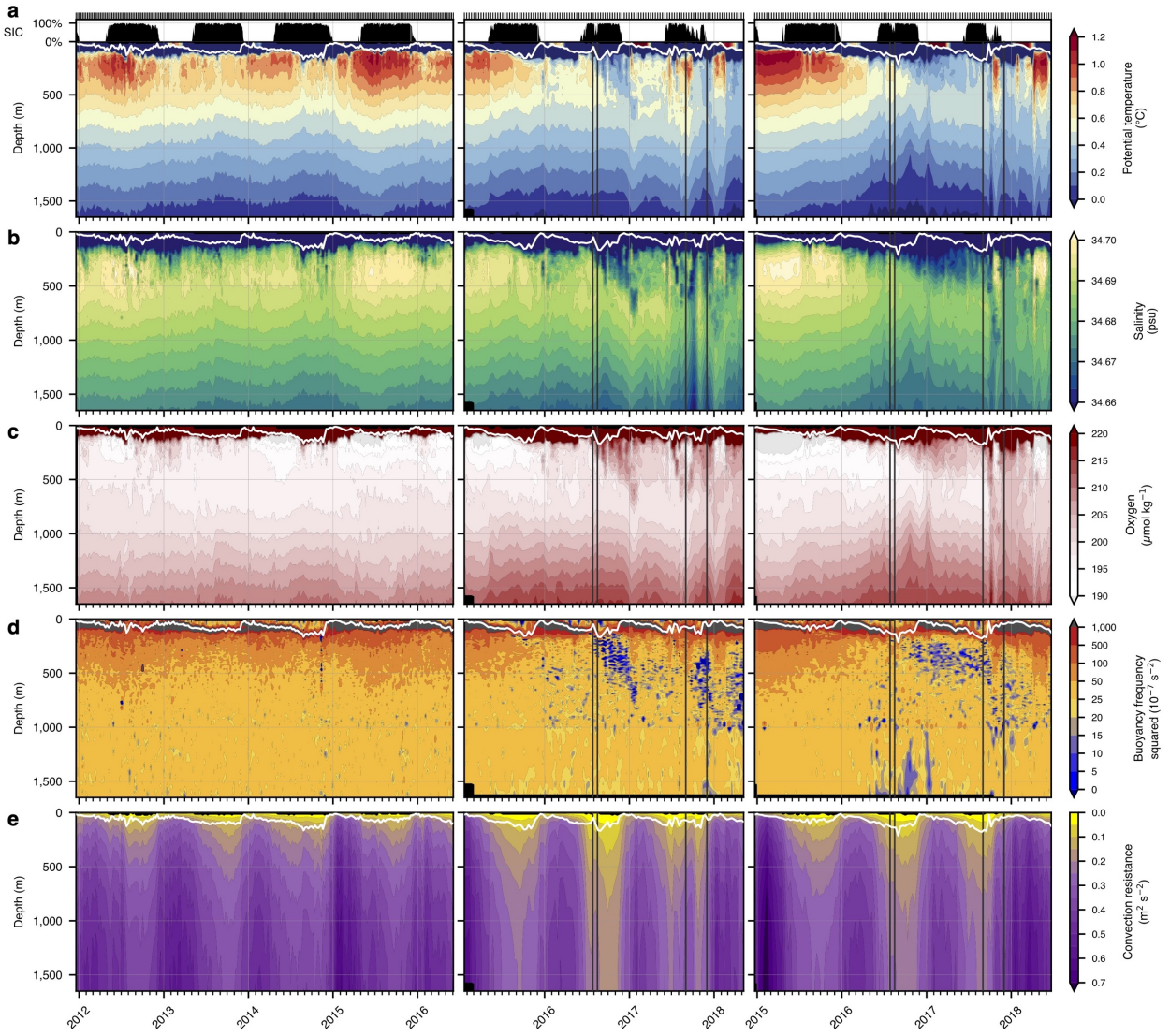

Supplementary Figure 2.11: Full set of profiling float hydrographic observations from Maud Rise from 2011–2018. (a–e) Complete depth sections of potential temperature (**a**), salinity (**b**), dissolved oxygen (**c**), buoyancy frequency squared (N^2) (**d**), and convection resistance (see Methods section "Derived oceanographic quantities") (**e**) from profiling floats 5903616 (left), 5904468 (center), and 5904471 (right), as shown in Figure 2.4. Individual profiles are marked at the top (black ticks). Mixed-layer depth is indicated in white. Vertical lines in each panel mark the start and end dates of the 2016 and 2017 polynyas. Along-trajectory SIC, primarily from AMSR2-ASI, is shaded at the top in black (see Methods section "Sea ice concentration data").

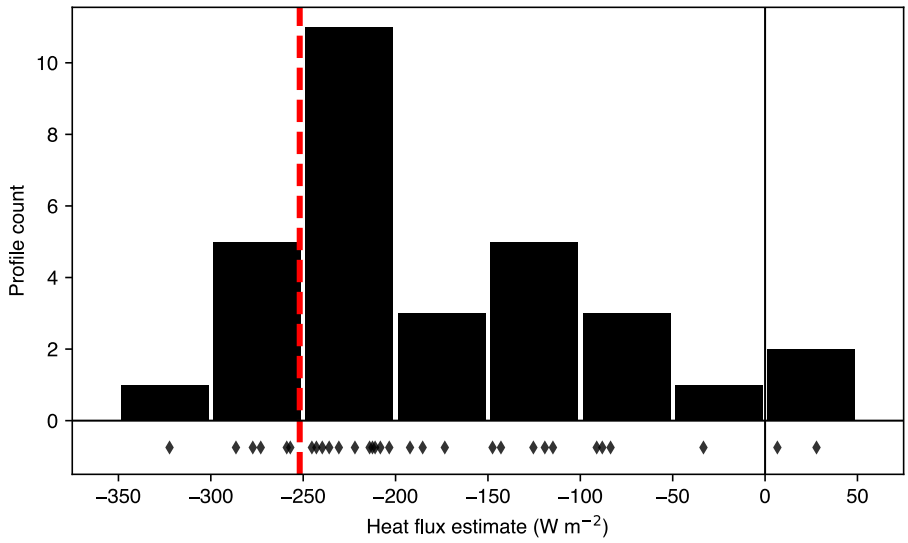

Supplementary Figure 2.12: Heat loss during the 2016 polynya estimated from hydrographic observations. Heat flux estimates (n = 31; diamonds at the bottom correspond to histogram above) computed using potential temperature profiles from floats 5904468 and 5904471 following the opening of the 2016 polynya (see Methods section "Polynya heat flux estimates"). The dashed red line marks the average open-water ocean-atmosphere turbulent heat flux within the 2016 opening, estimated using a bulk flux algorithm as 252 W m^{-2} (see Methods section "Atmospheric reanalysis").

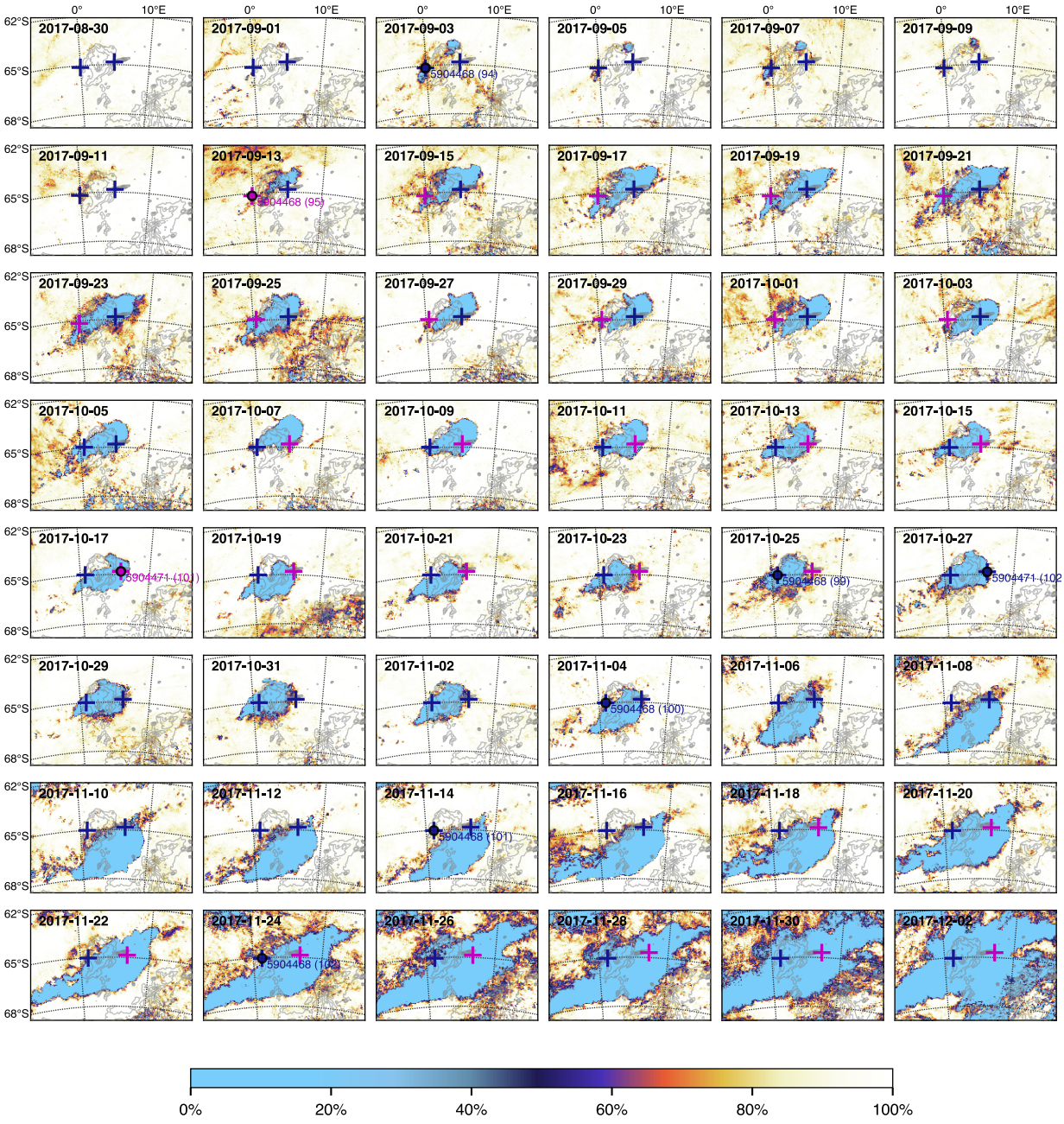

Supplementary Figure 2.13: Sea ice concentration during the 2017 polynya. SIC from AMSR2-ASI around Maud Rise is shown every other day from 30 August to 2 December 2017. Estimated locations of SOCCOM profiling floats 5904471 and 5904468 are marked in blue; locations of profiling floats following an ice-free profile with a known position fix are marked in pink (see Methods section "Hydrographic data"). A circle marker and profile number indicate that a hydrographic profile was obtained on that date. Bathymetry shallower than 3,500 m is contoured at intervals of 500 m to highlight Maud Rise (center) as well as Astrid Ridge (bottom right), an extension of the Antarctic continental shelf.

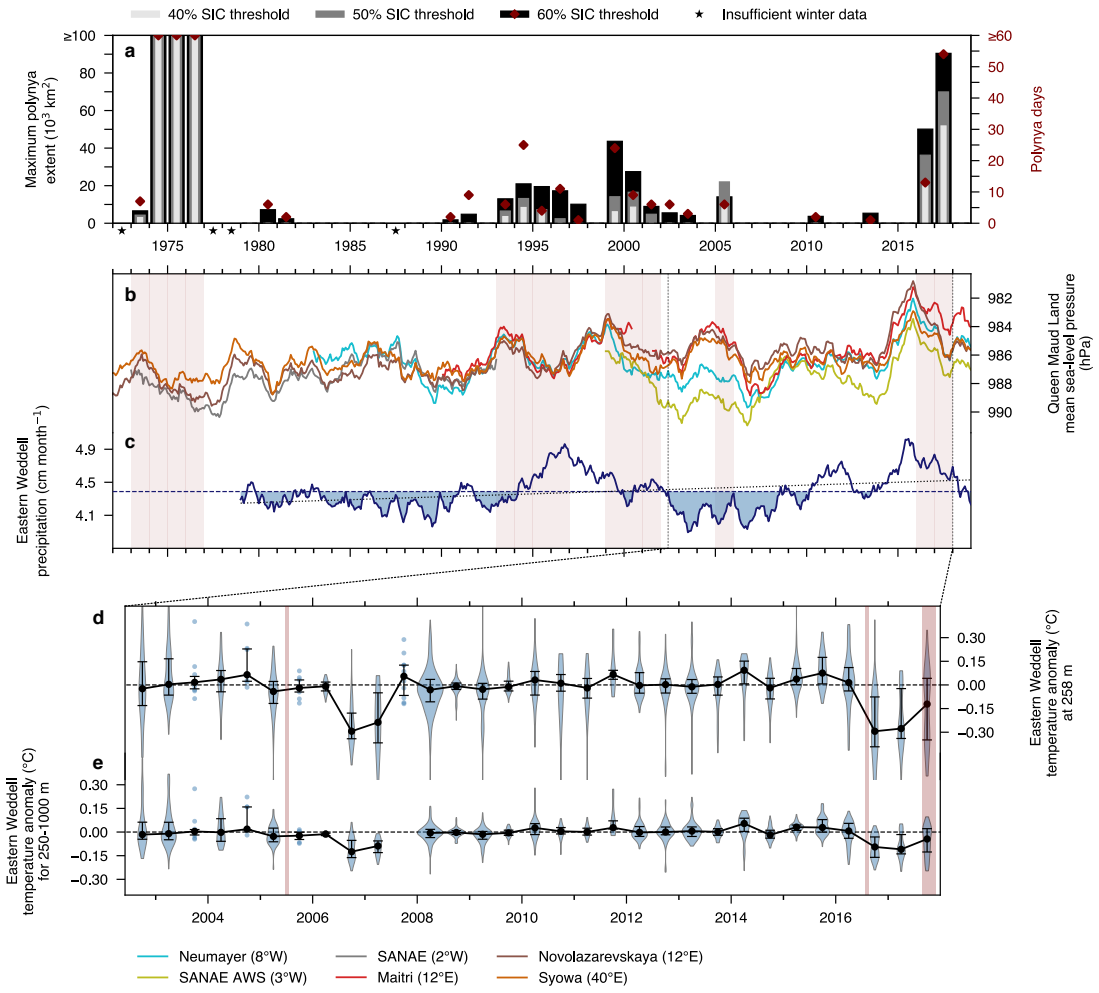

Supplementary Figure 2.14: Additional relationships between past polynyas near Maud Rise, climate forcing, and sub-pycnocline temperatures. (a) Annual maximum polynya extent (bars) and number of polynya days (red diamonds; see Methods section "Polynya identification"), as in Figure 2.5a. Maximum polynya extent is calculated for three SIC thresholds representing increasingly strict polynya definitions: 60%, 50%, and 40%. Polynya days are quantified using the 60% threshold. Stars indicate years with incomplete or absent SIC records. Years with polynya activity at the 50% threshold are shaded vertically in red in **(b–c)**, and likewise in **(d–e)**, except vertical shading delimits the actual major polynya events. **(b)** Mean sea-level pressure records from Queen Maud Land meteorological stations, 1972–2018 (see legend and Methods section "Meteorological station records"). **c**, Eastern Weddell average precipitation from ERA-I reanalysis between 1979 and 2018, shaded below its mean value to indicate years with polynya-favorable conditions (that is, lower atmosphere–ocean freshwater flux), consistent with Figure 2.5. Time series in **(b)** and **(c)** are filtered using a two-year centered running mean to highlight longer-term fluctuations. **(d)** Biannually binned eastern Weddell region (within 500 km of Maud Rise) shipboard, float, and instrumented seal temperature observations at 258 m from 2002 to 2017, expressed as anomalies from WAGHC gridded hydrographic climatology (see Methods section "Sub-pycnocline temperature records"). Error bars denote median and 25%–75% IQR. Violin plots summarize the data distribution for $n > 10$, and individual anomalies are shown for $5 \le n \le 10$. Periods with $n < 5$ are not plotted. **(e)** As in **(d)** but showing average temperature anomalies from WAGHC climatology between 250–1,000 m (see Methods section "Sub-pycnocline temperature records"). See Supplementary Table 2.1 for trends and significance for **(c–e)**.

2.8 Supplementary table

Supplementary Table 2.1: Correlations and trends for climate indices and sub-pycnocline temperature records. Pearson correlation coefficients (*r*) between climate indices from Figure 2.5 and Supplementary Figure 2.14 are listed for the lag within ±3 years at which the absolute value of the correlation is maximal. Lags are cited within parentheses in months; positive values indicate the index on the top axis leads and the index on the vertical axis lags. Except where noted (see footnotes), correlations were calculated after applying a 12-month centered running mean to mitigate seasonality, with a minimum filter window of 6 months. Linear trend estimates and significance (*p*) were computed using a two-sided Wald test. At the top right, trends are shown for climate indices, assessed using the original, unfiltered time series. At the bottom right, trends are shown for both the full period of sub-pycnocline temperature anomaly records before the 2016 polynya as well as the subperiod beginning in 2008, calculated using the biannual median values (see Supplementary Figure 2.14d–e). We analyze the subperiod beginning in 2008 separately because the amount of float and elephant seal observations within the eastern Weddell region increased sharply that year (Supplementary Figure 2.6).

	1	2	3	4	5	6	7	Period	Trend (decade^{-1})	*p*
1 Southern Annular Mode (SAM) index†	1.00 (0)	-0.71 (0)	-0.82 (0)	-0.38 (-1)	-0.51 (0)	0.30 (-1)	0.36 (-1)	1972-2018	0.25	0.00
2 Weddell Low SLP		1.00 (0)	0.84 (0)	0.48 (0)	0.61 (0)	-0.55 (-1)	-0.38 (0)	1979-2018	-0.24 hPa	0.13
3 Novolazarevskaya SLP†			1.00 (0)	0.48 (0)	0.59 (0)	-0.50 (-1)	-0.31 (0)	1972-2018	-0.81 hPa	0.00
4 Maud Rise wind stress curl				1.00 (0)	0.50 (0)	-0.40 (-2)	-0.56 (0)	1979-2018	$-0.07 \cdot 10^{-7}$ N m^{-3}	0.16
5 Weddell gyre wind stress curl†					1.00 (0)	-0.47 (-1)	-0.67 (0)	1979-2018	$-0.05 \cdot 10^{-7}$ N m^{-3}	0.02
6 E. Weddell winter storm days per month*†						1.00 (0)	0.33 (3)	1979-2018	0.50	0.01
7 E. Weddell precipitation							1.00 (0)	1979-2018	0.07 cm month^{-1}	0.15
E. Weddell 258-m temperature anomaly								Jan. 2008 - Jun. 2016	0.07°C	0.04
								Jul. 2002 - Jun. 2016	0.05°C	0.17
E. Weddell 250-1000-m temperature anomaly								Jan. 2008 - Jun. 2016	0.03°C	0.11
								Jul. 2002 - Jun. 2016	0.03°C	0.03

* *Six-month (winter only) running mean applied.*

† *Series detrended (original series found to have significant trend, that is, two-sided $p < 0.05$).*

Chapter 3:

LAGRANGIAN RECONSTRUCTION OF SNOW ACCUMULATION AND LOSS ON ANTARCTIC SEA ICE

3.1 Abstract

Snow cover on Antarctic sea ice exerts a strong influence on the thermodynamics and freshwater balance of the coupled sea ice–upper ocean system. Yet our understanding of the temporal and spatial variation of snow depth on sea ice across the Southern Ocean has been limited by a sparsity of observations, uncertainties in remote sensing retrievals, and highly idealized model representations. We present a new numerical model that simulates the mass evolution and bulk density of snow on Antarctic sea ice over 21 years (February 2003–February 2024), yielding the most sophisticated circumpolar reconstruction yet developed. Hourly snowfall from atmospheric reanalysis is accumulated along Lagrangian sea ice parcel trajectories determined by remotely sensed ice motion fields. The single-layer model incorporates physically or empirically informed parameterizations of key snow erosion and transformation processes: snow surface and wind-blown snow sublimation, transport into leads, rain-related and non-rain-related melt, wind-enhanced compaction, compaction from overburden pressure, and the large-scale effects of sea ice convergence and divergence. Free model parameters are calibrated by optimizing the model fit to measurements from 29 snow buoys deployed in the Weddell Sea. The resulting reconstruction indicates that one-third of annual snowfall intercepted by Antarctic sea ice is lost to the atmosphere or ocean or to melt processes prior to complete sea ice melt, with blowing snow

sublimation contributing the most but no single loss pathway dominating. Our climatological annual snow mass budget closes to within 18%, with an estimated meteoric freshwater flux of 284 mSv (1 mSv = 1,000 $m^3 s^{-1}$) released to the Southern Ocean, equivalent to more than two-thirds of the freshwater flux provided by sea ice. This meteoric flux consists of 236 mSv from snow and snow-ice and 27 mSv from snow-derived superimposed ice, both released upon complete ice melt, as well as 22 mSv from snow blown into leads. Comparison of our reconstructed net snow accumulation with a CryoSat-2 snow depth retrieval suggests that widespread annual snow-ice formation of 20–30 cm occurs across the Antarctic seasonal ice zone. Net snow accumulation trends during the model reconstruction period mirror the spatial pattern of recent declines in sea ice concentration but are statistically insignificant in circumpolar averages for all seasons, in contrast to significant decreasing trends in sea ice extent over the same period.

3.2 Introduction

Snow deposited on sea ice is closely coupled to the underlying ice and ocean and overlying atmosphere. In the Antarctic, the interception of snow by sea ice, its redistribution due to ice transport, and its subsequent melt exert a strong influence on water mass transformation in the Southern Ocean (Abernathey et al., 2016; Haumann et al., 2016b). Snow cover has a thermal conductivity over six times lower than for sea ice and therefore insulates the underlying ice, reducing the rate of basal ice growth but also increasing its sensitivity to ocean heat fluxes (Maykut & Untersteiner, 1971; Semtner, 1976; Eicken et al., 1995; Massom et al., 2001). At the same time, the persistence of a thick snow cover over multiple years may shield the underlying ice from melt, contributing to the maintenance of perennial ice cover in areas such as the western Weddell Sea and Bellingshausen Sea (Eicken et al., 1995). On smaller spatial scales, an Arctic observing campaign found variations in snow depth on level ice could explain as much as three-quarters of the variability in sea ice thickness (Itkin et al., 2023). The heterogeneous thickness and properties

of snow on sea ice also affect underlying ice-associated algal communities by modifying light transmission and thermal insulation (Mundy et al., 2005; Arndt et al., 2017). Recent decreases in Antarctic sea ice extent (Parkinson, 2019; Purich & Doddridge, 2023; J. Wang et al., 2024) raise the question of the role that snow on sea ice may play, particularly in modulating the freshwater balance of the upper ocean and thus its stratification and ocean-ice heat fluxes, as well as how these recent declines may affect snow accumulation.

Snow on Antarctic sea ice impacts not only how the coupled ocean-ice-snow system operates, but also the measurement of sea ice thickness itself. The depth and density of the overlying snow cover must be known to account for its isostatic contribution when estimating ice thickness using satellite laser or radar altimetry, and snow parameters are the largest source of uncertainty in these calculations (Zhou et al., 2018; Kwok et al., 2020). While it is known that snow cover on Antarctic sea ice is generally thicker than snow on Arctic sea ice (Massom et al., 2001), the depth and density of snow on sea ice remain poorly constrained, with even a reliable climatological baseline lacking in the Antarctic (Webster et al., 2018). Available measurements are limited and sparse due to the difficulty of accessing the Southern Ocean in winter. These include visual records of snow thickness on ice floes broken and overturned along the hull of passing ships (Worby, Geiger, et al., 2008), assorted in situ measurements from snow pits, snow probes, and snow cores (e.g., Sturm et al., 1998; Worby, Markus, et al., 2008; Arndt & Paul, 2018), and observations of snow accumulation from autonomous instruments deployed on drifting pack ice and fast ice in the Weddell Sea (henceforth “snow buoys”; Nicolaus et al., 2021; Arndt et al., 2024).

Remote sensing offers the promise of continuous circumpolar estimates of snow depth on Antarctic sea ice, albeit with different challenges. Antarctic snow depth has long been estimated using empirical algorithms applied to passive microwave satellite radiometry (Markus & Cavalieri, 1998, 2006; Comiso et al., 2003; Shen et al., 2022; Yan et al., 2023, 2024), but these retrievals are sensitive to weather effects, snow metamorphic properties such as wetness and grain size, and ice deformation (e.g., Kern et al., 2011; Markus et al., 2011; Rostosky et al., 2020).

Additionally, retrievals based on satellite laser or radar altimetry, or combinations of the two, have been used (Kern & Ozsoy-Çiçek, 2016; Kacimi & Kwok, 2020; Garnier et al., 2021; Fons et al., 2023). Aerial repeat surveys from Operation IceBridge have also generated snow depth measurements in some years and regions (e.g., Kwok & Kacimi, 2018). Overall, the practical utility of remote sensing estimates has been limited by uncertainties concerning the depth of radar penetration within the snowpack (e.g., Ricker et al., 2014; Kacimi & Kwok, 2020), the short coverage periods and lack of up-to-date data for many products, necessary time averaging, and the scarcity of seasonally and regionally diverse validation data sets.

Observationally constrained model reconstructions are a natural answer, but these also require validation data as well as accurate input forcing and simulations of key processes that influence net snow accumulation. The latter presents a challenge: for example, estimates of the magnitude of snow loss due to the trapping of wind-blown snow in leads vary substantially from 0% to 50% of all deposited snow (Eicken et al., 1994; Déry & Tremblay, 2004; Leonard & Maksym, 2011; Toyota et al., 2016; Liston et al., 2020; Clemens-Sewall et al., 2023). The potential importance of processes like sublimation (Fichefet & Morales Maqueda, 1999; Déry & Yau, 2002; Chung et al., 2011) and rainfall on snow (Dou et al., 2019; Boisvert et al., 2020; Stroeve et al., 2022) is also uncertain. These processes are highly dependent on the dynamic and variable weather conditions around Antarctica, where abrupt changes in wind, temperature, and precipitation are common (Sturm & Massom, 2017). Additionally, the formation of snow-ice from isostatic flooding of the snowpack by seawater—which is ubiquitous in the Antarctic, unlike in the Arctic, due to its thinner sea ice cover (Massom et al., 2001)—cannot be constrained by a model reconstruction without knowledge or estimation of sea ice thickness.

Existing model reconstructions of snow on Antarctic sea ice have either simulated the net accumulation of snow along Lagrangian sea ice drift pathways or accounted for ice motion within a fixed Eulerian frame. For snow on Antarctic sea ice, these include the recent CPOM Antarctic Snow on Sea Ice Simulation (CASSIS), a Lagrangian model forced by ERA5 atmospheric

reanalysis that incorporates blowing snow loss to the ocean, katabatic snow transport from the Antarctic continent, and a fixed snow-ice formation fraction (Lawrence et al., 2024); an Eulerian simulation forced by ERA-40 reanalysis that represented snow-ice formation and the effects of ice divergence (Maksym & Markus, 2008); and a coupled snow and sea ice modeling study that accounted for snow-ice formation, snow surface sublimation, and lead trapping, and examined the sensitivity of the coupled system evolution to key parameters under climatological forcing (Fichefet & Morales Maqueda, 1999). In the Arctic, reconstruction efforts include SnowModel-LG, a multilayer Lagrangian snow evolution model that simulates sublimation (both from the snow surface and blowing snow), melt, superimposed ice, and ice dynamics (Liston et al., 2020; Stroeve et al., 2020; Horvath et al., 2023); the NASA Eulerian Snow on Sea Ice Model (NESOSIM), a two-layer snow budget model that includes parameterizations of accumulation, compaction, lead trapping, and ice advection and divergence (Petty et al., 2018; Cabaj et al., 2023); and a Lagrangian reconstruction in which the effects of sublimation and divergence were approximated (Blanchard-Wrigglesworth et al., 2018)—all of which were forced by reanalysis data. While each of these approaches has offered valuable insight into snow processes, many rely on parameterizations that are ad hoc or poorly constrained, which may reduce confidence in the ability of some existing reconstructions to accurately reconstruct the time evolution of snow.

A robust reconstruction methodology has the potential to illuminate the fate of snow deposited on Antarctic sea ice by identifying the factors controlling net snow mass accumulation in time and space and quantifying how much, when, and where freshwater fluxes from snowfall are released to the Southern Ocean. In this study, we develop a new Lagrangian model of snow evolution on Antarctic sea ice that integrates the combined influence of snow accumulation, erosion, and transformation mechanisms (Section 3.3.3) and describe the data used to force, calibrate, and evaluate it (Section 3.3.1 and 3.3.2). We adapt and synthesize a set of parameterizations that each have a firm physical or empirical basis (Section 3.3.4). We then calibrate their relative magnitudes by adjusting eight model free parameters to optimize the

model fit to matched in situ observations of snow accumulation from Lagrangian snow buoys in the Weddell Sea (Section 3.3.5). Finally, we assess the calibration results (Section 3.4.1); quantify the climatological snow budget and its spatial patterns (Section 3.4.2 and 3.4.3); compare our estimates to remote sensing retrievals of snow depth, allowing us to infer snow-ice formation, and discuss bulk snow density (Section 3.4.4); and diagnose interannual trends in snow accumulation (Section 0).

3.3 Data and methods

3.3.1 Model input data

Data used as input for the model during its simulation period of 15 February 2003 to 14 February 2024 include passive microwave remote sensing retrievals of Antarctic sea ice concentration and snow depth on sea ice, remotely sensed sea ice motion estimates, and atmospheric reanalysis. All products were regridded to the European Centre for Medium-Range Weather Forecasts (ECMWF) ERA5 reanalysis grid, which is uniform in longitude and latitude (0.25° x 0.25°), using a geospatial bilinear remapping algorithm.

3.3.1.1 Sea ice concentration

Daily sea ice concentration (SIC) estimates from passive microwave satellite radiometry, $f_{\mathrm{SIC,PMW}}$ (0–100%), measured by the Advanced Microwave Scanning Radiometer for EOS (AMSR-E; 2002–2011) and AMSR2 (2012–present) sensors were obtained using the University of Bremen's ARTIST Sea Ice (ASI) product, version 5.4, on a 6.25 km polar stereographic grid (Spreen et al., 2008; Beitsch et al., 2014). AMSR-E and AMSR2 data were unavailable on 289 days during the model simulation period, including the 273 days from 5 October 2011 to 3 July 2012 between the AMSR-E and AMSR2 sensors. Days of fully absent AMSR-E/2 data were substituted with daily passive microwave SIC measured by the Special Sensor Microwave Imager (SSM/I) and Special

Sensor Microwave Imager/Sounder (SSMIS) radiometers. These fields were obtained using the National Oceanic and Atmospheric Administration (NOAA) and National Snow and Ice Data Center (NSIDC) Climate Data Record (CDR) product, version 4, through 31 December 2023 and the NOAA/NSIDC Near-Real-Time (NRT) CDR product, version 2, from 1 January 2024 onwards, both provided on a lower-resolution, 25 km polar stereographic grid (Meier et al., 2021a, 2021b). Additionally, AMSR-E/2 SIC data were partially missing on 39 days, most often within narrow linear streaks or swatches, identified using a criterion of over 500 grid cells with at least a 50% difference in SIC between the AMSR and CDR products after remapping both to the ERA5 grid and filling missing values with a SIC of 0%. On these days of partially missing AMSR SIC data, the CDR or NRT CDR estimates were substituted in the missing grid cells.

3.3.1.2 Passive microwave snow depth

Passive microwave snow depth retrievals from AMSR-E and AMSR2 are used for model initiation each year as well as validation of the model reconstructions. The NSIDC AMSR-E and AMSR2 Level 3 products provided on a 12.5 km polar stereographic grid were derived from an empirical algorithm developed using SSMI data in the Southern Ocean that relies on the spectral gradient ratio between the 18.7 GHz and 37 GHz vertical polarization channels (Markus & Cavalieri, 1998; Cavalieri et al., 2014; Meier et al., 2018). Limitations of the snow depth estimates include a technical upper retrieval limit of 50 cm and applicability to dry snow conditions only. However, snow depths thicker than 0.5 m are still provided. These generally exist only in the western Weddell Sea at the time of model initiation (February 15 of each year; see Section 3.3.3), limiting the geographic impact of potential biases to this region of multiyear sea ice as well as the northern Weddell Sea, which receives ice drift from lower latitudes. A recent study proposing a new snow depth retrieval method using lower frequency channels of AMSR-E/2, which are more sensitive to thicker snow, finds comparable snow depths of ~60 cm in the western Weddell Sea in summer (Shen et al., 2022). However, neither retrieval is well-suited for measuring snow on multiyear sea

ice because its emission signal can mirror that of snow; thus, uncertainties owing to the snow depth initialization would exist regardless of the choice of product.

Due to weather contamination and snow grain size and density uncertainties, the daily fields are provided as five-day running averages and are considered here to represent the central (third) day. After regridding, snow depths over all dates from 5 days before to 5 days after the Lagrangian parcel initialization date (15 February for free-running simulations, or a date determined by the snow buoy observations; see Section 3.3.3) were averaged for use in model initialization to further reduce noisiness, such as from weather effects. During the gap between AMSR-E and AMSR2 from October 2011 to July 2012, a climatological value of these averages calculated over 2003–2024 was used for model initialization instead.

3.3.1.3 Sea ice motion

Remotely sensed estimates of sea ice motion are used to determine the movement of Lagrangian parcels in the model (Figure 3.1a). The NSIDC Polar Pathfinder daily product, version 4.1, through 31 December 2023 and the NSIDC 'Quicklook' Polar Pathfinder weekly product, version 1, from 1 January 2024 onwards, both provided on a 25 km Equal-Area Scalable Earth (EASE) grid, were obtained for this purpose (Tschudi, Meier, & Stewart, 2019; Tschudi, Meier, Stewart, et al., 2019; Tschudi et al., 2020). The Polar Pathfinder estimates rely on automated tracking of ice displacement from SSM/I and SSMIS passive microwave measurements using maximum cross correlation techniques, with ice drift vectors composited over each 24-hour period.

Schwegmann et al. (2011) assessed the performance of the Polar Pathfinder product, version 3, using a compilation of Weddell Sea drifting sea ice buoys. They concluded that the remotely sensed drift speeds were biased low by an average of 34.5% compared to the buoys, with mean differences of $\Delta u_i = -1.2$ cm s^{-1} and $\Delta v_i = -1.0$ cm s^{-1}. Nonetheless, the satellite and buoy drift components were well-correlated ($r \approx 0.6$), indicating good agreement in drift direction. The Polar Pathfinder product was subsequently updated to version 4, with corrections to previous over-

filtering of motion vectors leading to an increase in Antarctic-wide sea ice drift speed by 0–2 cm s^{-1}, a change of around +1 cm s^{-1} during the SSM/I and SSMIS period from 1987 onwards (Tschudi et al., 2020). Version 4 also corrects circular artifacts in the version 3 ice motion data that had been identified (Szanyi et al., 2016). As version 4 of the Polar Pathfinder product fully or almost fully corrects the slow bias assessed by Schwegmann et al. (2011), no further major bias corrections appear to be warranted. We therefore do not include the scaling factor of 1.357 applied by Haumann et al. (2016) to the version 3 data and—perhaps mistakenly—by Shi et al. (2021) to the version 4 data.

Prior to remapping to the ERA5 grid, the EASE grid-oriented ice motion components were rotated to obtain the eastward and northward ice motion vectors u_i and v_i. The weekly data for 2024 were linearly interpolated to daily resolution after shifting their assigned dates to the central (fourth) day of each week, and linear interpolation was similarly used to fill 9 days with missing data during 2003–2023. Additionally, ice motion grid cells with missing ice drift vectors but with SIC greater than 0% were identified, generally confined to two narrow bands along the sea ice edge and the Antarctic continent. Two-dimensional nearest-neighbor interpolation naively based on longitude and latitude grid cell indices (rather than geospatial distances) was then used to fill these missing Polar Pathfinder grid cells, which importantly prevents simulated Lagrangian sea ice parcels adjacent to the Antarctic continent from remaining static and accumulating excessive amounts of snow. The downside of this approach is that some sea ice parcels may unrealistically originate from or transit through areas of landfast ice. Nonetheless, a visual comparison of parcel trajectories with a mapping of Antarctic fast ice suggests this is uncommon except for parcels originating in a region of persistent fast ice offshore of the Filchner-Ronne Ice Shelf in the Weddell Sea (Fraser et al., 2021).

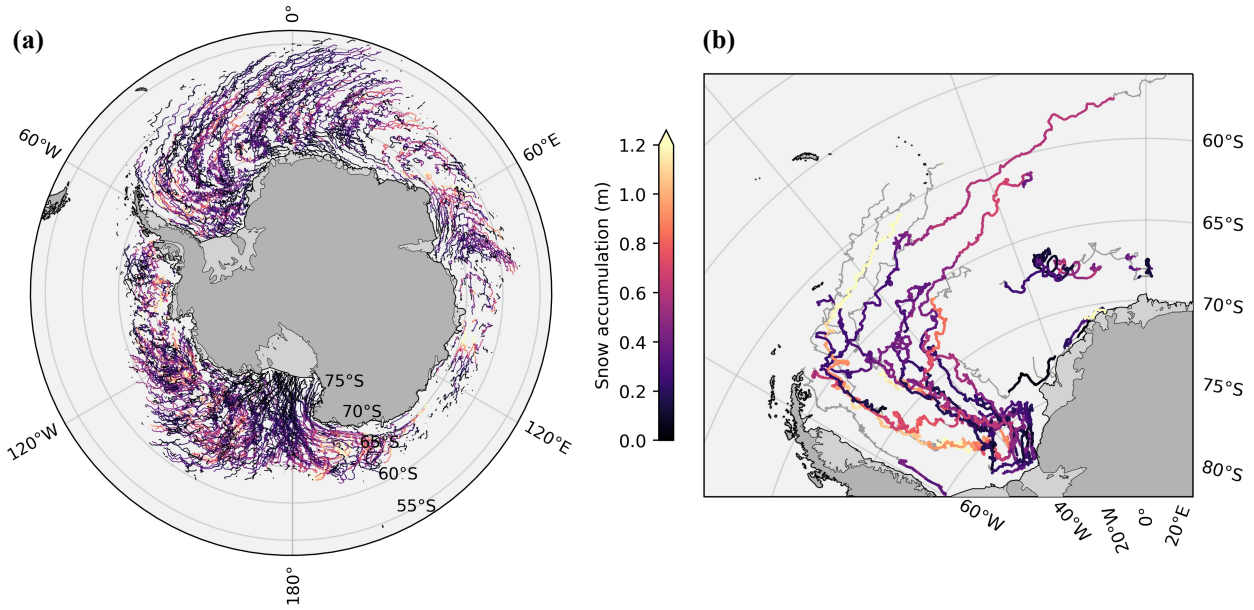

Figure 3.1: Simulated sea ice parcel drift trajectories and observed snow buoy drift. (a) One year of sea ice parcel drift trajectories simulated in the model from 15 February 2021 to 14 February 2022, with parcel movement determined using remotely sensed sea ice motion vectors. Every 250th sea ice parcel is shown here. Lines are colored by the reconstructed net snow accumulation. **(b)** Drift trajectories of 29 snow buoys in the Weddell Sea from 2013 to 2022, with colors indicating net snow accumulation measured by ultrasonic sensors on the buoys and grey lines indicating periods lacking data.

3.3.1.4 Atmospheric reanalysis

ECMWF's ERA5 fifth-generation atmospheric reanalysis, produced using 4D-Var data assimilation, is used as input to the physical parameterizations in the snow model (Hersbach et al., 2020; Copernicus Climate Change Service, 2023). Hourly fields at 0.25° x 0.25° resolution were obtained for the following variables: S, the time-mean snowfall rate, and P_{tot}, the time-mean total precipitation rate (kg m^{-2} s^{-1}), from which the time-mean rainfall rate R was calculated as $(P_{\mathrm{tot}} - S)$; u_{10} and v_{10}, the eastward and northward components of wind velocity at 10 m (m s^{-1}), from which the 10-m wind speed, U_{10}, was calculated; T_a, the 2-m air temperature (°C); T_d, the 2-m dewpoint temperature (K); P_s, the surface atmospheric pressure (hPa); and $f_{\mathrm{SIC,ERA5}}$, the reanalysis sea ice concentration (0%–100%).

An evaluation of ERA5 precipitation against other reanalysis products showed strong consistency in the spatial patterns and interannual variability of snowfall over the Southern Ocean but a ~200 mm yr^{-1} spread in the magnitude of snowfall across five reanalyses (Boisvert 2020). ERA5 snowfall within the Antarctic seasonal ice zone was found to exhibit a similar spatial pattern to CloudSat-derived estimates. This significant uncertainty in the magnitude of reanalysis snowfall, but not its large-scale patterns, motivates the inclusion of a scaling parameter for ERA5 snowfall in our model calibration procedure.

Similar to other atmospheric analyses, ERA5 has been shown to have a warm bias in estimated surface temperature over Antarctic and Arctic sea ice likely due to its inaccurate representation of low clouds, with additional contributions from its treatment of sea ice as a constant-thickness slab with no overlying snow (C. Wang et al., 2019; Graham, Cohen, et al., 2019; Zhaohui Wang et al., 2024). That said, near-surface air temperatures from ERA5 are used in this study without corrections for two reasons: biases appear to be small near 0°C (Graham, Cohen, et al., 2019; King et al., 2022), where they would be most influential, and are only well-quantified in the Antarctic for sea ice skin temperatures—rather than near-surface air temperatures—under clear-sky conditions (Zhaohui Wang et al., 2024), which are less relevant for snow mass accumulation and loss processes.

Other key ERA5 reanalysis parameters appear to be fairly accurate over sea ice, with studies finding a minimal 10-m wind speed bias (less than 0.2 m s^{-1} at wind speeds greater than 5 m s^{-1}) and small surface pressure biases over Weddell Sea pack ice (King et al., 2022) and negligible 10-m wind speed bias over Arctic sea ice (Graham, Cohen, et al., 2019).

3.3.2 Calibration, validation, and comparison data

3.3.2.1 Snow buoys

Snow accumulation observations from 29 snow buoys drifting on sea ice in the Weddell Sea between 2013 and 2022 (Figure 3.1b) are used for calibration of free parameters in the snow

model, excluding 11 snow buoys deployed on fast ice in Atka Bay, Queen Maud Land (Nicolaus et al., 2017). The snow buoys are simple autonomous platforms developed by the Alfred Wegener Institute (AWI) and MetOcean Telematics consisting of a main body installed below the sea ice surface and a mast carrying a cross-shaped frame with four ultrasonic sensors at its ends, which each sit 1.5 m above the main body and measure their distance to the snow surface at approximately hourly resolution (Nicolaus et al., 2021). The platform also includes a surface temperature sensor, barometer, ice ablation shield, and GPS and data transmission modules. The lifetime of each snow buoy is highly variable, ranging from a month to 1–2 years. We average snow height measurements from the four ultrasonic sensors and linearly interpolate over data gaps of up to one day in the averaged time series.

The Lagrangian nature of observations from snow buoys deployed on drifting ice floes allows for an apt comparison to simulated Lagrangian parcels in our model. Furthermore, snow buoys measure changes in net snow accumulation relative to their deployment baseline, and thus processes such as snow-ice conversion or superimposed ice formation may take place with corresponding decreases in actual *snow depth* yet minimal change in the measured *snow accumulation*, or surface height. This is an advantage for the purposes of model calibration, as snow-ice conversion is not represented in our model and thus the snow buoy observations offer a rather direct analogue to the reconstructed snow accumulation along the same drift trajectory, albeit at the local scale of point measurements rather than the grid cell averages that our model represents. In contrast, ship-based observations of snow depth, generally visual estimates collected as ice floes become upturned against the hull of the ship, exclude snow that has been transformed into basal layers of ice following flooding or melt processes. Additionally, the ship-based observations collected in the Antarctic Sea Ice Processes and Climate (ASPeCt) archive are known to be biased towards areas of thinner, undeformed sea ice and snow due to the nature of ship navigation (Worby, Geiger, et al., 2008). Both of these caveats preclude a meaningful

comparison between ship-based observations and our model estimates, and so we do not use ASPeCt data for calibration or validation of the model.

3.3.2.2 CryoSat-2 snow depth estimates

A retrieval of snow depth on Antarctic sea ice using CryoSat-2 satellite radar altimetry data is compared with model output, along with the AMSR-E/2 snow depth estimates. The CryoSat-2 retrieval method applies waveform modeling and an optimization procedure to individual radar returns to estimate the snow depth, a fit parameter of the model, which together with the snow freeboard (its height above the sea surface) enables the calculation of sea ice thickness (Fons et al., 2023). The retrieved snow depths were found to compare well to another product derived from CryoSat-2 and ICESat-2 (Kacimi & Kwok, 2020) and, as expected, skew higher than the ship-based ASPeCt observations. The monthly estimates span July 2010 through August 2021 and are provided on a 25 km polar stereographic grid; the data are averaged here as a monthly climatology, which is remapped to the ERA5 grid as described in Section 3.3.1.

3.3.2.3 Sea ice extent index

As a point of comparison to simulated snow-related trends, we use Southern Hemisphere monthly-averaged sea ice extent (SIE) data obtained from the NSIDC Sea Ice Index, version 3 (Fetterer et al., 2017). The SIE estimates are derived from daily SSM/I and SSMIS passive microwave SIC data using a minimum SIC threshold of 15% to determine sea ice-covered areas, with all such areas counting towards the total daily extent. We truncate the index time series to the model simulation period of March 2003 to February 2024.

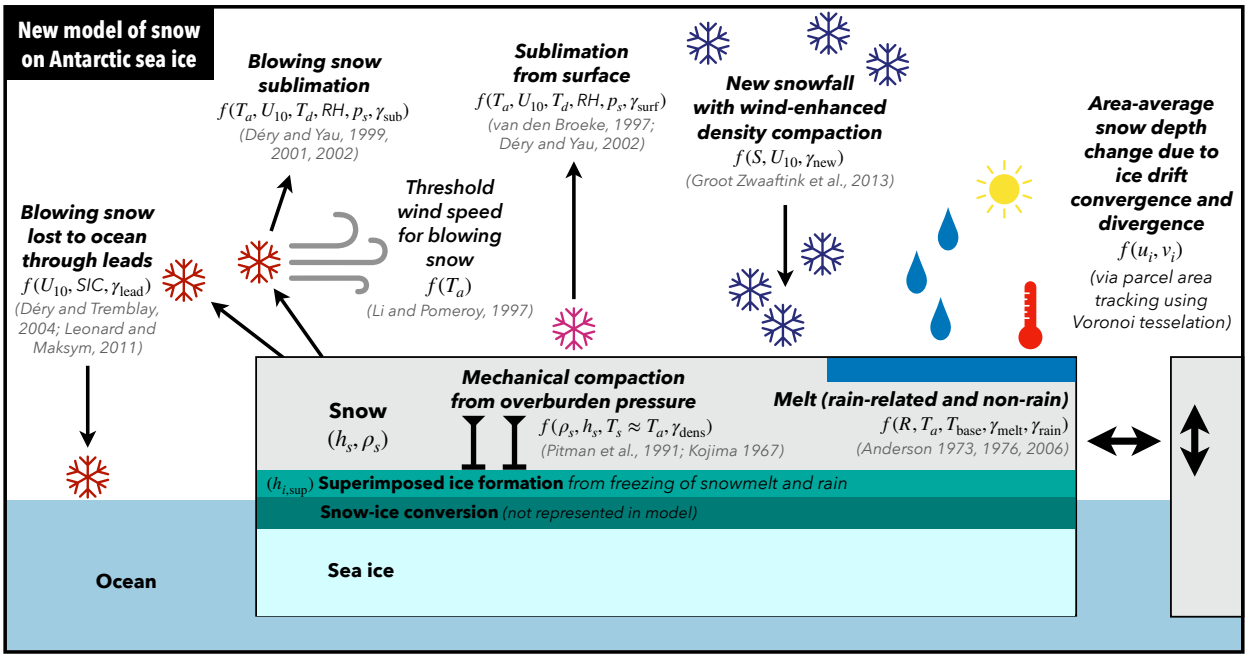

Figure 3.2: Summary of snow input, loss, and transformation processes included in the Lagrangian model reconstruction. Their primary originating sources, parameter dependencies, and other key variables are noted.

3.3.3 Model overview

The single-layer Lagrangian snow reconstruction model is intended to simulate the most critically important accumulation, loss, and transformation processes for snow on Antarctic sea ice with enough complexity to express key parameter dependencies. At the same time, it remains sufficiently computationally lightweight to allow for an iterative calibration procedure (Section 3.3.5). We express the model budget for snow accumulation on sea ice as the sum of the following terms (each expressed throughout in units of m snow h^{-1}):

$$\frac{\partial h_s}{\partial t} = Q_{\text{dyn}} - Q_{\text{dens}} - Q_{\text{melt}} - Q_{\text{rain}} + Q_{\text{dep}} - Q_{\text{sub}} - Q_{\text{lead}} - Q_{\text{surf}}\,, \tag{3.1}$$

where $\frac{\partial h_s}{\partial t}$ represents the net accumulation rate of snow depth at the ice surface; Q_{dep} is the rate of new snow deposition, after accounting for wind-enhanced density compaction of fresh snow; Q_{surf} is the rate of sublimation from the snow surface; Q_{sub} is the sublimation rate of wind-blown snow;

Q_{lead} is loss to the ocean due to the trapping of blowing snow in sea ice leads; Q_{dens} is the rate of mechanical compaction of the snowpack; Q_{melt} and Q_{rain}, respectively, are non-rain-related and rain-related snow melt, the meltwater from both of which is assumed to refreeze into a layer of superimposed ice; and Q_{dyn} represents the net large-scale impact of sea ice dynamics on snow depth, namely area-averaged thickening of snow due to ice convergence and area-averaged thinning due to ice divergence and subsequent snow-free new ice formation. Free parameters are included in all the budget terms except Q_{dyn}, allowing their synchronous adjustment to optimize the model fit to snow buoy observations using the procedure described in Section 3.3.5. Key model parameter settings and constants are listed in Table 3.1.

The model tracks the time evolution of four main state variables: snow depth, h_s (units of m in equations throughout); bulk snow density, ρ_s (kg m^{-3}); superimposed ice thickness, $h_{i,\mathrm{sup}}$ (m); and parcel area (km^2; see Section 3.3.4.7). To summarize the model operation: ERA5 hourly reanalysis snowfall is accumulated along Lagrangian trajectories determined by the Polar Pathfinder sea ice motion vectors. Changes in snow depth and bulk density due to deposition, loss, and transformation terms (Section 3.3.4) are computed using ERA5 reanalysis variables supplemented by passive microwave SIC data, acting sequentially in the order listed in Eq. (3.1). Lastly, model output along the Lagrangian trajectories are binned and gridded in a volume- and mass-conserving way, enabling analysis within an Eulerian frame of reference (Section 3.3.4.8).

The model is normally initialized with the creation of Lagrangian 'parcels' that each represent a large region of drifting sea ice. When running in its calibration mode, however, each parcel represents point measurements at the location of one AWI snow buoy and the movement of parcels in longitude, latitude, and time is prescribed using the observed snow buoy trajectories. Otherwise, in its free-running mode, the model initializes parcels on February 15 of each year, around the climatological Antarctic sea ice extent minimum, and evolves until February 14 of the following year, after which parcels are re-initialized without any memory from the prior one-year

period. This prevents interannual model drift due to any accumulated biases and enables the efficient parallelization of the one-year model runs across multiple cores of a server.

The model period of 15 February 2003 to 14 February 2024 was selected due to the availability of AMSR-E/2 snow depth on sea ice from June 2002 onwards. For a free-running simulation, sea ice parcels are initialized at every 0.25° x 0.25° grid point where SIC ≥ $f_{\mathrm{SIC},0}$, a threshold ice concentration for parcel existence set at 15%, with h_s set as the ±5-day average AMSR-E/2 snow depth (see Section 3.3.1.2). When running in calibration mode, sea ice parcels are initialized at exact snow buoy locations using the ±5-day average AMSR-E/2 snow depth at the nearest grid point. Bulk snow density ρ_s is set initially at $\rho_{s,0}$ = 320 kg m^{-3} (Massom et al., 1997; Song et al., 2020), the value also used for the normalization of terms in the snow depth tendency budget when visualizing model output (Figure 3.7, Figure 3.9, Figure 3.10), and superimposed ice thickness $h_{i,\mathrm{sup}}$ is initialized as 0 cm. In a free-running simulation, parcel areas are also calculated at this time using Voronoi tesselation (Section 3.3.4.7).

The model evolves forward using an outer loop with a daily time step, which updates the parcel locations, determines the creation of new parcels, and handles the destruction of unneeded parcels. In a free-running simulation, new parcel longitude and latitude are determined using the azimuth and displacement computed from the previous day's Polar Pathfinder ice motion vectors. Parcels where the nearest grid point SIC ≤ $f_{\mathrm{SIC},0}$ are marked as no longer in existence, that is, the ice is assumed to have completely melted into the ocean. The deposition of snow or superimposed ice into the ocean upon parcel destruction is recorded, with variables tracking the date, longitude and latitude (set as the midpoint of the previous and current days' parcel locations), and snow depth (normalized to $\rho_{s,0}$) or superimposed ice thickness (fixed at a density of $\rho_{i,\mathrm{sup}}$ = 850 kg m^{-3}, per Nicolaus et al., 2003) released into the ocean. New parcels, representing newly formed sea ice along the ice edge or within large areas of open water within the ice pack, are introduced by first binning existing parcels onto the ERA5 grid, then adding new parcels at the center of grid cells that have SIC ≥ $f_{\mathrm{SIC},0}$ yet contain no existing parcels. For new parcels in a free-running

Table 3.1: Parameter settings and constants in the snow model.

Parameter or constant	Value	Significance and origin
Δt	1 h	Model time step for calculation of all snow depth tendency terms in Eq. (3.1) except for Q_{dyn}
$\rho_{s,0}$	320 kg m^{-3}	Bulk snow density for model initiation and normalization of fluxes in model output (Massom et al., 1997; Song et al., 2020)
$\rho_{i,\text{sup}}$	850 kg m^{-3}	Superimposed ice density (Nicolaus et al., 2003)
ρ_i	917 kg m^{-3}	Density of ice
ρ_w	1000 kg m^{-3}	Density of liquid water
$f_{\text{SIC,o}}$	0.15	Sea ice concentration threshold for sea ice parcel existence
δ_A	0.25	Parcel area scaling tolerance (±) when accounting for convergent or divergent ice motion
k_n	4000 K	Baseline value of parameter representing the temperature dependence of the snow compactive viscosity (Pitman et al., 1991)
R_{thresh}	0.25 mm h^{-1}	Minimum rainfall rate for rain-on-snow melt parameterization to be active (E. A. Anderson, 2006)
UADJ	0.15 mm mbar^{-1}	6-hour average wind function factor in the NWS SNOW-17 model rain-on-snow parameterization (Franz et al., 2008)
σ	6.12×10^{-10} mm SWE K^{-4} hr^{-1}	Stefan-Boltzmann constant, expressed in terms of snow melt (E. A. Anderson, 2006)
$P_{s,0}$	1012 mbar	Approximate surface atmospheric pressure
z_0, z_q	1×10^{-3} m	Aerodynamic roughness lengths for momentum and moisture over sea ice (Jordan et al., 1999)
R_d	287.053 J K^{-1} kg^{-1}	Dry air gas constant (Stull, 2000)
R_v	461.5 J kg^{-1} K^{-1}	Individual gas constant for water vapor (Rogers & Yau, 1989)
κ	0.4	von Kármán constant
T_0	273.16 K	Freezing temperature of water
g	9.8 m s^{-2}	Acceleration due to gravity

simulation, h_s and $h_{i,\text{sup}}$ are initialized at 0 cm and ρ_s is set to $\rho_{s,0}$; in calibration mode, new parcels are initialized with the ±5-day average AMSR-E/2 snow depth nearest to buoy locations. Updated areas are then calculated for all active parcels and used to scale h_s and $h_{i,\text{sup}}$ to account for the effects of large-scale ice convergence and divergence in a volume-conserving way (see Section 3.3.4.7). Around 500,000 parcels are formed and tracked during each one-year simulation.

An inner model loop with an hourly time step updates snow and ice state variables using the physical parameterizations described in Section 3.3.4, which rely on ERA5 reanalysis and passive microwave SIC data. In a free-running simulation, reanalysis and SIC values are obtained from the grid point nearest to the midpoint of the previous and current days' parcel longitude and

latitude (i.e., the parcel location at hour 12:00, assuming a linear translation in space). In calibration mode, the precise hourly locations of snow buoys are used instead.

3.3.4 Parameterizations of snow processes

3.3.4.1 Compaction from overburden pressure

A snowpack will increase in density and decrease in depth over time due to mechanical compaction and fragmentation of snow grains subject to the overlying load of snow and air, a metamorphic process that happens more rapidly at warmer temperatures. We adopt a parameterization for the settling, or densification, rate of snow due to self-loading from Pitman et al. (1991), which is based on a model by Kojima (1967) calibrated to field measurements of terrestrial snow in Hokkaido, Japan. This expression has been used by Lynch-Stieglitz (1994), Slater et al. (1998), and others; other comparable formulations based on Kojima (1967) are ubiquitous. It assumes that the snow layer is approximately isothermal; as an approximation, we equate snowpack temperature with the overlying 2-m air temperature, T_a (°C). The rate of change of bulk snow density (kg m^{-3} s^{-1}) is set to:

$$\frac{\partial \rho_s}{\partial t} = \frac{1}{2} h_s \rho_s^2 g \cdot (10^7 \text{ m s kg}^{-1}) \cdot \exp\left(14.643 - \frac{\gamma_{\text{dens}}^{-1} k_n}{\min(T_0, T_0 + T_a)} - 0.02\rho_s\right), \qquad (3.2)$$

where g is the gravitational acceleration (9.8 m s^{-2}), T_0 is the freezing temperature of water (273.16 K), and k_n is an empirical parameter representing the temperature dependence of the compactive viscosity of snow. Kojima (1967) proposed a range of 2600–4600 K for k_n. Here we adopt an initial estimate of 4000 K, similar to Pitman et al. (1991), and apply an inverse scaling factor γ_{dens} for the purposes of model calibration, in which an increase in γ_{dens} will produce more rapid compaction. This scaling factor will likely subsume the effects of other snow diagenetic processes (e.g., grain sintering) that are not explicitly represented in this parameterization.

After obtaining the change in snow density, $\Delta\rho_s$, over one time step, Δt = 1 h, the change in snow depth is computed as:

$$Q_{\text{dens}} = \frac{h_s|_{t-1}}{\Delta t}\left(\frac{\Delta\rho_s}{\rho_s|_{t-1} + \Delta\rho_s}\right). \quad (3.3)$$

3.3.4.2 Wind-enhanced compaction of fresh snowfall

During blowing snow events at higher wind speeds, new and recently deposited snow grains decrease in size due to fragmentation during collisions with each other or the snow surface and become more rounded due to abrasion and enhanced sublimation. This enables closer, more efficient packing of snow grains upon settling, significantly increasing the density of the surface snow layer compared to that of new snowfall (Walter et al., 2024). We adopt an empirical parameterization of this process developed by Groot Zwaaftink et al. (2013) on the basis of 128 density measurements of the snow surface (upper 10 cm) on the Antarctic Plateau, with a modification by Keenan et al. (2021) to extend it to all wind speeds. For simplicity, we apply this formulation to all new snowfall, whose density $\rho_{s,\text{new}}$ is therefore set at:

$$\rho_{s,\text{new}} = \left(361\ \text{kg m}^{-3}\right) \cdot \log_{10}\left(U_{10,100\text{h}}\right) + \left(33\ \text{kg m}^{-3}\right) \text{ when } U_{10,100\text{h}} > 1\ \text{m s}^{-1}, \quad (3.4)$$

$$\rho_{s,\text{new}} = 33\ \text{kg m}^{-3} \text{ when } U_{10,100\text{h}} \leq 1\ \text{m s}^{-1}. \quad (3.5)$$

Similar to Groot Zwaaftink et al. (2013), we use the 100-h forward-looking (left-edge) rolling average 10-m wind speed, $U_{10,100\text{h}}$ (m s^{-1}), to reflect the timescale on which wind packing can occur after a new snowfall event, as a new snow layer will rapidly become strongly bonded due to diagenetic effects such as sintering and wind crust formation. For example, using an equation developed by Box et al. (2004) that parameterizes these effects based on the force required to disaggregate bonds of snow particles of a certain age, we estimate that only about one-third of a fresh snow layer will remain available for aeolian transport 100 hours after deposition. Note that for computational efficiency, the model implementation of $U_{10,100\text{h}}$ relies on 100-h wind speed averaged at the location of snowfall and does not account for the advection of sea ice parcels, thus assuming drifting sea ice experiences a similar average wind speed over 100 h as if it were stationary.

To obtain the change in snow depth due to new snowfall over Δt = 1 h, a scaling factor γ_{new} is applied to allow calibration of the ERA5 reanalysis snowfall rate S (kg m^{-2} s^{-1}), for which potential biases in magnitude are uncertain (see Section 3.3.1.4):

$$Q_{\text{dep}} = \frac{\gamma_{\text{new}}\, S}{\rho_{s,\text{new}}} \cdot \frac{(3600\ \text{s})}{\Delta t}\ . \tag{3.6}$$

The bulk density of the snow layer is then updated as a weighted average of the previously existing and freshly deposited snow.

3.3.4.3 Non-rain and rain-related snow melt

We implement two parameterizations of snow melt, one for melt due to changes in the snowpack net energy balance associated with radiative fluxes and warm air in times when rainfall is absent or insignificant (henceforth "non-rain" conditions) and the second for melt during significant rain-on-snow (ROS) events. As our model is not intended to comprehensively represent snow thermodynamics, we adopt simple formulations from the National Weather Service (NWS) SNOW-17 operational model (E. A. Anderson, 1973, 1976, 2006), which has been used for decades for the purpose of snow melt and streamflow forecasting. While intended for land surface use, their functional forms capture fundamental parameter dependencies on air temperature and rainfall rate, to which we add three free parameters for calibration to the snow and meteorological conditions typical of the Antarctic seasonal ice zone (SIZ). Melt can only occur when at least a portion of the snowpack has warmed to the freezing point, a condition which both the non-rain and ROS parameterizations assume has occurred; we rely on the scaling parameters to make adjustments if this is not the case and melt is predicted too frequently. The original, unscaled form of the ROS melt parameterization also assumes that solar radiation is minimal due to overcast conditions, that the dewpoint and rain temperature are both equal to the ambient (2-m) air temperature T_a, and that the relative humidity is high at around 90%.

Both snowmelt and rainfall liquid water mass are conserved in the model, assumed to percolate downwards before refreezing within a new or existing superimposed ice layer with a

density of $\rho_{i,\mathrm{sup}}$ = 850 kg m^{-3} (Nicolaus et al., 2003). Superimposed ice layers have been observed to form at the base of the snowpack on Antarctic sea ice (e.g., Arndt et al., 2021), but internal ice layers due to surface crusts that become buried may also be present within the snowpack and intercept percolating meltwater (Massom et al., 2001). Our single-layer model is agnostic as to the depth at which ice layers form, but their combined thickness, $h_{i,\mathrm{sup}}$, is tracked as superimposed ice.

Non-rain melt is approximated using a "degree-day" approach and allowed to be active during hourly periods with no rain or very light rainfall ($R < R_{\mathrm{thresh}}$, where R_{thresh} is 0.25 mm h^{-1} = 0.25 kg m^{-2} s^{-1}, per Anderson, 2006). Q_{melt} (m of snow h^{-1}) is computed as the smaller of the total melt rate or the current snow depth divided by the time step:

$$Q_{\mathrm{melt}} = \min\left(\frac{h_s}{\Delta t}, \frac{\rho_w}{10^3 \rho_s \Delta t} \cdot \frac{\gamma_{\mathrm{melt}}}{(6\ \mathrm{h})}\left(\max(0°\mathrm{C}, T_a - T_{\mathrm{base}}) + \gamma_{\mathrm{rain}} \cdot M_{r,\mathrm{direct}}\right)\right), \tag{3.7}$$

where ρ_w is the density of liquid water (1000 kg m^{-3}) and γ_{melt} is the 6-hour 'melt factor' specific to a region's typical meteorological conditions. For reference, a possible range of 1–2 mm snow water equivalent (SWE) °C^{-1} 6 h for maximum summer melt in an alpine context is offered by Girotto et al. (2024); we treat γ_{melt} as a tunable parameter. T_{base} is the threshold air temperature above which snow melt tends to occur, defined as MBASE in the NWS SNOW-17 model. This is typically around 0°C, per Anderson [1973], and we consider T_{base} to be a tunable parameter as well.

γ_{rain} is the tunable scaling parameter for all rain-related melt. $M_{r,\mathrm{direct}}$ (mm SWE) in both Eqs. (3.7) and (3.9) represents the snow melt from energy released directly in the snowpack from any rainfall (R, expressed in kg m^{-2} s^{-1}), including trace amounts:

$$M_{r,\mathrm{direct}} = \left(12.5\ °\mathrm{C}^{-1}\right) \cdot \max(T_a, 0°\mathrm{C}) \cdot \frac{R}{\rho_w}. \tag{3.8}$$

ROS melt is applicable during hourly periods of significant rainfall ($R \geq R_{\mathrm{thresh}}$) with a melt rate, Q_{rain}, that is the sum of three terms, including $M_{r,\mathrm{direct}}$:

$$Q_{\text{rain}} = \frac{\rho_w}{10^3 \rho_s \Delta t} \cdot \gamma_{\text{rain}} \cdot \left(M_{r,\text{direct}} + M_{r,\text{rad}} + M_{r,\text{turb}} \right). \quad (3.9)$$

The second term, $M_{r,\text{rad}}$ (mm SWE), represents the snow melt from net radiative transfer during the meteorological conditions typical of rainfall, particularly increased downward longwave radiation:

$$M_{r,\text{rad}} = \max\begin{pmatrix} 0 \text{ mm SWE}, \\ \Delta t \cdot \sigma \cdot [(T_a + T_0)^4 - T_0^4] \end{pmatrix}, \quad (3.10)$$

in which σ is the Stefan-Boltzmann constant, expressed in terms of snow melt (6.12×10^{-10} mm SWE K^{-4} hr^{-1}).

The third term, $M_{r,\text{turb}}$ (mm SWE), represents melt due to turbulent latent and sensible heat exchange during rainfall events:

$$M_{r,\text{turb}} = \max\left(\begin{matrix} 0 \text{ mm SWE}, \\ \frac{8.5\Delta t}{(6\text{ h})} \cdot \text{UADJ} \cdot \left[\left(0.00057\ ^\circ\text{C}^{-1} \right) P_{s,0} T_a + (0.9 e_s - [6.11 \text{ mbar}]) \right] \end{matrix} \right), \quad (3.11)$$

in which the variable UADJ is the empirical average 6-hour wind function factor during ROS periods in the NWS SNOW-17 model (for which we use 0.15 mm $mbar^{-1}$ 6 h, per Franz et al., 2008), $P_{s,0}$ is an approximate surface atmospheric pressure (1012 mbar), and e_s (mbar) is the saturation vapor pressure over water at T_a, computed using an empirical formula from Rogers and Yau (1989):

$$e_s = 6.112 \exp\left(\frac{17.67\ T_a}{T_a + 243.5} \right). \quad (3.12)$$

Processes related to liquid water retention in the snowpack are not explicitly represented in this parameterization, as it is assumed that both rainfall and snowmelt freeze quickly, but their cumulative effects over time may be incorporated through the rain-induced melt scaling parameter γ_{rain}. Relevant processes include melt metamorphism, enhancement of destructive (equi-temperature) metamorphism, and a decrease in the compactive viscosity coefficient in the presence of liquid water (E. A. Anderson, 1976; T. Yamazaki et al., 1993; H.-P. Marshall et al., 1999; Abolafia-Rosenzweig et al., 2024). Note that metamorphism following rain events may also

increase the bulk density of snow, as has been observed in detail during the Multidisciplinary drifting Observatory for the Study of Arctic Climate (MOSAiC) expedition on Arctic sea ice (Stroeve et al., 2022), which this parameterization does not resolve.

3.3.4.4 Snow surface sublimation

Static-surface sublimation or deposition may occur as a continuous exchange between the air and the snow surface below or sea ice surface, if not covered by snow. Similar to the reanalysis-based reconstruction of Déry and Yau (2002), we assume that the shallow near-surface air layer quickly becomes saturated and therefore sublimation from the surface becomes minimal during blowing snow events. Therefore, we consider surface sublimation to be conditional on 10-m wind speed, U_{10} (m s^{-1}), remaining below the threshold at which dry snow transport by saltation starts to occur. This threshold is dependent on cohesion and frictional forces between snow particles and during snow particle collisions, the strength of which are related to the ambient temperature. We set the 10-m threshold wind speed for snow transport, U_t (m s^{-1}), using the temperature-dependent formula of Li and Pomeroy (1997), in which a = 9.43 m s^{-1}, b = 0.18 m °C^{-1} s^{-1}, and c = 0.0033 m °C^{-2} s^{-1}:

$$U_t = a + bT_a + cT_a^2 \,. \tag{3.13}$$

Following van den Broeke (1997) and Déry and Yau (2002), the supply-limited surface sublimation, Q_{surf} (with positive values implying net sublimation and negative values indicating net deposition), is calculated as:

$$Q_{\text{surf}} = \max\left(\frac{h_s}{\Delta t},\ -\gamma_{\text{surf}}\,\rho_a\,u^*q^* \cdot \frac{(3600\text{ s})}{\rho_s \cdot \Delta t}\right) \text{ when } U_{10} < U_t \,, \tag{3.14}$$

$$Q_{\text{surf}} = 0 \text{ m h}^{-1} \text{ when } U_{10} \geq U_t \,. \tag{3.15}$$

In Eq. (3.14), γ_{surf} is a tunable scaling factor and ρ_a is the air density (kg m^{-3}), computed following Stull (2000) as:

$$\rho_a = \frac{100P_s}{R_d(T_a + T_0) \cdot (1 + 0.61q_v)} \,, \tag{3.16}$$

in which P_s is the surface atmospheric pressure from ERA5 (hPa) and R_d is the dry air gas constant (287.053 J K^{-1} kg^{-1}). q_v is the specific humidity in the air (kg kg^{-1}), which can be computed using the 2-m dewpoint temperature from ERA5 (T_d; units K) using a form of the Magnus-Tetens equation provided by Kong and Yau (1997):

$$q_v = \frac{(3.8\ \text{hPa})}{P_s} \exp\left(\frac{17.27(T_d - T_0)}{T_d - (35.86\ \text{K})}\right) . \tag{3.17}$$

The two remaining factors are the friction velocity, u^* (m s^{-1}), which represents the intensity of turbulence produced by wind shear, and the humidity scale, q^* (kg kg^{-1}), which represents the scale of turbulent moisture variability. Following Garratt (1992), they can be defined as:

$$u^* = \frac{\kappa U_{10}}{\ln\left(\frac{[10\ \text{m}] + z_0}{z_0}\right)} , \tag{3.18}$$

$$q^* = \frac{\kappa q_{\text{i,sat}}(\text{RH}_i - 1)}{\ln\left(\frac{[10\ \text{m}] + z_q}{z_q}\right)} . \tag{3.19}$$

In these formulae, κ is the von Kármán constant (0.4) and z_0 and z_q (m) are the aerodynamic roughness lengths for momentum and moisture, respectively, which we take to be equal, $z_0 = z_q$. For the roughness lengths, we adopt a typical value for sea ice, 1×10^{-3} m, per Jordan et al. (1999). RH_i is the relative humidity with respect to ice, taken to be 2 m above the surface:

$$\text{RH}_i = \frac{q_v}{q_{\text{i,sat}}} , \tag{3.20}$$

where $q_{\text{i,sat}}$ is the saturation mixing ratio over ice (kg kg^{-1}) from Kong and Yau (1997), noting that the 2-m air temperature T_a is expressed in units of °C, unlike T_d in Eq. (3.17):

$$q_{\text{i,sat}} = \frac{(3.8\ \text{hPa})}{P_s} \exp\left(\frac{21.87\ T_a}{T_a + T_0 - (7.66\ \text{K})}\right) . \tag{3.21}$$

Note that in saturated conditions ($\text{RH}_i > 1.0$), q^* becomes positive and deposition to the snow surface, rather than sublimation, will occur.

3.3.4.5 Blowing snow sublimation

Blowing snow occurs when wind blowing over sea ice entrains loose particles of snow from the ice. During the suspension of snow grains in the air, sublimation can occur if the atmospheric boundary layer environment is subsaturated. We consider the following parameterization to be a maximum potential sublimation rate, $Q_{\text{sub,max}}$, ignoring snow supply, which we address below using the partitioning with $Q_{\text{lead,max}}$ described in Eq. (3.31). The formulation for $Q_{\text{sub,max}}$ considers the effects of wind speed, temperature, and humidity and was derived by Déry and Yau (2001) using a double-moment numerical model of blowing snow, yielding estimates that correlated well (R^2 = 0.95) with observations of sublimation from a Canadian Arctic tundra site. Blowing snow sublimation is expected only during conditions of 10-m wind speed above U_t, as specified in Eq. (3.13); subfreezing 2-m air temperature; and subsaturated air with respect to ice. We include a unit conversion factor, k (1.1574×10^{-5} d s^{-1}), and a tunable scaling factor, γ_{sub}:

$$Q_{\text{sub,max}} = \gamma_{\text{sub}}\, k\, Q'_{\text{sub}} \cdot \frac{(3600\text{ s})}{\rho_s \cdot \Delta t} \text{ when } T_a < 0°\text{C}, U_{10} \geq U_t, \text{RH}_i \leq 1.0\,, \tag{3.22}$$

$$Q_{\text{sub,max}} = 0\text{ m h}^{-1} \text{ when } T_a \geq 0°\text{C}, U_{10} < U_t, \text{or RH}_i > 1.0\,. \tag{3.23}$$

The expression Q_{sub}' represents the following:

$$Q'_{\text{sub}} = \begin{pmatrix} a_0 + a_1\xi + a_2\xi^2 + a_3\xi^3 + a_4U_{10} + a_5\xi U_{10} \\ + a_6\xi^2 U_{10} + a_7U_{10}^2 + a_8\xi U_{10}^2 + a_9U_{10}^3 \end{pmatrix} \text{kg m}^{-2}\text{ d}^{-1}\,, \tag{3.24}$$

where the dimensionless coefficients a_0 through a_9 are listed in Appendix Appendix Table 3.3 below and ξ (units of m^2 s^{-1}) is a thermodynamic term in which ρ_i is the density of ice (917 kg m^{-3}):

$$\xi = \frac{-1 \times 10^{12} \cdot (\text{RH}_i - 1)}{2\rho_i(F_k + F_d)}\,. \tag{3.25}$$

F_k and F_d (m s kg^{-1}) represent the conductivity and diffusion terms, respectively, associated with sublimation of snow. Each is dependent on temperature. Following Equation 7.17 in Rogers and Yau (1989):

$$F_k = \left(\frac{10^3 \cdot L}{R_v(T_a + T_0)} - 1\right)\frac{10^3 \cdot L}{KT_a}\,, \tag{3.26}$$

$$F_d = \frac{R_v(T_a + T_0)}{10^2 \cdot De_s}\,. \tag{3.27}$$

In these formulae, R_v is the individual gas constant for water vapor (461.5 J kg^{-1} K^{-1}), e_s is the saturation vapor pressure over water (mbar) from Eq. (3.12), L is the latent heat of condensation (J g^{-1}), K is the coefficient of thermal conductivity of air (J m^{-1} s^{-1} K^{-1}), and D is the coefficient of diffusion of water vapor in air (m^2 s^{-1}). The latter three parameters—L, K, and D—are tabulated in Appendix Appendix Table 3.4 in terms of their dependence on T_a, assuming a surface pressure of 1000 hPa for K and D. We fit third-order polynomials to each parameter to interpolate between the temperatures specified.

This representation of blowing snow sublimation relies on the tuning parameter γ_{sub} to account for the fact that older snow is lofted by the surface wind less easily than freshly deposited snow. A new snow layer rapidly becomes strongly bonded due to sintering, wind crust formation, seawater and brine wicking (capillary suction), and occasional rain penetration and refreezing (Sturm & Massom, 2017), diagenetic processes that prevent saltation and suspension of snow and are collectively termed “lock-up” (Sturm et al., 1998). Explicitly incorporating lock-up effects in a model would require tracking the age distribution of snowfall events and its complex metamorphic history—in other words, the snowpack stratigraphic structure. The tuning parameter γ_{sub} subsumes additional physical processes that may limit the amount of snow mass available for aeolian transport, such as preferential accumulation along ridges or other morphological features that can aerodynamically shelter snow. Field observations off East Antarctica by Toyota et al. (2016) suggest that this sheltering effect can substantially limit snow loss to leads in areas of rough, deformed ice, and other observations in the Bellingshausen Sea by Leonard and Maksym (2011) suggest that blowing snow may occur as little as half of the time that

wind speeds are high enough to support blowing snow initiation by the Li and Pomeroy (1997) threshold, U_t.

3.3.4.6 Transport into leads

Blowing snow may result in significant loss of snow mass into leads ("lead trapping") as well as preferential redistribution along microrelief and ridges in regions of deformed ice, processes that depend on the balance of suspension, saltation, and gravitational settling of snow grains as well as the geometric characteristics of leads and surface roughness elements. While redistribution is otherwise neglected in our model due to the large-scale, area-averaged nature of its snow mass budget, lead trapping is a potentially important loss mechanism as well as a freshwater flux to the ocean, if deposited snow melts within the lead rather than refreezing into a frozen slush layer (see discussion in Section 3.4.3). A boundary-layer blowing snow model developed by Déry and Tremblay (2004) demonstrates that the "lead trapping efficiency" of suspended snow depends primarily on the along-fetch lead size and spacing distribution, wind speed, and friction velocity. For a range of conditions, the authors show that a lead can collect between 60–100% of blowing snow. Similarly, Leonard and Maksym (2011) report near-total loss of snow to leads during a field experiment in the Bellingshausen Sea in which conditions became supply-limited, that is, there was inadequate unconsolidated new snow supply to permit further aeolian transport despite high wind conditions.

We parameterize the maximum potential amount of blowing snow deposited into the ocean through leads during periods of active wind transport ($U_{10} \geq U_t$; see Section 3.3.4.4) using the following relation:

$$Q_{\text{lead,max}} = \gamma_{\text{lead}}\, f_{\text{OW}}\, Q'_{\text{lead}} \cdot \frac{(0.0417\ \text{d})}{\rho_s \cdot \Delta t} \text{ when } U_{10} \geq U_t\ , \tag{3.28}$$

$$Q_{\text{lead,max}} = \ 0\ \text{m h}^{-1}\ \text{ when } U_{10} < U_t\ . \tag{3.29}$$

The local open water fraction ($f_{\mathrm{OW}} = 1 - f_{\mathrm{SIC,PMW}}$) is obtained from daily AMSR-E/2 SIC data at a resolution of 6.25 km (Section 3.3.1.1). The two-dimensional numerical simulations of Déry and Tremblay (2004) suggest that the rate of snow mass loss to leads varies over two orders of magnitude across different distances of blowing snow over sea ice (i.e., lead spacings) of 0.1 km to 10 km, but surprisingly little across different distances of fetch over open water (i.e., lead widths). Based on this result, the number density of leads appears to be more influential than the open water fraction. Nonetheless, f_{OW} is used as an imperfect proxy for lead frequency or density, for which only climatological fields based on thermal infrared remote sensing (Reiser et al., 2019, 2020) and recent estimates for the ICESat-2 period of 2018 onwards using a surface type classification scheme (Petty et al., 2021) are currently available for the Antarctic SIZ. The tunable scaling factor γ_{lead} is intended to incorporate the as-yet unquantified relationship between f_{OW} and lead density and width; the effects of lead orientation relative to winds; processes that may limit the total amount of snow available for aeolian transport, such as aerodynamic shielding; and uncertainty about the lead trapping efficiency and parameterization of Q'_{lead} below.

A functional form is adopted for the relationship between Q'_{lead}, the snow mass flux into leads (mm SWE $\mathrm{d^{-1}} \equiv \mathrm{kg\ m^{-2}\ d^{-1}}$), and the 10-m wind speed U_{10} that is informed by the simulations of Déry and Tremblay (2004; see their Table 1, presented below as Appendix Appendix Table 3.5), assuming a 1 km lead spacing, similar to Eicken et al. (1994). We fit a third-order polynomial to their results, which are specified in wind speed increments of 5 m $\mathrm{s^{-1}}$, after adding a point at Q'_{lead} = 0 mm SWE $\mathrm{d^{-1}}$ for a wind speed of 0 m $\mathrm{s^{-1}}$:

$$Q'_{\mathrm{lead}} = (-0.0357 + 3.9083 \cdot U_{10} - 0.4026 \cdot U_{10}^2 + 0.0141 \cdot U_{10}^3)\ \mathrm{mm\ SWE\ d^{-1}}\ . \qquad (3.30)$$

The rate of lead trapping therefore increases dramatically at higher wind speeds as snow mass is transported over leads more rapidly.

If the sum of the maximum potential blowing snow sublimation ($Q_{\text{sub,max}}$) and lead trapping ($Q_{\text{lead,max}}$) is greater than the current snow depth (h_s), the calculated maximum values of the two loss terms are used as weights to partition the available blowing snow:

$$Q_{\text{sub}} = \min\left(Q_{\text{sub,max}}, \left[\frac{Q_{\text{sub,max}}}{Q_{\text{sub,max}} + Q_{\text{lead,max}}} \cdot \frac{h_s}{\Delta t}\right]\right), \tag{3.31}$$

$$Q_{\text{lead}} = \min\left(Q_{\text{lead,max}}, \left[\frac{Q_{\text{lead,max}}}{Q_{\text{sub,max}} + Q_{\text{lead,max}}} \cdot \frac{h_s}{\Delta t}\right]\right). \tag{3.32}$$

3.3.4.7 Effects of ice dynamics

As the simulated Lagrangian sea ice parcels are advected using observed sea ice drift vectors (Section 3.3.3), convergent and divergent motion will occur. Assuming ice volume conservation, convergence will lead to large-scale, area-averaged ice thickening while divergence will create areas of open water where new ice growth can occur, often rapidly (von Albedyll et al., 2021). We assume a similar volume-conserving paradigm for snow depth, which will experience dynamical thickening in areas of ridging and rafting due to ice convergence or area-averaged thinning in regions where new, snow-free ice is formed due to divergence. Superimposed ice thickness is treated in the same way.

We implement snow and superimposed ice volume conservation during ice convergence and divergence using a technique known as Voronoi tessellation, which is a geometric subdivision of a space into the polygonal regions closest to each of a set of points, in this case the centroids of the sea ice parcels. At each daily time step of the model (Section 3.3.3), contiguous regions of sea ice with $f_{\text{SIC,PMW}} > 0\%$ are identified and a Voronoi partitioning is computed using the *Voronoi* function in the SciPy library (Virtanen et al., 2020). Voronoi polygons are clipped to the boundaries of sea ice regions and projected to an EASE grid, and the area A (km^2) of the polygon corresponding to each parcel is calculated. The corresponding change in the snow depth h_s and superimposed ice thickness $h_{i,\text{sup}}$ (not shown, but implemented similarly) of a given sea ice parcel between the previous day $t-1$ and the current day t is:

$$Q_{\mathrm{dyn}} = \left(\frac{A|_{t-1}}{A|_t} - 1\right) \cdot \frac{h_s|_t}{\Delta t} \quad \text{when } (1-\delta_A) \leq \frac{A|_{t-1}}{A|_t} \leq (1+\delta_A)\,, \tag{3.33}$$

$$Q_{\mathrm{dyn}} = 0 \text{ m h}^{-1} \quad \text{when } \frac{A|_{t-1}}{A|_t} < (1-\delta_A) \text{ or } \frac{A|_{t-1}}{A|_t} > (1+\delta_A)\,, \tag{3.34}$$

where δ_A is 0.25, signifying a maximum area-scaling tolerance of ±25%. Instances of parcel area scaling exceeding this tolerance are uncommon and mostly due to truncation (geometric clipping) or expansion of Voronoi polygons along the sea ice edge. While the area scaling factor $\left({A|_{t-1}}/{A|_t}\right)$ is not entirely physically meaningful on a daily basis for a single parcel, whose polygonal boundaries will change depending on the relative position of parcel centroids, the scaling factors nonetheless embody the effects of convergent and divergent motion upon averaging Q_{dyn} over time or space to reduce noisiness. It is likely, however, that Q_{dyn} will underestimate the full effects of divergence, as highly divergent conditions are at least partially accounted for when a 0.25° x 0.25° grid cell becomes devoid of existing parcels and a new sea ice parcel is instantiated, explicitly simulating new ice formation (Section 3.3.3).

3.3.4.8 Conversion from Lagrangian to Eulerian frame

The sea ice parcel area, A, computed through Voronoi tessellation is in some sense a model construct that is not necessarily physically meaningful prior to time- and/or space-averaging (Section 3.3.4.7). However, its calculation and tracking enables volume (or mass) conservation when translating the extrinsic properties h_s and $h_{i,\mathrm{sup}}$, snow depth tendency terms $Q_{\{\dots\}}$, and the variables representing the release of snow and superimposed ice to the ocean from the Lagrangian parcel frame of reference onto a regular grid (i.e., into an Eulerian frame). This regridding is carried out after the completion of a model run for all variables recorded along parcel trajectories, including bulk snow density ρ_s. Two-dimensional area-weighted binning of daily values is used to aggregate all parcels whose centroids are located within a given cell of the ERA5 grid, coarsened by a factor of three to a 0.75° x 0.75° grid in order to reduce noisiness, particularly in Q_{dyn}. For

Table 3.2: Free parameters in the model. For each tuning parameter, the paper section in which it is introduced, its initial value and standard deviation used to generate an initial distribution of candidate values for the successive halving optimization procedure, its final optimized value after rung 14 of the tuning ladder, and other details are listed.

Parameter	Section	Initial value	Initial standard deviation	Final value (rung 14)	Significance
γ_{dens}	2.4.1	1.0	0.1	0.978	Inverse scaling factor for k_n, the compactive viscosity of snow, modifying the rate of mechanical compaction due to overburden pressure
γ_{new}	2.4.2	1.0	0.25	1.186	Scaling factor for Q_{dep}, the rate of new snowfall deposition
T_{base}	2.4.3	0.0°C	1.0°C	−0.179°C	Threshold air temperature in Q_{melt} above which non-rain snow melt tends to occur (~0.0°C, per Anderson, 1973)
γ_{melt}	2.4.3	1.5 mm °C^{-1} (6 h)	0.5 mm °C^{-1} (6 h)	1.678 mm °C^{-1} (6 h)	6-hour melt factor in Q_{melt} relating non-rain snow melt rate to air temperature (~1–2 mm °C^{-1} [6 h], per Girotto et al., 2024)
γ_{rain}	2.4.3	1.0	1.0	1.547	Scaling factor for Q_{rain}, the snow melt rate due to significant rainfall events
γ_{surf}	2.4.4	1.0	1.0	1.273	Scaling factor for Q_{surf}, the rate of snow surface sublimation
γ_{sub}	2.4.5	1.0	1.0	0.897	Scaling factor for $Q_{\text{sub,max}}$, the maximum (non-supply-limited) rate of blowing snow sublimation
γ_{lead}	2.4.6	1.0	1.0	0.205	Scaling factor for $Q_{\text{lead,max}}$, the maximum (non-supply-limited) rate of lead trapping of blowing snow

the extrinsic properties and snow depth fluxes—but not ρ_s, an intrinsic property—the values for each parcel are additionally scaled by two factors: $f_{\text{SIC,PMW}}$, to account for partial ice cover within grid cells, as well as the ratio $\left(\Sigma A / A_{0.75°}\right)$, where ΣA is the sum of all parcel areas in a grid cell and $A_{0.75°}$ is the coarsened ERA5 grid cell area, a function of latitude.

3.3.5 Model calibration procedure

The snow accumulation, loss, and transformation parameterizations detailed in Section 3.3.4 include eight tuning parameters (listed in Table 3.2) that incorporate the effects of unrepresented processes and account for unknown biases in input data and the parameterizations themselves. We develop an iterative procedure that adjusts these parameters, optimizing the model fit to

observations of snow accumulation collected by 29 snow buoys drifting primarily in the western, northern, and central Weddell Sea from 2013–2022 (Section 3.3.2.1). These regions exhibit significant spatial and interannual variability of observed snow on sea ice properties and a diversity of meteorological conditions for testing the model parameterizations (Massom et al., 1997; Markus & Cavalieri, 2006; Arndt & Paul, 2018), albeit with lower snowfall rates compared to the rest of the Antarctic SIZ (Boisvert et al., 2020).

Optimization is an under-constrained problem for the snow model at hand, likely with many local minima in goodness-of-fit metrics and thus many possible "optimal" parameter sets. However, the likelihood of a robust calibration is bolstered by the independence and intermittency of the parameterizations comprising the snow accumulation budget under certain conditions: for example, only one term, Q_{dep}, can add snowfall (Q_{surf} provides negligible deposition), and only during reanalysis snowfall periods; only one term, Q_{lead}, is proportional to the open-water fraction f_{OW}; rain-related melt, Q_{rain}, is only active during periods of significant rainfall; non-rain melt, Q_{melt}, cannot be active at the same time and is only applicable during periods of warm air temperature ($T_a > T_{\mathrm{base}}$); and Q_{surf} and Q_{sub} are likewise mutually exclusive. Q_{dens} is the only process active at all times.

It is important to choose an appropriate optimization strategy that is sensitive to the model characteristics. Some techniques, for example, assume a linear response to varying parameters. The adjoint method requires a well-behaved tangent linear model (as well as a differentiable model configuration), and a Green's function approach assumes a linear response to small perturbations. The response of our snow model to varying parameters, however, is highly nonlinear, as its parameterizations are intermittently active—triggered by episodic conditions—and state-dependent, i.e., requiring snow to be available in order to be lost. This favors the use of other parameter optimization methods, which include simple grid search and random search strategies (Bergstra & Bengio, 2012) as well as less computationally expensive multi-armed bandit algorithms that allocate more resources to promising areas of the parameter space, balancing

exploration with selection under uncertainty (Karnin et al., 2013). We choose a bandit-type optimization framework common in machine learning known as successive halving, in which the performance of N candidate parameter sets are evaluated and the best-performing half of parameter sets are promoted to the next iteration, or rung, of the tuning ladder (and the bottom half discarded). The parameter space of the promoted half is used to determine the subsequent candidate batch, and so on until a stopping criterion or computational budget has been reached (Karnin et al., 2013; Jamieson & Talwalkar, 2016; Liam Li et al., 2018).

Successive halving is implemented using candidate pools of $N = 54$ combinations of the eight tuning parameters for each run (see Figure 3.3 for the evolution of parameter values and goodness-of-fit metrics):

1. The algorithm is initialized in rung 0 using a sample of 54 random values drawn from a one-sided truncated normal distribution bounded by $(0.0, \infty)$ for each of the parameters except for T_{base}, for which a standard normal distribution is used. The distributions are generated using a central value of 1.0 for each parameter (except for T_{base} and γ_{melt}) with a standard deviation specified based on a subjective judgment of the uncertainty in the underlying parameterization (see Table 3.2 for initial values and standard deviations, including their origins in the literature in the case of T_{base} and γ_{melt}). A 55^{th} simulation is added to each rung using the baseline parameter set used to generate the random distributions. A one-time simulation is also run to evaluate the model performance with γ_{new} set to 1.0 and all snow loss parameterizations and mechanical compaction turned off, i.e., with the model accumulating snow only.
2. For each of the one baseline and 54 random parameter sets, the model is run in calibration mode with parcels evolving along the snow buoy trajectories, forced by ERA5 reanalysis and AMSR-2/E sea ice concentration data, as detailed in Section 3.3.3.

3. The buoy observations used to assess the model performance are resampled to daily averages and the entire snow accumulation time series for each buoy is shifted to align its starting snow depth with that of the model parcel. The following goodness-of-fit metrics are calculated between the 54 model ensemble members and the buoy observations, as well as the baseline run and the buoy observations: root mean square error (RMSE) of snow accumulation; mean error (bias); and bias of the daily snow accumulation tendency.
4. The 27 of the 54 total parameter sets yielding the lowest RMSE are considered the top half of the ensemble. The ensemble median and standard deviation of each of the eight parameters are calculated across this top half and used as the baseline values to generate 54 random parameter sets in the next tuning rung.
5. Steps (2) through (4) are repeated as long as the ensemble average RMSE and/or the baseline parameter set RMSE continue to improve (decrease) by at least 0.1 cm. The last baseline parameter set that satisfied this criterion, from rung 14, is chosen as the final, optimized set of parameter values (listed in Table 3.2).

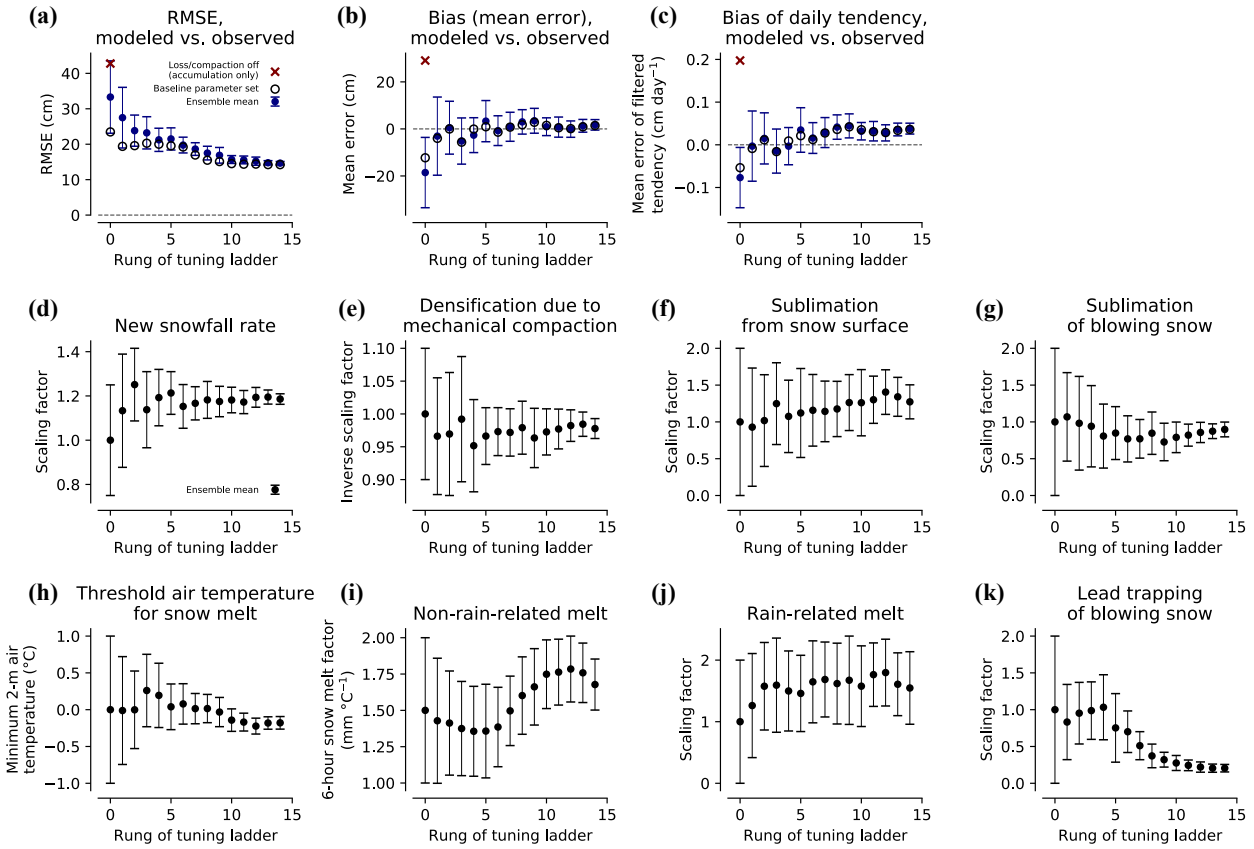

Figure 3.3: Evolution of the successive halving procedure used to optimize the model fit to snow buoy observations in the Weddell Sea. Each panel shows the ensemble distribution for 54 candidate parameter sets over the 14 iterations, or rungs, before the stopping criterion was reached. **(a)-(c)** Ensemble mean and standard deviation (blue) and values for the baseline parameter set (black open circles) of the root mean square error (RMSE) of snow accumulation, bias of snow accumulation, and the bias of the daily snow accumulation tendency, respectively, comparing the model to the buoy measurements. The comparable values for a model run with only snow accumulation and no loss or transformation processes are also marked (red cross). **(d)-(k)** Ensemble median and standard deviation of the eight free parameter values over the tuning rungs.

3.4 Results and discussion

3.4.1 Model calibration and snow buoy observations

The final set of eight calibrated parameters yields a model RMSE of 14.2 cm, bias of +1.4 cm, and daily snow accumulation tendency bias of +0.04 cm d^{-1} relative to the matched Weddell Sea snow buoy measurements (Figure 3.3a–c). In comparison, the simulation of snow accumulation only (with loss and mechanical compaction parameterizations turned off) yields a much higher model

RMSE of 42.8 cm and bias of 29.1 cm, illustrating the importance of accounting for loss processes, while the simulation prior to tuning, with all physical processes active, yielded a RMSE of 23.5 cm and bias of −12.3 cm, indicating that parameter calibration led to an improvement in fit and greater net snow accumulation. This increase was accomplished through the scaling factor for new snowfall deposition, γ_{new} = 1.186; the inverse scaling factor for compaction, γ_{dens} = 0.978, which decreased the rate of mechanical compaction; and the scaling factors for blowing snow sublimation (γ_{sub} = 0.897) and lead trapping (γ_{lead} = 0.205), which both decreased the rate of snow lost during wind transport (Figure 3.3d–e, Figure 3.3g, Figure 3.3k). On the other hand, snow surface sublimation and both non-rain and rain-related melt all increased owing to calibration. The more rapid and/or monotonic convergence of γ_{new}, γ_{rain}, and γ_{lead} (Figure 3.3d, Figure 3.3j–k) suggest that these parameterizations—or at least their scaling factors—are the best constrained by the available observations. The notable decrease in γ_{lead} after tuning is consistent with the parameterization for lead trapping used in this model being the most dependent on unvalidated assumptions, particularly the relationship between open-water fraction and lead frequency (Section 3.3.4.6).

The need to increase snowfall input by 18.6% (γ_{new} = 1.186) in this model suggests that ERA5 snowfall may be an underestimate in the Antarctic SIZ. For context, an average scaling factor of 1.58 for ERA5 snowfall in the Arctic Ocean was similarly obtained by bias-correcting output from the Lagrangian model SnowModel-LG using NASA Operation IceBridge observations from 2009–2016 (Liston et al., 2020). Unlike our calibration procedure, however, other model parameters were not adjusted concurrently in that study. The SnowModel-LG finding contrasts with a comparison to CloudSat observations that concluded that ERA5 snowfall over the Arctic Ocean may be biased high, rather than low, particularly in winter (Cabaj et al., 2020), as well as a separate study that found minimal climatological bias in ERA5 snowfall in winter compared to North Pole drifting station records (A. P. Barrett et al., 2020). These differing conclusions

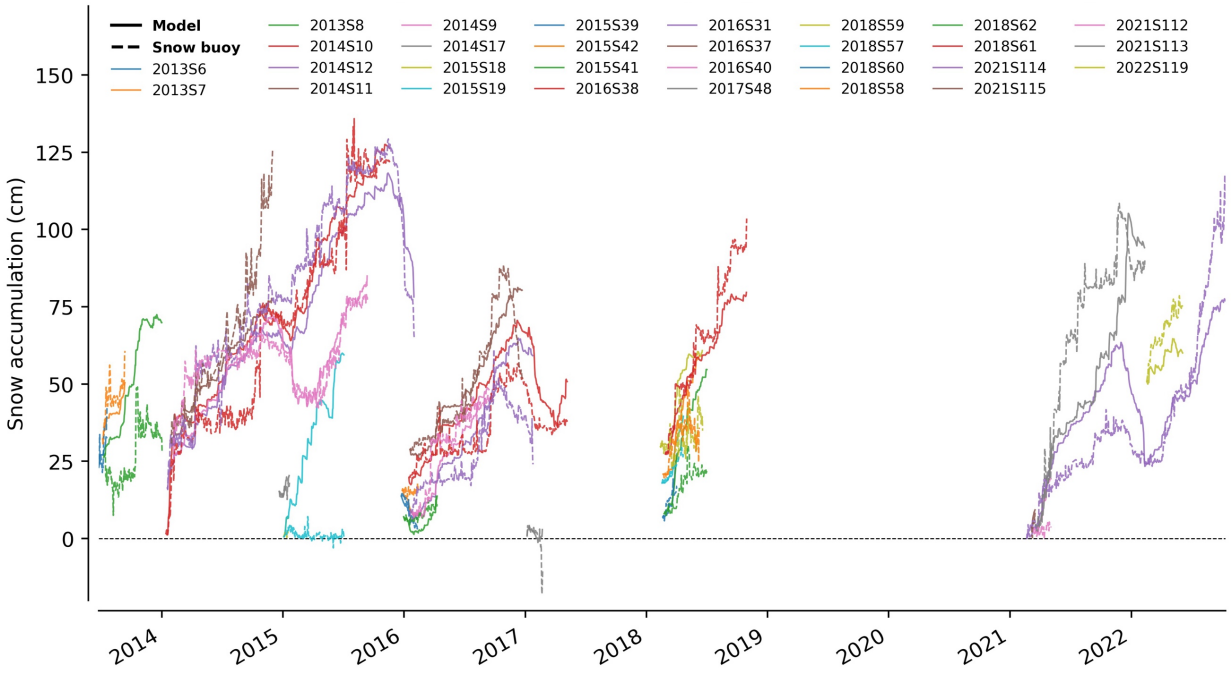

Figure 3.4: Model–buoy comparison after calibration of model free parameters. Snow accumulation measured by the 29 snow buoys in the Weddell Sea (dashed lines) and reconstructed by the fully calibrated model along the buoy trajectories (solid lines). Snow buoys are labeled with their IDs, which include the deployment year.

highlight the uncertainties that can arise from the diversity of available validation data sets and techniques.

Figure 3.4 depicts the calibrated model evolution along the snow buoy trajectories and the actual buoy measurements. This comparison underscores both the challenge of reproducing highly localized point measurements using an incomplete modeling framework yet also a clear correspondence, in many cases, between the simulated and observed records. The timing, if not always the magnitude, of major ablation events appear well-captured, including those seen at the end of the 2014S12 buoy record, the start of 2015 for buoy 2014S9, and the end of 2021 for buoy 2021S114. It is worth noting that the use of RMSE as a goodness-of-fit metric may encourage over-correcting, as possibly seen in the record of buoy 2021S114. In other words, because the model and observations will diverge over time due to accumulated biases, thus increasing RMSE, it is possible that the tuning procedure will compensate for bias in one parameterization by creating

an opposite bias in another to minimize this divergence. Even so, this does not appear to be a systematic issue across the model–buoy records.

A closer inspection of one and a half years of observations from buoy 2014S9 compared to the matched model simulations is illustrative (Figure 3.5). The buoy was deployed in the southwest Weddell Sea and drifted northward then eastward, following the prevailing clockwise circulation of the Weddell gyre (see the trajectory that terminates in the far northeast corner of Figure 3.1b). Only accounting for snow deposition in the model—omitting loss processes and mechanical compaction—leads to a more than twofold overestimate of snow accumulation, which occurs year-round at a steady rate (Figure 3.5a). While observed snow depths exceed even those in the no-loss simulation in initial months—an indication of underestimated ERA5 snowfall and/or nonlocal snow advection or redistribution—the model eventually catches up, possibly over-correcting during the ablation event in early 2015.

It is tempting to infer causality in the apparent correspondence between rainfall and snow ablation events (Figure 3.5a). Boisvert et al. (2020) examine the same snow buoy record and conclude that both ROS events and warm temperatures were responsible for the snow loss (see their Figure 14 for comparison). However, our model parameterizations point to the above-freezing air temperatures that tend to coincide with rain as accounting for nearly all ablation during these periods, with non-rain-related melt responsible for 35.2% of cumulative snow loss, 70 times greater than rain-related melt (Figure 3.5b). Significant rain events are in fact more rare and brief than a daily resolution time series might suggest: buoy 2014S9, for example, saw only 24 one-hour periods with ERA5 rainfall rates above the threshold $R_{\text{thresh}} = 0.25$ mm h^{-1} prescribed in the ROS parameterization used in this study. This partitioning of simulated loss mechanisms also highlights noticeable increases in lead trapping and blowing snow sublimation as the buoy approached the marginal ice zone (MIZ) at the end of its drift, the former likely due to an increased open-water fraction.

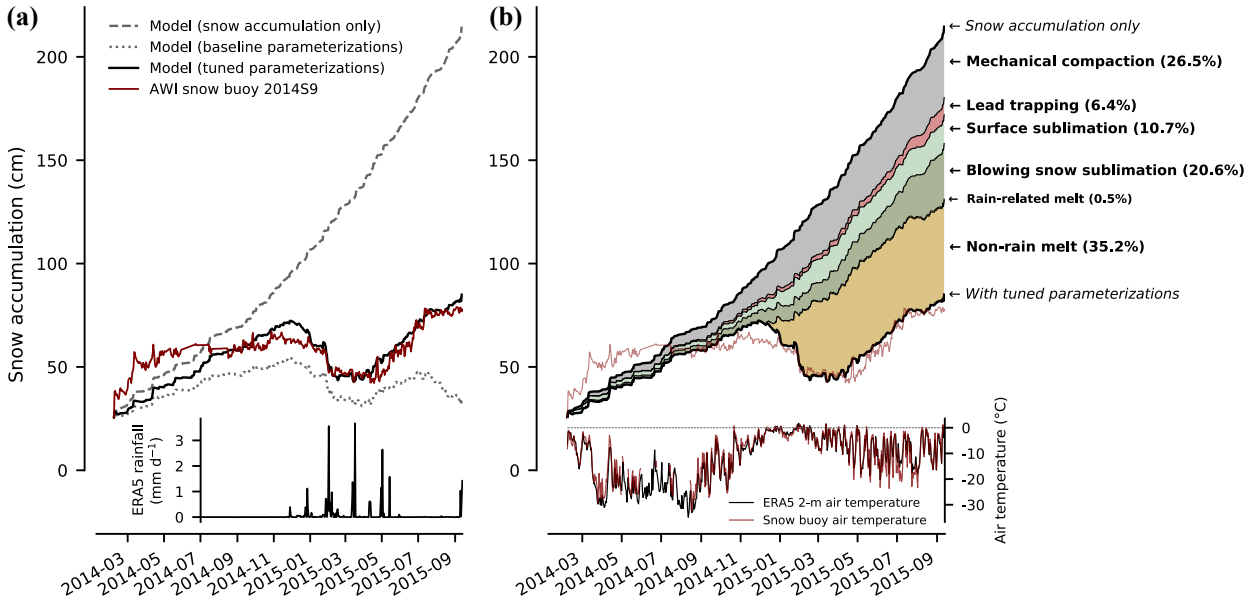

Figure 3.5: One and a half years of observed and reconstructed snow accumulation along the trajectory of snow buoy 2014S9, presented as an illustrative example. **(a)** Buoy measurements (solid red line) and simulated results with loss processes and mechanical compaction turned off (dashed grey line), all parameterizations in their default configurations (dotted grey line), and the final calibrated parameterizations (solid black line). Daily rainfall rates along the buoy trajectory from ERA5 are shown at bottom. **(b)** Partitioning of loss processes' cumulative contributions to the difference between the simulation of snow accumulation only and the full model with calibrated parameterizations. Daily air temperature from ERA5 (black) and the buoy (red) are shown at bottom.

Significant non-rain-related snow melt in early 2015 (Figure 3.5b) is estimated to have led to the formation of 28.7 cm of superimposed ice, assuming that all meltwater refreezes within the snowpack. This is an uncommonly large amount compared to ice core observations from the northwestern Weddell Sea (Arndt et al., 2021), likely due to the extended time spent by this particular snow buoy at northern latitudes, that would represent 34% of the final snow depth, which our model does not explicitly treat as affected by liquid water and processes like melt metamorphism. In actuality, much of the snow matrix would probably be infiltrated by meltwater with a corresponding decrease in the snow-only depth. Our model also does not account for likely snow-ice conversion following seawater flooding from the substantial snow load, as discussed in Section 3.4.2 and Section 3.4.4. Nonetheless, the model mass budget for total meteoric freshwater

(derived from snowfall and rainfall) should remain accurate, regardless of these uncertainties in conversion processes.

3.4.2 Climatological snow mass budget

Figure 3.6 depicts the climatological snow on sea ice mass budget for the Antarctic SIZ over 2003–2024, integrated over areas with active sea ice cover only. What appears to be a pronounced seasonality in new snowfall in fact strongly resembles the seasonal cycle of Southern Hemisphere sea ice area or extent, indicating continuous snowfall year-round (Figure 3.6a). Snow release to the ocean from sea ice melt, in contrast, provides a pulse of freshwater to the ocean that is mostly confined to spring and summer (September–February). Interannual variability in these two terms remains within a relatively narrow range, at least when spatially averaged over such a large region. Blowing snow sublimation and lead trapping exhibit more muted seasonal cycles that both mirror changes in SIE, reflecting wind speeds high enough to support aeolian transport of snow throughout the winter. The persistent role of lead trapping is supported by the presence of open water in the interior of the ice pack (likely both leads and polynyas) even during mid-winter, rather than just when sea ice is melting back in spring. Most snow surface sublimation and non-rain melt is restricted to a few months, with the latter peaking after the maximum rate of sea ice loss and snow release to the ocean is attained in December, likely due to favorable changes in the snowpack energy balance associated with elevated air temperatures and solar radiation.

The climatological mass budget for snow on Antarctic sea ice closes to within 18%, with estimated total annual loss (11,023 Pg) exceeding new snow deposition (9,312 Pg; Figure 3.6b). This smaller amount of snow deposited on sea ice reflects ERA5 reanalysis snowfall rates that have already been increased by 18.6% owing to calibration to snow buoy observations (Section 3.4.1). This relatively small residual is remarkable, given that our model lacks any explicit constraints to ensure budget closure apart from the calibration procedure, which relied solely on measurements from the Weddell Sea. Furthermore, the model integrates a patchwork of

parameterizations that have neither been commonly used in conjunction nor previously adapted to a Lagrangian reconstruction framework.

Loss processes occurring before the complete melt of sea ice—including melting and subsequent freezing into superimposed ice—account for one-third of the cumulative annual snow mass budget (Figure 3.6b). Among these, blowing snow sublimation contributes the most, though no single loss pathway dominates. Surprisingly, rain-related melt is negligible, contributing less than 1% to annual snow loss, compared to 7% from melt unrelated to rain (see discussion in Section 3.4.1). Importantly, the large term representing snow released to the ocean upon sea ice melt includes snow that has been converted into snow-ice, a process that incorporates seawater and is not simulated by our model. Consequently, this snow release term should be interpreted more broadly as a freshwater flux of meteoric origin.

The amount, location, and timing of snow entering the ocean is of vital importance for the salinity budget of the Southern Ocean, which influences water mass transformation and processes like vertical mixing (Timmermann et al., 2001; Ren et al., 2011; Kjellsson et al., 2015; Haumann et al., 2016b; Pellichero et al., 2018; E. A. Wilson et al., 2019). Our reconstruction estimates a freshwater flux of 295–349 mSv (1 mSv = 1,000 $m^3\ s^{-1}$) of snowfall intercepted by sea ice, using the model output value and the value from a budget fully balanced by loss as a possible range. The total meteoric freshwater flux into the ocean originating from snow (excluding rain) is 284 mSv, representing 81–96% of the total intercepted snowfall on sea ice, with the remainder sublimating to the atmosphere. This flux can be divided into three components: 236 mSv released into the ocean upon complete sea ice melt, a 27 mSv flux of snowmelt-derived superimposed ice that is also released during sea ice melt, and a lead trapping flux of 22 mSv that enters the ocean throughout the winter during wind-blown snow transport.

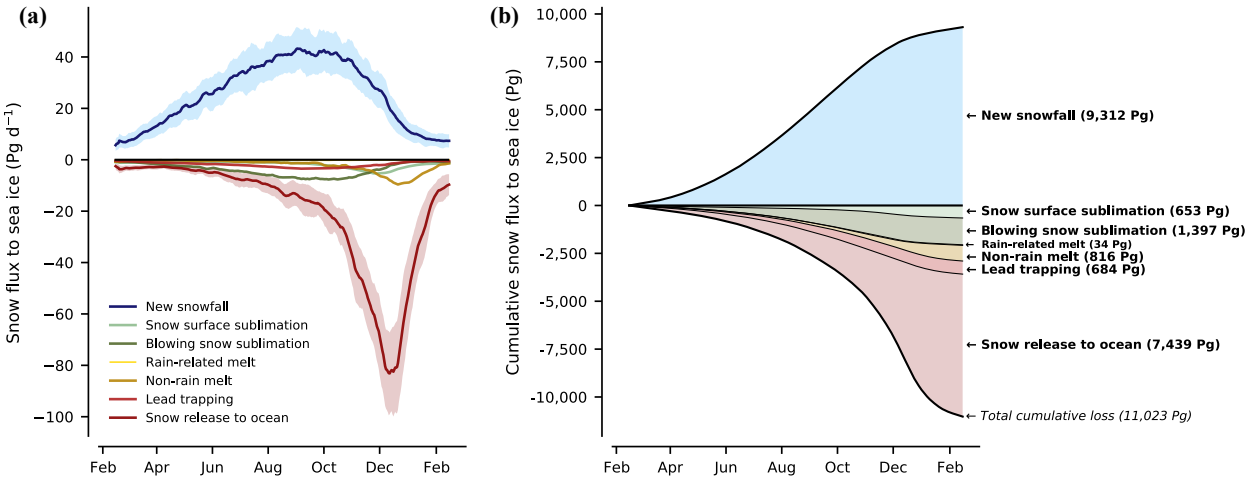

Figure 3.6: Climatological snow on sea ice mass budget for the Antarctic SIZ from the model reconstruction (2003–2024). The simulation period is February 15 to February 14 of the following year. **(a)** Climatological snow fluxes in Pg d^{-1} (1 Pg = 10^{12} kg), where positive values represent snow deposited on sea ice and negative values denote loss to either the atmosphere (snow surface and blowing snow sublimation), superimposed ice layer (rain-related and non-rain melt), or ocean (lead trapping and snow release upon sea ice melt). 7-day rolling average values are shown for ease of visualization. Shading indicates the interannual variability of new snowfall and snow release to the ocean (±1σ over 2003–2024). **(b)** Cumulative snow fluxes over the model year, with total values listed at the right. Note rain-related melt is small and difficult to distinguish in both panels.

This total meteoric flux into the ocean is equivalent to over two-thirds of the annual 410 ± 110 mSv freshwater flux arising from the melting of sea ice across the entire Southern Ocean computed by Haumann et al. (2016), who used remote sensing data and a sea ice thickness reconstruction from the data-assimilating model of Massonnet et al. (2013) to calculate sea ice volume change and divergence. The former study also estimated that 50 mSv of snow on Antarctic sea ice is converted to snow-ice, based on loose observational constraints on the proportion of snow-ice formation to total ice formation compiled by Massom et al. (2001). Combined with our model results, this implies that around 21% of snow mass released to the ocean upon sea ice melt has been incorporated into snow-ice, but the approximate nature of this calculation should be emphasized.

Our estimates of snow-related freshwater fluxes are qualitatively similar to a previous observation-based estimate, albeit with significant simplifying assumptions, that precipitation and sea ice freshwater fluxes each contribute an approximately equal amount to buoyancy gain in

the Southern Ocean SIZ (Pellichero et al., 2018; see their Supplementary Note 2). This conclusion, however, differs markedly from that of Abernathey et al. (2016), who assessed precipitation- and ice-related freshwater fluxes using the Southern Ocean State Estimate (SOSE; Mazloff et al., 2010). SOSE assimilates ocean temperature and salinity data, sea ice concentration, and other observational sources to constrain the MITgcm model. The model's ocean state is adjusted through the adjoint method, which alters initial conditions and, crucially, atmospheric forcing such as precipitation. Abernathey et al. report annual freshwater fluxes of 140 mSv from snowfall intercepted by Antarctic sea ice and 360 mSv from sea ice freezing and melting, excluding the melt of overlying snow. This estimate from SOSE represents only 40–47% of the total snowfall deposition on Antarctic sea ice that is assessed by our reanalysis-based, calibrated model reconstruction. This discrepancy suggests that the adjoint method has compensated for biases in the model's representation of sea ice and snow-on-sea-ice physics by roughly halving the amount of snowfall forcing compared to original reanalysis data. Such an adjustment would allow the total simulated freshwater flux (from both snow and sea ice) to match ocean observations, while masking excessive sea ice melt in MITgcm—which implies overestimated sea ice formation rates and ice thickness. Consistent with this, Abernathey et al. report that SOSE exhibits sea ice thickness that is 20–40 cm too thick in the Weddell and Ross Seas (see their Supplementary Information), a positive bias that is common among coupled climate models (P. R. Holland et al., 2014). These uncertainties highlight the importance of accurately partitioning Southern Ocean freshwater fluxes between snow and sea ice. A freshwater input to the ocean that is correct in total but contains an unrealistically low proportion of snow will require overly high sea ice growth rates to compensate, with implications for brine rejection and ocean stratification near the Antarctic continent where sea ice formation is greatest.

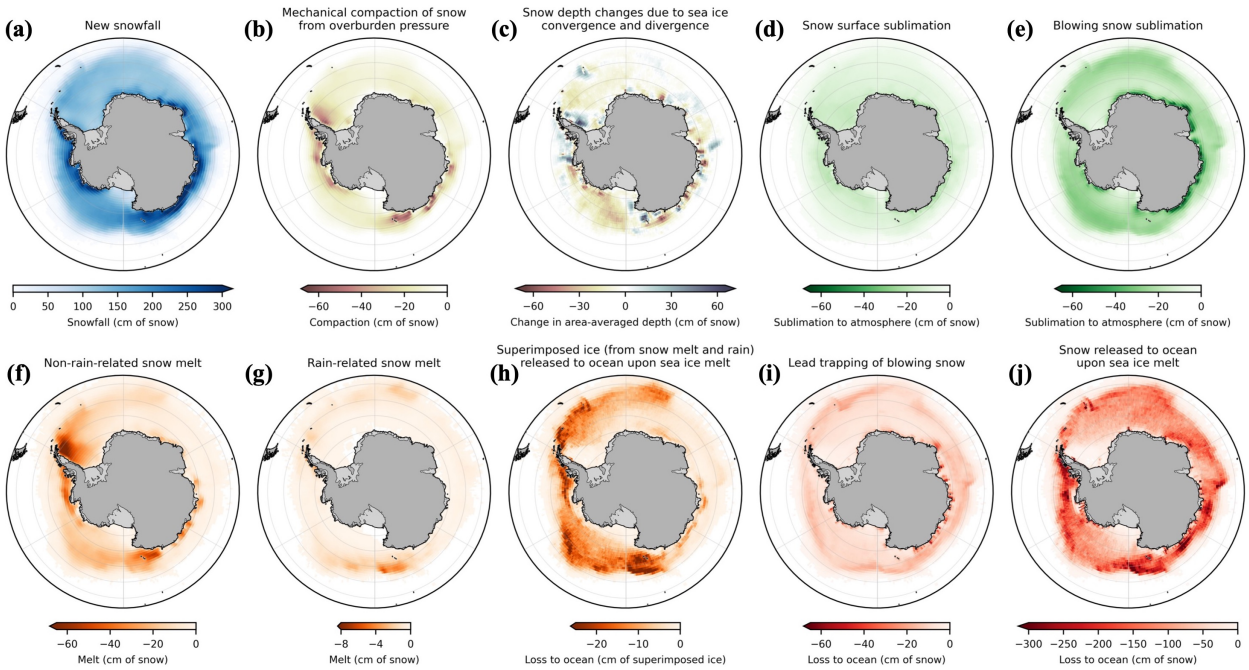

Figure 3.7: Average annual contributions to the net snow accumulation budget in the model reconstruction (2003–2024). Positive values indicate greater net snow accumulation. All contributions are expressed as changes in snow depth, normalized from their time-varying bulk snow density to a density of $\rho_{s,0}$ = 320 kg m^{-3}. The color schemes correspond to the fate of snow: blue signifies snow deposition onto sea ice; blue-grey and pink represent mass-conserving increases and decreases in area-averaged snow thickness, respectively; green denotes snow sublimation to the atmosphere; orange includes snow melt and superimposed ice formed from snow melt and rain (note that panel **[h]**, showing superimposed ice released to the ocean, is not part of the snow accumulation budget); and red represents direct snow flux to the ocean. Note that different color scales are reflected in the colorbar lengths.

3.4.3 Spatial distribution of snow accumulation and loss processes

Figure 3.7 illustrates the spatial patterns of reconstructed snow fluxes, presented as annual contributions to the net snow accumulation budget averaged over the model period of 2003 to 2024. Snowfall deposition of around 1–2 m occurs across the Antarctic SIZ, with bands of higher snowfall rates observed along the continent, particularly off East Antarctica and the Amundsen Sea-Bellingshausen Sea coastline (Figure 3.7a). This pattern broadly aligns with estimates from CloudSat snowfall observations over the Southern Ocean, although the comparison is not perfect, as the latter encompasses both ice-covered and ice-free periods (Boisvert et al., 2020).

As expected, mechanical compaction is most pronounced along the coastline in areas of high net snow accumulation (Figure 3.7b and Figure 3.8a). Although compaction is not included in the snow mass budget, as it is a mass-conserving process, it reduces snow depths by approximately 20 cm across most of the Antarctic SIZ. Large-scale sea ice divergence contributes to area-averaged snow thinning by a similar amount within the Weddell and Ross gyres (Figure 3.7c), areas where an ice-concentration budget indicates that divergent ice drift supports the formation of new ice without snow cover (P. R. Holland & Kwok, 2012; P. R. Holland & Kimura, 2016). In areas of convergent motion where our reconstruction indicates snow thickening, snow depth may in actuality remain relatively unchanged. This is because snow can become flooded and frozen into snow-ice or even lost to the ocean during sea ice ridging. However, our model identifies only limited regions of convergence, primarily in the Bellingshausen Sea and western Weddell Sea, suggesting that these impacts may be small (Figure 3.7c).

Blowing snow sublimation exhibits a distinct spatial pattern, with higher rates at northern latitudes and a narrow band of more intense sublimation along the East Antarctic coastline, likely driven by high wind speeds and dry, subsaturated air descending from the Antarctic continent in areas of katabatic outflow (Figure 3.7e). This pattern differs somewhat from a previous estimate of blowing snow sublimation over Antarctic sea ice by Déry and Yau (2002), who applied the same parameterization that our model implements to ERA15 reanalysis data from 1979 to 1993. Their results show more fragmented regions of high sublimation along the East Antarctic coast and an additional area of high activity in the northern Ross Sea, which is not as prominent in our estimates. In contrast, snow surface sublimation is spatially diffuse and occurs at lower magnitudes in both our reconstruction (Figure 3.7d) and the Déry and Yau (2002) estimates. Fichefet and Morales Maqueda (1999) use a model to estimate that as much as 0.45 m of snow could be removed annually by surface sublimation, which is also substantially higher than our reconstruction, though not if blowing snow—which was not represented in their model—is added. The authors note that conditions over Antarctic sea ice are more conducive to snow sublimation

than in the Arctic, as the drier air and stronger winds produce higher latent heat fluxes that are three times higher on average.

Hotspots of snow ablation from non-rain melt processes are evident in the Bellingshausen Sea, western Weddell Sea, and offshore of the Wilkes Basin, as well as broadly across the Ross Sea (Figure 3.7f). The western Weddell Sea and Wilkes Basin hotspots are coincident with key regions of cyclogenesis identified from storm tracks over the Southern Ocean (Yuan et al., 2009), likely reflecting warm air transport. Superimposed ice formed during these snow ablation events is transported downstream, along the trajectories of ice drift (Figure 3.1a), and is subsequently released to the ocean in the northern latitudes of the Weddell and Ross gyres and farther north offshore of the Wilkes Basin (Figure 3.7h).

Although lead trapping of blowing snow and snow release to the ocean upon complete sea ice melt differ greatly in magnitude, both show highest losses concentrated along the sea ice edge (Figure 3.7i–j). These patterns, however, likely arise from distinct physical processes: high lead trapping estimates in the MIZ result from the greater fraction of open water in this dynamic region, while the concentration of snow released to the ocean in this area reflects intense melting of snow-covered sea ice transported from higher latitudes. For context, Eicken et al. (1994) estimated an annual mass loss of 10 cm SWE of snow blown into leads in the Weddell Sea using simple empirical relations to wind speed. This corresponds to approximately 31 cm of snow, roughly twice our estimate for the entire Antarctic SIZ, in which lead trapping in the Weddell Sea appears to be, if anything, lower than in other regions. The order-of-magnitude estimate of Leonard and Maksym (2011) that about half of all snow deposited on Antarctic sea ice during the month of September is lost to leads is also higher than our reconstruction.

To our knowledge, our method for reconstructing lead trapping of blowing snow (Section 3.3.4.6) is the most sophisticated that has been implemented in a large-scale model of snow on sea ice. It incorporates nonlinear and linear dependencies on wind speed and open water fraction, respectively, with the wind speed relationship derived from numerical simulations. It uses a well-

validated, temperature-dependent wind speed threshold for aeolian snow transport, and lead trapping is adjusted concurrently with other loss mechanisms to optimize the model's fit to in situ observations of snow accumulation.

By comparison, Fichefet and Morales Maqueda (1999) divert a fixed fraction of new snowfall to the ocean in their simulation of snow on Antarctic sea ice. Lecomte et al. (2013) allow lead trapping only at the time of initial snow deposition, using the open-water fraction and an arbitrary scaling parameter to determine the fraction of snowfall redirected into leads. Lecomte et al. (2015) introduce an empirical wind speed threshold and a wind speed dependency, but still rely on an arbitrary tuning parameter. The NESOSIM model reconstruction of Petty et al. (2018) parameterizes snow loss to leads in the Arctic Ocean as proportional to wind speed and a tunable blowing snow constant and assumes blowing snow to be active above a fixed threshold wind speed, with the parameterization calibrated to snow depth observations in Cabaj et al. (2023).

In contrast to our approach and other models, the SnowModel-LG Lagrangian model of snow on Arctic sea ice of Liston et al. (2020) and Stroeve et al. (2020) does not represent blowing snow loss to leads at all. Liston et al. argue this process is likely minimal due to several factors: quick refreezing and filling of leads, the lower frequency of Arctic leads compared to the path length scale of blowing snow erosion from sublimation, more effective snow capture by surface roughness elements, lock-up effects (see Section 3.3.4.5), limited snow transport in the moisture-rich MIZ, and a lack of supporting field observations. While these arguments may find validation in the scaling down of our lead trapping parameterization to 21% of its original magnitude during calibration to snow buoy observations (see γ_{lead} in Table 3.2 and discussion in Section 3.4.1), their applicability to Antarctic sea ice conditions is uncertain. Compared to the Arctic, leads are relatively prevalent in the Southern Ocean, associated with strong ocean currents and tides (Reiser et al., 2019) and predominantly divergent sea ice drift (e.g., P. R. Holland & Kwok, 2012). In any case, our model estimates a significant snow mass loss from lead trapping of 684 Pg y^{-1}, representing 6% of the total annual mass budget for snow on Antarctic sea ice (Figure 3.6b).

3.4.4 Snow depth, snow-ice formation, and bulk snow density

Figure 3.8 compares the snow accumulation in our model reconstruction with the snow depth from two remote sensing products, presenting climatological averages over the four seasons. The reconstruction estimates net snow accumulation on sea ice of 14.0 cm in fall, 23.5 cm through winter, 34.7 cm through spring, and 27.4 cm through summer, based on daily spatial averages within ice-covered areas (Figure 3.8a; see also Figure 3.9b). Spatial patterns are generally diffuse but feature regions of markedly higher snow accumulation (~70 cm through spring) in the western Weddell Sea, the Bellingshausen Sea, along the Amundsen Sea coast, and along the East Antarctic coastline from Queen Mary Land eastward. These patterns remain evident in summer, despite snow ablation across the Antarctic SIZ. The thick snow in the western Weddell Sea coincides with dynamical thickening from convergent ice motion (Figure 3.7c). Elsewhere, these hotspots align closely with areas of elevated snowfall (Figure 3.7a), with the patterns slightly broadened due to the effects of ice drift (Figure 3.1a).

It is important to distinguish between snow accumulation and snow depth, which are considered here to be distinct metrics. Snow depth, measured via snow cores or snow pits on sea ice or estimated remotely using radar altimetry or passive microwave radiometry, excludes any basal snow layer that has been converted into ice. On the other hand, net snow accumulation, as simulated by our model, similarly reflects the balance of snow mass gain and loss to the atmosphere and ocean but accounts for the effects of only one conversion process—the formation of superimposed ice from snow melt—albeit with a simplistic treatment (see Section 3.3.4.3 and Section 3.4.1).

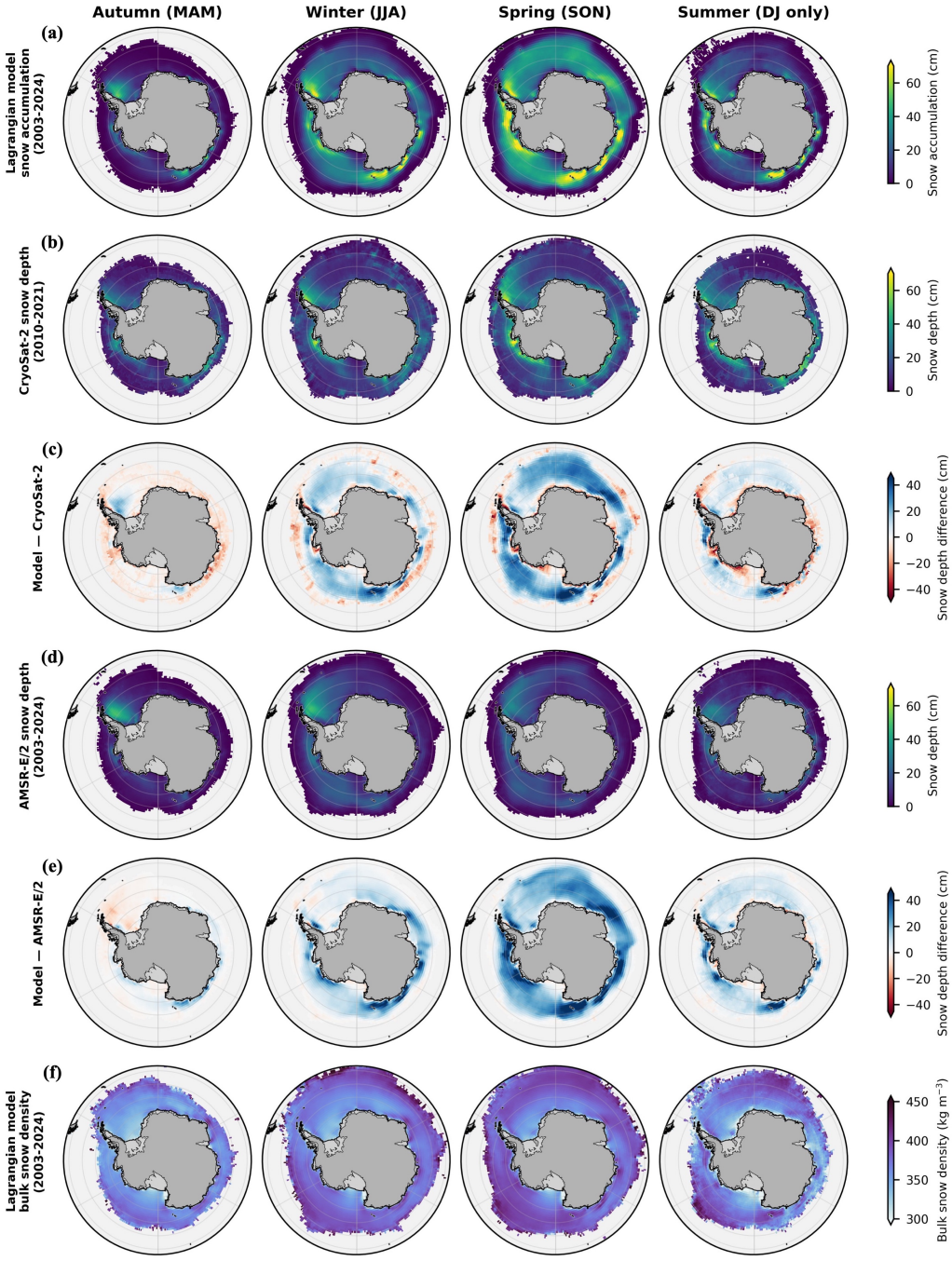

Figure 3.8: Comparisons between the model reconstruction (2003–2024) and snow depth from two remote sensing products. Columns are averages for autumn (March-April-May), winter (June-July-August), spring (September-October-November), and summer (December-January only, as the model is initialized and terminated in mid-February). **(a)** Simulated net snow accumulation. **(b)** Snow depth on sea ice from a monthly CryoSat-2 retrieval from July 2010 to August 2021 (Fons et al., 2023). **(c)** Differences between the reconstructed snow accumulation and CryoSat-2-based snow depths. **(d)** Snow depth on sea ice estimated from AMSR-E and AMSR2, averaged from daily data from 15 February 2003 to 14 February 2024 (Markus & Cavalieri, 1998; Cavalieri et al., 2014; Meier et al., 2018). **(e)** Differences between reconstructed snow accumulation and AMSR-E/2 snow depths. **(f)** Model reconstruction of bulk snow density.

Our model does not simulate snow-ice formation, a key conversion process that occurs when snow on sea ice becomes flooded by seawater and freezes into a new layer of solid ice. Ice core measurements suggest that snow-ice constitutes 8–38% of total ice thickness, varying regionally around Antarctica (Massom et al., 2001). This formation is most prevalent in areas with high snow deposition and low ice growth rates, a situation conducive to the isostatic depression of ice freeboard below the ocean surface, referred to as "negative freeboard" (Webster et al., 2018). This process is less common in the Arctic, with exceptions in areas experiencing strong storm events (e.g., Merkouriadi et al. 2017). Processes such as sea ice deformation under convergent drift and wave overwash may also contribute to snow-ice formation in certain regions of the Southern Ocean (e.g., Massom et al., 1998).

Comparing our model's net snow accumulation with a CryoSat-2 radar altimetry-based snow depth retrieval (Fons et al., 2023; see Section 3.3.2.2) clearly demonstrates the distinction between these two metrics (Figure 3.8b–c). Subtracting the two fields reveals positive differences of 20–30 cm across the Antarctic SIZ by spring, which we interpret as evidence of widespread snow-ice formation of that magnitude. While potential biases in the CryoSat-2 snow depth retrieval cannot be ruled out, the consistent discrepancy between these observations and our model's observationally calibrated estimates of net snow accumulation—excluding snow-ice formation—strengthens our interpretation.

Additionally, interpreting the difference field in Figure 3.8c as indicative of snow-ice formation aligns with observations that suggest this process is ubiquitous across the Southern Ocean, including the central Weddell Sea and the Amundsen-Bellingshausen Seas (Eicken et al., 1994; Massom et al., 1997, 2001; Sturm et al., 1998). The timing of the differences, peaking in spring (September–November), is also consistent with our understanding that snow-ice formation generally starts to occur in the latter half of winter, as snow accumulates while ice growth slows (Eicken et al. 1995; Singh et al. 2021), with Southern Ocean snow-ice volume reaching a maximum in November (Fichefet & Morales Maqueda, 1999).

A similar method for estimating snow-ice formation was used by Maksym and Markus (2008), who synthesized ice motion and ERA-40 reanalysis snowfall data to reconstruct snow accumulation. They interpreted any accumulation exceeding passive microwave snow depth estimates as indicative of snow-ice conversion. Although their reconstruction did not account for other loss processes and likely overestimated snow accumulation off East Antarctica due to biases in ERA-40 snowfall data, their estimates of September snow-ice thickness across the Antarctic SIZ (see their Figure 7) align closely, both in magnitude and spatial pattern, with the calculated difference between our simulated snow accumulation and snow depth from AMSR-E and AMSR2 (Figure 3.8e). However, this correspondence is less robust for snow depth from CryoSat-2 (Figure 3.8c), highlighting the sensitivity of this approach to the choice of satellite snow depth retrieval.

Our model reconstruction shows the seasonal evolution of bulk snow density, with a SIZ average of 348 kg m^{-3} in fall increasing to 367 kg m^{-3} in winter, 377 kg m^{-3} in spring, and returning to 349 kg m^{-3} in summer (Figure 3.8f; see also Figure 3.9c). This seasonal variation is influenced by two parameterized processes in the model: wind-enhanced compaction of fresh snowfall, which determines the density of a new snow layer based on the first 100 h of wind speeds that it experiences after deposition, and mechanical compaction due to overburden pressure. The spatial distribution of bulk snow density, which tends to be lower at higher latitudes, reflects these processes. Formation of new sea ice near the continent implies a thinner, less compacted snow cover at high latitudes (Figure 3.1a), where fresh snowfall will also be less dense owing to lower average wind speeds. This is supported by an approximately linear decrease in zonally-averaged ERA5 10-m wind speed from 55°S to 80°S across all seasons (not shown).

Our estimates of bulk snow density are broadly consistent with in situ observations, which include, for example, mean winter snow densities of 320 kg m^{-3} and 360 kg m^{-3} from snow pits during cruises in the Weddell Sea and Indian Ocean sector, respectively, though significant variability is observed across locations (Massom et al., 2001). In any case, the greater spatial variability in bulk snow density compared to its seasonal variability in our model reconstruction

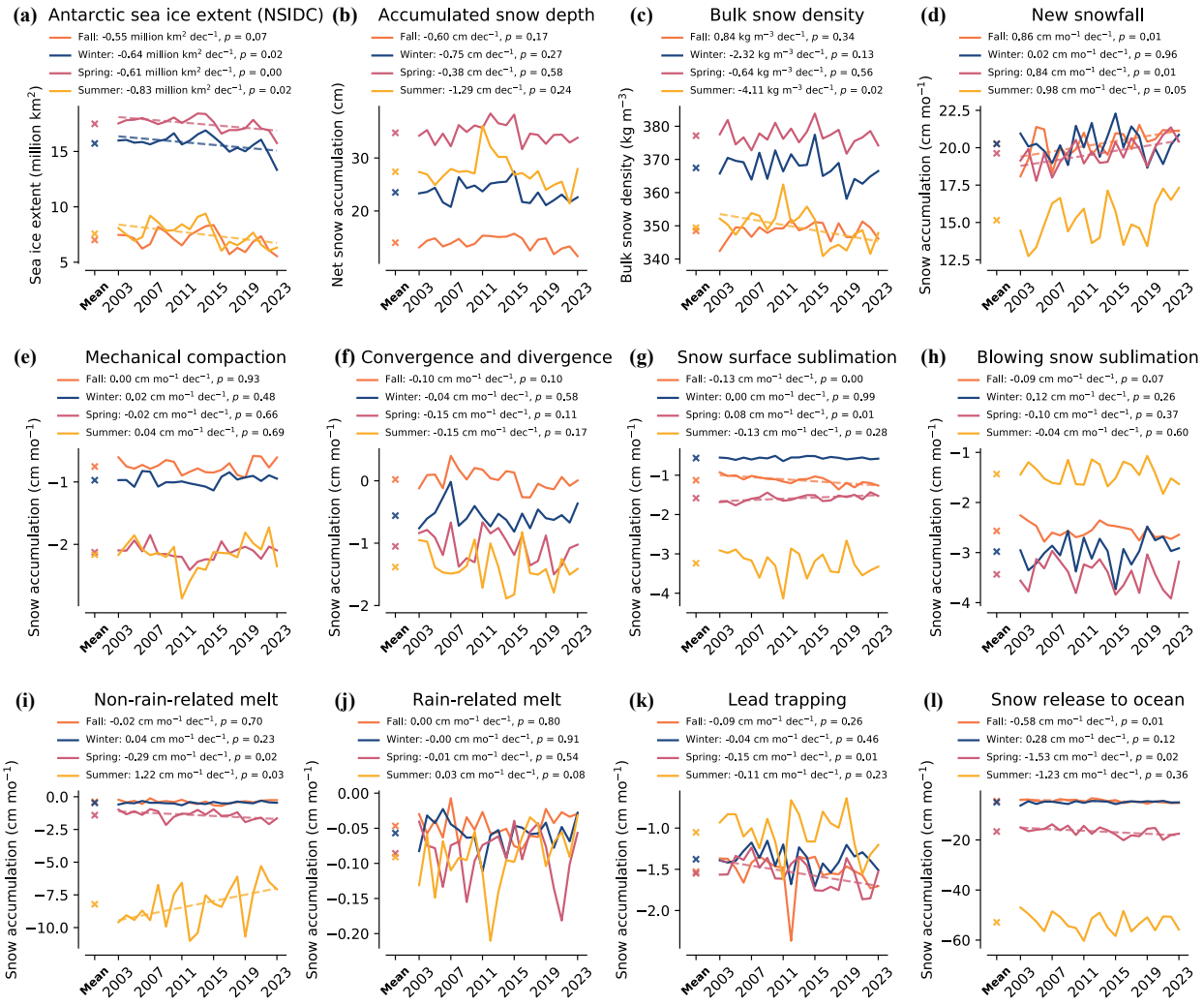

Figure 3.9: Trends in observed sea ice and reconstructed snow variables by season. Trends in **(a)** Antarctic sea ice extent (see Section 3.3.2.3) and **(b)–(l)** snow model reconstruction variables over the model period of 2003–2024. Seasons are defined as fall (MAM), winter (JJA), spring (SON), and summer (DJ, spanning two years so that the period is contiguous), and seasonal mean values are marked with crosses. For snow model variables, each seasonal average for a given year is calculated from daily spatial averages, weighted by the latitudinally varying grid cell area, with snow depth tendencies normalized to a bulk snow density of $\rho_{s,0}$ = 320 kg m^{-3}. Dashed lines indicate significant linear trends ($p \leq 0.05$). For panels **(d)–(l)**, positive values or trends signify greater snow accumulation on sea ice, while negative values or trends denote loss, i.e., contributions to reduced accumulation. Note the different y axis scales.

suggests that adopting only temporally varying snow depths, as used in some modeling and remote sensing efforts (e.g., Kurtz & Markus, 2012; Fons et al., 2023; Lawrence et al., 2024), may be an oversimplification.

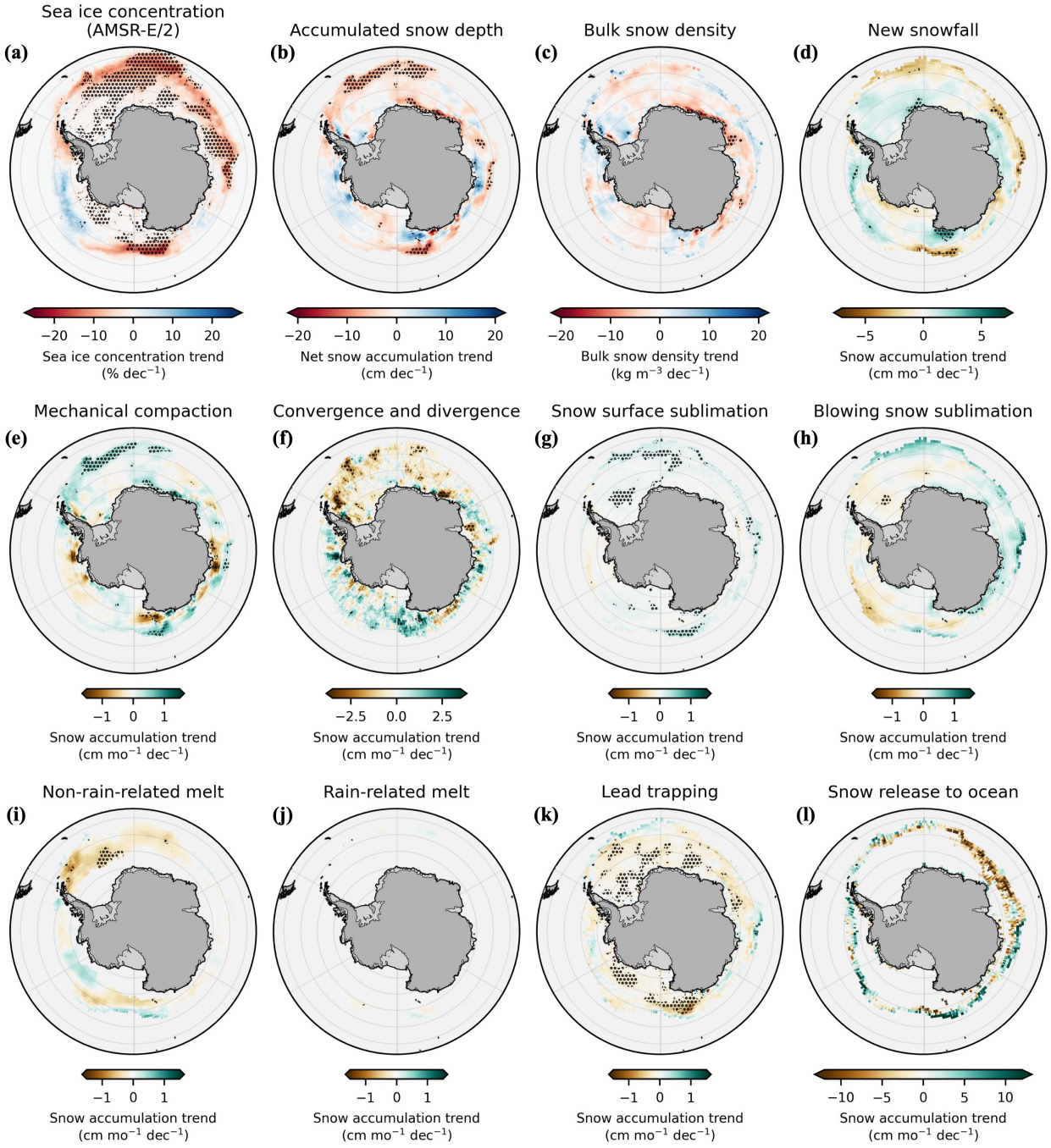

Figure 3.10: Circumpolar mapping of trends in observed sea ice and reconstructed snow variables. Spatial distribution of trends during winter and spring (June–November) only in **(a)** AMSR-E/2 observed sea ice concentration and **(b)–(l)** snow model reconstruction variables, each averaged from daily fields with trends diagnosed for the model period of June 2003 to November 2023. Stippled regions (black dots) indicate grid cells with significant ($p \leq 0.05$) linear trends. Similar to Figure 3.9, positive trends in panels **(d)–(l)** signify greater snow accumulation on sea ice, while negative trends denote increased loss, i.e., reduced accumulation. Snow depth tendencies have been normalized to a bulk snow density of $\rho_{s,0}$ = 320 kg m^{-3}. Note that different color scales are reflected in the colorbar lengths.

3.4.5 Interannual trends

Finally, we analyze trends in the snow model reconstruction variables by season over the 2003–2024 model period (Figure 3.9) and for winter and spring (June–November) across the Antarctic SIZ from 2003–2023 (Figure 3.10). For context, comparable trends observed in the Antarctic SIE index (Section 3.3.2.3) and in SIC from AMSR-E/2 are also presented. The SIE record shows statistically significant declines in all seasons except fall, driven largely by abrupt drops in recent years (Figure 3.9a; see Section 3.2). Regionally, declines in SIC are evident during winter and spring throughout much of the Southern Ocean, with the exception of the Amundsen Sea and the area off Wilkes Land in East Antarctica, where increases are observed (Figure 3.10a).

In comparison, net snow accumulation in our model reconstruction exhibits weak decreasing trends across all seasons, but none are statistically significant when diagnosed as circumpolar averages (Figure 3.9b). Yet when mapped around Antarctica for winter and spring (Figure 3.10b), areas of statistically significant decline emerge, mostly in the northern Weddell Sea and west of the Ross Sea, alongside a broader pattern of statistically insignificant trends that nonetheless closely mirror those in SIC. In particular, increased snow accumulation is apparent in the Amundsen Sea, while decreases dominate elsewhere, with some deviations from the SIC pattern offshore of East Antarctica. This suggests that reduced sea ice persistence, associated with earlier melt and/or a smaller ice-covered area in recent years, has limited the accumulation of snow along the drift trajectories of sea ice floes. Nevertheless, linear trends remain obscured in all seasons by significant interannual variability (Figure 3.9b), partially a reflection of the step change in sea ice extent that occurred around 2016 (Purich & Doddridge, 2023). This overall interpretation is supported by our finding that total snow mass deposition integrated across the Antarctic SIZ tracks the seasonal cycle of SIE (Figure 3.6a; Section 3.4.2), implying steady snowfall rates year-round and a likely causal link between ice floe age and snow accumulation. Furthermore, recent decreases in bulk snow density during winter and summer, on the order of –5 to –10 kg m^{-3} (Figure 3.9c), are also evident throughout the SIZ in winter and spring (Figure 3.10c). These

changes may similarly reflect shorter residence times during which snow on sea ice is subject to mechanical compaction, a conclusion supported by spatial patterns showing lessened compaction in areas of SIC decline (Figure 3.10e).

Counteracting the overall trends in snow accumulation are weakly positive trends in new snowfall across regions of the SIZ that have not experienced substantial SIC declines in winter and spring (Figure 3.10d). These trends are statistically significant in circumpolar averages for fall and spring, yielding increases of 0.8–0.9 cm mo^{-1} dec^{-1} in both seasons (Figure 3.9d). Additionally, non-rain-related melt exhibits a significant decrease in summer, favoring increased snow retention (Figure 3.9i), perhaps due to reduced exposure of snow to warmer air temperatures and elevated radiative fluxes at northern latitudes, a consequence of SIE contraction. While other variables show indistinct or inconsistent spatial patterns in winter and spring trends, lead trapping notably shows small but significant increases in magnitude (contributing to reduced snow accumulation) across the SIZ (Figure 3.10k). Furthermore, convergence and divergence trends form a distinct bipolar pattern, with increased ice divergence driving snow thinning in the Atlantic sector and enhanced ice convergence leading to snow thickening in the Pacific sector (Figure 3.10f).

Although differences in time periods complicate direct comparisons, Lawrence et al. (2024) identify trends in their snow depth reconstruction over 1982–2021 that bear a close resemblance to the spatial patterns seen in our results. Specifically, they report increased snow depth in the Weddell Sea and west of the Ross Sea, coupled with decreases in the Amundsen-Bellingshausen region. They similarly attribute these patterns to changes in sea ice age driven by trends in sea ice extent. By contrast, the circumpolar snow accumulation trends that we diagnose for 2003–2024 are opposite in sign to those reported by Maksym and Markus (2008) in their reconstruction of snow accumulation and depth on Antarctic sea ice for 1979–2001. Their findings reflect the earlier, multi-decadal period of gradually increasing SIE, unaffected by the recent abrupt declines

(Parkinson, 2019), underscoring the strong coupling that we infer between snow accumulation and the persistence and extent of sea ice.

3.5 Conclusions

In this study, we have introduced the conceptual framework and results of the most sophisticated reconstruction of snow on Antarctic sea ice yet developed. Our model occupies a middle ground between high-complexity, multilayer snow evolution models like SnowModel-LG (Liston et al., 2020; Stroeve et al., 2020), which simulates snowpack thermodynamics and detailed processes like snow redistribution but has only been applied to the Arctic Ocean, and lighter-weight reconstruction models (Maksym & Markus, 2008; Blanchard-Wrigglesworth et al., 2018; Petty et al., 2018; Lawrence et al., 2024), which prioritize ease of interpretability and lower computational requirements, enabling sensitivity experiments and calibration techniques (e.g., Cabaj et al., 2023).

A robust calibration procedure adjusts free parameters in the model to optimize its fit to observations, and the model proves capable of reproducing the evolution of snow measured by the Weddell Sea autonomous buoys used for calibration within expected deviations. Specifically, the model achieves an RMSE of 14.2 cm and a bias of +1.4 cm when compared to the matched buoy observations, despite the different scales represented: the model's 0.25° x 0.25° grid versus the point measurements of the buoys. The calibration results in a near-closure of the climatological simulated snow mass budget for the entire Antarctic SIZ, within 18%, bolstering confidence in a model constructed from a patchwork of physical and empirical approaches largely adapted from the context of terrestrial snow modeling. However, this near-budget closure does not rule out the possibility of larger, potentially compensating biases within the parameterizations of individual processes.

The core set of snow process parameterizations incorporated in the model all seem to play an important role—with the exception of rain-related melt—in determining the fate of the one-third of snow mass lost prior to seasonal ice melt. Notably, several of these erosion and transformation processes are absent in many coupled climate models. These include processes involving wind-blown snow and density compaction; snow density in such models is often prescribed rather than treated as a prognostic variable. Still, considerable uncertainties remain as to the magnitude and mechanisms of these processes, particularly lead trapping of blowing snow. Our model also excludes several potentially influential but poorly constrained processes that are challenging to represent accurately, such as the metamorphic effects of liquid water and the role of snow age in diagenetic lock-up of the snowpack. Critically, snow-ice conversion is not explicitly represented in our reconstruction. Instead, we estimate its contribution by subtracting a radar altimetry-based snow depth retrieval from our snow accumulation results. Snow-ice formation evidently constitutes a substantial component of the snow and sea ice mass budgets, making it essential to adjust the evolution of snow depth accordingly when using reconstructions to validate or refine remote sensing capabilities. For models like ours that do not explicitly simulate sea ice formation, combining the snow-only accumulation estimates with reliable observational sea ice thickness data is needed to infer snow-ice formation. However, no such product exists that can provide comprehensive seasonal and regional coverage.

The resulting snow mass budget from our model is nonetheless informative, underscoring the importance of treating snow on Antarctic sea ice as more than just a layer governed solely by snowfall and its eventual release to the ocean during ice melt. Freshwater fluxes from snow will influence the vertical density stratification of the upper ocean, which is itself a potential driver of interannual trends in Antarctic sea ice (Goosse & Zunz, 2014). A precise accounting of the timing and magnitude of snow fluxes into the ocean is therefore important. Yet the potential impact of lead trapping on the mixed-layer salinity budget has gone unaddressed within the oceanographic literature, which typically assumes snow is not available for release until the spring melt (e.g.,

Gordon et al. 1984; Martinson and Iannuzzi 1998). Failing to consider this and other snow loss processes could lead to unintended consequences when modeling the upper ocean within the Antarctic SIZ, resulting in excessive snow accumulation, snow-ice formation, and spurious brine rejection into the upper ocean. Such inaccuracies could erode density stratification in regions already prone to convective overturning (Martinson, 1990; Campbell et al., 2019; E. A. Wilson et al., 2019) or exacerbate ice melt by promoting the entrainment of warm pycnocline waters. This dynamic could establish a "conveyer belt" effect, where sea ice grows from the top from flooding while melting at its base due to elevated ocean heat fluxes (Lytle & Ackley, 2001; Maksym et al., 2012).

Overall, Antarctic sea ice serves as a dynamic catchment basin for snowfall over the Southern Ocean, intercepting and funneling it towards hotspots of sea ice melt. We find that snow on sea ice provides a meteoric freshwater flux to the ocean equivalent to more than two-thirds of the flux provided by sea ice melt across the entire SIZ (Haumann et al., 2016b). Our estimate, which is twice that of a previous data-assimilating model (Abernathey et al., 2016), highlights the powerful role of sea ice as a temporal and spatial filter: delaying the release of snow to the ocean until spring melt—except in cases of lead trapping or loss during ridging—and transporting snow en masse towards lower latitudes, where its release is concentrated in a narrow band identified by our model. This filtering process profoundly influences water mass transformation in the Southern Ocean (Pellichero et al., 2018). Snow input contributes buoyancy to upwelled deep waters destined for lower latitudes, while its northward transport away from the Antarctic continent allows precursors of bottom waters to densify, sustaining the global overturning circulation (Talley, 2008; Lago & England, 2019). Our trend analysis indicates a close alignment between recent changes in sea ice and reconstructed snow accumulation, suggesting that if the seasonal extent and persistence of Antarctic sea ice continue on their apparent new, lower trajectory (Purich & Doddridge, 2023), snow can be expected to follow suit.

3.6 Data availability

All data in this study are publicly available. The AMSR-E and AMSR2 sea ice concentration data are available from University of Bremen (last access: 31 March 2024) at https://seaice.uni-bremen.de/sea-ice-concentration/amsre-amsr2/ (Spreen et al., 2008; Beitsch et al., 2014). The CDR and CDR-NRT sea ice concentration data are available from NSIDC (last access: 31 March 2024) at https://doi.org/10.7265/efmz-2t65 and https://doi.org/10.7265/tgam-yv28, respectively (Meier et al., 2021a, 2021b). The AMSR-E and AMSR2 snow depth on sea ice retrievals are available from NSIDC (last access: 17 March 2024) at https://doi.org/10.5067/AMSR-E/AE_SI12.003 and https://doi.org/10.5067/RA1MIJOYPK3P, respectively (Cavalieri et al., 2014; Meier et al., 2018). Polar Pathfinder sea ice motion data are available from NSIDC (last access: 12 November 2024) at https://doi.org/10.5067/INAWUWO7QH7B and https://doi.org/10.5067/O0XI8PPYEZJ6 (Tschudi, Meier, & Stewart, 2019; Tschudi, Meier, Stewart, et al., 2019). The ECMWF ERA5 atmospheric reanalysis fields are available from the Copernicus Climate Change Service (last access: 24 April 2024) at https://doi.org/10.24381/cds.adbb2d47 (Copernicus Climate Change Service, 2023). The snow buoy measurements are available from AWI (last access: 9 February 2024) at https://data.meereisportal.de/relaunch/buoy.php (Nicolaus et al., 2017). The CryoSat-2 snow depth estimates are available on Zenodo at https://doi.org/10.5281/zenodo.7327711 (Fons et al., 2023). The sea ice extent index is available from NSIDC (last access: 16 November 2024) at https://doi.org/10.7265/N5K072F8 (Fetterer et al., 2017).

3.7 Appendix

Appendix Table 3.3: Coefficients for Q'_{sub} in Eq. (3.24), from Déry and Yau (2001).

Coefficient	Value
a_0	3.78407×10^{-1}
a_1	-8.64089×10^{-2}
a_2	-1.60570×10^{-2}
a_3	7.25516×10^{-4}
a_4	-1.25650×10^{-1}
a_5	2.48430×10^{-2}
a_6	-9.56871×10^{-4}
a_7	1.24600×10^{-2}
a_8	1.56862×10^{-3}
a_9	-2.93002×10^{-4}

Appendix Table 3.4: Tabulation of latent heat of condensation L and thermal conductivity and diffusion coefficients K and D from Rogers and Yau (1989), Tables 2.1 and 7.1.

T_a (°C)	L (J g^{-1})	K (J m^{-1} s^{-1} K^{-1})	D (m^2 s^{-1})
−40	2603	2.07×10^{-2}	1.62×10^{-5}
−30	2575	2.16×10^{-2}	1.76×10^{-5}
−20	2549	2.24×10^{-2}	1.91×10^{-5}
−10	2525	2.32×10^{-2}	2.06×10^{-5}
0	2501	2.40×10^{-2}	2.21×10^{-5}
5	2489	-	-
10	2477	2.48×10^{-2}	2.36×10^{-5}
15	2466	-	-
20	2453	2.55×10^{-2}	2.52×10^{-5}
25	2442	-	-
30	2430	2.63×10^{-2}	2.69×10^{-5}

Appendix Table 3.5: Simulated rate of blowing snow mass lost to a lead with fetch (width) of 1 km and spacing of 1 km, from Déry and Tremblay (2004), Table 1, in relation to 10-m wind speed.

U_{10} (m s^{-1})	Q'_{lead} (mm SWE d^{-1})
10	12.5
15	16.2
20	29.1
25	66.0

Chapter 4:

ANTARCTIC SEA ICE FORMATION AND MELT RATES ESTIMATED FROM OCEAN SALINITY OBSERVATIONS

4.1 Abstract

Ice-capable autonomous profiling floats have amassed an extensive collection of year-round salinity measurements from the Southern Ocean seasonal ice zone. We develop a methodology for estimating Antarctic sea ice formation and melt rates using local mixed-layer salinity budgets constructed along the drift trajectories of individual floats. Atmospheric reanalysis and remote sensing data are incorporated to constrain budget terms, with ice-related freshwater fluxes inferred as the residual. Applying this Lagrangian salinity budget framework to over 16,000 under-ice profiles collected by more than 300 Argo floats, mainly since 2008, reveals that sea ice growth and melt account for nearly half of the annual contributions to changes in mixed-layer salinity. The remaining budget is split roughly equally between freshwater fluxes from snow and other processes combined, including entrainment, upwelling, evaporation, advection, and diffusion. The seasonal cycle of sea ice exhibits a pronounced asymmetry, with a prolonged net growth phase that slows in mid-winter, followed by the initiation of rapid melt in October. This analysis yields the first observationally grounded circumpolar climatology of Antarctic sea ice growth and melt rates, showing net annual sea ice production near the continent transitioning to net annual melt around 65°S. In November and December, widespread sea ice melt within the interior of the ice pack—far from the retreating ice edge—suggests that spring melt may be more spatially extensive than what can be diagnosed using sea ice extent or concentration alone. This

float-based methodology highlights the potential to reconstruct climatological Antarctic sea ice thickness using autonomous ocean measurements, which would provide a valuable observational constraint to complement and validate remote sensing retrievals of this critical climate variable.

4.2 Introduction

The past two decades has seen increasing recognition that the global ocean overturning is tightly coupled to freshwater fluxes from the formation and melt of sea ice in the Southern Hemisphere. Brine rejection during sea ice formation near the Antarctic continent densifies a portion of upwelled deep water masses, driving the formation of Antarctic Bottom Water (Ohshima et al., 2013; Tamura et al., 2016; Silvano et al., 2020). Meanwhile, the majority of these upwelled waters are transported northward, where they are transformed into lighter density classes that comprise the upper branch of the overturning by freshwater fluxes associated with sea ice melt and precipitation (Saenko et al., 2002; J. Marshall & Speer, 2012; Abernathey et al., 2016). These transformations are mediated by the predominantly northward, wind-driven transport of sea ice and its overlying snow cover, which acts as a mechanism for redistributing buoyancy from waters near the Antarctic continent to regions closer to the Antarctic Circumpolar Current (Haumann et al., 2016b; Pellichero et al., 2018).

The abrupt decline in Antarctic sea ice extent observed in recent years (Parkinson, 2019; Purich & Doddridge, 2023) would imply concomitant changes in the location, magnitude, and timing of sea ice-related freshwater fluxes. Subsurface ocean warming has been implicated as a potential factor in the recent sea ice trends (Meehl et al., 2019; Eayrs et al., 2021; L. Zhang et al., 2022; J. Wang et al., 2024), suggesting that causality in the other direction—changes in freshwater fluxes leading to variations in the sea ice extent—may be a possibility. This is because brine rejection and sea ice melt can result in vertical redistributions of salt and the accumulation of subsurface heat, which has been suggested to produce regionally distinct sea ice extent trends

through feedbacks operating on interannual timescales (Goosse & Zunz, 2014; Lecomte et al., 2017; Haumann et al., 2020). In any case, the processes through which warm subsurface water can be entrained into the surface layer, where its heat will affect sea ice, are highly sensitive to the freshwater balance of the upper ocean, which sets its stratification (Gordon & Huber, 1984; Martinson, 1990; Kjellsson et al., 2015; Bronselaer et al., 2018; E. A. Wilson et al., 2019; J. Wang et al., 2024). The importance of characterizing this freshwater balance is underscored by the multitude of related changes that are ongoing or predicted for the ice-covered Southern Ocean: surface freshening associated with hydrological cycle intensification and glacial melt (de Lavergne et al., 2014; Rye et al., 2020), poleward shifts in storm tracks (Chang et al., 2012), increased snowfall (Liu & Curry, 2010), and changes in the cyclonicity of ice drift in some sectors (P. R. Holland & Kwok, 2012).

The net sea ice formation rate at a given location directly corresponds to the rate of change of sea ice thickness. This relationship suggests—ignoring certain methodological complexities—that if formation rates can be reliably quantified and integrated over time and space, sea ice thickness can be derived. Such a connection has significant implications, as sea ice thickness is a critical climate variable that mediates ocean–atmosphere energy fluxes and momentum transfer (McPhee, 2017). It also represents the under-observed “third dimension” of sea ice volume in the Southern Hemisphere, where sea ice concentration (SIC) and extent retrieved using satellite passive microwave radiometry remain the primary indicators of sea ice change. Accurately estimating sea ice thickness from space has proven challenging, partly due to the scarcity and navigational biases of the ship-based observations available for validation purposes, which skew towards regions of thinner ice (Worby, Geiger, et al., 2008). Additionally, thickness estimation based on ice freeboard measured by laser altimetry requires constraining the depth and density of overlying snow, whose isostatic contribution introduces the largest uncertainty in these calculations (Zwally et al., 2008). Nevertheless, recent advances offer promising methods for

retrieving Antarctic sea ice thickness and snow depth from spaceborne remote sensing (Kacimi & Kwok, 2020; Garnier et al., 2021; Shen et al., 2022; Fons et al., 2023; Yan et al., 2024).

Various other approaches for generating circumpolar estimates of sea ice thickness and associated freshwater fluxes have provided valuable insights but come with significant limitations. Tamura et al. (2011) used satellite detection of the thickness of thin sea ice (< 0.2 m) to estimate heat and salt fluxes linked to ice growth and melt, but their method assumes minimal ice production at higher thicknesses, likely underrepresenting fluxes. Holland and Kimura (2016) inferred sea ice freezing and melt as comprising most of the residual in a SIC budget diagnosed from remote sensing data. However, this two-dimensional framework represents an approximation of thermodynamic changes and cannot quantify changes in ice volume. Global or regional numerical model simulations offer another alternative by incorporating observational constraints such as atmospheric reanalysis data, sea ice concentration retrievals, and ocean observations. These data-assimilating simulations yield comprehensive estimates of sea ice thickness and associated freshwater fluxes (Massonnet et al., 2013; J. Zhang, 2014; P. R. Holland et al., 2014; Abernathey et al., 2016; Kusahara et al., 2019), but remain susceptible to biases that require careful correction (e.g., Haumann et al., 2016). For instance, the Southern Ocean State Estimate (SOSE) overestimates sea ice thickness in the Weddell and Ross Seas by 20–40 cm, even with the assimilation of ocean observations (Abernathey et al., 2016). This bias is likely associated with compensating errors in freshwater fluxes caused by unrealistically low snow accumulation on sea ice (Campbell & Riser, in prep).

The use of ocean salinity measurements within the Antarctic seasonal ice zone (SIZ) could offer a complementary strategy. Studies based on sparse observations have characterized the salinity of the Southern Ocean winter mixed layer under sea ice as dominated by three main processes: brine rejection associated with ice growth; entrainment, which is the incorporation of saltier pycnocline waters during convective or turbulent mixed-layer deepening; and precipitation or other freshwater input from sea ice advection, which compensates wintertime salt input

(Gordon et al., 1984; Gordon & Huber, 1990; Martinson, 1990; Wong & Riser, 2011). Initial efforts to construct mixed-layer salinity budgets for the Southern Ocean by combining gridded observational fields with remote sensing and atmospheric reanalysis data excluded the SIZ due to a paucity of observations (Dong et al., 2009; Ren et al., 2011). However, large budget residuals approaching the ice edge pointed to a substantial influence from sea ice. More recently, increased under-ice observations from profiling floats and instrumented seals have enabled the construction of a climatological mixed-layer salinity budget for the seasonal ice zone (Pellichero et al., 2017, 2018). This analysis reinforces the long-standing view that entrainment and ice-related fluxes are the primary drivers of winter variations in mixed-layer salinity. However, it aggregates freshwater fluxes from precipitation, evaporation, and sea ice into a combined air-ice-sea term, stopping short of an explicit constraint on ice-induced fluxes. Furthermore, the analysis of Pellichero et al. (2017) excludes the effects of geostrophic advection and horizontal eddy diffusion, which could potentially be important in certain regions.

In this study, local mixed-layer salinity budgets under sea ice are constructed (Section 4.3.3 and 4.3.4) using Argo profiling float measurements (Section 4.3.1) and auxiliary data sources (Section 4.3.2) along the drift trajectories of floats in the Antarctic SIZ. Observations from one float deployed in the Ross Sea (WMO ID 5904183) as part of the Southern Ocean Carbon and Climate Observations and Modeling (SOCCOM) project (Riser et al., 2018; Sarmiento et al., 2023) depict the typical SIZ pattern of mixed layer deepening and salinification in fall and mixed layer shoaling and freshening in spring (Figure 4.1b–c). The results of this budget framework are applied to seven years of observations from the Ross Sea float (Section 4.4.1). The methodology is then applied to the full circumpolar array of under-ice floats, with the results visualized using composites for budget terms within the Antarctic SIZ (Section 4.4.2). Lastly, we evaluate a float-derived circumpolar climatology of sea ice formation and melt in the context of previous estimates (Section 4.4.3).

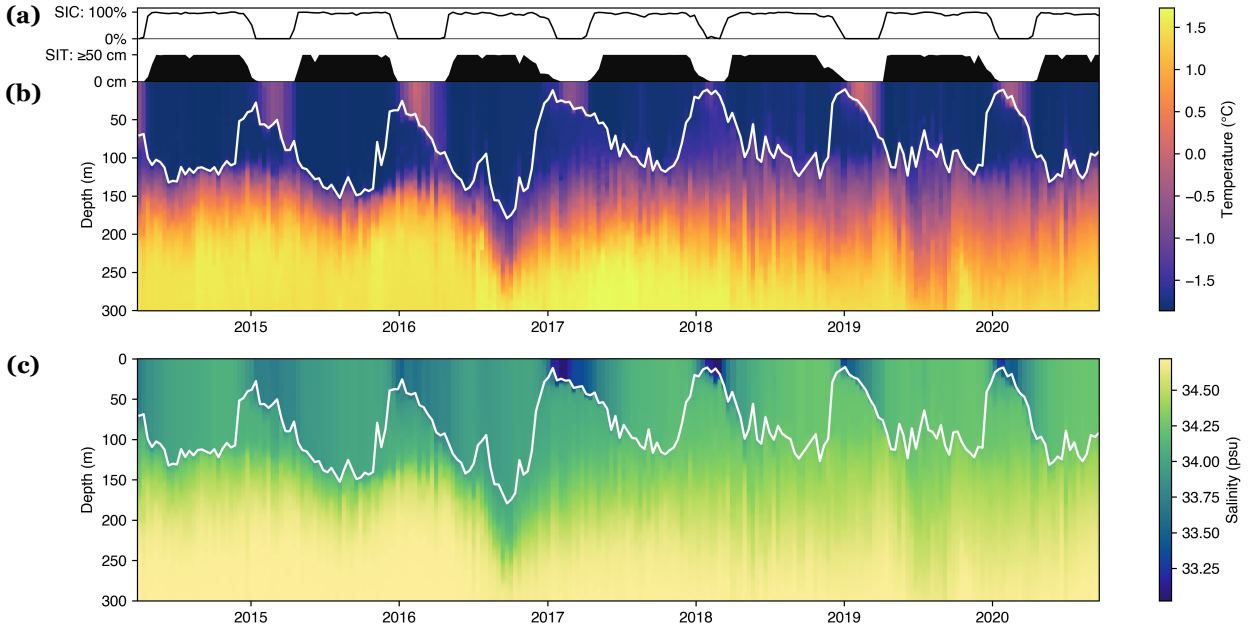

Figure 4.1: Seven years of temperature and salinity profiles collected in the central Ross Sea at 10-day intervals from Argo float 5904183. (a) Sea ice concentration (SIC) from ASMR2 and thin sea ice thickness (SIT) from SMOS are shown as averages calculated within the time-varying uncertainty regions along the float trajectory, which has been linearly interpolated under sea ice. Note that the SMOS product has a maximum retrievable sea ice thickness of 50 cm. **(b)** Temperature and **(c)** salinity measured by the float, with the calculated mixed layer depth (Section 4.3.4) in white.

4.3 Data and methods

4.3.1 Profiling float data

Data from all Argo floats that have measured temperature and salinity in the Southern Ocean south of 55°S were downloaded from the US-GODAE Global Data Assembly Center (GDAC) (Argo, 2021). We rejected floats with fewer than 10 profiles, floats for which fewer than 90% of profiles were collected at intervals between 6 and 14 days (as normal sampling occurs at 7–10 day intervals), floats with profile timestamps that were not increasing monotonically, initial deployment profiles, and individual profiles with a shallowest depth below 25 m or a deepest depth above 500 m. Both real-time ("R") and delayed-mode ("D") profiles were used, and depths at which quality control flags for pressure, temperature, and salinity were all good ("1") or probably good ("2") were retained. 1,082 Argo floats met the inclusion criteria, including 16,665

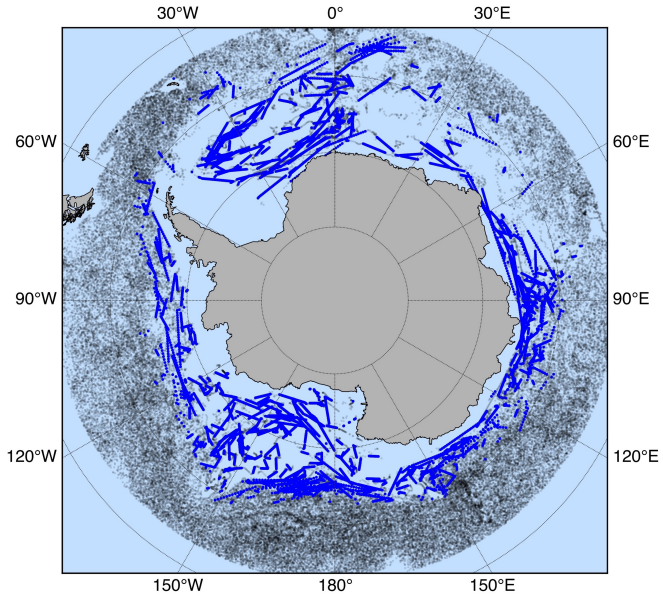

Figure 4.2: Under-ice drift trajectories of Argo profiling floats used in salinity budget analysis. Trajectories beneath sea ice from 336 floats are linearly interpolated between known locations (blue). Profiles with known positions are also shown (black points).

pairs of consecutive under-ice profiles from 336 floats (Figure 4.2). Nearly all under-ice profiles are from between 2008 and 2022, with a limited number from 2005–2007.

To avoid sea ice, an ascending ice-enabled float monitors the median temperature between 50 and 20 m, and if a near-freezing temperature is detected, the float aborts its ascent and stores the profile without a position fix for transmission upon spring ice melt (Klatt et al., 2007; Riser et al., 2018). We linearly interpolate the locations of these under-ice profiles along great circle routes between known positions. Position uncertainties are assigned as a quadratic function of the time from the nearest known position using the relationship found by Chamberlain et al. (2018) for acoustically-tracked under-ice floats in the Weddell Sea, in which the maximum position uncertainty (at the midpoint between known fixes) increases at a rate of 0.48 km per total days under ice. These time-dependent position uncertainty values represent the radii of circular averaging regions used to estimate budget terms for each float profile. The averaging regions are defined on the 0.25° x 0.25° European Centre for Medium-Range Weather Forecasts (ECMWF)

ERA5 reanalysis grid, to which all other data products mentioned henceforth are regridded using a geospatial bilinear remapping algorithm.

4.3.2 Auxiliary and validation data

Sea ice concentration (A_{SIC}) is obtained from the University of Bremen AMSR2 passive microwave product derived using the ARTIST Sea Ice (ASI) v5.4 algorithm on a 6.25 km polar stereographic grid (Beitsch et al., 2014), with data from the merged NASA Goddard Space Flight Center 25-km product, version 3, distributed by the National Snow and Ice Data Center (NSIDC) (Meier, Fetterer, Savoie, et al., 2017) used on dates when AMSR2 data is unavailable. The University of Bremen daily Level 1C thin sea ice thickness product, version 6.20, from the L-band microwave sensor Soil Moisture and Ocean Salinity (SMOS), which retrieves sea ice thicknesses up to 50 cm, is obtained on a 12.5 km polar stereographic grid for visualization purposes alongside profiling float data (Huntemann et al., 2014). Values may be unreliable outside of March to October due to changes in emission properties associated with surface moisture during melt.

The 10-m wind speed vector components ($\boldsymbol{U}_{10}$) and time-mean evaporation rate (E), snowfall rate (S), and total precipitation rate (P_{tot}) are obtained from hourly ERA5 atmospheric reanalysis data provided at 0.25° resolution (Hersbach et al., 2020). Time-mean rainfall rates are calculated as ($P_{\mathrm{tot}} - S$). Estimated ice drift velocities ($\boldsymbol{U}_i$) are from the NSIDC Polar Pathfinder daily ice motion product, version 4.1, at 25 km resolution, which uses automated tracking of ice displacement from passive microwave measurements (Tschudi et al., 2020). Ice motion components on the original Equal-Area Scalable Earth (EASE) grid are rotated to obtain eastward- and northward-oriented vectors before remapping to the ERA5 grid.

We use geostrophic current velocities ($\boldsymbol{u}_g$) derived from sea surface height even during times of sea ice cover using satellite radar altimetry, which detects specular echoes originating in sea ice leads. This monthly CryoSat-2 dynamic ocean topography product spans the period 2011–2016 with a resolution of 50 km (Armitage et al., 2018). Climatological monthly values over that period

are used for other years, and in all cases, geostrophic velocity fields are interpolated linearly in time to the day-of-year of a particular float profile. Background lateral gradients of salinity are obtained from the monthly WOCE/Argo Global Hydrographic Climatology (WAGHC; Gouretski 2018), which has a horizontal resolution of 0.25° and represents a nominal period of 1985–2016. The climatology is provided on depth levels with a vertical resolution of 5 m near the surface, increasing gradually to around 40 m at a depth of 250 m. The three-dimensional WAGHC salinity fields are also interpolated linearly in time to the day-of-year of a float profile. Lastly, mesoscale eddy diffusivities are taken from the observation-based, full-depth global estimates of Groeskamp et al. (2020), which are generally within the range $\kappa = O(50\text{-}100)$ m^2 s^{-1} within the seasonally ice-covered Southern Ocean.

As a point of comparison to the float-based estimates of sea ice-related freshwater fluxes, we use an estimate of annual mean net freshwater fluxes in the Southern Ocean over 1982–2008 due to sea ice freezing, including snow-ice formation, and melting (Haumann et al., 2016a, 2016b). These estimates are based on a synthesis of model and observational data, incorporating sea ice thickness from a data-assimilating ocean–ice model (NEMO-LIM2; Massonnet et al., 2013) that has been bias-corrected using ICESat-1 laser altimetry and ship-based observations. Sea ice concentration and motion data were integrated to produce a mass balance reconstruction of sea ice volume change and divergence. This methodology provides one of the most robust constraints currently available on ice-related freshwater fluxes in the Southern Ocean.

4.3.3 Lagrangian framework

Rather than using gridded, interpolated observational fields, some investigators have constructed local salinity budgets or used simple models to directly estimate net sea ice freshwater fluxes in the Southern Ocean using time series from tethered (e.g., Aoki et al. 2020), profiling float (e.g., Wong & Riser 2011; Campbell et al. 2019; Porter et al. 2019), or biological (e.g., Charrassin et al. 2008; Meredith et al. 2011) observing platforms, or even simple comparisons of

sparse observations throughout the winter season (e.g., Gordon & Huber 1990). In particular, the work by Charrassin et al. (2008) informs the approach pursued here. Comparing instrumented seal observations off East Antarctica to a coupled sea ice–ocean model, the authors found that net sea ice formation rates could be reasonably estimated from the observations by simply assuming that salinity changes in the upper 100 m of the ocean were entirely due to freshwater fluxes from sea ice. However, these past efforts have been limited to regional studies each using no more than two dozen observing platforms. We improve and extend this conceptual approach using a large compilation of under-ice observations.

Our particular method of constructing Lagrangian mixed-layer salinity budgets along float drift trajectories is designed to address three key limitations inherent in the conventional approach employed by previous studies that have derived budgets from gridded observational fields (e.g., Ren et al., 2011; Pellichero et al., 2017):

1. Gridding sparse observations generally requires an optimal interpolation or objective mapping scheme, which is highly sensitive to the particular methodology and often poorly constrained parameters that are selected, such as an anisotropic decorrelation length scale (C. H. Heuzé et al., 2015).
2. These procedures aggregate ocean measurements into monthly climatological fields of observed and derived parameters, usually temperature, salinity, and mixed-layer depth. At times, this aggregation may introduce artificial lateral gradients due to interannual variability captured by the sparse observations. Moreover, this approach severs the connection between the resulting budget estimates—such as freshwater fluxes from sea ice formation and melt—and the original ocean observations, limiting their interpretability. In this case, this standard approach would prevent further analysis in the float-following frame of reference. Starting from gridded climatological fields also prevents the potential estimation of time trends in the resulting budget terms.

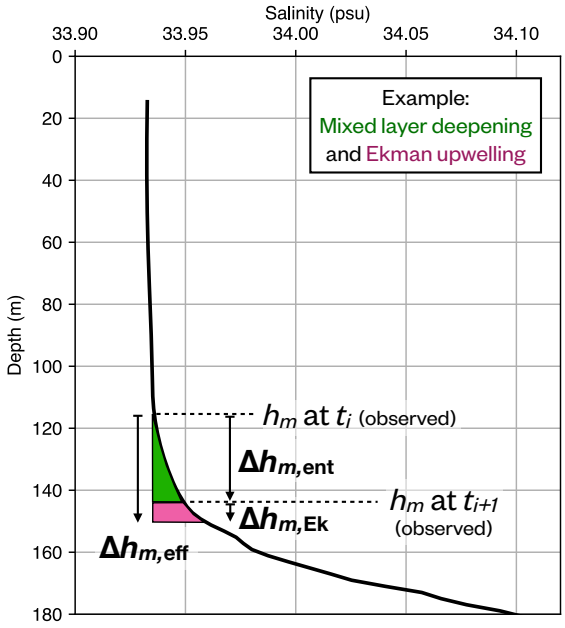

Figure 4.3: Schematic showing total entrainment inferred based on observed changes in mixed layer depth and calculated Ekman upwelling. Illustrated here using a typical float salinity profile are the contributions to total effective entrainment ($\Delta h_{m,\mathrm{eff}}$) owing to observed mixed layer deepening between times t_i and t_{i+1} (in green; $\Delta h_{m,\mathrm{ent}}$) and Ekman upwelling (in pink; $\Delta h_{m,\mathrm{Ek}} = w_{\mathrm{Ek}}\Delta t$), with shaded areas representing the integrated salinity flux. See Section 4.3.4 for more details.

3. Specific to this mixed layer budget, relying on gridded climatological observations limits the precision with which entrainment fluxes can be estimated. While monthly-average entrainment rates can be calculated from such data, the property gradients at the base of the mixed layer—on which entrainment fluxes depend—will be highly smoothed compared to the sharper gradients seen in original observations. Entrainment is an episodic process, often driven by storm-induced mixing (e.g., Fer et al., 2017), and is likely asynchronous across space and time. The resulting fluxes are highly sensitive to the instantaneous property gradients at the base of the mixed layer. Diagnosing these fluxes from observations is more accurately achieved in a Lagrangian framework by comparing consecutive vertical profiles from individual floats and calculating integral quantities, using the observed change in mixed layer depth between profiles to establish the bounds of integration (Figure 4.3; Eq. [4.10]).

A key limitation of constructing a localized, float-following salinity budget is that spatially extensive hydrographic property fields are not available for the calculation of non-local budget terms such as horizontal (Ekman and geostrophic) advection and eddy diffusion. This requires the substitution of climatological fields, making the budget no longer diagnosed solely from observations specific to a given date and raising the issues from items (1) and (2) above. However, background lateral gradients may be the only climatological property required, and they may be fairly time-invariant. For this reason, the overall budget may remain nearly Lagrangian, with the bulk of its constraints originating from localized data specific to the time period of interest.

Additionally, a core assumption inherent in an along-trajectory budget—unless the impacts of float advection can be accounted for—is that the net contribution from lateral inhomogeneities is relatively small and can be neglected, especially when averaging across floats in time and space. Formally, this can be expressed as approximately equating the Lagrangian, or material, time derivative of the mixed-layer salinity S_m with its local time derivative observed at a float's changing location, thus neglecting the advective component associated with the background flow field along the float trajectory, $\boldsymbol{u}_{\text{float}}$:

$$\frac{DS_m}{Dt} = \frac{\partial S_m}{\partial t} + (\boldsymbol{u}_{\text{float}} \cdot \nabla S_m) \approx \frac{\partial S_m}{\partial t} \,. \tag{4.1}$$

This simplifying assumption finds support in three lines of argument. First, floats may exhibit quasi-Lagrangian drift at their parking depth of 1,000 m but are not necessarily Lagrangian with respect to surface currents, which can differ substantially. However, the strongly barotropic circulation across most of the Weddell and Ross gyres, with a minimal baroclinic component (Reeve et al., 2019; Y. Wang et al., 2024), suggests that floats may remain relatively coupled to a surface parcel of water, at least in those gyre regions. Second, temporal variations in under-ice mixed layer salinity are significantly greater in magnitude than horizontal gradients, so the overall signal should be dominated by the former. This is evidenced by a decorrelation length scale of 350 km found for float measurements of upper-ocean salinity in the Weddell gyre by Chamberlain et

al. (2018), who also calculated an average drift speed of around 2.2 km d^{-1} and 2.8 km d^{-1} for satellite-tracked and acoustically-tracked floats, respectively. In contrast, Gille and Kelly (1996) found that a typical temporal decorrelation scale for the open Southern Ocean is O(34 days)—which may be even shorter for upper-ocean salinity in ice-covered regions, given the pronounced seasonal cycle (e.g., Figure 4.1c). These estimates imply that, during a typical winter under sea ice, the spatial variability experienced along the drift trajectory of a float may be at least four times smaller than the temporal variability observed, even before accounting for the flow-following nature of the float. Third, this assumption is further reinforced qualitatively by high-resolution numerical simulations, which reveal a predominantly homogeneous and less energetic upper ocean beneath sea ice. Submesoscale activity is apparently minimal except near sea ice leads, where inhomogeneous buoyancy forcing can lead to sharp property gradients and submesoscale eddy generation (e.g., Mensa & Timmermans, 2017; Cohanim et al., 2021). This suggests that uncorrelated variability in space should play an insignificant role in the overall mixed-layer salinity budget.

4.3.4 Mixed-layer salinity budget

We formulate our along-trajectory mixed-layer salinity budget similarly to Dong et al. (2009), Ren et al. (2011), and Pellichero et al. (2017), with some modifications:

$$\frac{DS_m}{Dt} \approx \frac{\partial S_m}{\partial t} = \underbrace{(E-P)\frac{S_m}{h_m}}_{\substack{\text{Evaporation,}\\ \text{rainfall,}\\ \text{snow flux}}} - \underbrace{w_{\text{ent+Ek}}\frac{\Delta S}{h_m}}_{\substack{\text{Effective}\\ \text{entrainment,}\\ \text{adjusted for}\\ \text{Ekman upwelling}\\ \text{or downwelling}}} - \underbrace{\boldsymbol{u}_{\text{Ek}}\cdot\nabla\boldsymbol{S}_{\text{Ek}}}_{\substack{\text{Horizontal}\\ \text{Ekman}\\ \text{advection}}} - \underbrace{\boldsymbol{u}_g\cdot\nabla\boldsymbol{S}_m}_{\substack{\text{Horizontal}\\ \text{geostrophic}\\ \text{advection}}} + \underbrace{\kappa\nabla^2\boldsymbol{S}_m}_{\substack{\text{Horizontal}\\ \text{eddy}\\ \text{diffusion}}} + \underbrace{I\frac{S_m}{h_m}}_{\substack{\text{Residual}\\ \text{(presumed}\\ \text{ice growth}\\ \text{and melt)}}} . \quad (4.2)$$

The initial simplifying assumption of equating the Lagrangian derivative of mixed-layer salinity S_m with its local tendency $\left(\frac{\partial S_m}{\partial t}\right)$ is discussed above in Section 4.3.3 and formalized in Eq. (4.1). Here, E and P are evaporation and total precipitation; h_m is mixed-layer depth; $w_{\text{ent+Ek}}$ is the combined entrainment and Ekman vertical velocity, computed as an effective entrainment

velocity; ΔS is the bulk salinity gradient at the base of the mixed layer (note that this term is computed below in a more sophisticated manner than expressed in Eq. [4.2], using an integral quantity for entrained or upwelled salt; see Eq. [4.10]); $\boldsymbol{u}_{\mathrm{Ek}}$ and $\boldsymbol{u}_g$ are the horizontal Ekman and geostrophic velocity vectors; $\boldsymbol{S}_{\mathrm{Ek}}$ is Ekman layer salinity (treated as distinct from mixed-layer salinity); κ is the horizontal eddy diffusivity; and I is the sea ice freshwater contribution from brine rejection or sea ice melt (units of m s^{-1}). The application of the budget along the uncertain, linearly interpolated trajectories of floats drifting under sea ice warrants a special adaptation: all budget terms are computed as averages within the circular regions defined above in Section 4.3.1 using the time-dependent position uncertainty from Chamberlain et al. (2018). This procedure also serves as a filter to mitigate noisiness in the budget terms owing to sharp and likely uncertain gradients, particularly along the sea ice edge and in areas of varying sea ice concentration.

First, in order to calculate mixed-layer average salinity (S_m), surface-referenced potential density (σ_θ) is computed from float profiles of temperature and salinity using the Gibbs SeaWater Oceanographic Toolbox of TEOS-10 (https://teos-10.github.io/GSW-Python/). The mixed layer depth (h_m; see, e.g., Figure 4.1b–c) is determined as the depth at which σ_θ exceeds its value at 10 m, estimated using interpolation or nearest-neighbor extrapolation, by at least 0.03 kg m^{-3} (de Boyer Montégut et al., 2004; Dong et al., 2008). Mixed-layer salinity is then calculated as the average salinity between 0 m and h_m using profiles linearly interpolated to 0.1-m spacing and extrapolated to 0 m (as an approximation) using the shallowest salinity measurement, as floats do not collect measurements all the way to the surface or the underside of sea ice.

To calculate the Ekman terms, ocean stress ($\boldsymbol{\tau}_o$) is taken to be a weighted average over the ice-free ($\boldsymbol{\tau}_{ao}$) and ice-covered ($\boldsymbol{\tau}_{io}$) areas of a grid cell, using the AMSR2 sea ice concentration (A_{SIC}):

$$\boldsymbol{\tau}_o = A_{\mathrm{SIC}}\boldsymbol{\tau}_{io} + (1 - A_{\mathrm{SIC}})\boldsymbol{\tau}_{ao} \, . \tag{4.3}$$

Air-ocean (ice-free) stress components are computed using 10-m wind speed velocities ($\boldsymbol{U}_{10}$) from ERA5; air density (ρ_a = 1.29 kg m^{-3}, per Kim et al. [2017]); and the Large and Pond (1981) formulation for the drag coefficient ($C_{D,ao}$) assuming a neutrally stable boundary layer, which we extend linearly for wind speeds above 25 m s^{-1}:

$$\left(\tau_{ao}^{x}, \tau_{ao}^{y}\right) = \rho_a C_{D,ao} |\boldsymbol{U}_{10}| \boldsymbol{U}_{10} \,. \tag{4.4}$$

Ice-ocean stress is computed using a reference seawater density (ρ_w = 1027.5 kg m^{-3}), a fixed ice-ocean drag coefficient ($C_{D,io}$ = 0.0056, per McPhee et al. [1999]), and the difference between ice drift velocities ($\boldsymbol{U}_i$) obtained from NSIDC Polar Pathfinder daily ice motion vectors (Tschudi et al., 2020) and surface ocean velocities ($\boldsymbol{U}_w$):

$$\left(\tau_{io}^{x}, \tau_{io}^{y}\right) = \rho_w C_{D,io} |\boldsymbol{U}_i - \boldsymbol{U}_w| (\boldsymbol{U}_i - \boldsymbol{U}_w) \,. \tag{4.5}$$

Surface ocean velocities are estimated using an iterative procedure developed by Kim et al. (2017) in a study of the ice-covered Amundsen Sea that assumes a fully developed Ekman spiral under sea ice. Equations (4.5) and (4.6) are solved, starting with $\boldsymbol{U}_w = 0$, until convergence is achieved, as defined by changes in both U_w^x and U_w^y smaller than 1 × 10^{-7} m s^{-1} with a maximum of 50 iterations:

$$\begin{pmatrix} U_w^x \\ U_w^y \end{pmatrix} = \begin{pmatrix} \cos(\pi/4) & -\sin(\pi/4) \\ \sin(\pi/4) & \cos(\pi/4) \end{pmatrix} \begin{pmatrix} \tau_{io}^{x} \Big/ \sqrt{\rho_w^2 f K_z} \\ \tau_{io}^{y} \Big/ \sqrt{\rho_w^2 f K_z} \end{pmatrix} , \tag{4.6}$$

where f is the Coriolis parameter. A constant value is used for the vertical eddy viscosity (K_z = 0.05 m^2 s^{-1}, per Kim et al. [2017]).

From total ocean stress (Eq. [4.3]), the Ekman upwelling rate, Ekman depth, and associated horizontal velocity components can be derived:

$$w_{\mathrm{Ek}} = \frac{1}{\rho_w f} \left(\frac{\partial \tau_o^y}{\partial x} - \frac{\partial \tau_o^x}{\partial y} \right) , \tag{4.7}$$

$$h_{\mathrm{Ek}} = \min\left(h_m, \sqrt{2K_z/|f|}\right) , \tag{4.8}$$

$$u_{\mathrm{Ek}} = \frac{\tau_o^y}{\rho_w f h_{\mathrm{Ek}}}, \qquad v_{\mathrm{Ek}} = -\frac{\tau_o^x}{\rho_w f h_{\mathrm{Ek}}}\,. \tag{4.9}$$

The Ekman depth (h_{Ek}) is taken to be the shallower of the float-observed mixed layer depth (h_m) and a formulation of the Ekman depth, following Pond and Pickard (1983). Valid estimates for the quantities involving $\boldsymbol{\tau}_o$ are obtained over all areas except for narrow bands along the sea ice edge and Antarctic continent, where ice motion vectors from the Polar Pathfinder product are undefined.

The salinity tendency from entrainment and Ekman upwelling are calculated together using the assumption that upwelling represents an upwards translation of the vertical salinity profile and a downwards translation under conditions of downwelling, as illustrated in Figure 4.3. First, the amount of vertical entrainment or detrainment is quantified from observations by looking forward to the mixed-layer depth of the following profile: $\Delta h_{m,\mathrm{ent}} = h_m(t_{i+1}) - h_m(t_i)$. This observed change is then adjusted based on the computed Ekman upwelling or downwelling rate (w_{Ek}) to produce an "effective" total entrainment: $\Delta h_{m,\mathrm{eff}} = \Delta h_{m,\mathrm{ent}} + w_{\mathrm{Ek}}\Delta t$, where Δt is the time between profiles. The effective entrainment will be positive under conditions of: (1) observed mixed-layer deepening and Ekman upwelling, (2) observed mixed-layer deepening and Ekman downwelling less than the observed entrainment, or (3) observed mixed-layer shoaling but Ekman upwelling greater than the observed detrainment. If the effective entrainment is negative, mixed-layer salinity remains unchanged. The inferred mixed-layer salinity tendency between the current and subsequent float profile owing to the combined effects of entrainment and Ekman upwelling or downwelling is computed by integrating the amount of salt entrained from below the base of the current mixed layer (Figure 4.3):

$$\frac{\partial S_m}{\partial t} \approx -w_{\mathrm{ent+Ek}}\frac{\Delta S}{h_m} = \frac{\left(\frac{1}{h_m + \Delta h_{m,\mathrm{eff}}}\int_{\mathrm{o\ m}}^{h_m+\Delta h_{m,\mathrm{eff}}} S(t_i)\,dz\right) - S_m(t_i)}{\Delta t}\,. \tag{4.10}$$

While this integration procedure offers the benefit of precision when applied to consecutive float profiles (see Section 4.3.3), a downside is that it precludes the possibility of later decomposing the combined tendency term into entrainment and Ekman components.

The contributions of mesoscale eddies to upwelling and downwelling are not represented here due to an inability to constrain their magnitude. While the influence of mesoscale eddies on the halocline depth in ice-covered regions can potentially be significant, as shown in a conceptual study of the Beaufort Gyre by Manucharyan and Spall (2016), impacts at more localized scales are uncertain. A recent study using eddy tracking applied to a multi-mission satellite altimetry product for the ice-covered Southern Ocean finds that mesoscale eddies are predominantly cyclonic with a generally smaller surface expression in areas of full sea ice cover, compared to areas with lower ice cover (Auger et al., 2023). This suggests a positive contribution to mixed-layer salinity, greatest along the ice edge, that is unaccounted for in this budget.

The horizontal advection and eddy diffusion terms are computed using a mixture of observations (including reanalysis data) and climatological lateral gradients in salinity, as discussed in Section 4.3.3). Changes in mixed-layer salinity owing to horizontal Ekman advection are computed using the Ekman velocity components ($\boldsymbol{u}_{\mathrm{Ek}}$) derived in Eq. (4.9), following Eq. (4.2). The background gradient in climatological salinity ($\nabla \boldsymbol{S}_{\mathrm{Ek}}$) is obtained from the interpolated WOCE/Argo Global Hydrographic Climatology (WAGHC; see Section 4.3.2), averaged within the Ekman layer defined by h_{Ek}. Advective tendencies are calculated using a second-order upwind scheme, interpolating bilinearly to the WAGHC salinity field along the advective azimuth from the float location. The length scale is chosen such that the Courant-Friedrichs-Lewy (CFL) condition ($|U\Delta t/\Delta x|$), which must be less than 1.0, is equal to 0.5. This procedure is repeated for every grid point within the uncertainty averaging region, with the results averaged to produce a final advective tendency.

Horizontal geostrophic advection is estimated similarly, following Eq. (4.2). Geostrophic current velocities ($\boldsymbol{u}_g$) are obtained from the interpolated CryoSat-2 dynamic ocean topography

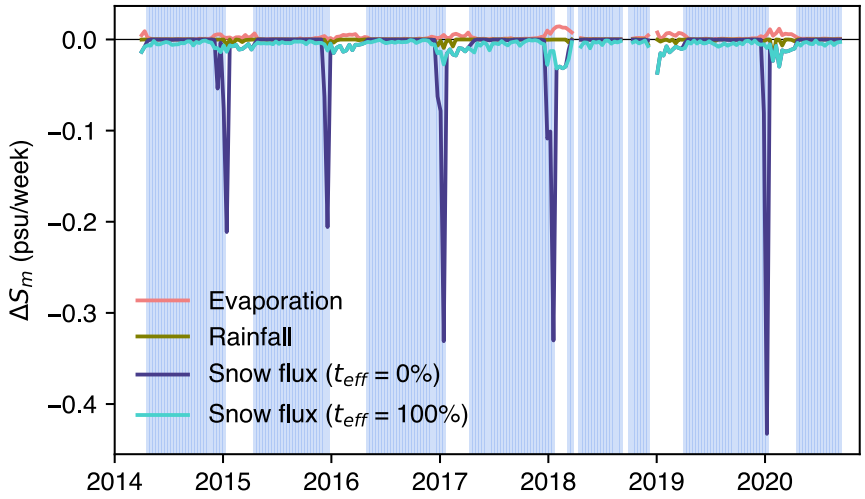

Figure 4.4: Freshwater fluxes from precipitation and evaporation for Argo float 5904183. The impact of snow release into the ocean on mixed-layer salinity changes (ΔS_m) is shown using the two extreme cases of no snow lost through leads ($t_{\text{eff}} = 0\%$, indicating all snowfall accumulates along the float trajectory and is released according to the stepwise ice melt parameterization) and all snow lost through leads ($t_{\text{eff}} = 100\%$, indicating no snow accumulates along the float trajectory).

product (Section 4.3.2; recall that climatological values are used outside of the period of available data from 2011–2016), and WAGHC salinity fields are averaged within the depth range of the mixed layer, defined by float-observed h_m.

Horizontal eddy diffusion, as defined in Eq. (4.2), is estimated using the Laplacian of WAGHC mixed-layer average salinity, calculated using a five-point stencil, again for each location within the uncertainty averaging region. The stencil grid size is set as the local east-west distance (i.e., longitude converted to distance) between adjacent grid cells, with values obtained using bilinear interpolation to the WAGHC field. Mesoscale eddy diffusivities (κ) are from the observational, depth-resolved product of Groeskamp et al. (2020; see Section 4.3.2), averaged within the mixed layer.

ERA5 reanalysis-derived evaporation is assumed to originate completely from the ice-free portion of grid cells, while rainfall over sea ice is assumed to percolate through the ice matrix and be deposited instantaneously into the ocean. The treatment of snowfall presents a greater challenge. Snow accumulates along the drift trajectories of sea ice and is primarily released to the

ocean upon complete ice melt in spring (e.g., Blanchard-Wrigglesworth et al., 2018; Liston et al., 2020; Lawrence et al., 2024; Campbell & Riser, in prep). However, some snow may enter the ocean sooner. While it has been generally assumed within the oceanographic literature that snow flux through leads is negligible (e.g., Martinson, 1990), field observations suggest that as much as half of all snow on Antarctic sea ice may be lost to leads during episodes of blowing snow (Leonard & Maksym, 2011). Based on simple empirical relationships between snow mass transport and wind speed as well as assumptions about the spacing and trapping ability of leads, Eicken et al. (1994) estimate that around 31 cm of snow may be blown in to leads annually in the Weddell Sea. As a crude representation of this process, we assume that a fraction t_{eff} of snowfall, representing the snow trapping efficiency of leads (Déry & Tremblay, 2004), is deposited instantaneously into the ocean through leads during periods of sea ice cover (Figure 4.4). Assumptions embedded in this partitioning include that leads are ubiquitous within the Antarctic sea ice pack—which is supported by a satellite retrieval of lead frequency (Reiser et al., 2019)—and that blowing snow episodes are frequent. The latter is substantiated by the low threshold wind speed for transport of snow (around 7-9 m s^{-1} under typical conditions; Li & Pomeroy, 1997), which implies much of deposited snow will be subject to wind transport prior to becoming "locked-up" due to metamorphic processes (Sturm et al., 1998).

The remainder of snowfall ($1 - t_{\mathrm{eff}}$) is allowed to accumulate along the float trajectory, simulating deposition on sea ice. This is an extreme approximation: while profiling floats in the Antarctic SIZ may remain relatively coupled to surface currents due to predominantly barotropic flow (Section 4.3.3), sea ice drift trajectories do not necessarily match the direction or magnitude of surface currents. Nonetheless, this approach offers a mechanism to track the accumulation of snow so that its release upon complete ice melt can be included in the salinity budget. Furthermore, this accumulation will occur over a realistic period of time—given that most Antarctic sea ice outside of the western Weddell Sea is first-year ice, rather than multiyear ice

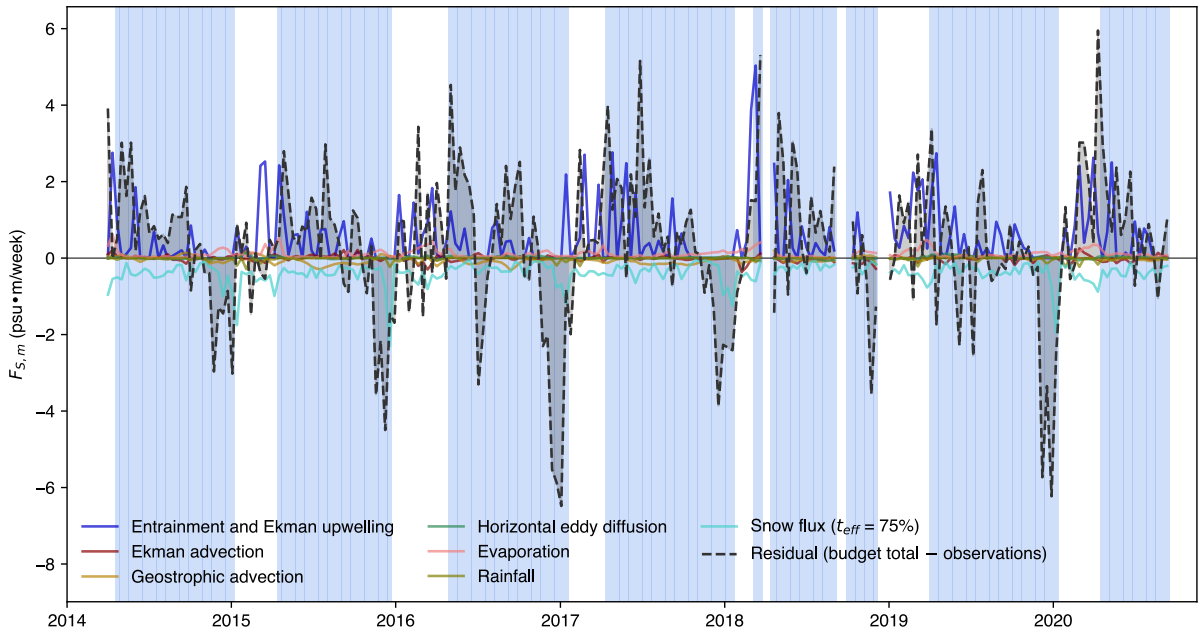

Figure 4.5: Mixed-layer salinity budget terms evaluated along the trajectory of Argo float 5904183. Salinity fluxes to the mixed layer are shown for each component of the mixed-layer salinity budget, assuming a lead trapping efficiency of $t_{\mathrm{eff}} = 75\%$. Vertical shaded bars represent periods of sea ice cover. Black shading inside the dashed lines indicates the budget residual, inferred to be predominantly freshwater fluxes owing to sea ice formation (positive) or melt (negative).

(Melsheimer et al., 2023)—and probably within a similar (or at least nearby) region to where the snow deposition that ultimately is received by the ocean actually occurred.

The following stepwise parameterization of snow release upon sea ice melt is implemented (see dark blue line in Figure 4.4 for the results of this approach, applied to Argo float 5904183): when observed sea ice concentration (A_{SIC}) at the float location decreases below 75%, one-quarter of accumulated snow is released into the ocean; when SIC decreases below 50%, one-third of the remaining snow is released; and finally, when SIC decreases below 25%, all the remaining snow is released. This simulates a gradual melt process consistent with the inhomogeneous patterns observed along a retreating sea ice edge. Note that other loss mechanisms for snow on sea ice, such as sublimation (e.g., Fichefet & Morales Maqueda, 1999; Chung et al., 2011), are neglected in this simple parameterization. Snow-ice formation—the conversion of snow to ice after the flooding of an ice floe with seawater and its subsequent freezing (Massom et al., 2001)—is also

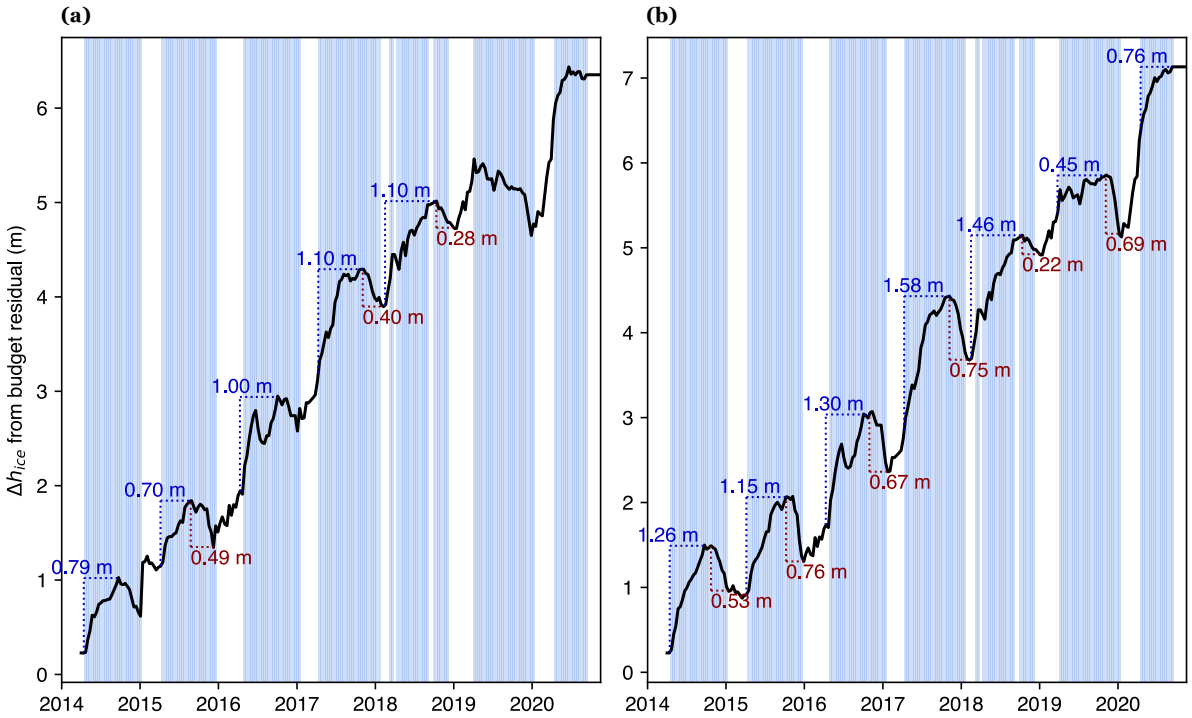

Figure 4.6: Accumulated sea ice thickness changes estimated along the trajectory of Argo float 5904183. Sea ice growth and melt have been inferred as the residual of the mixed-layer salinity budget (see Figure 4.5) and are accumulated over time to derive sea ice thickness changes, illustrated here for the two extreme cases of **(a)** no snowfall lost to leads (lead trapping efficiency of $t_{\mathrm{eff}} = 0\%$) and **(b)** all snowfall immediately lost to leads (lead trapping efficiency of $t_{\mathrm{eff}} = 100\%$). Vertical shaded bars represent periods of sea ice cover. Blue numbers indicate estimated net winter ice growth and red numbers indicate net spring ice melt, computed as the difference between seasonal maxima in accumulated ice thickness and the initial or final value, respectively, during the period of ice cover. Labels were not added in cases where subjective assessment of the seasonal variations indicated an indistinct or rapidly changing initial or final value. Note the different y-axis limits.

not represented, although the resulting mixed-layer salinification due to brine rejection will be interpreted as ice formation in the salinity budget.

As a final step, ice growth and melt are inferred as the residual of the mixed-layer salinity budget (Figure 4.5). To translate mixed-layer salinity fluxes into sea ice thickness changes (Figure 4.6), ice salinity is assumed to be 8 g kg^{-1} during the fall (growth) season and 5 g kg^{-1} during the spring (melt) season, with mid-winter values between fall and spring (6.5 g kg^{-1}), based on Antarctic average values simulated by Vancoppenolle et al. (2009). Periods of ice growth and melt are determined using the difference between SIC at the current float profile time and location and

SIC averaged across the previous six float profiles. When this difference is greater than +10%, growth is assumed to be occurring; when the difference is less than −10%, melt is inferred. Note that this parameterization is non-conservative because sea ice brine drainage flux throughout the winter is neglected, which may lead to a slight overestimation of ice formation rates in mid to late winter.

4.3.5 Climatological composites

Climatological composites for each salinity budget component, including the residual term, are created using the full set of along-trajectory budget estimates for the available floats. First, the salinity fluxes calculated at the float profile intervals are linearly interpolated to daily resolution. These time series are then binned by day-of-year, latitude, and longitude, collecting data in 2° latitude bands and 5° longitude bands. Lastly, the median of salinity fluxes within each bin is computed, requiring at least five estimates per bin. Resulting time series, composited over day-of-year only, are filtered using a 15-day centered rolling average for ease of visualization.

A circumpolar climatology of sea ice growth and melt rates is generated by coarsening (de-accumulating) the along-trajectory estimates for each float to daily resolution, then masking these time series to include only times and locations at which AMSR2 sea ice concentration was greater than 5%. After binning by day-of-year, latitude, and longitude, similar to above, the median sea ice thickness tendency value is computed for all bins containing at least five estimates. No smoothing is applied. Total annual net sea ice production, as well as growth-only and melt-only components, is estimated as the sum of the daily medians within each 2° latitude band.

4.4 Results and discussion

4.4.1 Along-trajectory mixed-layer salinity budget

Application of the Lagrangian mixed-layer salinity budget framework (Eq. [4.2]) to data from individual Argo floats, such as WMO ID 5904183 in the Ross Sea, gives insight into the relative magnitude of budget terms and their variations in time. Salinity fluxes resulting from the combined influence of entrainment and Ekman upwelling or downwelling ("effective entrainment") are always positive, representing salinity input to the mixed layer. Effective entrainment is highly episodic, with consecutive 10-day float cycles often showing high amounts followed by small (or zero) amounts of entrainment (Figure 4.5). This reflects the observed stepwise deepening of the winter mixed layer under sea ice, interspersed with occasional episodes of mixed layer shoaling, or detrainment (Figure 4.1b–c). If these bursts of effective entrainment were to occur in tandem with large values of the calculated budget residual, this would indicate sea ice formation happening concurrently with processes that tend to increase mixed-layer depth. Instead, however, the opposite is clearly seen in the record of float 5904183 (Figure 4.5), where entrainment mostly occurs out of phase with inferred sea ice formation (positive values in the budget residual). We infer that entrainment is predominantly caused by turbulent mixing under conditions of high wind speeds, characteristic of synoptic cyclones that tend to transport warm air into the Antarctic SIZ (Ward et al., 2023) and thus limit thermodynamic sea ice growth. Entrainment of warmer, saltier pycnocline water during storms will also reduce ice growth rates by increasing ocean-ice heat fluxes (E. A. Wilson et al., 2019), as observed in field measurements from the Weddell Sea (McPhee et al., 1996, 1999). In contrast, ice growth is favored during quiescent, colder conditions. The phasing observed in Figure 4.5 suggests that brine rejection makes a minimal contribution towards overall mixed-layer deepening despite some convective mixing associated with brine rejection.

Calculation of remaining budget terms shows that freshwater fluxes due to snow are substantial and continuous throughout the winter, assuming a high value for lead trapping efficiency of $t_{\mathrm{eff}} = 75\%$ (Figure 4.5). Decreasing lead trapping—thus increasing snow accumulation—would result in a stronger pulse of reserved freshwater from snow released upon spring ice melt (Figure 4.4) and therefore reduced estimates of both sea ice formation and melt. In other words, a temporal distribution of snow release to the ocean that is skewed towards the end of winter will lead to a more muted seasonal cycle of inferred ice growth and melt, as illustrated in Figure 4.6a (all snowfall accumulates) in comparison to Figure 4.6b (all snowfall is lost to lead trapping). The two extreme treatments of snow fluxes lead to estimates for sea ice thickness changes that can vary by more than 50% (e.g., 0.40 m vs. 0.74 m of ice melt estimated in late 2017). The sensitivity of the budget residual to the treatment of snow highlights the important role of this part of the coupled ocean–ice–snow system and the need to better constrain the presently uncertain magnitude of snow loss processes like lead trapping—parameterized here in a rudimentary fashion—as well as blowing snow sublimation, which is not represented here. It is also worth noting that the inability to compute Ekman-related terms (upwelling and advection) near the sea ice edge due to an absence of Polar Pathfinder sea ice drift velocity data results in some periods in which the budget residual—and thus sea ice growth and melt—cannot be calculated (Figure 4.5).

The feasibility of inferring sea ice formation and melt from the mixed-layer salinity budget residual is supported by a clear pattern of positive residual values during the first two-thirds of each winter, indicating brine rejection from ice growth, and negative residual values during the latter third, indicating freshwater input from ice melt (Figure 4.5). Translating these salinity fluxes into equivalent sea ice thickness changes yields reasonable values on the order of 1 m of annual net ice growth and 0.5 m of net ice melt (Figure 4.6), albeit with significant interannual variability and high sensitivity to the treatment of snow fluxes, as discussed. These estimates derived from measurements by float 5904183 indicate that the central Ross Sea is a region of

variable annual net sea ice export with a multiyear average of around 0.5 m, reflected in the upwards trending curves for accumulated sea ice thickness changes. This appears qualitatively consistent with the Haumann et al. (2016b) model–data synthesis estimates of net freshwater fluxes, which show net ice export as weakly favored in the central Ross Sea.

The Lagrangian budget methodology also allows for the detection of specific events such as a brief ice melt episode in mid-2016, which can be diagnosed from the drop in area-averaged sea ice thickness retrieved by SMOS along the float trajectory (Figure 4.1a; note that a broad region featuring even larger amounts of ice thinning is seen in the vicinity of the float track [not shown]), mixed-layer shoaling in the float observations (Figure 4.1b–c), and 0.2–0.3 m of rapid ice thinning inferred from the salinity budget (Figure 4.6). Such a signal could not be diagnosed in the traditional budget approach that relies on climatological gridded fields (Section 4.3.3).

4.4.2 Circumpolar mixed-layer salinity budget

Figure 4.7 presents a climatological circumpolar mixed-layer salinity budget for the Antarctic SIZ south of 61°S constructed using all available float observations (Section 4.3.5). The partitioning between budget terms reveals the sea ice growth and melt signal (shaded curve) to be the dominant signal in nine out of 12 months, accounting for nearly half (46%) of annual changes in mixed-layer salinity. The seasonal cycle exhibits a pronounced asymmetry with a prolonged, eight-month-long net growth phase from February to September that transitions to rapid melt in mid-October (Figure 4.7a). This is consistent with previous findings from the Southern Ocean State Estimate (SOSE), a data-assimilating model, which show brine rejection continuously densifying water masses within the neutral density range of Upper Circumpolar Deep Water for two-thirds of the year, followed by freshwater input transforming lighter intermediate and mode waters in a briefer pulse of sea ice and snow melt (Abernathey et al., 2016). This asymmetric cycle stands in contrast to the nearly symmetric seasonal cycle of Arctic sea ice. One theory suggests this asymmetry may originate from regular seasonal variations in the westerly and easterly wind

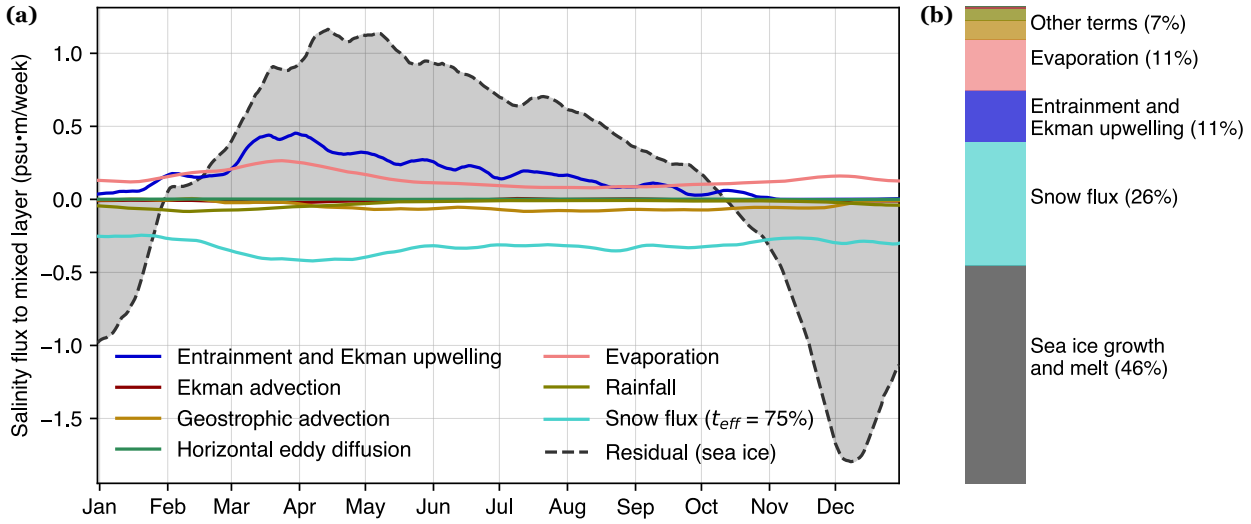

Figure 4.7: Climatological mixed-layer salinity budget for the Antarctic SIZ south of 61°S. (a) Composites for each budget term are calculated using interpolation in time and binning by day-of-year, latitude, and longitude; time series shown are filtered using a 15-day centered rolling average (see Section 4.3.5). A lead trapping efficiency of t_{eff} = 75% is assumed. **(b)** Relative contributions of each budget term to annual changes in mixed-layer salinity, calculated as the annual average of each budget term's magnitude (i.e., its absolute value) divided by the summed magnitudes of all budget terms.

belts encircling Antarctica, which serve to prolong the fall freeze-up and accelerate the spring melt-back of sea ice (Eayrs et al., 2019, 2020). Other work, however, indicates that the asymmetry is primarily driven by the non-sinusoidal seasonal cycle of incident solar radiation (Roach et al., 2022). The shift that we observe from SIZ-average net ice formation to net ice melt in mid-October (Figure 4.7a) occurs nearly a month after the switch from a positive rate of change in Antarctic sea ice extent to a negative rate of change, shown by Eayrs et al. (2019) to take place in the second half of September. This may reflect the persistence of conditions favorable to ice growth at high latitudes even after the ice edge has begun to retreat, itself a lagged indicator of net ice melt along the ice edge.

The climatological budget indicates that the remaining budget after sea ice fluxes is split roughly equally between contributions from snow fluxes (26%) and all other processes. Of these, most important are the combined effects of entrainment and Ekman upwelling (11%)—which are greatest in early winter—and evaporation (11%)—which shows a more muted seasonal cycle,

lowest in mid-winter (Figure 4.7a–b). Our results align closely with those of Pellichero et al. (2017), who employed the conventional method of deriving a mixed-layer salinity budget from gridded climatologies of mixed-layer properties created by interpolating sparse observations. Their analysis similarly shows salinity fluxes from entrainment peaking in March, a negligible contribution from Ekman advection, and a pronounced seasonal cycle controlled by freshwater fluxes. However, notable differences in both methodology and results exist beyond those outlined in Section 4.3.3. Pellichero et al. additionally incorporated observations from instrumented seals and ships, accounted for vertical eddy diffusion but omitted geostrophic advection as a budget term, and did not explicitly distinguish between sources of freshwater fluxes—whether from sea ice, precipitation, or evaporation. This final aspect of their approach, which relied on five model-based products to represent the combined freshwater flux term, limits the potential for direct comparison.

In our budget, freshening from snowfall counteracts salinification driven by both evaporation and the entrainment or upwelling of saltier pycnocline waters, resulting in a net effect that appears to be relatively minor—comparable in magnitude to advection and eddy diffusion combined. This finding raises the question of whether the budget could be constructed from entrainment, Ekman upwelling, and evaporation and precipitation alone. It is reasonable to consider neglecting the small advective and diffusive contributions, for which our methodology requires climatological fields of upper-ocean salinity and eddy diffusivity and, in some years, climatological geostrophic velocities. Doing so would allow the budget to be constructed solely using contemporaneous observations, remote sensing, and reanalysis. However, while an accurate budget probably could be constrained in many regions without including the advective or diffusive terms, this is not the case in regions with more energetic flows. For instance, Meredith et al. (2011) found that sea ice formation rates inferred from salinity measurements collected by an elephant seal near the South Orkney Islands largely reflected advective influences from upstream conditions in the northwestern Weddell Sea. Similarly, under-ice profiling float

observations from the Ross Sea continental shelf demonstrate that seasonal variations in upper-ocean salinity cannot be explained without accounting for the lateral advection of meltwater (Porter et al., 2019). These examples serve as cautionary reminders of the hazards associated with oversimplified budgets. Nonetheless, it remains uncertain whether advective and diffusive terms can be estimated with sufficient accuracy to make a useful contribution to a Lagrangian budget, or if their inclusion merely introduces additional noise—an issue that warrants further investigation. One potential solution is to derive these terms from data-assimilating models, such as SOSE (Mazloff et al., 2010; Verdy & Mazloff, 2017). While this would compromise the observational "purity" of the budget, it could offer stronger constraints on certain processes.

4.4.3 Sea ice formation and melt rates

Figure 4.8 displays a mapped monthly circumpolar climatology of sea ice growth and melt, derived from along-trajectory mixed-layer salinity budgets spanning all 336 under-ice Argo floats. The asymmetric seasonal cycle highlighted in Figure 4.7a is evident, along with a notable meridional progression of ice melt, where earlier and more rapid melting occurs at lower latitudes. While some variability and noise are present across grid cells—particularly near the sea ice edge—the broader pattern is striking: widespread sea ice formation of approximately 1 cm d^{-1} from April to July, minimal ice growth across most of the SIZ from August to October, and melt rates of 1–2 cm d^{-1} through January, with higher rates concentrated along the retreating ice edge. This product marks the first circumpolar climatology of Antarctic sea ice growth and melt rates based on in situ observations, rather than relying primarily on remote sensing or model-derived estimates.

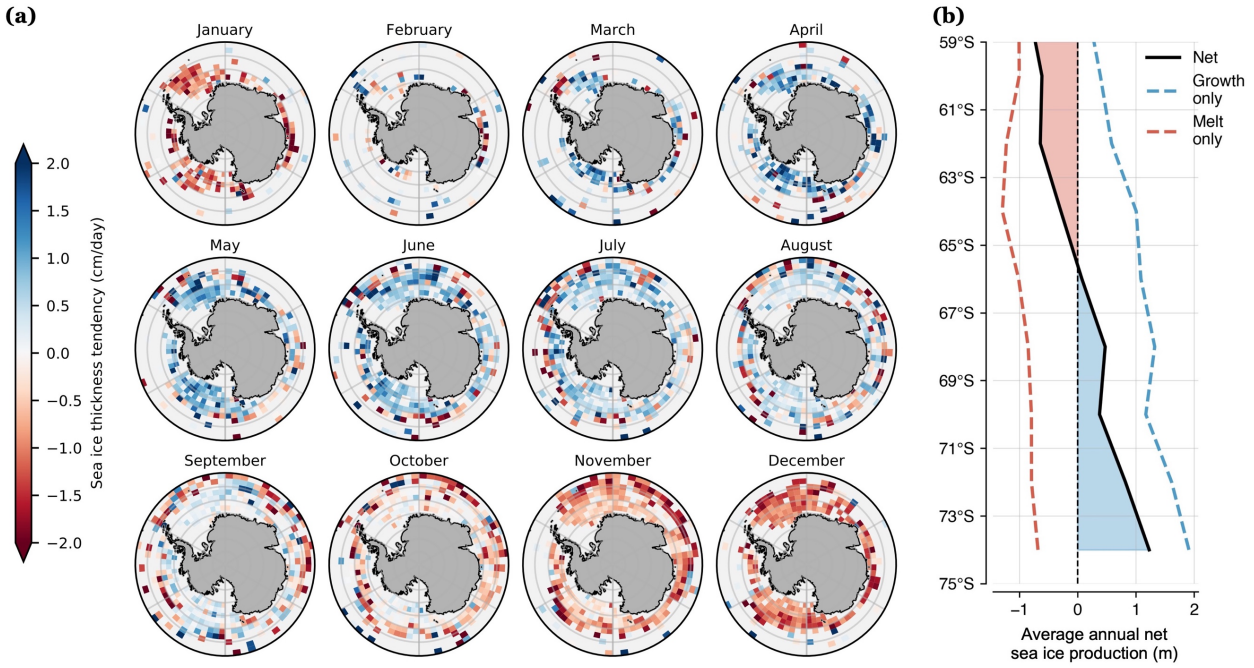

Figure 4.8: Climatology of sea ice growth and melt inferred from Argo float observations. (a) Monthly average sea ice thickness tendencies estimated from Lagrangian salinity budgets derived along the drift trajectories of 336 under-ice Argo floats. Composites for each budget term are calculated using interpolation in time and binning by day-of-year, latitude (within 2° bins), and longitude (within 5° bins; see Section 4.3.5). A lead trapping efficiency of $t_{\text{eff}} = 75\%$ is assumed. **(b)** Zonally averaged annual net sea ice production estimates (black line), the balance of total brine rejection from ice growth (dashed blue line) and freshwater fluxes from ice melt (dashed red line).

Extensive melt within the interior of the ice pack during November and December, not just along the contracting ice edge, suggests a spring melt process that may be more spatially distributed than traditionally understood (Figure 4.8a). This “inside-out” melting, which is not necessarily apparent from sea ice concentration, becomes abruptly visible each year as contiguous interior areas of likely thinner sea ice (not shown) break out into what might be termed “false open-ocean polynyas.” Unlike true open-ocean polynyas maintained by convective mixing, these ice-free regions are presumably generated by warming air temperatures and increased shortwave radiation, with lateral melt amplified by the ice–albedo feedback. These rapidly growing spring polynyas commonly emerge above Maud Rise in the Weddell Sea, as seen following the mid-winter open-ocean polynyas of 2016 and 2017 (Campbell et al., 2019), as well as along the Ross Sea Polynya and parts of the East Antarctic coastline. As seasonal melt progresses, these interior

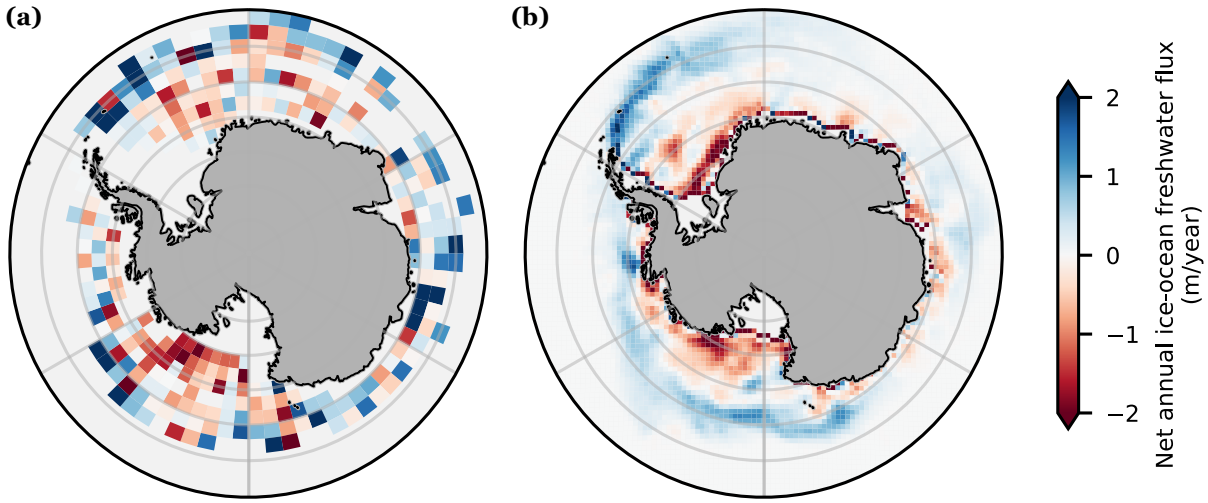

Figure 4.9: Comparison of annual net freshwater fluxes from sea ice formation and melt derived from Argo floats and a model–observation synthesis. (a) Annual total ice-related freshwater fluxes estimated from Lagrangian salinity budgets derived along the drift trajectories of 336 under-ice Argo floats, accumulated from Figure 4.8. **(b)** Comparable annual total ice-related freshwater fluxes from a data-assimilating model, bias-corrected by Haumann et al. (2016b) using observations and remote sensing data. Note that snow-ice conversion is included in both estimates of sea ice freezing.

ice-free areas expand and coalesce with the open ocean. This phenomenon implies a marked seasonal cycle in sea ice thickness, one that is not readily apparent from seasonal averages or thickness distributions derived from remote sensing estimates (Kacimi & Kwok, 2020; Fons et al., 2023).

Consistent with the model–observation synthesis product of Haumann et al. (2016b; Section 1.3.2), we find annual net sea ice production near the Antarctic continent that transitions to net annual melt at around 65°S (Figure 4.8b). These annual net values represent the balance of components that are substantially larger—for example, approximately 2 m of ice production and 1 m of melt near the Antarctic continent, for a net annual ice production of 1 m. This gradient in net ice production is maintained by the generally northward, wind-driven transport of sea ice (P. R. Holland & Kwok, 2012) as well as the predominance of divergent ice drift at higher latitudes, which spurs new ice formation in areas of open water (P. R. Holland & Kimura, 2016).

Comparing our annual net freshwater fluxes with those from a data-assimilating model, bias-corrected by Haumann et al. (2016b)—one of the most sophisticated estimates of sea ice-related freshwater fluxes presently available for the Southern Ocean (Section 4.3.2)—shows moderate qualitative agreement, particularly in the interior of the Ross Sea and the northern edge of the Weddell Sea (Figure 4.9). The estimates differ, however, in the northern Ross Sea, where the float-based estimates indicate net ice formation in an area where the Haumann et al. product suggests net ice melt; along the East Antarctica coastline, where the floats estimate more intense and spatially extensive ice melt; and in the interior of the Weddell Sea, where the floats infer greater net ice formation. Notably missing in our float-based estimates are sea ice formation within coastal polynyas (Tamura et al., 2008) and areas of multiyear ice, which are largely in the western Weddell Sea (Melsheimer et al., 2023). These omissions are a consequence of the limitations of Argo floats, which cannot profile in shallow continental shelf regions due to their 1,000-m drift depth (unless parked on the seabed; Porter et al., 2019), and their limited battery capacity, which limits survival during multiyear drift under perennial sea ice. While these limitations can account for the absence of significant ice formation along the Antarctic continent in our float-based estimates, present in the Haumann et al. product, they cannot explain the discrepancies observed in the Weddell Sea interior and the outer margin of the Ross Sea. It is possible that differences in the nominal time period for each product—1982 to 2008 for the model–observation synthesis and approximately 2008 to 2022 for our float-based estimates—could play a role in these patterns.

4.5 Conclusions

In this study, we adapt the conventional method of constructing mixed-layer budgets from gridded sparse observations to enable the direct estimation of budget terms along the drift trajectories of Argo floats beneath Antarctic sea ice. This Lagrangian approach provides an interannually resolved quantification of budget terms for individual floats, allows precise

calculation of entrainment fluxes using the geometry of salinity profiles, and facilitates the investigation of specific, time-limited phenomena such as intermittent sea ice thinning events. We demonstrate that reasonable estimates of sea ice formation and melt rates can be inferred from the substantial budget residual, though we also highlight its sensitivity to uncertainties in the magnitude and timing of freshwater fluxes from snow. By applying this Lagrangian mixed-layer salinity budget methodology to nearly two decades of under-ice Argo observations, we produce a climatological budget that aligns with prior estimates, while providing the first observationally grounded estimate of sea ice freezing and melt across the Antarctic SIZ. Key insights from this new climatology include a pattern of "inside-out" spring melt, which is more spatially extensive than what can be diagnosed from sea ice concentration alone, as well as noticeable differences in freshwater fluxes compared to previous estimates, particularly in the interior of the Weddell Sea and along the outer margin of the Ross Sea.

Several opportunities exist to improve and expand upon the methodology presented here. For one, the linearly interpolated float drift trajectories under sea ice represent an acceptable approximation given the coarse spatial binning of results, but more realistic interpolation schemes exist for float trajectories that aim to conserve potential vorticity (Chamberlain et al., 2018) or follow isobaths (K. Yamazaki et al., 2020). A major assumption of this along-trajectory budget approach is that the advective component of the material derivative, due to the float drift, is small and can be neglected (Section 4.3.3). This could be tested using an observing system simulation experiment (OSSE) with a high-resolution ocean–ice model and a correction term for float advection introduced if necessary. Furthermore, for completeness in regions with little to no float coverage—particularly areas of high ice production near the Antarctic coast that may contribute about three-quarters of total Southern Ocean-wide brine rejection (Haumann et al., 2016b)—the estimates of freshwater fluxes could benefit from incorporating existing estimates of ice production in coastal polynyas (Tamura et al., 2008) or instrumented seal observations from the Marine Mammals Exploring the Oceans Pole to Pole (MEOP) compilation (Roquet et al., 2014;

Treasure et al., 2017; Siegelman et al., 2019). Key challenges with incorporating the latter data include the deep (>500 m) mixed layers on the continental shelf, which sometimes extend to the seafloor; fast movement and irregular sampling intervals; and the possibility of biased sampling (e.g., preferential foraging in polynyas or thin-ice areas). One benefit of the tagged seal data is that all vertical profiles feature GPS position fixes, so interpolation of profile locations would not be needed. Lastly, a newer, higher-resolution altimetry product that extends the record of geostrophic velocities in the ice-covered Southern Ocean (Auger, Prandi, et al., 2022; Auger, Sallée, et al., 2022) could supplant or replace the CryoSat-2 product currently in use.

Ultimately, the full potential of the sea ice growth and melt rates estimated here will be realized only if they can be accurately integrated over time and space to calculate climatological sea ice thicknesses, enabling applications ranging from model assimilation to the validation of remote sensing retrievals. This should be possible using a framework that accumulates ice thickness changes along Lagrangian drift trajectories of sea ice, although harmonizing estimates from observations across different years could pose difficulties. Paired with snow accumulation estimates along the same ice drift trajectories from a recently developed model reconstruction (Campbell & Riser, in prep), this approach could also constrain rates of snow-ice conversion. This process, likely ubiquitous in the Southern Ocean, occurs when heavy snow loads cause isostatic flooding of ice floes (Massom et al., 2001). Additionally, the associated salt fluxes into the ocean from brine rejection during snow-ice formation could be estimated.

In the past eight years, rapid changes in Antarctic sea ice extent have illuminated significant gaps in our understanding of interactions between the Southern Ocean and its sea ice cover (Eayrs et al., 2021; Purich & Doddridge, 2023; J. Wang et al., 2024). One such gap is the current reliance on observed sea ice concentration and extent as diagnostic variables for sea ice change. These are of limited utility when examining oceanic influences such as trends in Ekman upwelling of warm subsurface waters (e.g., Meehl et al., 2019) that may modify not only where ice is present, but also how quickly it grows and decays. While sea ice thickness estimated from a data-assimilating

model suggests that Southern Ocean ice thickness covaries well with concentration and extent on multidecadal time scales (Massonnet et al., 2013), observing this “third dimension” of ice thickness remains critical for a fuller understanding of interannual sea ice change. Continuous, year-round measurements from autonomous ocean observing platforms, such as Argo profiling floats, offer the potential to provide new insights into the sensitivity of Antarctic sea ice growth and melt to future changes in the ocean, atmosphere, and snow cover.

Chapter 5:

CRACKING THE CODE: AN EVIDENCE-BASED APPROACH TO TEACHING PYTHON IN AN UNDERGRADUATE EARTH SCIENCE SETTING

This chapter is reproduced from:

Campbell, E.C.*, Christensen, K.M.*, Nuwer, M., Ahuja, A., Boram, O., Liu, J., Miller, R., Osuna, I., Riser, S.C. (2024). Cracking the code: An evidence-based approach to teaching Python in an undergraduate earth science setting. *Journal of Geoscience Education*, in press. doi:10.1080/10899995.2024.2384338. (* *Co-first authors, reflecting equal contributions to this work*)

5.1 Abstract

Scientific programming has become increasingly essential for manipulating, visualizing, and interpreting the large volumes of data acquired in earth science research. Yet few discipline-specific instructional approaches have been documented and assessed for their effectiveness in equipping geoscience undergraduate students with coding skills. Here we report on an evidence-based redesign of an introductory Python programming course, taught fully remotely in 2020 in the School of Oceanography at the University of Washington. Key components included a flipped structure, activities infused with active learning, an individualized final research project, and a focus on creating an accessible learning environment. Cloud-based notebooks were used to teach fundamental Python syntax as well as functions from packages widely used in climate-related disciplines. By analyzing quantitative and qualitative data from surveys, online learning platforms, student work, assessments, and a focus group, we conclude that the instructional

design facilitated learning and supported self-guided scientific inquiry. Students with less or no prior exposure to coding achieved similar success as peers with more experience, an outcome likely mediated by higher engagement with course resources. We believe that the constructivist approach to teaching introductory programming and data literacy that we present could be broadly applicable across the earth sciences and in other scientific domains.

5.2 Introduction

Data programming has become a foundation of research in today's geoscientific disciplines. As the volume and size of data sets have steadily increased, so have the complexity and ubiquity of the computational techniques used for analysis and visualization. Some argue that innovation in earth science research will increasingly be driven by one's competency in translating ideas into computer code (Jacobs et al., 2016).

The field of oceanography is no exception to this "data tsunami," with more hydrographic casts collected in the past two decades than over the previous 100 years (Brett et al., 2020). Unprecedented collaborative initiatives such as the Argo profiling float array (Wong et al., 2020), the National Science Foundation's Ocean Observatories Initiative (OOI; Greengrove et al., 2020), and remote sensing platforms such as satellite altimeters (Scheick et al., 2023) are continuously adding to expansive, publicly available data sets. In addition to these observational programs, hard drives at institutions across the world are being filled with terabytes of data generated by numerical simulations. From highly resolved ocean general circulation models to the lower-resolution global climate models assessed in the Intergovernmental Panel on Climate Change (IPCC) reports, the natural ocean is being reproduced with ever-increasing fidelity (Haine et al., 2021). The resulting challenges in accessing and analyzing these data require new computational tools that enable truly open science, further motivated by the notion that "research conducted openly and transparently leads to better science" (National Academies of Sciences, Engineering,

and Medicine, 2018). At the same time, modeling and observation-focused oceanographers use highly unstandardized computational methods that may deviate from best practices in software engineering, as highlighted in an ethnography of oceanographers' programming practices (Kuksenok et al., 2017).

Discipline-specific computational coursework and data literacy are thus a critical part of a modern oceanographic undergraduate curriculum, and we infer the same applies across many geoscience disciplines. While students can collect and analyze small-scale data sets through hands-on fieldwork and labs that are common elements of undergraduate earth science curricula, working with larger, professionally collected data sets may require familiarity with a programming language (Kastens et al., 2015). Historically, introductory programming education has been the responsibility of computer science departments, with a focus on data structures and algorithms. Geoscience-specific programming instruction will necessarily reflect distinct goals and tools compared to computer science (Grapenthin, 2011) or data science (R. E. Anderson et al., 2015; Lasser et al., 2021), namely, the use of coding to derive insight into natural systems through mathematical manipulation, visualization, and interpretation of idiosyncratic data, often in the time and space domains. Yet formal scientific computing instruction is often absent in earth science curricula, including oceanography (Old, 2019), except for highly scaffolded modules that employ coding in courses where programming is not the primary focus (e.g., Rowe et al., 2021). Even in courses that more extensively utilize programming within activity modules, such as those distributed by Project EDDIE (Environmental Data-Driven Inquiry and Exploration), pre-written code is usually provided to students (O'Reilly et al., 2022). In this void, brief but intensive hands-on workshops like those offered by Software Carpentry (https://software-carpentry.org; Wilson, 2016), Data Carpentry (https://datacarpentry.org/; Irving, 2019), scientific societies (e.g., Arms et al., 2020), and academic institutions (e.g., Timms & Guyon, 2023) have provided crucial training to young scientists. These short workshops, however, give learners limited opportunities to apply new coding skills to their own research in a supervised setting. In lieu of formalized

instruction, many earth science students teach themselves programming during research experiences or in graduate programs, which can lead to the propagation of ad hoc, inefficient, and outdated practices.

Incorporating programming into an earth science curriculum additionally opens the door to a constructivist approach to teaching scientific concepts—one that encourages students to use experimentation and self-guided inquiry to build on previous learning, construct new knowledge, and engage in critical reflection (Hadjerrouit, 2008; Bada, 2015). The iterative, reflective process of writing and refining scientific code makes it naturally suited to this individualized model of learning. In practice, a constructivist pedagogy often involves active techniques such as project-based investigation, cooperative learning, and inquiry-based activities. These have been shown to improve student competencies in information recall, analysis, and quantitative reasoning in a large-enrollment introductory oceanography course (Yuretich et al., 2001).

Throughout higher education, there is an increasing recognition that effective teaching requires a focus on active learning, which can be described broadly as students engaged in their learning due to the use of intentional teaching practices (Prince, 2004). Active modalities include those designated as "high-impact educational practices" (Kuh et al., 2017). Yet traditional lecturing still represents about three-quarters of class time across STEM undergraduate and graduate courses today (Stains et al., 2018). In a survey of almost 200 undergraduate oceanography professors, for example, three-quarters indicated that they use data in their instruction but are most likely to teach using lectures, rather than creating opportunities for active inquiry (McDonnell et al., 2015). There is strong evidence that using active learning techniques increases students' understanding and retention of material in STEM courses, with disproportionate benefits for underrepresented students and students who learn in different ways (Haak et al., 2011; Freeman et al., 2014; Theobald et al., 2020). One reason these strategies appear to be effective is that they often require an instructor to implement more structure in their course through, for example, regular and intensive practice using scaffolded activities (Haak et al., 2011).

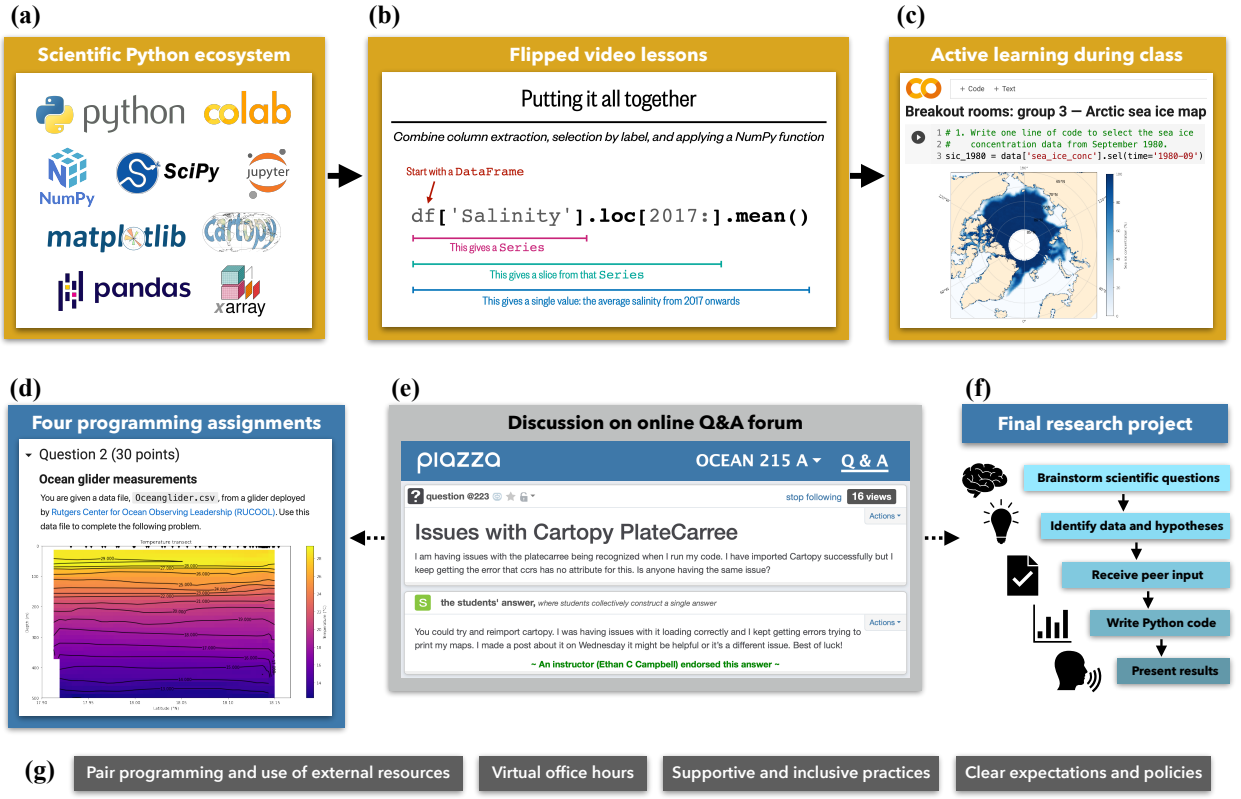

Figure 5.1: Key course elements: (a) Python platforms and software libraries that were taught (see Supplementary Table 5.3 for specific functions, operators, and methods); **(b)** flipped video lessons, with a slide demonstrating how colors, fonts, design elements, and a minimal working example help to explain Python syntax; **(c)** class sessions focused on active learning, showing a completed portion of a group activity; **(d)** programming assignments, with an illustrative plot; **(e)** discussion on the Piazza Q&A forum, showing a student question and a peer answer endorsed by an instructor; **(f)** the final research project, represented as the sequence of assigned components; **(g)** underlying course elements that fostered an effective learning environment. Solid arrows indicate the progression from foundational material (a) to content delivery (b) and application (c); dashed arrows indicate the contributions of discussion forum engagement (e) to students' work on assignments (d) and the final project (f).

Evidence supports the efficacy of active learning strategies in geoscience classrooms— particularly peer instruction, case studies, and problem-based activities (McConnell et al., 2017).

Embedding computing skills into a geoscience curriculum faces the challenge of introducing students to unfamiliar skills such as algorithmic thinking and overcoming a steep learning curve, similar to teaching a foreign language (Jacobs et al., 2016). Perhaps for these reasons—as well as a lack of accessible software tools and insufficient computational power in previous decades (Hays et al., 2000)—existing examples of courses using geoscience data have often focused on interactive

online modules, portals, or widgets that are constrained in their data sets and capabilities (e.g., Ellwein et al., 2014; Klug et al., 2017; Greengrove et al., 2020). Software such as Microsoft Excel or specialized tools like Ocean Data View face similar limitations. In comparison, programming skills are more versatile, enabling the analysis of virtually any data set from any domain and empowering students to conduct independent or mentored research projects.

Our study reports on an evidence-based redesign of an undergraduate oceanography course that teaches introductory Python programming and data analysis techniques. In subsequent sections, we highlight key course elements (summarized schematically in Figure 5.1) and assess the efficacy of the redesign from the standpoint of student engagement and learning.

5.3 Implementation

5.3.1 Course history and development

"Methods of oceanographic data analysis" (OCEAN 215) has been taught annually as a degree requirement in the School of Oceanography at the University of Washington since its establishment in 2015. It was the first introductory Python course offered by the department. Over a ten-week quarter, classes met in person two times each week in two-hour sessions that featured a mix of traditional lecturing and dedicated homework time. The course was well-received by students, who rated it as "very good" (4 on a scale from 1–5) across a variety of metrics in final course evaluations from 2015, 2016, 2017, and 2019 (Figure 5.2), and has been perceived as demanding relative to other courses in students' curricula (see Supplementary Figure 5.8).

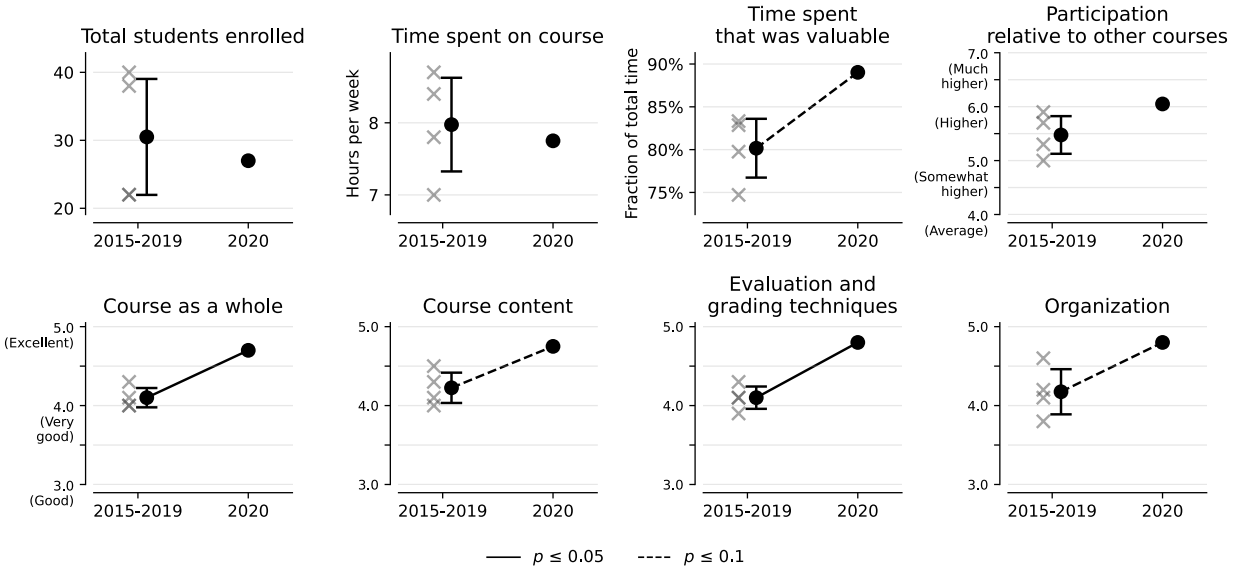

Figure 5.2: Selected metrics from anonymous final student evaluations in 2015, 2016, 2017, 2019, and 2020. Metrics shown are class medians for 2015, 2016, 2017, and 2019 (gray crosses), except for "Total students enrolled"; 2015–2019 mean or 2020 class median (black points); and 2015–2019 standard deviation (bars). Changes from 2015–2019 to 2020 were tested for a significant increase at the 95% (solid line) or 90% (dashed line) confidence level using a one-tailed *t*-test for all metrics except for "Total students enrolled" and "Time spent on course," which were tested for a significant change using a two-tailed *t*-test (no significant change was identified for either). For more details, see Evaluation section "Surveys and evaluations." An absence of a line connecting the 2015–2019 and 2020 data indicates no statistically significant improvement or difference. Note that *y*-axes have been truncated from the full 1–5 scale ("Very poor" to "Excellent") or 1–7 scale ("Much lower" to "Much higher"). For the full set of evaluation metrics, see Supplementary Figure 5.8.

However, instructors of other oceanography courses reported that many students who completed OCEAN 215 later had difficulty with core Python programming tasks. A review of past senior theses—projects in which students execute original research—revealed that students often reverted to less versatile, non-coding solutions like Microsoft Excel and Ocean Data View. Given that former students rated the course content as highly useful in evaluations (see Supplementary Figure 5.8), we speculate that their subsequent hesitancy in applying Python skills was due to a lack of recurrent exposure in the curriculum (see also Conclusions section "Impact") as well as weaknesses in the course design. Possible shortcomings include an overreliance on non-interactive lectures, a lack of student-driven inquiry, assignments' use of unrealistically clean scientific data, and course elements that were not reflective of current scientific Python practices.

Table 5.1: Core topics and concepts taught in OCEAN 215. Topics listed here are not necessarily in chronological order as taught in the course, and class time was not necessarily allocated in equal proportions to each topic.

Topic	Key concepts and skills
Why code in Python?	The power of programming is its versatility. Python is open source, stable, popular, free, and ideal for scientific data analysis. Google Colab offers advantages in a classroom setting compared to other programming environments.
Variables and object types	Variables store Python objects, which include numbers, booleans, strings, lists, tuples, dictionaries, and module-specific objects. Objects can be altered, indexed, sliced, iterated over, or used in mathematical operations. Assigning meaningful variable names makes for clearer code.
Logical operations and control flow	Objects can be compared using logical operations (and, or, is/equals, greater/less than, in, not). Loops and if-statements facilitate repetitive and conditional actions.
Packages and functions	Installing and using packages extends the capabilities of Python. Built-in, imported, and user-created functions accomplish common tasks and make for more compact, efficient code. Online documentation can be used to understand functions' arguments and outputs.
Data files	Oceanographic data are often stored in CSV and netCDF files, which can be read into Python, displayed, indexed, sliced, and manipulated using functions in the NumPy, Pandas, and Xarray packages. Real-world data sets can be obtained from public repositories and frequently contain messy or missing data.
Working with data	Data can be stored in multi-dimensional NumPy arrays and labeled structures specific to the Pandas and Xarray packages. These packages, as well as others like SciPy, have functions that average, sort, group, correlate, resample, smooth, regress, interpolate, and perform other computations on the data. Understanding common error types and tracing errors from their line of origin allow for methodical debugging of code.
Plotting	Line, scatter, bar, contour, pseudocolor, and other types of plots available from the Matplotlib package can be used to visualize data. Geospatial data can be projected onto maps using Cartopy. Appropriately customizing and labeling a plot is essential for interpretability.
Scientific skills	The modern scientific method is driven by data exploration, but also relies on traditional research skills like formulating hypotheses, interpreting the scientific significance of visualizations, effectively communicating results, and giving and receiving feedback from peers and mentors.

The course was restructured (Figure 5.1 and Table 5.1) and subsequently co-taught during a 10-week quarter in 2020 by two graduate students, both of whom had served as TAs in past years. Twenty-five undergraduate students completed the course, a typical class size (Figure 5.2). All except two were oceanography majors or later declared an oceanography major. The majority were third-year students, with other years represented, reflecting the flexibility of the oceanography curriculum. To ensure the broadest possible audience for the course, previous coding experience was not required and a prerequisite of one quarter of calculus from previous iterations of the course was removed. Elements retained from previous iterations included the

basic format of four structured programming assignments as well as twice-weekly classes and office hours; however, the latter were conducted virtually rather than in a physical classroom.

In 2020, the COVID-19 pandemic forced a swift transition to virtual instruction. The timing of this course in Autumn 2020, however, allowed for careful planning of an online learning framework, rather than the forced adoption of emergency remote instruction necessary in the first half of 2020 (Hodges et al., 2020; Donham et al., 2022). Nonetheless, disruptions outside of the classroom were still present: students were isolated on campus or sequestered at home with family, mental health declined, and some became sick or had loved ones fall ill (Furman & Moldwin, 2021). With these realities in mind, the course redesign paid special attention to the need for a supportive and accommodating learning environment (Shay & Pohan, 2021).

The updates to the course were guided by past experience as TAs, consultation with previous teaching teams and department faculty, the need for fully virtual instruction during the pandemic, and a desire to infuse the course with evidence-based pedagogical elements. Changes included content that reflected the current scientific Python ecosystem (Table 5.1), cloud-based coding notebooks, flipped video lessons, discussions on an online question-and-answer (Q&A) forum, use of data from a wider range of earth science domains, a student-designed final research project, encouragement of pair collaboration and use of external resources, efforts to center accessibility, and a syllabus with explicit policies, expectations, and the following end-of-quarter student learning objectives (SLOs):

1. Understand why the Python programming language is ideal for data analysis.
2. Write, execute, and debug Python code.
3. Access, read, transform, visualize, and interpret oceanographic data with confidence using Python.
4. Explore the ever-expanding universe of packages and tools available for creating and sharing code.

5. Formulate and investigate scientific research questions using programming and data analysis skills.
6. Adopt best practices in programming and data visualization that facilitate collaboration and information-sharing, both within the classroom and the broader scientific community.

All course materials were original, created by the graduate instructors, and are available for free reuse and adaptation under a CC-BY-4.0 license at https://ethan-campbell.github.io/OCEAN_215/.

5.3.2 Course content

In an introductory classroom setting, the choice of programming language matters. Python is an ideal candidate, as it is easy to learn, versatile, and free to use. First released three decades ago, Python is increasingly ubiquitous within earth science (Lin, 2012) and is widely used outside the scientific community, particularly in industry, making it valuable for students seeking a career outside of academia (Srinath, 2017). The language features concise, easily read, higher-level syntax that allows one to focus on data exploration, enabling more efficient science, while streamlining workflows starting from remote data access through to analysis and visualization (Lin, 2012; Ayer et al., 2014; Jacobs et al., 2016). For those learning programming for the first time, a primary challenge is thinking algorithmically, that is, developing structured code to solve a problem. Compared to Python, lower-level programming languages commonly taught in introductory computer science courses (such as Java and C++) require substantial syntactical overhead that can distract from achieving that pedagogical goal (Pears et al., 2007; Srinath, 2017).

Python offers other advantages. Its open-source nature has fostered a large active developer community, which has contributed to its stability and the dissemination of numerous multipurpose packages that extend its functionality. The fact that Python is free prevents a reliance on expensive commercial solutions that can render analysis code inaccessible to scientists

outside of well-resourced university environments (Gentemann et al., 2021). These qualities stand in contrast to MATLAB, a scientific programming language also popular in geoscientific research. Despite the clear benefits of teaching Python in an earth science context, we find only one documented example of an instructional approach for a conventional (quarter- or semester-long) course in the existing literature (Jacobs et al., 2016).

The updated OCEAN 215 covered scientific Python skills needed for oceanographic data analysis, starting with fundamental Python syntax, as well as data management and research practices (Table 5.1). Students learned core functions (see Supplementary Table 5.3) from versatile, interoperable, and open-source software libraries widely used in climate-related disciplines: NumPy, a fundamental library for multidimensional array computing (Harris et al., 2020); Matplotlib, a visualization library (Hunter, 2007); Cartopy, a mapping toolbox (Met Office, 2022); SciPy, a scientific and statistical analysis library (Virtanen et al., 2020); Pandas, a toolkit for working with 1-D and 2-D data (McKinney, 2010); and Xarray, a toolkit for label-based, coordinate-aligned manipulation of multidimensional netCDF files (Hoyer & Hamman, 2017). No textbook was required in order to allow flexibility in the topics addressed and avoid high textbook costs that have a disproportionately negative impact on historically underserved students (Jenkins et al., 2020). Students were encouraged to reference online documentation and use their knowledge of general function syntax to expand their Python capabilities beyond the course content. Lessons also addressed programming best practices, such as modularizing code, adhering to variable naming conventions, writing comments, and applying consistent style and formatting (G. Wilson et al., 2014), as well as effective visualization principles, including legibility and labeling (Hepworth et al., 2020) and considerations of accuracy and accessibility when choosing colormaps for visualizations (Thyng et al., 2016). These concepts were introduced with examples and data from oceanographic disciplines (physics, chemistry, biology, and marine geology) and other domains (e.g., cryosphere, atmosphere, and climate) using scaffolding to familiarize students with new topics.

5.3.3 Course elements

5.3.3.1 Programming platform

Google Colaboratory (Colab), a cloud-based, in-browser Python development environment modeled after Jupyter notebooks, was chosen as the coding platform for the course. Jupyter notebooks are widely used and can include a mix of interactive code blocks and narrative text, allowing for easy exploration of data and documentation of scientific workflows (Granger & Pérez, 2021; Perkel, 2021). In general, cloud-based computing has democratized the ability to conduct complex analyses of earth science data sets, creating new opportunities for innovation, transparency, and reproducibility (Gentemann et al., 2021).

Google Colab was chosen as the teaching platform over alternatives like an integrated development environment (IDE) and Jupyter notebooks. Unlike IDEs, Colab requires no local installation of Python or additional software, so students can start coding immediately with minimal device-specific troubleshooting. Notebooks also avoid the cognitive overhead associated with learning command-line syntax or a professional-level IDE (Pears et al., 2007; Jacobs et al., 2016). Unlike Jupyter notebooks, Colab does not require server configuration and integrates with Google Drive, facilitating file sharing and submission of assignments. Comments can be added to notebooks for grading purposes, similar to Google Docs, and built-in edit history can confirm students' compliance with deadlines. While constraints exist, such as a lack of transparent package management, computational limitations, and the need for an internet connection, the advantages of Google Colab outweigh its disadvantages in a classroom setting.

5.3.3.2 Flipped structure

For novice programmers, blended learning models have been shown in a systematic review to improve the learning experience, as they allow class time to be reserved for active learning and afford students more flexibility to plan and customize their study (Alammary, 2019). A flipped classroom approach was implemented by assigning 14 recorded lessons of approximately 30 min

each to be watched before synchronous (Zoom) classes. The lessons were divided into 41 tightly scripted segments of about 10 min each (see Supplementary Figure 5.9c). This was done with the goal of helping students maintain focus, as some evidence suggests the average student has an attention span of 15–20 min during traditional lecturing (Middendorf & Kalish, 1996). Prior study in a flipped classroom setting has also found condensing material into shorter (under 5 min or 10-20 min) videos is associated with higher student proficiency, engagement, and satisfaction than the use of longer (over 30 min) videos (Yu & Gao, 2022). In addition to segmenting videos, students were reminded to take breaks between segments. Flipped video watching and in-class participation were not graded, partially in recognition of pandemic stressors but also to accommodate individual circumstances without requiring students to disclose possibly sensitive information. The expectation was that assignment grades would be sufficiently impacted if students were not engaged in these activities.

Most lessons consisted of lectures that illustrated Python concepts using multiple representations, which has been suggested as a core pedagogical strategy for teaching programming (Hadjerrouit, 2008). For example, slides introducing a new concept would often include three distinct representations: a simplified overview of syntax and function arguments, a minimal example of the function or concept being used (e.g., Figure 5.1b), and a schematic or illustrative plot. Consistent fonts, color schemes, and other design elements were used to reliably indicate relationships between concepts and distinguish examples from core syntax. Some lessons used live-coding demonstrations rather than slides. Accompanying Colab notebooks were provided with each lesson to allow students to run code while watching.

5.3.3.3 Synchronous class sessions

In-class sessions were conducted using the Zoom platform. Students and instructors co-created community guidelines on the first day of the course. Each following synchronous class started with simple icebreakers asking students about their well-being and anonymous polls to gather

feedback about previous video lessons. Warm-up activities like these allay anxiety about classroom engagement, connect students with each other, and create a safer environment more conducive to active learning (Chlup & Collins, 2010; Bledsoe & Baskin, 2014). Concepts from the relevant flipped videos were then briefly reviewed, leaving ample time for students to ask lingering questions. In some class sessions, short activities were used to introduce topics not covered in lesson videos.

The majority of synchronous class time was spent conducting live coding demonstrations and facilitating tutorials that integrated concepts taught in the videos. Compared to using slides or copying and pasting blocks of existing code, live coding forces slower, more digestible instruction, allows instructors to be responsive to student questions in real-time, and inevitably allows students to see instructors' mistakes and how they are diagnosed and fixed (G. Wilson, 2016). Tutorials were designed with multiple goals in mind, in alignment with core considerations for programming activities laid out by Hadjerrouit (2008): (1) to encourage students to analyze the problem at hand and develop stepwise solutions; (2) to build on concepts that students previously learned, encouraging reuse and modification of previous code; and (3) to compare and contrast different ways of achieving the same analytical or graphical result. Based on positive mid-quarter feedback, the instructors emphasized these tutorials and live coding in the second half of the course.

A Google Colab notebook was prepared for each class, presenting a tutorial with four or five related but distinct problems that applied different concepts or functions to a real-world data set from oceanographic and related disciplines (e.g., Figure 5.1c). Data were curated by the instructors for their instructional potential. These exercises created opportunities to divide the classroom into 4-5 person groups that worked cooperatively within Zoom breakout rooms. A "think-pair-share" model (Yuretich et al., 2001; McConnell et al., 2017) was adopted: students first individually attempted a problem for a few minutes, then teamed up in their breakout room to discuss challenges encountered and optimal solutions, and lastly returned to the main Zoom

room, at which point a designated reporter from each group reviewed their results with the full class. Instructors monitored student discussions by moving between breakout rooms and provided guidance when needed. Groups' progress was tracked by watching a shared Google Doc configured ahead of time with templates in which each group filled in their final coding solutions. Occasionally randomizing group members allowed students to gain exposure to a variety of coding styles, social dynamics, and levels of confidence with the material.

5.3.3.4 Q&A forum

An online Q&A board, Piazza, was offered as an outlet for students to connect asynchronously with peers and instructors outside of class and office hours (Figure 5.1e). Piazza enables students to seek help on logistical or clarifying questions as well as their problem-solving processes, thereby reducing individual emails to instructors. The platform allows students to select the audience for their questions (instructors and/or classmates), post anonymously, respond to peers in threaded discussions, and collaboratively construct answers. Instructors may endorse and comment on student answers. Four brief check-ins (including Assignment #0) required Piazza submissions, and an additional quota of five substantive posts per student (i.e., those that contribute further insight to the discussion, rather than simply "Good work" or "I agree") was prescribed in the syllabus. We note that alternative platforms exist that provide similar functionality to Piazza and may be similarly effective.

5.3.3.5 Assignments and final project

Similar to the previous version of the course, students completed four programming assignments at two-week intervals. In the updated version, assignments consisted of approachable, multi-part problems in a Google Colab notebook that utilized real scientific data (Figure 5.1d). For example, one assignment tasked students with importing data collected by an ocean observing platform (a seaglider), identifying key summary statistics, creating a visualization of the glider's location and temperature measurements, and calculating trends in the data. Appropriate geoscience problems

were selected to exercise specific skills: atmospheric reanalysis fields depicting historical local weather conditions lent themselves to practicing dimensionality reduction operations using Xarray (e.g., calculating area-averaged snowfall rates over time), while a global bathymetry data set was ideal for applying knowledge of how to create and format contour plots using Cartopy.

Assignments incorporated elements of both "structured inquiry" and "guided inquiry," the second and third levels in the hierarchy of Banchi and Bell (2008). Questions were somewhat less structured compared to class activities, allowing students more flexibility to design their own solutions. This created opportunities to practice both programming skills and data literacy, creating a foundation for more sophisticated independent analysis of data sets. Without a midterm exam, assignments were instructors' main window into student progress. Instructors offered a one-time, two-week extension to allow flexibility while still requiring students to learn foundational material.

Students also completed an individually driven or collaborative final project (see Supplementary Text 5.1 for the project description handout). The goal was for students to write code to answer a scientific question by exploring a data set of their choice, supported by ample guidance from the instructors and peer review from classmates. Similar to the structure of an introductory data programming course described by Anderson et al. (2015), low-stakes checkpoints throughout the quarter required students to share their topic, data set, scientific questions, and hypotheses on the Piazza Q&A board, as well as offer feedback on at least three classmates' choice of data or questions. The project culminated in the delivery of a short final presentation. A rubric was provided to clearly communicate expectations and evaluation techniques for code, figures, and presentation content and delivery (see Supplementary Table 5.4). Rubrics may lead to increased student performance, and in any case, rubrics are recognized as a user-friendly tool for setting guidelines and enabling self-assessment (Brookhart & Chen, 2015).

Students were offered the option to collaborate in pairs on both the assignments and final project. When programming as a pair, one student serves as the “driver,” writing code, while the other observes, monitoring the code for defects and helping to problem-solve. Students were also allowed to reference external resources such as online documentation sites and Stack Overflow. Citations and acknowledgment of collaboration were expected in assignments and the final project, and students confirmed their agreement with the integrity policy in the initial survey (Assignment #0).

5.4 Evaluation

We adopted a two-pronged approach by first evaluating student achievement of SLOs using final project assessments and then exploring instructional approaches that helped students learn by using a variety of other data. Quantitative data include standardized course evaluations, an end-of-quarter student survey, engagement and usage metrics provided by the video and Q&A platforms, and graded assessments. Student focus groups and open-ended evaluation questions were qualitatively analyzed. Prior to analysis, all student-specific metrics were de-identified and coded by a coauthor who was not directly involved in quantitative analyses; identified versions were not used thereafter. This study was approved as qualifying for exempt status for institutional review by the Human Subjects Division at the University of Washington.

Table 5.2: Rubric used to classify students' final project questions and hypotheses based on the cognitive process dimension of the revised Bloom's taxonomy (Krathwohl, 2002). For the analyses in Figure 5.3b,c, multiple hypotheses and/or questions offered by students (up to three each) were assessed separately and weighted such that a student's three hypotheses, for example, would each contribute ⅓ of a point to their respective cognitive level's total count.

Cognitive level	Questions	Hypotheses
Level 1: Remember	*"Can the data be visualized using my skills?"* Intention to **recall** coding techniques taught in the course and **recognize** their proper use	**Recall of course material** (e.g., *the data can be depicted using a scatter/line/pseudocolor plot*)
Level 2: Understand	*"What stands out in the data?"* Intention to **summarize** the data; or *"Do the data resemble what we expect the ocean to look like?"* Intention to **interpret** the data and **classify** what is present by **comparison** to known examples	**Factual interpretation** (e.g., *the data will have X, Y features; the data will resemble X, Y other ocean data*)
Level 3: Apply	*"What [happens if…]"* Intention to **execute** or **implement** a specific procedure, such as **calculating** a correlation; or *"Does […]"* Intention to **answer** a binary (yes/no) question	**Specific results and relationships** (e.g., *the answer will be yes/no; X will show an increase over time; X and Y will show a positive correlation*)
Level 4: Analyze	*"How [does/do/is/are…]"* Intention to **characterize** or **test** a **straightforward** or **single-dimensional** relationship, phenomenon, or difference	**Contextual results and relationships** (e.g., *X and Y will show a positive correlation, but only under Z conditions; X and Y will vary with Z; X is characterized by Y patterns*)
Level 5: Evaluate	*"How [does/do…] affect…"* *"What [is/are…] the relationship between…"* Intention to **characterize** or **attribute** in an **open-ended** or **multidimensional** way; or *"Why [does/do/is/are…]"* Intention to **establish** causality by **integrating** external ideas or models and/or **connecting**, **contrasting**, or **weighing** multiple sources of information	**Explanations** (e.g., *X and Y will show a positive correlation because of mechanism Z; X and Y exhibit different features because of Z*)
Level 6: Create	*"What [does/do…] mean…"* *"How [does/do…] fit into…"* Intention to **evaluate** the **implications** of findings, **place** findings within old or new paradigms, **construct** or **produce** new frameworks, or **investigate** the **consequences** of phenomena using an open-ended approach	**Discovery** (e.g., *X is important because Y; X will differ from a past model Y, where a model is composed of two or more mechanisms; X can be explained using Y model;* or a hypothesis cannot be established due to a lack of prior information)

5.4.1 Student achievement

We use students' final projects as a barometer of their level of scientific reasoning, their final coding competency, and their achievement of course SLOs. First, questions and hypotheses posed by students in their projects were assessed based on the seven levels of the cognitive process dimension of the revised Bloom's taxonomy (Bloom et al., 1956; Krathwohl, 2002; see rubric in Table 5.2 for examples referenced in our classification), similar to the methodology of Kastens et al. (2020). Second, students' breadth of programming skills was evaluated computationally as the fraction of Python syntax elements taught in the course—namely, functions, operators, and methods—that were employed at least once in each student's submitted project code notebook (see Supplementary Table 5.3 for search terms used in the analysis). This metric varies widely between students (see Results section "Student learning outcomes") and thus offers significant discriminatory power, albeit limited by our exclusion of miscellaneous functions that were not taught in the course but were used by some students at higher skill levels. Third, the submitted projects were graded using a rubric that was provided to students ahead of time to delineate expectations and evaluation techniques (Supplementary Table 5.4). By mapping rubric subcategories onto four of the six corresponding SLOs and combining the graded scores within each category for each student, we create aggregate metrics of each student's final achievement of those key objectives.

5.4.2 Surveys and evaluations

Here we detail our use of four distinct assessments: an introductory survey, anonymous mid-quarter and final evaluations, and an end-of-quarter survey.

To gauge initial exposure to the Python programming language and coding in general, students were asked to share their prior experiences in an introductory survey distributed in the first week of class (Assignment #0). The instructors translated students' short-answer responses into a numeric rating (1–5) using a subjective analysis of their word choice (see rubric in

Supplementary Table 5.5 and Supplementary Figure 5.10). The factors considered were any previous coding languages learned, the reported efficacy of past learning experiences, and the time since last exposure to coding. The introductory survey also encouraged students to introduce themselves to the teaching team by sharing their pronouns and any anticipated accessibility, technology, or learning needs, which led to instructors making an effort to accurately caption all lesson videos.

We also obtained summary reports from final Instructional Assessment System (IAS) evaluations completed by OCEAN 215 students in Autumn 2015, 2016, 2017, 2019, and 2020 (results from Spring 2015 and Autumn 2018 were unavailable), which were administered and anonymized by the University of Washington. Standardized questions asked students to evaluate aspects of the course quality and their engagement with the course. While most questions were consistent across years, others evolved in their wording and thus required mapping or aggregation to enable comparison between years (as shown in Supplementary Table 5.6). Questions that could not be tracked across years were excluded. Students completed evaluations either in paper or online format, with the class response rate of around 70% in 2020 being somewhat higher than in past years (Supplementary Figure 5.8). As IAS summary reports correspond to specific instructors, we averaged the class median responses between the two graduate instructors for each question in 2020. Changes between 2015–2019 and 2020 were tested for a statistically significant increase using a one-sided *t*-test for questions where increases could objectively be viewed as a desired improvement: metrics on a 1–5 ("Very poor" to "Excellent") scale and the metrics "Time spent that was valuable" and "Participation relative to other courses." The remaining metrics were tested for a statistically significant change in either direction using a two-sided *t*-test.

Furthermore, we apply a standard qualitative approach (Creswell, 1998) to extract meaning from students' anonymous responses to open-ended questions in two IAS evaluations in 2020: a mid-quarter evaluation administered during weeks 4–5 of the course and the final evaluation. The

prompts are listed in Supplementary Table 5.7. We identified common or unique themes mentioned by students, grouped similar themes, coded responses by noting whether a theme was mentioned in either a subjectively positive context (e.g., an appreciative or affirming comment; assigned a value of +1) or subjectively negative context (e.g., an unenthusiastic or critical comment; assigned a value of –1), and tabulated the frequency of each context for all themes. We also excerpt illustrative quotes from students' responses throughout the text.

In addition to the university-managed IAS evaluations, a voluntary end-of-quarter Google Form survey was administered during the week after the final class to measure students' perceived success relative to the course SLOs. The response rate was 92%. Submissions were not anonymous, but instructors guaranteed to students that their responses would not impact their final course grades. As a final self-assessment of students' Python skills, we use responses to the question, "How proficient do you feel in writing, executing, and debugging Python code?", which were on a 6-point scale from "Least proficient" to "Most proficient."

5.4.3 Flipped video viewership

Panopto, the video hosting and delivery platform used in the course, provides instructors with usage statistics, including view counts, minutes delivered, percent completed, and last view time. Those metrics—associated with individual students, individual videos (both aggregated and disaggregated by student), and distinct video viewing sessions, where applicable—were downloaded, and student identities were anonymized as described above. Student-specific Panopto metrics computed include total minutes watched, minutes watched before the class for which a video was assigned, and minutes watched after class for the first time (i.e., late views).

5.4.4 Q&A forum engagement

Piazza, the online Q&A platform, also makes usage statistics available to instructors. The following student-specific metrics were downloaded, then anonymized as described above: days online,

answers, and total contributions (which include questions, notes, answers, and comments). Additionally, a time series of engagement was constructed based on unique users per day, as provided by Piazza. The time series was supplemented by a manual tabulation of daily Piazza activity within the following categories: student questions and notes related to programming; student scheduling, extension, or logistical requests; student answers and comments; student posts that were required for assignments; and instructor posts, answers, or comments. Where relevant, those categories were further divided by the chosen audience into total posts that were public and signed, public and anonymous, or private (i.e., visible to instructors only).

5.4.5 Final grades

Students' final grades are used to represent overall student achievement. Grades were recalculated to ignore two students' incomplete assignments (0% grades) that occurred due to personal circumstances, and the following weights were re-applied: 60% for assignments #0-#4 (weighted equally), 15% for Piazza posts, and 25% for final projects. Recalculating final grades raised their average from 95.0% to 95.9% and decreased their standard deviation from 5.7% to 3.8%.

5.4.6 Student focus group

Undergraduate students who completed OCEAN 215 in Autumn 2020 were considered for a focus group based on responses to the voluntary Google Form survey asking students to rate their interest in the project and provide a short paragraph about course elements that affected their learning positively or negatively. Five students were chosen based on the thoughtfulness of their written responses and the diversity of their academic backgrounds and experiences within the course. Selection was not dependent on students' grades in the course, and it was made clear that survey responses would not impact course grades. Three focus group sessions were held in the quarter following Autumn 2020, each lasting 1–2 h. In the sessions, the instructors asked

questions designed to provoke open and candid discussion about students' perception of course elements and took notes by paraphrasing comments. Focus group participants did not have access to the anonymized raw student data.

The five students were additionally invited to share short testimonials detailing their unique experiences in the course and were offered coauthorship on the study (as noted below in Author Contributions). The four testimonials that were submitted are presented in Supplementary Text 5.2 and excerpted throughout the text. The final testimonials were assembled from students' responses to their selection of a subset of the guiding questions included as Supplementary Table 5.8 and were edited for style and grammar and to limit the redundancy of themes mentioned. Insights gleaned from the focus group or testimonials are clearly denoted in the text. We use them as supporting evidence to depict students' perspectives about the course more holistically and accurately and to indicate areas where students felt the course could be modified to improve their experience.

5.5 Results

5.5.1 Student learning outcomes

Overall final project grades were all above 80%, with most students scoring high marks (80% or above) on four project rubric categories representing the quality of their code, visualizations, use of data, and scientific research (Figure 5.3e–h). These categories correspond to SLOs #2, #3, #5, and #6, with some overlap (see Supplementary Table 5.4). The widest spread in grades was in the category of scientific research (Figure 5.3h), in which 28% of students scored below 80%.

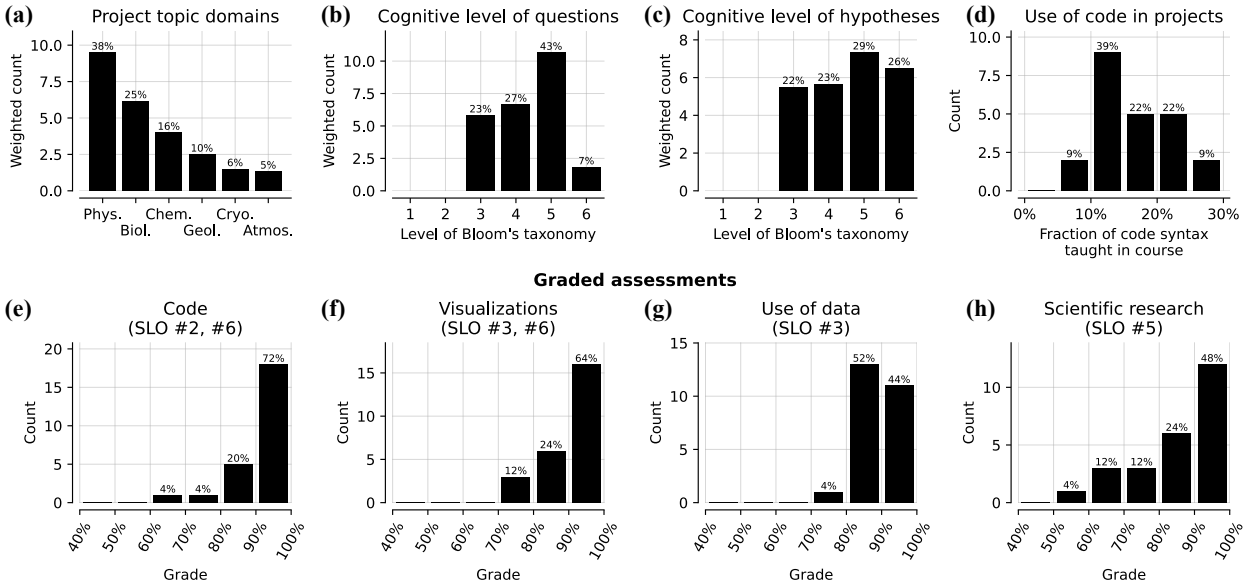

Figure 5.3: Assessment of students' final projects. (a) Distribution of domains of students' final projects. If a project topic touched multiple domains, each domain was weighted such that, for example, a project spanning three domains would contribute ⅓ of a point to each of the domains' total count. **(b,c)** Distribution of cognitive level of students' questions and hypotheses. Each student's questions and hypotheses (up to three each per student) were assessed based on the cognitive process dimension of the revised Bloom's taxonomy (Krathwohl, 2002) using the rubric and weighting described in Table 5.2, with higher levels of Bloom's taxonomy representing higher-order questioning and prediction. **(d)** The fraction of code syntax taught in the course that students used in their projects (see Supplementary Table 5.3 for assessment methodology and search terms). **(e–h)** Project grades within four named categories that correspond to student learning objectives (SLOs) outlined in the text (see Supplementary Table 5.4 for grading rubric and mapping to SLO categories). These categories (with rubric subcategories in parentheses) are code (correctness, functionality, tidiness, perseverance), visualizations (clarity, colormaps, labels, creativity), use of data (data collection, processing, results/interpretation), and scientific research (background, questions/hypotheses, explanations). Note the *x*-axes are truncated to 40%–100% for readability.

Students' final project topics spanned the oceanographic, cryosphere, and atmospheric domains (Figure 5.3a). Examples include applying time series analysis techniques to ocean monitoring data to assess the impact of climate change on coral bleaching, cleaning a global database to characterize the traits of hydrothermal vent fauna, and mapping blue whale tracks and satellite sea surface temperatures to infer relationships between environmental conditions and whale behavior. Scientific questions and hypotheses posed by students largely map onto higher levels of Bloom's taxonomy, exemplifying higher-order questioning and prediction (Figure 5.3b,c). The percentage of code syntax taught in the class that was used in each final project ranged

widely from 6% to 29% (Figure 5.3d) and exhibits no significant correlation with the assessed cognitive level of students' questions or hypotheses (not shown). In other words, students' level of scientific reasoning was not predictive of the analytical complexity of their finished projects.

5.5.2 Connecting course elements to student learning

By calculating correlations between a variety of anonymized data sources (see Evaluation), presented in Figure 5.4, we explore the impact of students' varying backgrounds and learning strategies on their course experiences and outcomes. Significantly, neither students' final grades nor their code usage in final projects is correlated with prior coding experience, indicating that previous exposure to Python was not predictive of success in the course. On the other hand, prior coding experience is positively correlated with self-assessments of Python skills in end-of-quarter surveys, the only metric showing a relationship with the self-assessments. Dichotomizing the class by prior coding experience (none/little versus some/moderate/lots) also reveals no statistically significant difference in final grades (Supplementary Figure 5.10). That said, less prior experience was associated with higher engagement with lesson videos and the Q&A forum (Figure 5.4). The breadth of Python skills used in final projects positively correlates with three key metrics: total lesson minutes watched, number of Q&A forum answers, and forum days online. This indicates that students who demonstrated strong coding competency had likely acquired more content knowledge, frequently shared that knowledge with peers, and were more engaged with the course. Variations in students' demonstrated Python skills cannot fully explain differences in their final grades, but the two show a positive nonlinear correlation. Students who earned higher grades tended to monitor the Q&A forum more frequently, collaborate more often with classmates using pair programming, and watch lesson videos before class.

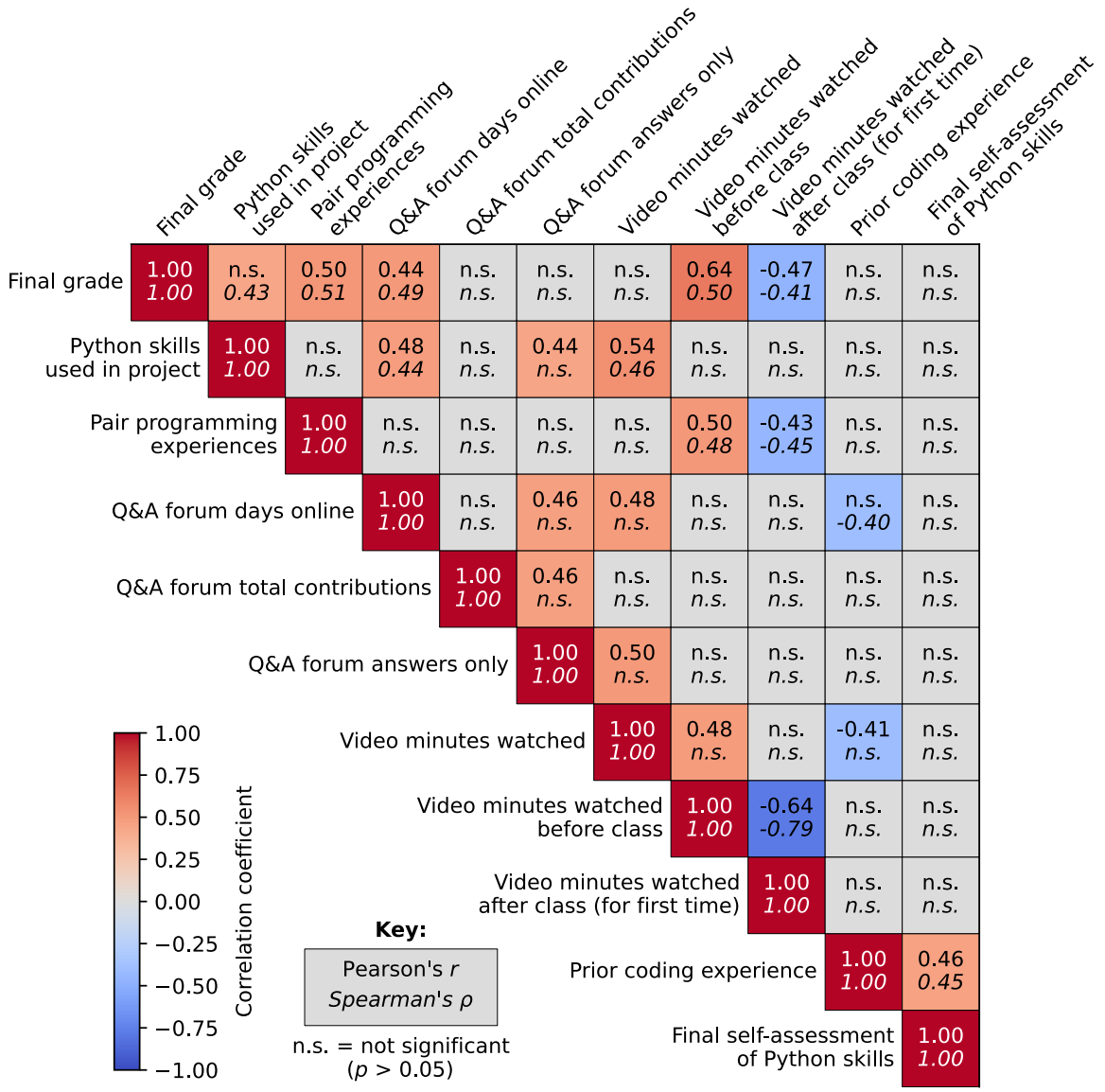

Figure 5.4: Correlations between student-specific anonymized metrics. Two tests were applied: Pearson's *r* (top values) and Spearman's *ρ* (lower values, italicized). Higher Pearson correlations indicate stronger positive linear relationships, while higher Spearman values indicate stronger monotonic relationships, which may not necessarily be linear. Correlations without statistical significance ($p > .05$) are indicated by "*n.s.*" Colors correspond to the larger of the two correlation coefficients by absolute value. For detailed information about each metric presented, see Evaluation section "Final grades" (for "Final grade"; column 1), Supplementary Table 5.3 (for "Python skills used in project"; column 2), Results section "Assignments and final project" (for "Pair programming experiences; column 3), Evaluation section "Q&A forum engagement" (for Q&A forum-related metrics; columns 4–6), Evaluation section "Flipped video viewership" (for video-related metrics; columns 7–9), Supplementary Table 5.5 (for "Prior coding experience"; column 10), and Evaluation section "Surveys and evaluations" (for "Final self-assessment of Python skills; column 11).

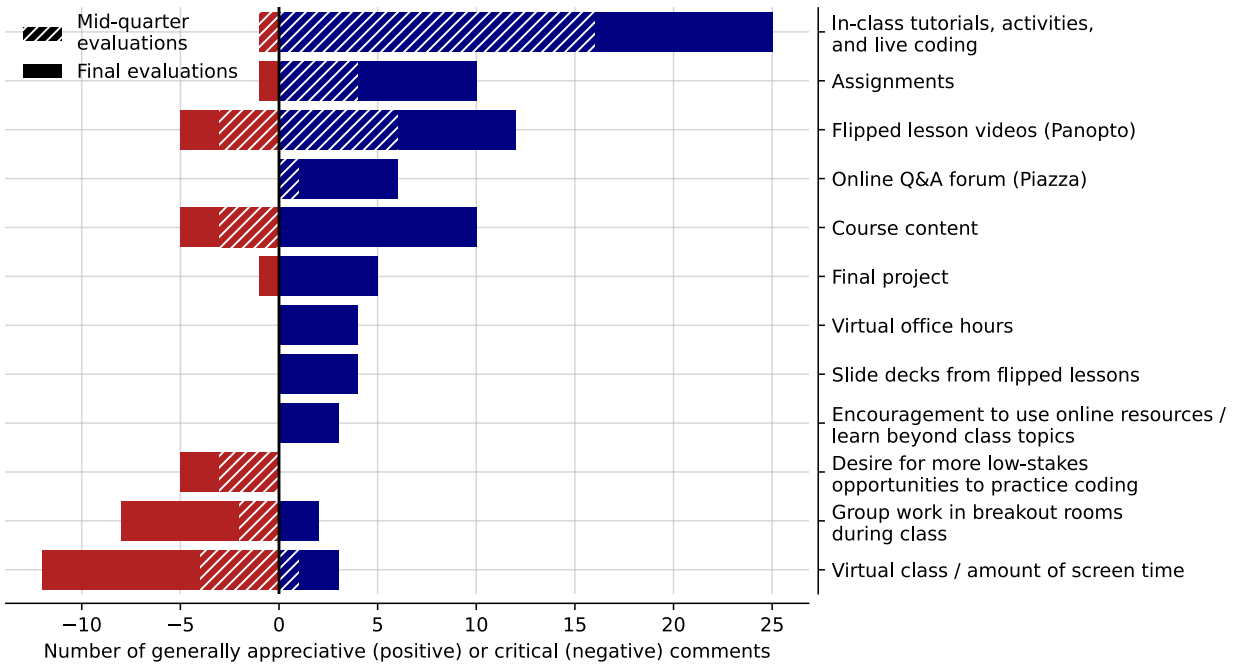

Figure 5.5: Themes identified in anonymous, open-ended student responses to surveys. Shown are responses to mid-quarter (hatched bars; n = 15 students) and final (solid bars; n = 20 students) evaluations in 2020, ranked according to the net positivity (blue) or negativity (red) of comments regarding those themes. Totals for mid-quarter and final evaluations are stacked, not overlapping, within each bar. Original question prompts are listed in Supplementary Table 5.7.

5.5.3 Role of course elements in student learning

5.5.3.1 Course content

Overall, students perceived the course positively in final evaluations, rating its content, evaluation techniques, organization, and the course as a whole markedly higher than in past years (Figure 5.2). Students' view of the course content evolved from a critical stance expressed in mid-quarter evaluations, with comments citing its abstract or challenging nature, to an appreciative view in final evaluations of the data skills they had acquired and their utility for conducting scientific research (Figure 5.5). One focus group participant who was a first-time coder wrote in their testimonial (Supplementary Text 5.2):

> *"I have always viewed research as something that is extraordinarily complicated. This class demonstrated that knowing a few basic Python functions and packages can provide a solid foundation to start conducting research."*

5.5.3.2 Flipped structure

In total, students spent 166 h watching lesson videos on the Panopto platform. According to viewership statistics, two-thirds of the watch time occurred before the class for which the video was assigned (Figure 5.6). Most lessons were released 1.5–3 d before the Zoom class meeting, and students generally watched lessons during the 24 h prior to class. The remaining one-third of total watch time occurred throughout the month following the relevant class, of which three-quarters were first-time views. While the total video lesson minutes watched by a student were correlated with the breadth of Python skills used in their final project (see Evaluation section "Student achievement"), the timing of their video lesson views was not (Figure 5.4).

Students in the focus group expressed that they appreciated the opportunity to watch videos at a convenient time and the ability to take breaks. Some shared that they would have viewed videos immediately before class regardless of release timing, while others said they would have taken advantage of a longer period of availability. While one student reported in their final course evaluation that "occasionally the length of the recorded lectures prevented [them] from finishing them entirely," we find no significant correlation in Panopto statistics between video or lesson duration and fraction watched (see Supplementary Figure 5.9f and Supplementary Figure 5.9h). These statistics also show that half of students watched nearly every video, with class-wide average video completion between 80% and 90% in most weeks (Figure 5.7a). Completion rates dropped near the end of the course, which student focus group participants suggested was due to high end-of-quarter demands in other courses and because the material covered didn't appear in assignments.

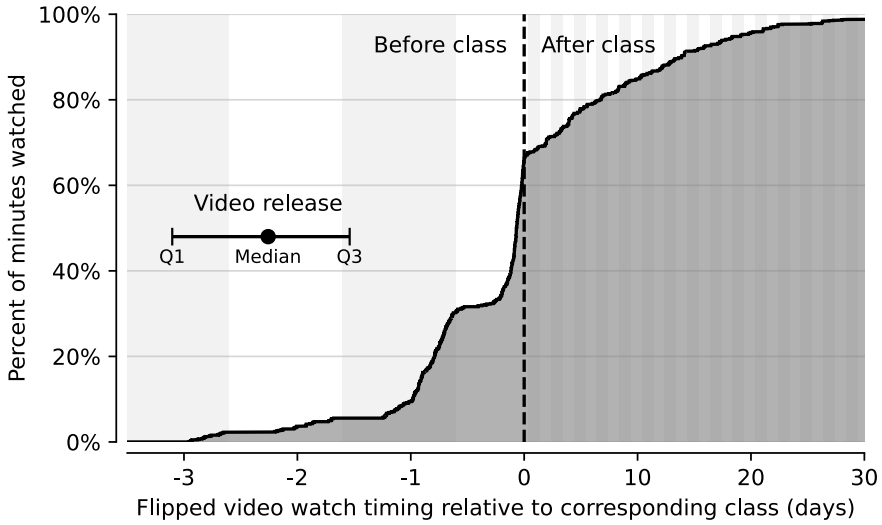

Figure 5.6: Timing of flipped Panopto video viewing sessions relative to the class for which each video was assigned. Viewing sessions were binned along the *x*-axis according to their timing before or after their corresponding class (with each viewing session weighted by its duration), then total minutes for each timing bin were summed from left to right to produce the cumulative distribution of watch timing shown here. The *y*-axis is the cumulative fraction of total video time delivered during the course (166.3 h over 41 videos), with video rewatches included. The median and interquartile range (25%–75%) of video releases by instructors, relative to the corresponding class, is included for reference, indicating that videos were generally released 1.5–3 d before they were due. Vertical shading corresponds to days; note the compressed positive *x*-axis scale.

Some students in the focus group reported re-watching videos to review material or using corresponding slide decks for the same purpose; one student took notes on the videos and later referenced those notes. In final course evaluations, students noted that having slide decks available benefited their learning (Figure 5.5), with one student sharing, "I was able to surprise myself with how much I could figure out through review when feeling helpless at first." Despite the addition of watching flipped videos (as well as a final project) to the overall course workload, students estimated in final evaluations that the amount of time they spent each week was similar to past years. Yet out of students' total time spent on the course, nearly 90% was perceived as valuable in advancing their education—a significant increase from past years ($p \leq .1$; Figure 5.2).

5.5.3.3 Synchronous class sessions

Interactive tutorials involving live coding demonstrations and individual activities were the most positively reviewed course element in students' mid-quarter and final evaluations (Figure 5.5). On the other hand, the large amount of screen time was the most frequently mentioned criticism in course evaluations (Figure 5.5). Students also offered criticism on the use of breakout groups in their evaluations, with one noting, "I didn't find the small group coding breakout rooms very helpful for coding, but they were nice for getting to know my classmates." Several students wished for more time and instructor guidance in breakout rooms, which contributed to their overall negative rating (Figure 5.5). Nonetheless, one focus group participant noted in their testimonial (Supplementary Text 5.2) that breakout rooms "forced us to come well-prepared for class" and in final course evaluations, students rated their overall participation as higher relative to other courses (6.0 on a 7-point scale, where 4.0 is "average"; Figure 5.2).

5.5.3.4 Q&A forum

Students visited Piazza once every 1–5 d on average, and engagement in the form of questions, answers, and comments closely tracked assignment deadlines and peaked while students worked on the final project (Figure 5.7a). Many questions from students were simple—for example, diagnosing a coding bug or clarifying the goal of an assignment—while others were more complex—such as seeking strategies to efficiently work with large data sets for one's final project. The forum saw 530 total student contributions, out of which two-thirds were voluntary, i.e., not required by a check-in or Assignment #0 (Figure 5.7b). The average response time to student questions by instructors or peers was 17 min.

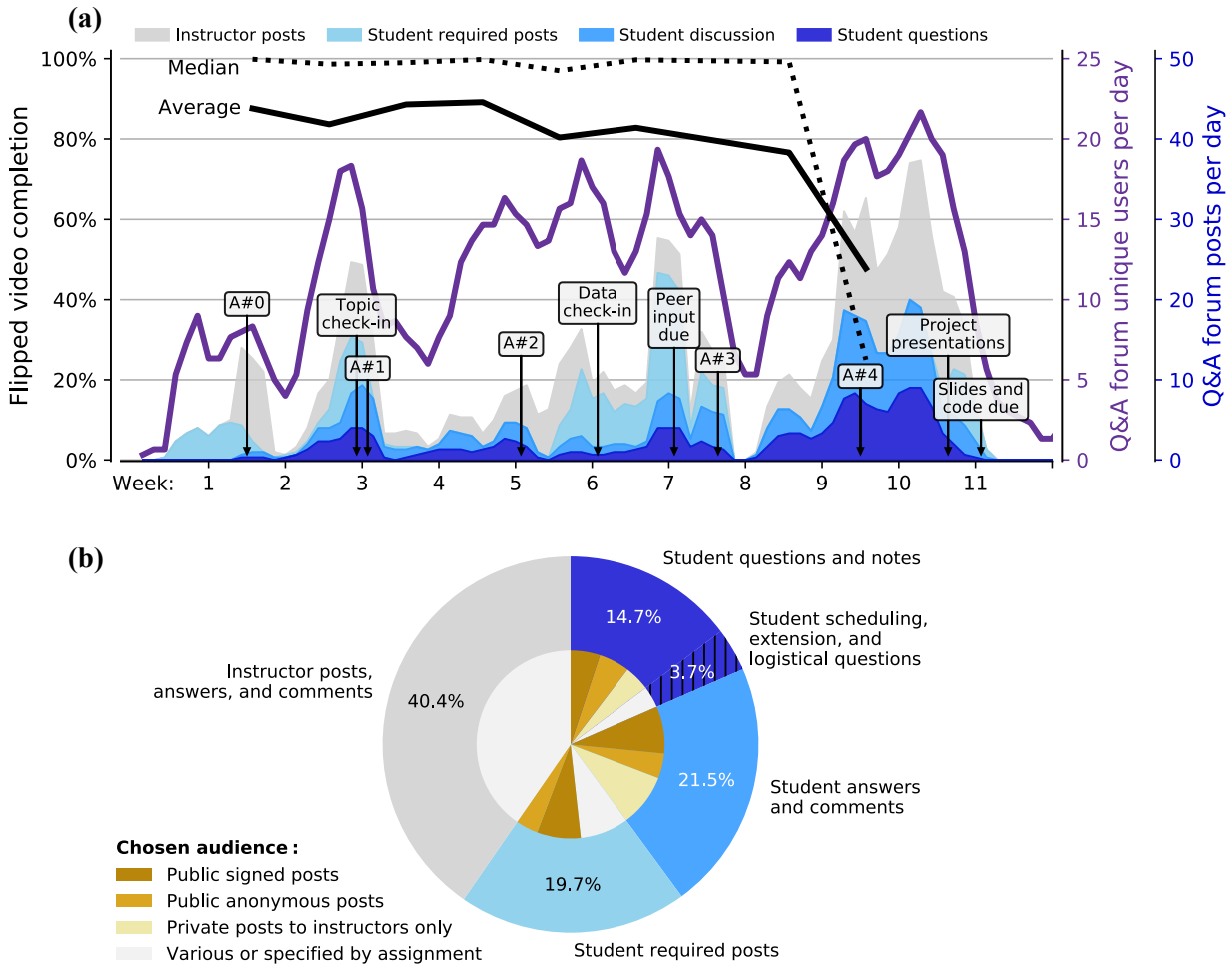

Figure 5.7: Student engagement with online platforms. (a) Flipped video completion rates over time from Panopto are presented as both the class-wide median (dotted black line) and average (solid black line). Note that video completion by student was allowed to exceed 100% due to repeat views. Piazza Q&A forum engagement is shown as unique users per day (purple) and posts per day, segmented by the type of post (shaded curves; see colors in legend). The timing of coursework deadlines (assignments ["A#."] and final project checkpoints) are indicated with arrows. **(b)** Usage of the Piazza Q&A online forum by students and instructors, segmented by type of post (outer) and further divided by chosen audience (inner). "Required posts" were those requested from every student for Assignment #0 and final project check-ins. "Public posts" were viewable by all users, while "private posts" were visible to instructors only. "Anonymous posts" refer to those in which the author was hidden from other students, but not from instructors.

Students selected the three audience options (public, either signed or anonymous, and private posts) with approximately equal frequency, depending on their needs (Figure 5.7b). Student focus group participants shared that the anonymous and private posting options were useful when they were worried that a question would be perceived as obvious or simple, or when

they were less sure of their answer. Final course evaluations show that students overall felt positively about having access to Piazza (Figure 5.5). One student shared their appreciation for the ability to post anonymously, stating that it "alleviated some anxiety about asking questions."

5.5.3.5 Assignments and final project

In course evaluations, most students viewed the assignments and final project as beneficial (Figure 5.5). We find that nearly half of the class—48% of students—took advantage of the pair programming option at some point, with 34% of students collaborating on any given assignment (including the final project) on average. Students generally chose the same classmate as their partner throughout the course. The number of times that a student worked collaboratively is presented as the metric "Pair programming experiences" in Figure 5.4. One focus group participant shared their experience in their testimonial (Supplementary Text 5.2):

> *"... we coded in completely different ways, and it was fascinating to see those differences. We were more effective together because we learned to compromise and collaborate to find the cleanest and fastest method between the two of us."*

The opportunity to synthesize course knowledge and the option to collaborate with classmates on final projects were specifically cited in students' final evaluations as positive elements of the course. The ability to use external materials and learn beyond class topics was similarly welcomed in final evaluations (Figure 5.5), and another student expressed in their testimonial:

> *"[Accessing online resources like Stack Overflow] developed essential skills and gave me the confidence to apply new concepts in my final project. This meant my research could be dictated by my curiosity and questions, as it should be, and not by the limitations of what concepts we had covered in class."*

That said, one critical final evaluation comment related to ambiguity about the rigor of science expected and the open-ended nature of project checkpoints.

5.6 Discussion

5.6.1 Student learning outcomes

We measured students' achievement of key SLOs (#2, #3, #5, and #6) by assessing their final projects, with the assumption that the projects represent a holistic demonstration of students' capabilities. Those assessments indicated clear success in achieving learning objectives. Students produced impressive and original work that reflected earnest attempts to investigate questions within the geosciences using effective coding and visualization techniques. The strength of the correlation between project code usage and video minutes watched suggests that students' content acquisition was particularly impactful for their coding competency (SLOs #2 and #3).

Consistent with research that found a weak correlation between tutor grades and self-assessments by over 3000 undergraduate students (Lew et al., 2010), we saw no link between students' self-assessment of programming skills in the end-of-quarter survey and their final grades. A caveat is that students were asked to rate their Python competence, rather than their final grade, and the two metrics may not be entirely comparable. That said, this result could still reflect the Dunning–Kruger effect, a cognitive bias in which those with the least knowledge tend to overestimate their performance or ability because they lack the competencies required for self-assessment (Kruger & Dunning, 1999). The lack of a relationship between students' final self-assessments and any metrics other than prior coding experience points to a persistent confidence from previous Python exposure that contributed to a perception of competence not necessarily reflected in higher grades or course-acquired skills. In contrast, our results suggest a leveling of the playing field in which those who came in with less previous knowledge of programming took full advantage of class resources, like lesson videos and Piazza, to ultimately reach the same level of proficiency as their peers, as shown in final grades and project code usage.

5.6.2 Role of course elements in student learning

5.6.2.1 Flipped structure

Consistent with a review supporting the efficacy of blended learning models (Alammary, 2019), our analysis of video watch timing, student focus group feedback, and course evaluations shows that our flipped structure enabled a diversity of strategies for content acquisition. Exposure to video content before working on related in-class activities may have helped students prepare for assignments, which comprised the majority of final grades. Nonetheless, our correlation metrics suggest that the total amount of time spent viewing lessons, not whether those lessons were watched before or after a class, was most influential in students' application of course content, as measured by Python skills used in their final projects.

In line with prior research on students' perspective of the flipped model (McCallum et al., 2015), our course structure generally received student approval in course evaluations (Figure 5.5). Students' overall positive evaluations of the course are notable given hardships related to the COVID-19 pandemic, as well as findings that show students often prefer passive lecturing over active learning due to the additional cognitive effort required to engage actively with material (Deslauriers et al., 2019).

Virtual teaching offers inherent accessibility benefits for students facing long commutes, disability-related challenges, and other barriers to in-person participation (Pichette et al., 2020). We believe that virtual office hours—regarded positively by students in course evaluations—indeed offered benefits for students who may have perceived office hours as an unfamiliar or unsafe space. Similarly, breakout rooms created privacy for students with questions on assignments or personal matters.

5.6.2.2 Synchronous class sessions

Course evaluations indicated that in-class activities and demonstrations were well-liked and engaging. However, the facilitation of breakout groups and large amount of screen time presented

challenges for students and instructors and were met with critical reviews. “Zoom fatigue” is a particular form of exhaustion that may result from the intensity of continuous, close-up eye contact and seeing oneself, reduced mobility when having to stay in a video frame, and increased cognitive load from having to exaggerate nonverbal cues (Bailenson, 2021). To mitigate these effects, regular breaks were taken during class, students were encouraged to take breaks during recorded videos, a video-optional policy was instituted on Zoom, and students were allowed to use the chat function to participate, though students’ criticisms about screen time show Zoom fatigue remained a challenge. These solutions are also imperfect—breaks take class time, teaching to students with cameras off can be disorienting, and chat messages can be difficult to monitor during instruction.

Though breakout rooms can allow for more individualized attention, the instructors had difficulty with distributing their finite time across groups and eliciting participation. Both can be linked to group size, and student focus group participants indeed shared mixed views on the number of students per group. Smaller groups could have encouraged more individual accountability at the expense of increasing demands on instructors’ time as they cycle between breakout rooms. Larger groups would have enabled instructors to provide more efficient guidance and increased opportunities for peer instruction but often suffer from uneven participation. The optimal configuration may depend on individual classroom circumstances.

5.6.2.3 Q&A forum

The wide range of question types that we observe on Piazza are in line with previous research in an undergraduate computer science setting, which similarly showed high participation rates when students are encouraged to use the platform by teaching staff (Vellukunnel et al., 2017). Our correlation analysis of student metrics also matches the positive relationship between question-asking on a Q&A forum and final grades found in that prior study. The apparent efficacy of Piazza may reside in the fact that voluntarily asking a question on a discussion forum, by definition,

constitutes a form of active learning, though posts may vary in their level of reasoning and connectedness (Vellukunnel et al., 2017). Active learning would presumably be maximized if students use Piazza to seek help after they have invested time into trying different solutions and consulting other resources, which is encouraged by the asynchronous nature of the forum. However, at times, the rapid responses to questions on Piazza observed in our course from both instructors and peers may have short-circuited this problem-solving process. While prompt instructor engagement is vital for establishing a strong teaching presence in a remotely taught course (Prince et al., 2020), it could be valuable for instructors to delay their responses so that peers have an opportunity to provide input first.

5.6.2.4 Assignments and final project

In each assignment notebook, copious scaffolding around each problem (e.g., step-by-step instructions, expected intermediate results, and links to documentation websites) was provided, which created an environment of "structured inquiry" and "guided inquiry," the second and third levels of the continuum of inquiry proposed by Banchi and Bell (2008). The assignments were designed to be challenging yet were viewed favorably by both the student focus group and the final evaluation respondents. Both, however, indicated a desire for more short, frequent, low-stakes practice opportunities to help reinforce concepts and check understanding. Such practice exercises centered on coding skills rather than scientific inquiry would exist outside of the hierarchy of Banchi and Bell (2008) and yet may be critical for providing a strong foundation when teaching a programming language.

In contrast to instructor-generated assignments, the final project elicited student-designed questions and hypotheses indicating cognition on higher levels of Bloom's taxonomy (Bloom et al., 1956; Krathwohl, 2002). The resulting research spanned a wide range of disciplines, topics, data sources, and analysis techniques. This reflects "open inquiry," an experience that is exceedingly rare in undergraduate oceanography teaching (McDonnell et al., 2015). Consistent

with a constructivist approach to learning (Bada, 2015), students in OCEAN 215 answered complex or potentially ill-structured questions using messy and incomplete real-world datasets (e.g., Ellwein et al., 2014; Klug et al., 2017) with instructor guidance mostly related to feasibility. As demonstrated by graded assessments of the projects, students successfully conducted research despite it having unknown outcomes. In similar courses that incorporate open-ended research, students have reported learning gains equivalent to those of dedicated summer research programs (Lopatto, 2010).

Pair programming has been known to improve student learning, performance, and satisfaction in the computer science classroom, without loss of competency on exams (e.g., Williams & Upchurch, 2001; McDowell et al., 2002). While not a causal analysis, we find a positive correlation between pair programming experiences and final grades. In a survey of undergraduates who conducted collaborative research, almost 80% reported that working in teams or pairs enhanced their research experience (Lopatto, 2010), consistent with feedback from our focus group and final evaluations. We found pair programming to be readily adaptable to the virtual classroom using Zoom screen-sharing, with the caveat that Colab notebooks must be refreshed to show updates and thus edits must be made by one user at a time rather than synchronously. One lesson learned was that some pairs will gravitate toward asynchronous collaboration (i.e., a division of labor, rather than true pair programming) unless it is specified that the coding must be done synchronously. Additionally, collaborations appeared to prove more successful when coding partners had a preexisting working relationship; naturally, this is less likely to occur in a remotely taught introductory class setting. Nonetheless, previous work has found equal benefits to student performance and confidence for students who pair program remotely using screen-sharing and audio connectivity compared to physically collocated student pairs (Hanks, 2005).

5.6.3 Accessibility and inclusivity

Instructional approaches focused on active learning and student engagement can help to combat inequities in the classroom (Theobald et al., 2020), but equally important are strategies that promote a culture of respect and foster a sense of belonging for students (Dewsbury & Brame, 2019). A classroom community built on mutual understanding and respect promotes engagement, especially among students with marginalized identities, by creating a supportive space to share ideas and ask questions (S. E. Barrett, 2021). With that in mind, efforts were made to ensure that the course was accessible for all students despite pandemic-related disruptions so that those with varying backgrounds and needs felt welcome. These supportive strategies, some of which are discussed elsewhere in this paper, included accommodating disabilities, captioning lesson videos, co-creating classroom norms, affirming students' gender identities, starting class with icebreakers and anonymous feedback polls, endeavoring to mitigate "Zoom fatigue," setting flexible attendance and extension policies, offering virtual office hours, facilitating the participation of students located in remote time zones, and offering one-on-one mentoring as needed. While our study design did not specifically assess their impact, the intentional incorporation of these elements likely influenced student outcomes and perceptions in the course.

Our overall approach of providing multiple modalities for student learning was consistent with a universal design for learning (UDL) framework that prioritizes equitable and inclusive teaching (Meyer et al., 2014; Capp, 2017). UDL outlines three core principles: (1) multiple means of representation, which our course accomplished through recorded lessons with text, auditory, and visual components, live coding demonstrations, and permissive use of external resources; (2) multiple means of action and expression, facilitated through practice opportunities and assignments with varying degrees of structure; and (3) multiple means of engagement, enabled by our use of individual as well as group work, verbal as well as chat-based participation, peer instruction, office hours, and the online forum.

5.7 Limitations

The robustness of our conclusions is limited by the relatively small sample size (25 students) and the study's focus on a single academic quarter. Additionally, missing IAS evaluations from Spring 2015 and Autumn 2018 are not included in our longitudinal comparison to previous years' course evaluations. In this comparison, we also cannot disentangle the various influences of the COVID-19 pandemic on learning from the impact of the curriculum changes that we made. Furthermore, we cannot quantify the impact of the new teaching team's positionality as graduate students on students' impression of course quality. A previous study, for example, found that professors who were perceived as younger received higher evaluations than professors teaching identical content who were perceived as older (Arbuckle & Williams, 2003).

While a pre-quarter assessment of student coding competency and attitudes would have been an ideal way to assess student growth, such an assessment was not conducted as the study design was conceived after the course had concluded. Data on students' age, race, and ethnicity were not collected for similar reasons, so we were unable to explore relationships between demographic profiles and students' experiences or success in the course. Likewise, student achievement for two of the six course SLOs (#1 and #3) could not be explicitly measured using available data, although an assessment of final projects found that students successfully met the remaining four SLOs.

A systematic approach is used to identify and tabulate themes in the evaluation responses (see Evaluation section). However, we do not apply the same technique to qualitative data from the student focus group or their testimonials. The small sample size (five students) and the non-representative nature of the group selected by instructors would limit the appropriateness and utility of such an approach. Furthermore, the focus group conversations were not open-ended, but rather guided by questions formulated by instructors after initial analyses of other data (e.g., evaluation results, student learning metrics, etc.). Focus group discussions were documented through paraphrased notes rather than an exact transcription, so direct quotes are not presented.

Testimonials were edited by instructors (as described in the Evaluation section "Student focus group"), further restricting the possibility of a quantitative thematic analysis approach.

5.8 Conclusions

5.8.1 Recommendations for future teaching

We recommend without reservations adopting the key elements that we describe in this paper, particularly flipped instruction, an online coding platform and discussion board, and strong attention to accessibility. That said, we encourage others to improve on our framework and regularly seek feedback from students, preferably in a format that allows for anonymity. For example, in course evaluations, students encouraged the addition of more frequent, low-stakes practice of basic skills to reinforce fundamental concepts (see Discussion section "Assignments and final project"). New practice opportunities would ideally be coupled with immediate feedback that guides further practice, which promotes efficient learning and refinement of conceptual understanding (Ambrose et al., 2010). While we did not implement graded comprehension checks for videos, these could be useful in a situation of lower engagement (Jacobs et al., 2016). Additionally, data literacy skills could be taught through higher-level exercises asking students to scrutinize the limitations, biases, and provenance of scientific data sets and make predictions and recommendations grounded in their analysis of data (see, e.g., Kastens & Krumhansl, 2017). Instructors may consider expanding our offering into a multi-course sequence to incorporate these elements.

We acknowledge the ongoing paradigm shift in many scientific fields toward "open science," a broadly defined set of ethics that encapsulates practices like code reproducibility, curation of data for reuse, and open journal access (Brett et al., 2020; Ramachandran et al., 2021). While these practices were not explicitly taught in this course, its emphasis on collaborative programming, well-documented code, and the scientific method as an open, transparent endeavor

speak to fundamental open science principles. Explicit instruction on advanced topics like reproducibility, data archival, version control using Git and GitHub (e.g., Blischak et al., 2016), manipulation of large data sets stored on the cloud (e.g., Gentemann et al., 2021), and command-line interfaces may be more appropriate for a separate, higher-level course. While this course relied on original content, instructors could consider offering excerpts from existing earth science-oriented Python textbooks as a resource (Alyuruk, 2019; DeCaria & Petty, 2021; Esmaili, 2021; Palomino et al., 2021; Wei-Bing Lin et al., 2022).

The pandemic likely accelerated existing trends in higher education toward multi-modal instruction and more engaging teaching practices (Lockee, 2021). Though universities have transitioned back to in-person teaching, an interested and highly-engaged instructor team could still offer a fully remote version of this course, potentially with minimal penalty in student performance and satisfaction compared to in-person instruction (Ghosh et al., 2022; Ramirez et al., 2022). We believe that the framework developed for this course is also well-suited to a hybrid approach that incorporates in-person tutorial and work sessions but retains the pedagogical and accessibility benefits of recorded lesson videos, virtual office hours, and platforms that enable regular online engagement. Since 2020, this course has been offered annually in-person at the University of Washington by other graduate instructor teams with a flipped structure and most of the key curriculum elements introduced in this study.

5.8.2 Impact

The impact of this course extends beyond the students who enrolled in Autumn 2020. The flipped lesson videos were uploaded to a dedicated YouTube channel (https://www.youtube.com/@ocean215python), where they have been collectively viewed more than 27,000 times as of June 2024, reaching 40 different countries. Furthermore, the graduate student instructors have benefited from the professional experience of developing a curriculum and managing a classroom. Opportunities such as this have been linked with the success of

doctoral students attaining future employment in higher education (Bettinger et al., 2016). Our department plans for a rotating cast of two graduate students to continue serving as the primary teaching team, with the guidance and support of a dedicated teaching mentor to develop their pedagogical skills.

For many undergraduate oceanography majors without a deeper interest in data science, multiple quarters may pass after completing OCEAN 215 before their next opportunity to use programming. For most, this comes in the form of their senior thesis. Students' demonstrated loss of coding skills during past intervening years (see Implementation section "Course history and development") is consistent with previous findings from online programming courses (Teusner et al., 2018). An exploratory analysis of programming usage in the senior theses of students who completed OCEAN 215 in Autumn 2020 compared to past senior theses nonetheless shows a notable increase in the use of coding languages, including Python, for computation and figure generation. While potential confounding factors related to differences between years prevent definite conclusions, this improvement suggests the value of our instructional design in fostering content acquisition and retention of skills.

Yet even an effective programming course's impacts will wane over time without regular, scaffolded opportunities for students to practice and apply programming skills. Barriers to incorporating programming into geoscience undergraduate curricula include coalescing around a primary language of instruction while realizing the benefits of exposing students to other languages—many instructors, for example, use MATLAB for research—and implementing a curriculum map that communicates a standard set of programming skills for students. Mastery and retention of a programming language requires repeated exposure and practice opportunities, and so programming should be integrated across all levels of an earth science curriculum. Effort should also be invested in creating supervised research opportunities for students that involve the use of programming and data analysis. More broadly, we see the need for earth science undergraduate curricula to adopt active, student-centered pedagogical practices that more

frequently allow students to construct knowledge through hands-on exploration of real-world data. Infusing earth science curricula with current data programming practices will naturally facilitate the achievement of these goals.

5.9 Code and data availability

The Python code used to generate the figures in this chapter is available at https://github.com/ethan-campbell/Python_teaching_paper and archived on Zenodo (Campbell & Christensen, 2024). The underlying student data analyzed in this study are not publicly available to ensure the privacy of student participants.

5.10 Supplementary figures

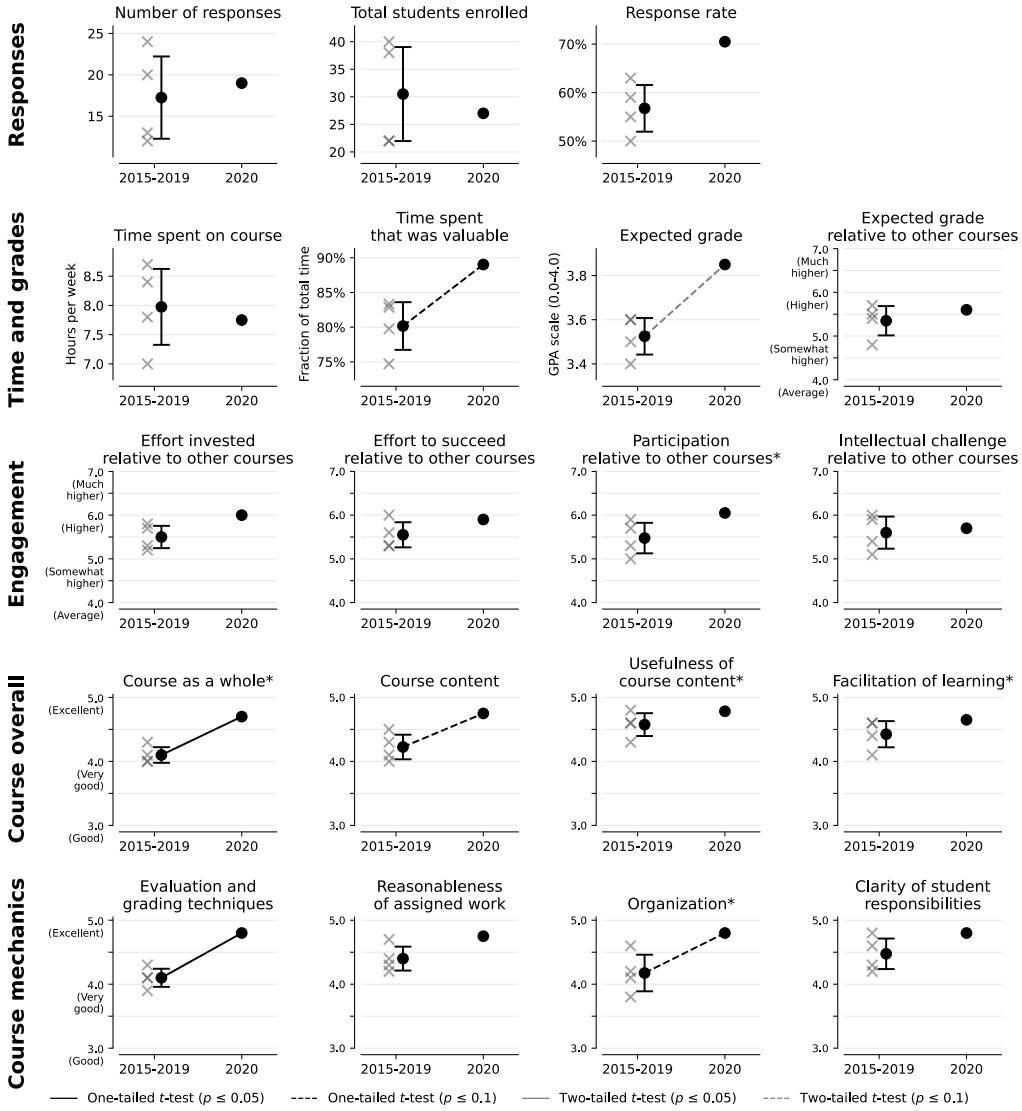

Supplementary Figure 5.8: All metrics from anonymous final student evaluations in 2015, 2016, 2017, 2019, and 2020 (see Evaluation section "Surveys and evaluations"). Differently worded questions, indicated with an asterisk (*), were mapped between years as shown in Supplementary Table 5.6. Metrics shown are class medians for 2015, 2016, 2017, and 2019 (gray crosses, except for those in the first row ["Responses"]); 2015–2019 mean or 2020 class median (black points); and 2015-2019 standard deviation (bars). Changes from 2015–2019 to 2020 were tested for a significant increase using a one-tailed (black line) *t*-test or a significant change using a two-tailed (gray line) *t*-test at the 95% (solid line) or 90% (dashed line) confidence level according to the methodology detailed in Evaluation section "Surveys and evaluations." An absence of a line connecting the 2015–2019 and 2020 data indicates no statistically significant improvement or difference. Note that y-axes have been truncated from the full 1–5 scale ("Very poor" to "Excellent") or 1–7 scale ("Much lower" to "Much higher"). Evaluation questions for which a consistent mapping across years was not possible were excluded; instructor-specific questions are also not shown.

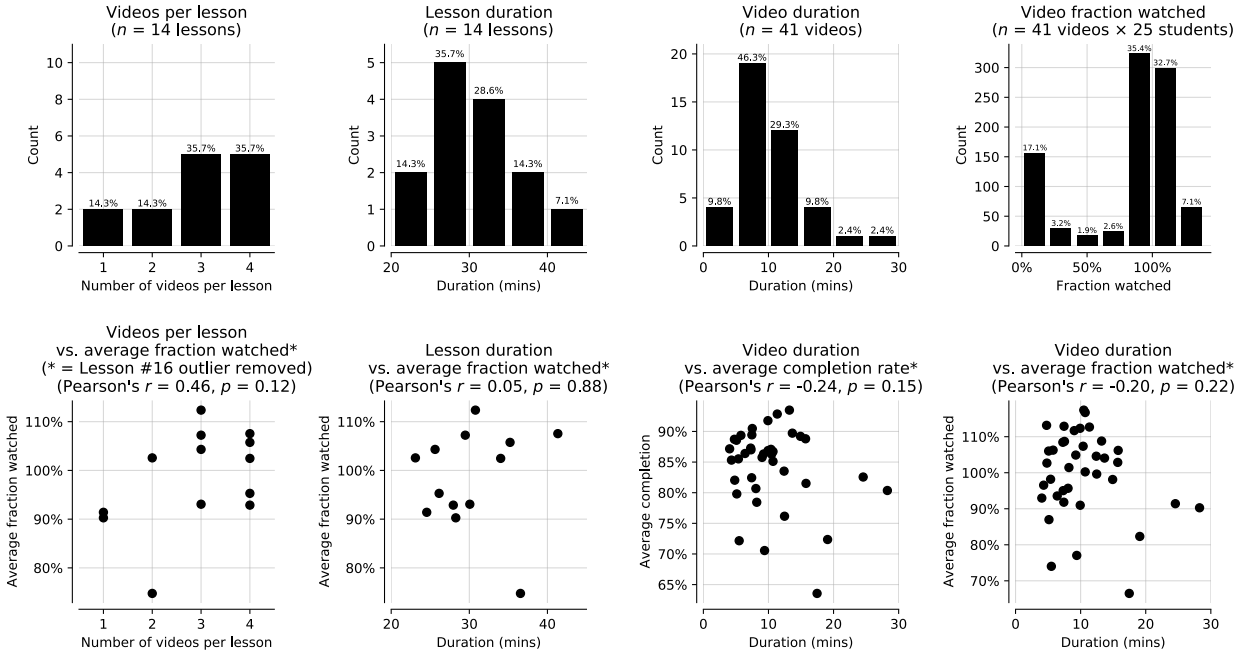

Supplementary Figure 5.9: Additional statistics on flipped lesson videos that were posted and viewed on the Panopto platform, based on video-specific metrics obtained from Panopto. Pearson's *r* represents the linear correlation between two variables. Note that none of the correlations tested in panels **(e–h)** were significant at the 95% ($p \leq 0.05$) or 90% ($p \leq 0.1$) confidence level. **(a)** Distribution of number of videos included per lesson (as the 14 topical lessons were usually split into multiple videos). **(b)** Distribution of the total duration of lessons. **(c)** Distribution of individual video duration. **(d)** Distribution of fraction of each video watched for each student. Fraction watched represents the total minutes that a specific video was viewed by a specific student divided by its duration, and thus can exceed 100% due to rewinds and repeat views. **(e)** Videos per lesson vs. video fraction watched, averaged across all students. Note that the final video lesson (Lesson #16) was excluded as an outlier due to its lower viewership where indicated using an asterisk (*). **(f)** Lesson duration vs. fraction watched, averaged across all students. **(g)** Video duration vs. completion rate, averaged across all students. Completion rate represents the fraction of a video that was viewed at least once, and thus is capped at 100% for a specific student and video (unlike "fraction watched"). **(h)** Video duration vs. fraction watched, averaged across all students.

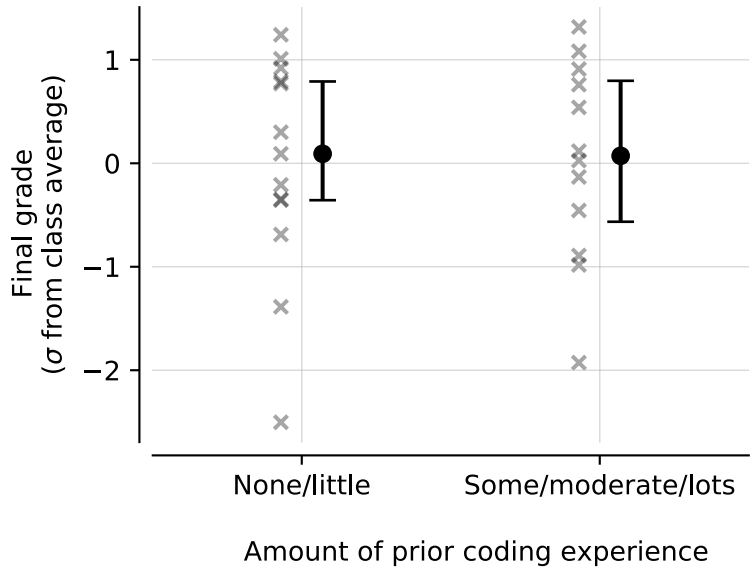

Supplementary Figure 5.10: Final course grades dichotomized by amount of prior coding experience. Coding experience was assessed using students' written responses to the Assignment #0 survey (see Supplementary Table 5.5 for rubric and methodology) and is divided here into two groups with none/little experience (score of 1 or 2) and some/moderate/lots of experience (score of 3, 4, or 5) containing approximately equal numbers of students. Final grades were recalculated to ignore two students' incomplete assignments (see Evaluation section "Final grades") and are expressed as standard deviations from the class average (gray crosses). Error bars represent the median and interquartile range (25%–75%) of final grades for each population. No significant difference in final grades was found between the two groups using a two-sided *t*-test ($p = 0.89$).

5.11 Supplementary tables

Supplementary Table 5.3: Functions, operators, and methods taught in the course that were used as search terms to assess the complexity of students' final project code. A Python script was used to count instances of each search term in students' project code notebooks, and the number of search terms used at least once (expressed as a percent of all search terms below) is presented as the metric "Python skills used in project" in Figure 5.4.

Topic	Search terms
Basic functions	'len(', 'print(', 'display(', 'range(', 'enumerate(', 'zip(', 'int(', 'float(', 'complex(', 'bool(', 'tuple(', 'type(', 'readline('
Lists	'list(', '.append(', '.extend(', '.insert(', '.remove(', 'del', '.pop(', '.reverse(', '.copy(', '.join(', '.sort('
Strings	'str(', '.lstrip(', '.rstrip(', '.upper(', '.lower(', '.count(', '.replace(', '.split(', '.format('
NumPy	'np.array(', '.dtype', '.astype(', 'np.append(', 'np.insert(', 'np.flip(', 'np.tolist(', '.sum(', '.mean(', '.median(', '.max(', '.min(', 'np.std(', 'np.pi', 'np.e', 'np.inf', 'np.nan', 'np.absolute(', 'np.round(', 'np.sqrt(', 'np.exp(', 'np.sin(', 'np.cos(', 'np.zeros(', 'np.ones(', 'np.full(', 'np.arange(', 'np.linspace(', '.size', '.ndim', '.shape', '.reshape(', ',flatten(', '.transpose(', '.vstack(', '.hstack(', 'np.genfromtxt(', 'np.meshgrid('
Time	'datetime.now()', '.year', '.month', '.day', '.hour', '.minute', '.second', '.microsecond', 'datetime.strptime', 'datetime.strftime', '.total_seconds()', 'timedelta', 'mdates.date2num('
Pandas	'.Series(', '.index', '.values', '.loc[', '.iloc[', 'pd.concat(', 'pd.DataFrame(', '.describe(', '.to_csv(', '.read_csv(', '.read_excel('
Xarray	'.open_dataset(', '.open_mfdataset(', '.attrs', '.isel(', '.sel(', '.item'
SciPy	'stats.linregress(', 'interpolate.interp1d(', 'interpolate.griddata('
Plotting	'.figure(', '.subplots(', '.xlabel(', '.ylabel(', '.set_xlabel(', '.set_ylabel(', '.grid', '.colorbar', '.set_label', '.clabel', '.invert_yaxis', '.gca', '.axes', '.coastlines', '.add_feature(', '.set_extent('
Plot types	'.plot(', '.scatter(', '.hist(', '.contour(', '.contourf(', '.pcolormesh('
Logic	' if ', ' while ', ' for ', ' is ', ' in ', ' not ', ' else:', ' elif ', ' and ', '~', '==', '!=', '>=', '<='

Supplementary Table 5.4: Grading rubric for students' final research projects. In the first column, corresponding main student learning objectives (SLOs) are appended to the rubric (see Implementation section "Course history and development" for the full numbered list of SLOs). Figure 5.3 depicts assessments of students' final projects using this rubric, grouped by theme and SLOs.

Corresponding main student learning outcome(s)		Limited (0-50%)	Good (50-75%)	Exceptional (75-100%)	
	Presentation content				
SLO #5 ("Formulate and investigate scientific research questions")	Background	Topic background is missing or severely lacking in detail.	Topic background is sufficient, but missing some details or lacks coherency.	Topic background is clear, complete, and relevant.	3 points
	Questions / hypotheses	Questions are not well-defined. Hypotheses are not substantiated.	Questions are well-defined. Hypotheses draw on prior knowledge.	Questions are well-defined and pertinent for the topic. Hypotheses draw on prior knowledge and have clear explanations for why they are expected.	2 points
SLO #3 ("Access, read, transform… and interpret oceanographic data with confidence using Python")	Data collection	Information about the data collection process is missing key details or is inaccurate. The limitations of the data are missing or not realistic.	Information about the data collection process is accurate, but missing some minor details. The limitations of the data are explained.	Information about the data collection process is complete and accurate. Underlying problems and limitations of the data are explained. Use of these data to answer the project questions is justified.	3 points
	Data processing	The student has made errors in processing their data. The student is missing steps.	The student has processed the data correctly. Steps for obtaining, loading, cleaning, and analyzing the data are well-defined.	The student has processed the data correctly and taken precautions to ensure that their results are appropriate. Steps for obtaining, loading, cleaning, and analyzing the data are well-defined.	3 points
	Results / interpretation	Results of the project do not attempt to answer the scientific questions. The data visualizations are not relevant.	Results of the project somewhat answer the scientific questions. Data visualizations are mostly appropriate for the data.	Results of the project answer, or earnestly attempt to answer, the scientific questions. Data visualizations are entirely appropriate for the data.	3 points

	Presentation skills				
N/A	Organization	The presentation is not in a logical order and the student makes no effort to guide the audience.	The presentation is organized in a logical order and takes some care to guide the audience.	The presentation is organized in a logical order and shows exceptional attention to guiding the audience.	2 points
	Timing	The student far exceeds their allotted time and/or has not made an effort to practice.	The student completes the presentation in somewhat over 5 minutes.	The student completes the presentation within 5 minutes and it is clear that they have practiced.	1 point
SLO #5 ("Formulate and investigate scientific research questions")	Explanation of ideas / information	The ideas and information explained in the presentation were not clear and were not relevant.	The ideas and information explained in the presentation were clear and relevant.	The ideas and information explained in the presentation were exceptionally clear, relevant, and coherent.	3 points
	Code				
SLO #2 ("Write, execute, and debug Python code"), SLO #6 ("Adopt best practices in programming")	Correctness	The student misuses code and does not produce reasonable results.	The student uses some coding techniques/tools learned throughout the quarter. The analysis produces reasonable answers that can be replicated with some effort.	The student properly and efficiently uses the coding techniques/tools learned throughout the quarter. The analysis produces reasonable answers that can be replicated easily.	8 points
	Functionality	The code does not run and has egregious errors.	The code is mostly able to run, but has some (small) errors.	The code runs efficiently with no errors.	5 points
	Tidiness	The code breaks proper etiquette and should not be shared with others.	The code mostly follows proper coding etiquette. The organization is somewhat lacking and would need review before sharing.	The code follows proper coding etiquette. It is organized and commented effectively so that it can easily be shared with another person.	6 points
	Perseverance	The student has made no effort to work through problems and hurdles.	The student has made some effort to work through problems.	The student has made a gallant effort to work through problems and documented in their code their best understanding of the problems they are facing.	5 points

	Visualizations				
SLO #3 ("… visualize… oceanographic data with confidence using Python"), SLO #6 ("Adopt best practices in… data visualization")	Plot clarity	The plots are unclear and do not make sense in the context of the project.	The plots are mostly clear and show some thought from the students about ways to present their data.	The plots are extremely clear and are effective tools to help the audience understand the results/analysis.	5 points
	Colormaps	The colormaps are not appropriate for the data being shown.	The colormaps are appropriate for the data being shown.	The colormaps are appropriate for the data being shown and take into account colorblindness, and perceptual accuracy.	3 points
	Proper labels	The plots are missing most/all labels or have improper labels.	The plots are labeled with general accuracy and completion.	The plots are labeled extremely accurately in a way that guides the audience through the figure.	5 points
	Creativity	The student made no effort to create original plots.	The student has made some effort to create original plots.	The student has created original plots that show the data/analysis in an extremely effective manner.	3 points

Supplementary Table 5.5: Rubric used to assess students' prior coding experience based on their written responses to the Assignment #0 survey during Week 1 of the course. Students were asked: "Do you have prior coding experience, and if so, with what language?" and "How comfortable do you feel using technology?" Responses to the first question were graded subjectively based on word choice on a scale from 1–5, using the keywords in quotes (e.g., "a little") when present. As noted below, additional points were awarded to weight responses in favor of prior exposure to Python or similar high-level and/or interpreted languages (MATLAB, Java, R). Points were subtracted to account for less relevant prior experience. If no level of coding proficiency was provided, the base number used was from the students' "comfort with technology" statement ("Very comfortable": 4; "Fairly comfortable": 2). Results are used in Supplementary Figure 5.10 and presented as the metric "Prior coding experience" in Figure 5.4.

1	**2**	**3**	**4**	**5**
No experience	Minimal experience (e.g., "a little", "small", "tiny amount")	"Some" or "moderate" experience	Experience	Experience (with full additions)

Additions (maximum total: +1.0)	**Subtractions (maximum total: -0.5)**
+0.5 for one of MATLAB, Java, R	-0.5 if response mentions many years since their previous experience
+1.0 for Python or multiple languages	-0.5 if response mentions that their previous experience was not useful

Supplementary Table 5.6: Mapping of university-administered IAS final course evaluation questions from 2015–2019 to 2020. The mapping allows the slightly different evaluation questions from the two periods to be compared in Figure 5.2 and Supplementary Figure 5.8. Metrics listed are the median of responses collected for each class.

Paraphrased question	Original evaluation question(s) (2015–2019)	Original evaluation question(s) (2020)	Metric and units
Time spent on course	On average, how many hours per week have you spent on this course, including attending classes, doing readings, reviewing notes, writing papers and any other course related work?		Hours per week
Time spent that was valuable	From the total average hours above, how many do you consider were valuable in advancing your education?		Hours per week, expressed as percent relative to response to question above
Expected grade	What grade do you expect in this course?		GPA scale (0.0–4.0)
Expected grade relative to other courses	Do you expect your grade in this course to be:		1-7 scale ("Much lower" to "Much higher")
Effort invested relative to other courses	The amount of effort you put into this course was:		
Effort to succeed relative to other courses	The amount of effort to succeed in this course was:		
Participation relative to other courses	Your involvement in course (doing assignments, attending classes, etc.) was:	Relative to similar courses taught in person, your participation in this course was:	
Intellectual challenge relative to other courses	The intellectual challenge presented was:		
Course as a whole	The course as a whole was:	The remote learning course as a whole was:	0–5 scale ("Very poor" to "Excellent")
Course content	The course content was:		
Usefulness of course content	Relevance and usefulness of course content were:	Average of: "Usefulness of reading assignments in understanding course content was:", "Usefulness of written assignments in understanding course content was:", "Usefulness of online resources in understanding course content was:"	
Facilitation of learning	Amount you learned in the course was:	The effectiveness of this remote course in facilitating my learning was:	
Evaluation and grading techniques	Evaluative and grading techniques (tests, papers, projects, etc.) were:		

Reasonableness of assigned work	Reasonableness of assigned work was:	
Organization	Course organization was:	Organization of materials online was:
Clarity of student responsibilities	Clarity of student responsibilities and requirements was:	
Instructor's contribution to the course	The instructor's contribution to the course was:	
Effectiveness of instructor's teaching	The instructor's effectiveness in teaching the subject matter was:	
Quality of instructor answers and feedback	Average of: "Explanations by instructor were:", "Instructor's ability to present alternative explanations when needed was:", "Instructor's interest in whether students learned was:", "Answers to student questions were:"	Quality/helpfulness of instructor feedback was:

Supplementary Table 5.7: Open-ended questions asked in university-administered IAS mid-quarter and final course evaluations in 2020. Students' anonymous responses are tabulated in Figure 5.5 and are excerpted throughout this study.

Evaluation period	**Question**
Mid-quarter	What is helping you to learn in this course?
	What is hindering your learning in this course?
	What can your instructor do to improve your learning in this course?
Final	Was this class intellectually stimulating? Did it stretch your thinking? Why or why not?
	What aspects of this class contributed most to your learning?
	What aspects of this class detracted from your learning?
	What suggestions do you have for improving this class generally?
	If this course were offered remotely again, what suggestions do you have to improve the student experience?

Supplementary Table 5.8: List of guiding questions offered to undergraduate student focus group for structuring their testimonial submissions, which are presented in Supplementary Text 5.2 (also see Evaluation section "Student focus group"). Students were encouraged to address one or more of the questions in their submissions.

1. How did your prior experience with coding (or lack of prior experience) impact your experience with the course? If you have prior coding experience and it was self-taught, what do you see as the benefits of learning scientific programming in a structured environment rather than teaching it to yourself? If your prior coding knowledge was learned from course(s), how did we teach programming that was different and more or less effective than those past course(s)?

2. How did the accessibility elements that we implemented (e.g., captioning, syllabus late policy, extensions, not grading on attendance, breaks during class, virtual office hours, making slide decks available, video optional on Zoom, ability to use chat during class, no course prerequisites, extra credit opportunities, etc.) affect your success in the course?

3. How did the expectations and norms established in the course impact your experience?

4. How did you navigate the course policies we created on collaboration and original work? If you worked with a partner on assignments and/or the final project, what was your experience like? Was it productive/challenging/surprising, and how did the technological tools we used (Colab, Zoom) facilitate it? What advice would you give to professors who are teaching a programming course and want to create opportunities for collaboration?

5. How did the key course elements (recorded videos, in-class activities, assignments, final project, etc.) and technological platforms (Google Colab, Piazza, Zoom, Google Drive/Docs, Canvas) help or hinder your learning?

6. Instead of a textbook, we allowed use of external resources (e.g., documentation websites, Stack Overflow, etc.). How did this compare to having a textbook for the course?

7. How did guidance from the instructors and classmates (via Piazza or in class) help you complete assignments and shape and execute your final project?

8. In what ways did the class help you learn about oceanography sub-disciplines (marine geology, chemistry, physics, biology) or other earth science subjects adjacent to oceanography (e.g., cryosphere, meteorology, climate)? What value do you see in teaching programming in an oceanography curriculum rather than a computer science department?

9. How do you feel this course fit into your overall undergraduate education? How did this course prepare you for future research, like your senior thesis? In what ways do you feel more capable now that you have Python in your arsenal?

10. How do you feel this course shaped your career/life goals or motivation to pursue oceanography or data science during and after college?

11. What was it like taking this class during the pandemic? How does this course compare to other classes you've taken remotely during the pandemic?

5.12 Supplementary text

Supplementary Text 5.1. Final project assignment handout. Note that the grading rubric presented as Supplementary Table 5.4 (modified to include corresponding SLOs) was also distributed to students. A list of due dates is not included here.

OCEAN 215 | Autumn 2020 | **Final project**

During this course, you will conduct a small scientific research project from start to finish. You will choose a topic, produce a scientific question related to your topic, suggest a hypothesis, locate data that will help support or reject your hypothesis, analyze/visualize this data using Python, and present your findings to the class. Along the way, you will be responsible for giving your input on other students' projects and you will receive input from other students as well. To further reflect the collaborative nature of scientific research, we also encourage you to post any questions or challenges you encounter during this project to the class on Piazza. **If you wish, you may work with a partner on this project. See below for important information if you choose this option.**

The majority of this project will involve writing Python code to analyze and visualize your chosen data. We will dedicate a substantial amount of class time for this work, during which instructors and peers will be present to help you work through coding challenges. Throughout the quarter, there are a number of due dates for different parts (see the table above) designed to guide you through completing your research. The expectations for the deliverables of this project are detailed below:

1. **Topic check-in:** Consider a topic of research that you would like to examine. If you are having trouble identifying a topic, contact the instructors privately on Piazza so they can help you find something that interests you. Once you have identified your topic, create a private note to the instructors on Piazza in the 'final_project' folder that answers the questions below.
    - What research topics or questions are you interested in?
    - What type(s) of data would help you look into those topics/questions?

2. **Data check-in:** Locate data that will help you look into your selected topic. We will set aside some class time for students to work on this. You can start your exploration by using an internet search engine to look up background information on your topic and find possible data sources. You can also use the oceanography data repositories (e.g. PO.DAAC, NASA Giovanni, BCO-DMO, etc.) listed in the Class #1 slides. As always, the instructors are also available to help you locate a fitting data source. In the 'final_project' folder of Piazza, respond to the data check-in post with answers to the questions below. Make sure that your response is visible to the whole class.
    - What data set(s) do you plan to use?
    - What is one scientific question that you might be able to answer using these data?
    - What is your hypothesis? What do you anticipate the answer to your scientific question is, and why? (try to bring in scientific knowledge from previous courses, published literature, and/or reliable internet sources)

3. **Piazza responses:** Respond to at least three other data check-in posts written by your classmates on Piazza with an additional question that they might be able to investigate using their data or about their topic. To reflect the collaborative nature of research, where colleagues often help to dictate research priorities, you will choose one question suggested by a classmate and one question of your own to investigate.

4. **Project presentations:** Present the results of your project to the class in a five-minute presentation. Presentation schedules will be posted to Canvas later this quarter. Your presentation should include the following:
    - Scientific background on your topic [~1 slide]
    - Two scientific questions (yours and a classmate's from Piazza) with your hypotheses [~1 slide]
    - Information about your data (How/when/where was it collected? What instruments were used? Are there any limitations to your data?) [~1 slide]

- Your process for obtaining, loading, cleaning, visualizing and analyzing the data. Describe your data file format(s) and structure(s) as well as any challenges you encountered [~1–2 slides]
- Answers to your scientific questions with associated plots and an explanation of your analysis results [~2–3 slides, ~2–3 figures]

5. **Slides and code:** Submit the slides from your project presentation, your data files/folders, and the code you wrote to analyze your data and create your figures. Your code should follow proper coding etiquette and your figures should be formatted properly. To submit your code, data, and slides, save them and put them in your individual class Google Drive folder. There is no written essay required for this project.

NOTE: Piazza posts that are required for the final project do not count towards the required five Piazza posts detailed in the syllabus.

Pair programming option

If you wish, you may work with a partner on this project. This could be a valuable opportunity to experience a research collaboration, work through coding challenges together, and accomplish even more analysis! If you choose this option, the following expectations supersede (override) the requirements listed elsewhere in this document:

- Starting with the **data check-in**, you and your partner may choose a single data set together, and share this identical data set on Piazza. However, please each offer a **different scientific question and hypothesis** in your Piazza posts (i.e. the two of you will come up with two questions and two hypotheses in total).
- For the **Piazza responses**, you and your partner should **each respond to three classmates' posts** (not including your partner's post), for a total of six posts. You will jointly choose **one question from a classmate and two questions of your own** to investigate for your project, for a total of three questions to investigate.
- For the **final project presentations**, please prepare a single **8–10 minute slideshow**, instead of a 5-minute slideshow. Include at least the number of slides specified above for each category. Trade off roles when presenting (i.e. each person should be presenting for about 4–5 minutes).
- You may submit separate Colab code notebooks, or a single joint Colab notebook. However, in all notebooks submitted, please indicate which student wrote each section of code using Python comments. **We expect that both partners will contribute approximately equally to writing code for the project.**
- You will be graded jointly and **will receive the same grade for the project**, except under extenuating circumstances to be determined on a case-by-case basis.

Grading breakdown

Project Part	Grading	Points
Topic check-in:	Complete/Incomplete	10 points
Data check-in:	Complete/Incomplete	15 points
Piazza responses:	Complete/Incomplete	15 points
Project presentation:	See rubric	20 points
Code:	See rubric	40 points
		(100 points total)

Supplementary Text 5.2. Testimonials shared by undergraduate student coauthors (see Evaluation section "Student focus group" for more details). The students were encouraged to address one or more of the guiding questions listed in Supplementary Table 5.8 in their submissions.

Other coding classes that I have taken have generally failed to place skills in the context of applications. Without examples of methods being used, there is less of an incentive to understand them. In contrast, this course provided the opportunity to work with oceanographic data, allowing us to recognize the significance of the methods we were applying. For instance, ocean glider data was used to teach about interpolation. This was engaging because we first visualized the original, non-interpolated data and could see the gaps due to the physical motion of the device, then compared this with the data interpolated using the same axes and color scale.

Additionally, the lack of a textbook in this course made it easier to approach methods beyond what we learned in class. Instead, we learned to answer questions by accessing online resources like Stack Overflow. Doing so developed essential skills and gave me the confidence to apply new concepts in my final project. This meant my research could be dictated by my curiosity and questions, as it should be, and not by the limitations of what concepts we had covered in class.

In general, research can seem intimidating to many students because it relies on an individual's creativity. In other classes with exclusively rigid assignments and predetermined tasks, there is little opportunity for students to form original ideas, let alone develop them. In this class, we used creativity and critical thinking skills to develop a final project that answered an independently formed question. This experience has helped to prepare me for research. -O.B.

—

I previously took a Fortran class at the Ocean University of China, which had two traditional lectures and one lab each week. In that class, most students were not engaged during the lectures, which led them to be bewildered when doing real coding. I have also been teaching myself MATLAB for three years, basically learning by doing tasks with the help of the internet. This process has often been time-consuming, and it has been hard to organize my notes in a logical way. In comparison to those experiences, this course provided a logical pathway into Python, especially for oceanography applications. Without this class, it would have taken ten times longer to acquire the same knowledge, which would also have been less clear.

In class, Zoom breakout rooms forced everyone to discuss and practice the coding, which in turn forced us to come well-prepared for class. Though Google Colab has limited storage (RAM) and is unable to process large data sets, it is great for starters. Most of my other classes have been about theory and previously derived conclusions in the field, but this class has provided a bridge between theory and practice. After taking this course, I would say that we can now start to connect math and data to discover the areas of science we are interested in. -J.L.

—

I have always viewed research as something that is extraordinarily complicated. This class demonstrated that knowing a few basic Python functions and packages can provide a solid foundation to start conducting research. Additionally, offering this class as part of an oceanography curriculum instead of relying on a computer science department allowed us to learn about programming skills in a way that directly applied to our interests and studies.

I liked the way that the course was set up, in which we learned the material in an asynchronous video first and then practiced it in class. This helped me to discover where my gaps in understanding were and to learn from other people who may have understood a concept better than I did. Google Colab may not be the most powerful programming platform, but it is streamlined and easy to use, which made it great for first-time coders like me. Piazza was also an exceptionally useful resource.

Many classes present an idealized version of how research works. This class didn't. It was an important learning experience when my final research project didn't yield the correlation I expected. This was frustrating since I put so much time and effort into the project, but it showed that a lack of correlation can be an important result and that one's research doesn't always have to produce a major scientific breakthrough. -R.M.

—

I came in with a little prior coding experience thanks to robotic projects that I completed with my father as a child. In taking this class, the love of coding that I had as a child was reignited. I hadn't realized how beneficial and necessary knowing a programming language would be for research. Having Python in my arsenal opened up research

opportunities that I wouldn't have been qualified for before and can aid me in branching out beyond oceanography in the future. The great experience I had in this class—and my realization that research and coding are extremely integrated—inspired me to pursue a minor in Data Science.

In this class, the coding assignments were based on real-world problem solving. I loved having the opportunity to work with a partner because we coded in completely different ways, and it was fascinating to see those differences. We were more effective together because we learned to compromise and collaborate to find the cleanest and fastest method between the two of us. Writing code on Zoom was a good alternative to in-person collaboration because we could share our screens and help pinpoint issues in each other's code. In addition, Piazza was helpful for me because it allowed anonymous or private questions, which avoids the uncomfortable feeling of asking a question that you think might be silly. I liked that we were able to get quick and helpful feedback on our code. It was a better way of communicating than those I have used in other classes, like email, which might get drowned out in a teacher's inbox, or Slack, which doesn't provide the anonymity that Piazza does. -I.O.

Chapter 6:

CONCLUSIONS

In this thesis, autonomous observing platforms and Lagrangian modeling were utilized to address three long-standing questions related to the Southern Ocean: what processes govern the formation of open-ocean polynyas in the Weddell Sea; whether Antarctic sea ice formation and melt can be accurately inferred from ocean observations; and how snow loss and transformation processes influence the fate of snow deposited on sea ice. The final chapter of the thesis describes and evaluates an evidence-based model for teaching introductory programming to undergraduate students within a geoscience context.

The two portions of this thesis that constitute new, unpublished work—Chapters 3 and 4—share a focus on constraining key aspects of the Antarctic cryosphere that are challenging to measure directly. In situ measurements of sea ice evolution, such as those from ice mass balance buoys, and sea ice thickness, often derived from ice cores or shipboard observations, are typically labor-intensive, costly, or limited by potential sampling biases stemming from ship navigation patterns and the infrequency of field campaigns. In situ measurements of snow depth on sea ice, obtained from snow pits, probes, and cores, present similar difficulties.

The new Lagrangian snow model and mixed-layer salinity budget developed in Chapters 3 and 4 are not without uncertainties and the possibility for systematic bias—limitations that also apply to remote sensing retrievals and coupled model simulations. Nevertheless, these techniques leverage existing resources to provide complementary year-round, spatially extensive views of these critical variables. Ice-capable profiling floats deployed through the global Argo program and

regional initiatives like the Southern Ocean Carbon and Climate Observations and Modeling (SOCCOM) project now offer nearly two decades of ocean observations within the Antarctic seasonal ice zone. Atmospheric reanalysis data and established parameterizations of key snow processes are also readily accessible. These new methods should not be regarded as a substitute for in situ observations, which remain essential for calibrating and validating indirect estimates of sea ice and its overlying snow. Maintaining and expanding the existing float array in ice-covered regions of the Southern Ocean is essential for enabling more robust constraints on the rapidly evolving Antarctic sea ice system.

The reconstructions of snow and sea ice presented here provide insights into the Antarctic seasonal ice zone's snow mass budget, associated freshwater fluxes, and spatial and temporal variations in sea ice growth and melt. There is certainly ample opportunity to refine the methods described in these pages, which could increase their utility as a benchmark for current and future observational and estimation approaches. A logical next step is to synthesize the reconstructions from Chapters 3 and 4, accumulating sea ice growth and melt rates along ice drift trajectories to derive sea ice thickness and incorporating net snow accumulation rates to estimate snow-ice conversion. Coupling this Lagrangian framework with a one-dimensional ocean model could constrain other processes such as the impact of meteoric freshwater fluxes on ocean stratification or the effects of storm events on ocean heat fluxes, consequent sea ice thinning, and snow-ice formation.

Future work should build on these reconstruction techniques to explore interactions within the Antarctic air-snow-ice-ocean system, further integrating and comparing them with remote sensing retrievals and in situ observations. Achieving a holistic understanding of this coupled system is essential for addressing pressing societally relevant questions about the current and future state of the Southern Ocean and its sea ice cover.

BIBLIOGRAPHY

Abernathey, R. P., Cerovečki, I., Holland, P. R., Newsom, E., Mazloff, M., & Talley, L. D. (2016). Water-mass transformation by sea ice in the upper branch of the Southern Ocean overturning. *Nature Geoscience*, *9*(8), 596–601. https://doi.org/10.1038/ngeo2749

Abolafia-Rosenzweig, R., He, C., Chen, F., & Barlage, M. (2024). Evaluating and enhancing snow compaction process in the Noah-MP Land Surface Model. *Journal of Advances in Modeling Earth Systems*, *16*(2), e2023MS003869. https://doi.org/10.1029/2023MS003869

Alammary, A. (2019). Blended learning models for introductory programming courses: A systematic review. *PLoS ONE*, *14*(9), e0221765. https://doi.org/10.1371/journal.pone.0221765

von Albedyll, L., Haas, C., & Dierking, W. (2021). Linking sea ice deformation to ice thickness redistribution using high-resolution satellite and airborne observations. *The Cryosphere*, *15*(5), 2167–2186. https://doi.org/10.5194/tc-15-2167-2021

Alyuruk, H. (2019). *R and Python for oceanographers: A practical guide with applications*. Amsterdam: Elsevier. https://doi.org/10.1016/C2016-0-05114-8

Amante, C., & Eakins, B. W. (2009). *ETOPO1 1 arc-minute global relief model: procedures, data sources and analysis, NOAA Technical Memorandum NESDIS NGDC-24*. National Geophysical Data Center, NOAA. https://doi.org/10.7289/V5C8276M

Amblas, D., & Dowdeswell, J. A. (2018). Physiographic influences on dense shelf-water cascading down the Antarctic continental slope. *Earth-Science Reviews*, *185*, 887–900. https://doi.org/10.1016/j.earscirev.2018.07.014

Ambrose, S. A., Bridges, M. W., DiPietro, M., Lovett, M. C., & Norman, M. K. (2010). What kinds of practice and feedback enhance learning? In *How learning works: Seven research-based principles for smart teaching* (pp. 121–152). John Wiley & Sons, Inc.

Anderson, E. A. (1973). *National Weather Service river forecast system: Snow accumulation and ablation model. NOAA Technical Memorandum NWS-HYDRO-17.*

Anderson, E. A. (1976). *A point energy and mass balance model of a snow cover. NOAA Technical Report NWS 19.*

Anderson, E. A. (2006). *Snow Accumulation and Ablation Model – SNOW-17.* National Weather Service. https://www.weather.gov/media/owp/oh/hrl/docs/22snow17.pdf

Anderson, R. E., Ernst, M. D., Ordóñez, R., Pham, P., & Tribelhorn, B. (2015). A data programming CS1 course. In *SIGCSE 2015 - Proceedings of the 46th ACM Technical Symposium on Computer Science Education* (pp. 150–155). https://doi.org/10.1145/2676723.2677309

Aoki, S., Ono, K., Hirano, D., & Tamura, T. (2020). Continuous winter oceanic profiling in the Cape Darnley Polynya, East Antarctica. *Journal of Oceanography*, *76*(5), 365–372. https://doi.org/10.1007/s10872-020-00550-w

Arbetter, T. E., Lynch, A. H., & Bailey, D. A. (2004). Relationship between synoptic forcing and polynya formation in the Cosmonaut Sea: 1. Polynya climatology. *Journal of Geophysical Research*, *109*(C4), C04022. https://doi.org/10.1029/2003JC001837

Arbuckle, J., & Williams, B. D. (2003). Students' perceptions of expressiveness: age and gender effects on teacher evaluations. *Sex Roles*, *49*(9–10), 507–516. https://doi.org/10.1023/A1025832707002

Argo. (2021). Argo float data and metadata from Global Data Assembly Centre (Argo GDAC). SEANOE. https://doi.org/10.17882/42182

Armitage, T. W. K., Kwok, R., Thompson, A. F., & Cunningham, G. (2018). Dynamic topography and sea level anomalies of the Southern Ocean: Variability and teleconnections. *Journal of Geophysical*

Research: Oceans, *123*(1), 613–630. https://doi.org/10.1002/2017JC013534

Arms, S., Chastang, J., Grover, M., Thielen, J., Wilson, M., & Dirks, D. (2020). Introducing students to scientific Python for atmospheric science. *Bulletin of the American Meteorological Society*, *101*(9), E1492–E1496. https://doi.org/10.1175/BAMS-D-20-0069.1

Arndt, S., & Paul, S. (2018). Variability of winter snow properties on different spatial scales in the Weddell Sea. *Journal of Geophysical Research: Oceans*, *123*(12), 8862–8876. https://doi.org/10.1029/2018JC014447

Arndt, S., Meiners, K. M., Ricker, R., Krumpen, T., Katlein, C., & Nicolaus, M. (2017). Influence of snow depth and surface flooding on light transmission through Antarctic pack ice. *Journal of Geophysical Research: Oceans*, *122*(3), 2108–2119. https://doi.org/10.1002/2016JC012325

Arndt, S., Haas, C., Meyer, H., Peeken, I., & Krumpen, T. (2021). Recent observations of superimposed ice and snow ice on sea ice in the northwestern Weddell Sea. *The Cryosphere*, *15*(9), 4165–4178. https://doi.org/10.5194/tc-15-4165-2021

Arndt, S., Maaß, N., Rossmann, L., & Nicolaus, M. (2024). From snow accumulation to snow depth distributions by quantifying meteoric ice fractions in the Weddell Sea. *The Cryosphere*, *18*(4), 2001–2015. https://doi.org/10.5194/tc-18-2001-2024

Auger, M., Prandi, P., & Sallée, J.-B. (2022). Southern Ocean sea level anomaly in the sea ice-covered sector from multimission satellite observations. *Scientific Data*, *9*, 70. https://doi.org/10.1038/s41597-022-01166-z

Auger, M., Sallée, J., Prandi, P., & Naveira Garabato, A. C. (2022). Subpolar Southern Ocean seasonal variability of the geostrophic circulation from multi-mission satellite altimetry. *Journal of Geophysical Research: Oceans*, *127*(6), e2021JC018096. https://doi.org/10.1029/2021JC018096

Auger, M., Sallée, J., Thompson, A. F., Pauthenet, E., & Prandi, P. (2023). Southern Ocean ice-covered eddy properties from satellite altimetry. *Journal of Geophysical Research: Oceans*, *128*(4), e2022JC019363. https://doi.org/10.1029/2022JC019363

Ayer, V. M., Miguez, S., & Toby, B. H. (2014). Why scientists should learn to program in Python. *Powder Diffraction*, *29*(S2), S48–S64. https://doi.org/10.1017/S0885715614000931

Bada, S. O. (2015). Constructivism learning theory: A paradigm for teaching and learning. *Journal of Research & Method in Education*, *5*(6), 66–70. https://doi.org/10.9790/7388-05616670

Bailenson, J. N. (2021). Nonverbal overload: A theoretical argument for the causes of Zoom fatigue. *Technology, Mind, and Behavior*, *2*(1). https://doi.org/10.1037/tmb0000030

Bailey, D. A., Rhines, P. B., & Häkkinen, S. (2005). Formation and pathways of North Atlantic Deep Water in a coupled ice-ocean model of the Arctic-North Atlantic Oceans. *Climate Dynamics*, *25*(5), 497–516. https://doi.org/10.1007/s00382-005-0050-3

Banchi, H., & Bell, R. (2008). The many levels of inquiry. *Science and Children*, *46*(2), 26–29.

Barrett, A. P., Stroeve, J. C., & Serreze, M. C. (2020). Arctic Ocean precipitation from atmospheric reanalyses and comparisons with North Pole drifting station records. *Journal of Geophysical Research: Oceans*, *125*(1), e2019JC015415. https://doi.org/10.1029/2019JC015415

Barrett, S. E. (2021). Maintaining equitable and inclusive classroom communities online during the COVID-19 pandemic. *Journal of Teaching and Learning*, *15*(2), 102–116. https://doi.org/10.22329/jtl.v15i2.6683

Behrens, E., Rickard, G., Morgenstern, O., Martin, T., Osprey, A., & Joshi, M. (2016). Southern Ocean deep convection in global climate models: A driver for variability of subpolar gyres and Drake Passage transport on decadal timescales. *Journal of Geophysical Research: Oceans*, *121*(6), 3905–3925. https://doi.org/10.1002/2015JC011286

Beitsch, A., Kaleschke, L., & Kern, S. (2014). Investigating high-resolution AMSR2 sea ice concentrations during the February 2013 fracture event in the Beaufort Sea. *Remote Sensing*, *6*(5), 3841–3856.

https://doi.org/10.3390/rs6053841

Bergstra, J., & Bengio, J. (2012). Random search for hyper-parameter optimization. *Journal of Machine Learning Research*, *13*(10), 281–305.

Bernardello, R., Marinov, I., Palter, J. B., Galbraith, E. D., & Sarmiento, J. L. (2014). Impact of Weddell Sea deep convection on natural and anthropogenic carbon in a climate model. *Geophysical Research Letters*, *41*(20), 7262–7269. https://doi.org/10.1002/2014GL061313

Bettinger, E. P., Long, B. T., & Taylor, E. S. (2016). When inputs are outputs: The case of graduate student instructors. *Economics of Education Review*, *52*, 63–76. https://doi.org/10.1016/j.econedurev.2016.01.005

Blanchard-Wrigglesworth, E., Webster, M. A., Farrell, S. L., & Bitz, C. M. (2018). Reconstruction of snow on Arctic sea ice. *Journal of Geophysical Research: Oceans*, *123*(5), 3588–3602. https://doi.org/10.1002/2017JC013364

Bledsoe, T. S., & Baskin, J. J. (2014). Recognizing student fear: The elephant in the classroom. *College Teaching*, *62*(1), 32–41. https://doi.org/10.1080/87567555.2013.831022

Blischak, J. D., Davenport, E. R., & Wilson, G. (2016). A quick introduction to version control with Git and GitHub. *PLOS Computational Biology*, *12*(1), e1004668. https://doi.org/10.1371/journal.pcbi.1004668

Bloom, B. S., Engelhart, M. D., Furst, E. J., Hill, W. H., & Krathwohl, D. R. (1956). *Taxonomy of educational objectives: The classification of educational goals. Handbook I: Cognitive domain*. London: Longmans.

Boehme, L., Lovell, P., Biuw, M., Roquet, F., Nicholson, J., Thorpe, S. E., Meredith, M. P., & Fedak, M. (2009). Technical note: Animal-borne CTD-Satellite Relay Data Loggers for real-time oceanographic data collection. *Ocean Science*, *5*(4), 685–695. https://doi.org/10.5194/os-5-685-2009

Boisvert, L. N., Webster, M. A., Petty, A. A., Markus, T., Cullather, R. I., & Bromwich, D. H. (2020). Intercomparison of precipitation estimates over the Southern Ocean from atmospheric reanalyses. *Journal of Climate*, *33*(24), 10627–10651. https://doi.org/10.1175/JCLI-D-20-0044.1

Box, J. E., Bromwich, D. H., & Bai, L.-S. (2004). Greenland ice sheet surface mass balance 1991–2000: Application of Polar MM5 mesoscale model and in situ data. *Journal of Geophysical Research*, *109*, D16105. https://doi.org/10.1029/2003JD004451

de Boyer Montégut, C., Madec, G., Fischer, A. S., Lazar, A., & Iudicone, D. (2004). Mixed layer depth over the global ocean: An examination of profile data and a profile-based climatology. *Journal of Geophysical Research*, *109*, C12003. https://doi.org/10.1029/2004JC002378

Boyer, T. P., Baranova, O. K., Coleman, C. F., Garcia, H. E., Grodsky, A., Locarnini, R. A., Mishonov, A. V., O'Brien, T. D., Paver, C. R., Reagan, J. R., Seidov, D., Smolyar, I. V., Weathers, K. W., & Zweng, M. M. (2018). *World Ocean Database 2018 (NOAA Atlas NESDIS 87)*. (A. V. Mishonov, Ed.). Silver Spring, MD: NOAA. https://doi.org/10.7289/V5NZ85MT

Bracegirdle, T. J. (2013). Climatology and recent increase of westerly winds over the Amundsen Sea derived from six reanalyses. *International Journal of Climatology*, *33*(4), 843–851. https://doi.org/10.1002/joc.3473

Brett, A., Leape, J., Abbott, M., Sakaguchi, H., Cao, L., Chand, K., Golbuu, Y., Martin, T. J., Mayorga, J., & Myksvoll, M. S. (2020). Ocean data need a sea change to help navigate the warming world. *Nature*, *582*(7811), 181–183. https://doi.org/10.1038/d41586-020-01668-z

Broecker, W. S., Sutherland, S., & Peng, T.-H. (1999). A possible 20th-century slowdown of Southern Ocean deep water formation. *Science*, *286*(5442), 1132–1135. https://doi.org/10.1126/science.286.5442.1132

van den Broeke, M. R. (1997). Spatial and temporal variation of sublimation on Antarctica: Results of a high-resolution general circulation model. *Journal of Geophysical Research: Atmospheres*, *102*(D25), 29765–29777. https://doi.org/10.1029/97JD01862

Bronselaer, B., Winton, M., Griffies, S. M., Hurlin, W. J., Rodgers, K. B., Sergienko, O. V., Stouffer, R. J., & Russell, J. L. (2018). Change in future climate due to Antarctic meltwater. *Nature*, *564*(7734), 53–58. https://doi.org/10.1038/s41586-018-0712-z

Brookhart, S. M., & Chen, F. (2015). The quality and effectiveness of descriptive rubrics. *Educational Review*, *67*(3), 343–368. https://doi.org/10.1080/00131911.2014.929565

Cabaj, A., Kushner, P. J., Fletcher, C. G., Howell, S., & Petty, A. A. (2020). Constraining reanalysis snowfall over the Arctic Ocean using CloudSat observations. *Geophysical Research Letters*, *47*(4), e2019GL086426. https://doi.org/10.1029/2019GL086426

Cabaj, A., Kushner, P. J., & Petty, A. A. (2023). Automated calibration of a snow-on-sea-ice model. *Earth and Space Science*, *10*(3), e2022EA002655. https://doi.org/10.1029/2022EA002655

Cabré, A., Marinov, I., & Gnanadesikan, A. (2017). Global atmospheric teleconnections and multidecadal climate oscillations driven by Southern Ocean convection. *Journal of Climate*, *30*(20), 8107–8126. https://doi.org/10.1175/JCLI-D-16-0741.1

Campbell, E. C., & Christensen, K. M. (2024). Analysis code for "Cracking the code: An evidence-based approach to teaching Python in an undergraduate earth science setting" [Computer software]. Zenodo. https://doi.org/10.5281/zenodo.8087943

Campbell, E. C., & Riser, S. C. (in prep). Lagrangian reconstruction of the accumulation and loss of snow on Antarctic sea ice.

Campbell, E. C., Wilson, E. A., Moore, G. W. K., Riser, S. C., Brayton, C. E., Mazloff, M. R., & Talley, L. D. (2019). Antarctic offshore polynyas linked to Southern Hemisphere climate anomalies. *Nature*, *570*(7761), 319–325. https://doi.org/10.1038/s41586-019-1294-0

Campbell, E. C., Christensen, K. M., Nuwer, M., Ahuja, A., Boram, O., Liu, J., Miller, R., Osuna, I., & Riser, S. C. (2024). Cracking the code: An evidence-based approach to teaching Python in an undergraduate earth science setting. *Journal of Geoscience Education*, in press. https://doi.org/10.1080/10899995.2024.2384338

Capp, M. J. (2017). The effectiveness of universal design for learning: a meta-analysis of literature between 2013 and 2016. *International Journal of Inclusive Education*, *21*(8), 791–807. https://doi.org/10.1080/13603116.2017.1325074

Carsey, F. D. (1980). Microwave observation of the Weddell Polynya. *Monthly Weather Review*, *108*(12), 2032–2044. https://doi.org/10.1175/1520-0493(1980)108<2032:MOOTWP>2.0.CO;2

Carval, T., Keeley, R., Yasushi, T., Yoshida, T., Loch, S., Schmid, C., Goldsmith, R., Wong, A. P. S., McCreadie, R., Thresher, A., & Tran, A. (2017). *Argo user's manual, version 3.2*. Argo Data Management Team. https://doi.org/10.13155/29825

Cavalieri, D. J., Markus, T., & Comiso, J. C. (2014). *AMSR-E/Aqua Daily L3 12.5 km Brightness Temperature, Sea Ice Concentration, & Snow Depth Polar Grids (AE_SI12, version 3)*. Boulder, CO: NASA National Snow and Ice Data Center (NSIDC) Distributed Active Archive Center (DAAC). https://doi.org/10.5067/AMSR-E/AE_SI12.003

Chamberlain, P. M., Talley, L. D., Mazloff, M. R., Riser, S. C., Speer, K., Gray, A. R., & Schwartzman, A. (2018). Observing the ice-covered Weddell Gyre with profiling floats: position uncertainties and correlation statistics. *Journal of Geophysical Research: Oceans*, *123*(11), 8383–8410. https://doi.org/10.1029/2017JC012990

Chang, E. K. M., Guo, Y., & Xia, X. (2012). CMIP5 multimodel ensemble projection of storm track change under global warming. *Journal of Geophysical Research: Atmospheres*, *117*, D23118. https://doi.org/10.1029/2012JD018578

Charrassin, J.-B., Hindell, M. A., Rintoul, S. R., Roquet, F., Sokolov, S., Biuw, M., Costa, D., Boehme, L., Lovell, P., Coleman, R., Timmermann, R., Meijers, A. S., Meredith, M. P., Park, Y.-H., Bailleul, F., Goebel, M. E., Tremblay, Y., Bost, C.-A., McMahon, C. R., Field, I. C., Fedak, M. A., & Guinet, C. (2008). Southern Ocean frontal structure and sea-ice formation rates revealed by elephant seals. *Proceedings of the National Academy of Sciences*, *105*(33), 11634–11639.

https://doi.org/10.1073/pnas.0800790105

Cheon, W. G., Park, Y.-G., Toggweiler, J. R., & Lee, S.-K. (2014). The relationship of Weddell Polynya and open-ocean deep convection to the Southern Hemisphere westerlies. *Journal of Physical Oceanography*, *44*(2), 694–713. https://doi.org/10.1175/JPO-D-13-0112.1

Cheon, W. G., Lee, S.-K., Gordon, A. L., Liu, Y., Cho, C.-B., & Park, J. J. (2015). Replicating the 1970s' Weddell Polynya using a coupled ocean-sea ice model with reanalysis surface flux fields. *Geophysical Research Letters*, *42*(13), 5411–5418. https://doi.org/10.1002/2015GL064364

Chlup, D. T., & Collins, T. E. (2010). Breaking the ice: Using ice-breakers and re-energizers with adult learners. *Adult Learning*, *21*(3–4), 34–39. https://doi.org/10.1177/104515951002100305

Chung, Y.-C., Bélair, S., & Mailhot, J. (2011). Blowing snow on Arctic sea ice: Results from an improved sea ice–snow–blowing snow coupled system. *Journal of Hydrometeorology*, *12*(4), 678–689. https://doi.org/10.1175/2011JHM1293.1

Clemens-Sewall, D., Polashenski, C., Frey, M. M., Cox, C. J., Granskog, M. A., Macfarlane, A. R., Fons, S. W., Schmale, J., Hutchings, J. K., von Albedyll, L., Arndt, S., Schneebeli, M., & Perovich, D. (2023). Snow loss into leads in Arctic sea ice: Minimal in typical wintertime conditions, but high during a warm and windy snowfall event. *Geophysical Research Letters*, *50*(12), e2023GL102816. https://doi.org/10.1029/2023GL102816

Cohanim, K., Zhao, K. X., & Stewart, A. L. (2021). Dynamics of eddies generated by sea ice leads. *Journal of Physical Oceanography*, *51*(10), 3071–3092. https://doi.org/10.1175/JPO-D-20-0169.1

Comiso, J. C., & Gordon, A. L. (1987). Recurring polynyas over the Cosmonaut Sea and the Maud Rise. *Journal of Geophysical Research*, *92*(C3), 2819–2833. https://doi.org/10.1029/JC092iC03p02819

Comiso, J. C., & Gordon, A. L. (1996). Cosmonaut polynya in the Southern Ocean: Structure and variability. *Journal of Geophysical Research: Oceans*, *101*(C8), 18297–18313. https://doi.org/10.1029/96JC01500

Comiso, J. C., & Steffen, K. (2001). Studies of Antarctic sea ice concentrations from satellite data and their applications. *Journal of Geophysical Research: Oceans*, *106*(C12), 31361–31385. https://doi.org/10.1029/2001JC000823

Comiso, J. C., Cavalieri, D. J., Parkinson, C. L., & Gloersen, P. (1997). Passive microwave algorithms for sea ice concentration: A comparison of two techniques. *Remote Sensing of Environment*, *60*(3), 357–384. https://doi.org/10.1016/S0034-4257(96)00220-9

Comiso, J. C., Cavalieri, D. J., & Markus, T. (2003). Sea ice concentration, ice temperature, and snow depth using AMSR-E data. *IEEE Transactions on Geoscience and Remote Sensing*, *41*(2), 243–252. https://doi.org/10.1109/TGRS.2002.808317

Copernicus Climate Change Service. (2023). *ERA5 hourly data on single levels from 1940 to present*. Copernicus Climate Change Service (C3S) Climate Data Store (CDS). https://doi.org/10.24381/cds.adbb2d47

Creswell, J. W. (1998). Data analysis and representation. In *Qualitative Inquiry and Research Design: Choosing Among Five Traditions* (1st ed., pp. 139–165). Thousand Oaks, CA: SAGE Publications.

DeCaria, A., & Petty, G. W. (2021). *Python programming and visualization for scientists* (2nd ed.). Sundog Publishing.

Dee, D. P., Uppala, S. M., Simmons, A. J., Berrisford, P., Poli, P., Kobayashi, S., Andrae, U., Balmaseda, M. A., Balsamo, G., Bauer, P., Bechtold, P., Beljaars, A. C. M., van de Berg, L., Bidlot, J., Bormann, N., Delsol, C., Dragani, R., Fuentes, M., Geer, A. J., Haimberger, L., Healy, S. B., Hersbach, H., Hólm, E. V., Isaksen, L., Kållberg, P., Köhler, M., Matricardi, M., McNally, A. P., Monge-Sanz, B. M., Morcrette, J.-J., Park, B.-K., Peubey, C., de Rosnay, P., Tavolato, C., Thépaut, J.-N., & Vitart, F. (2011). The ERA-Interim reanalysis: Configuration and performance of the data assimilation system. *Quarterly Journal of the Royal Meteorological Society*, *137*(656), 553–597. https://doi.org/10.1002/qj.828

Déry, S. J., & Tremblay, L. B. (2004). Modeling the effects of wind redistribution on the snow mass budget of polar sea ice. *Journal of Physical Oceanography*, *34*(1), 258–271. https://doi.org/10.1175/1520-0485(2004)034<0258:MTEOWR>2.0.CO;2

Déry, S. J., & Yau, M.-K. (2001). Simulation of blowing snow in the Canadian Arctic using a double-moment model. *Boundary-Layer Meteorology*, *99*(2), 297–316. https://doi.org/10.1023/A:1018965008049

Déry, S. J., & Yau, M.-K. (2002). Large-scale mass balance effects of blowing snow and surface sublimation. *Journal of Geophysical Research: Atmospheres*, *107*(D23), 4679. https://doi.org/10.1029/2001JD001251

Deslauriers, L., McCarty, L. S., Miller, K., Callaghan, K., & Kestin, G. (2019). Measuring actual learning versus feeling of learning in response to being actively engaged in the classroom. *Proceedings of the National Academy of Sciences*, *116*(39), 19251–19257. https://doi.org/10.1073/pnas.1821936116

Dewsbury, B., & Brame, C. J. (2019). Inclusive teaching. *CBE—Life Sciences Education*, *18*(2), fe2. https://doi.org/10.1187/cbe.19-01-0021

Dong, S., Sprintall, J., Gille, S. T., & Talley, L. (2008). Southern Ocean mixed-layer depth from Argo float profiles. *Journal of Geophysical Research*, *113*, C06013. https://doi.org/10.1029/2006JC004051

Dong, S., Garzoli, S. L., & Baringer, M. (2009). An assessment of the seasonal mixed layer salinity budget in the Southern Ocean. *Journal of Geophysical Research*, *114*(C12), C12001. https://doi.org/10.1029/2008JC005258

Donham, C., Pohan, C., Menke, E., & Kranzfelder, P. (2022). Increasing student engagement through course attributes, community, and classroom technology: Lessons from the pandemic. *Journal of Microbiology & Biology Education*, *23*(1), 1–6. https://doi.org/10.1128/jmbe.00268-21

Dou, T., Xiao, C., Liu, J., Han, W., Du, Z., Mahoney, A. R., Jones, J., & Eicken, H. (2019). A key factor initiating surface ablation of Arctic sea ice: earlier and increasing liquid precipitation. *The Cryosphere*, *13*(4), 1233–1246. https://doi.org/10.5194/tc-13-1233-2019

Dowdeswell, J. A., Batchelor, C. L., Dorschel, B., Benham, T. J., Christie, F. D. W., Dowdeswell, E. K., Montelli, A., Arndt, J. E., & Gebhardt, C. (2020). Sea-floor and sea-ice conditions in the western Weddell Sea, Antarctica, around the wreck of Sir Ernest Shackleton's Endurance. *Antarctic Science*, *32*(4), 301–313. https://doi.org/10.1017/S0954102020000103

Drucker, R., & Riser, S. C. (2016). In situ phase-domain calibration of oxygen Optodes on profiling floats. *Methods in Oceanography*, *17*, 296–318. https://doi.org/10.1016/j.mio.2016.09.007

Dufour, C. O., Morrison, A. K., Griffies, S. M., Frenger, I., Zanowski, H., & Winton, M. (2017). Preconditioning of the Weddell Sea polynya by the ocean mesoscale and dense water overflows. *Journal of Climate*, *30*(19), 7719–7737. https://doi.org/10.1175/JCLI-D-16-0586.1

Eayrs, C., Holland, D. M., Francis, D., Wagner, T., Kumar, R., & Li, X. (2019). Understanding the seasonal cycle of Antarctic sea ice extent in the context of longer-term variability. *Reviews of Geophysics*, *57*(3), 1037–1064. https://doi.org/10.1029/2018RG000631

Eayrs, C., Faller, D., & Holland, D. M. (2020). Mechanisms driving the asymmetric seasonal cycle of Antarctic Sea Ice in the CESM Large Ensemble. *Annals of Glaciology*, *61*(82), 171–180. https://doi.org/10.1017/aog.2020.26

Eayrs, C., Li, X., Raphael, M. N., & Holland, D. M. (2021). Rapid decline in Antarctic sea ice in recent years hints at future change. *Nature Geoscience*, *14*(7), 460–464. https://doi.org/10.1038/s41561-021-00768-3

Eicken, H., Lange, M. A., Hubberten, H.-W., & Wadhams, P. (1994). Characteristics and distribution patterns of snow and meteoric ice in the Weddell Sea and their contribution to the mass balance of sea ice. *Annales Geophysicae*, *12*(1), 80–93. https://doi.org/10.1007/s00585-994-0080-x

Eicken, H., Fischer, H., & Lemke, P. (1995). Effects of the snow cover on Antarctic sea ice and potential modulation of its response to climate change. *Annals of Glaciology*, *21*, 369–376.

https://doi.org/10.1017/S0260305500016086

Ellwein, A. L., Hartley, L. M., Donovan, S., & Billick, I. (2014). Using rich context and data exploration to improve engagement with climate data and data literacy: Bringing a field station into the college classroom. *Journal of Geoscience Education*, *62*(4), 578–586. https://doi.org/10.5408/13-034

Esmaili, R. B. (2021). *Earth observation using Python: A practical programming guide* (Vol. 75). Hoboken, NJ: American Geophysical Union and Wiley. https://doi.org/10.1002/9781119606925

Fahrbach, E., Hoppema, M., Rohardt, G., Schröder, M., & Wisotzki, A. (2006). Causes of deep-water variation: Comment on the paper by L.H. Smedsrud "Warming of the deep water in the Weddell Sea along the Greenwich meridian: 1977–2001." *Deep Sea Research Part I: Oceanographic Research Papers*, *53*(3), 574–577. https://doi.org/10.1016/j.dsr.2005.12.003

Fahrbach, E., Hoppema, M., Rohardt, G., Boebel, O., Klatt, O., & Wisotzki, A. (2011). Warming of deep and abyssal water masses along the Greenwich meridian on decadal time scales: The Weddell gyre as a heat buffer. *Deep Sea Research Part II: Topical Studies in Oceanography*, *58*(25–26), 2509–2523. https://doi.org/10.1016/j.dsr2.2011.06.007

Fairall, C. W., Bradley, E. F., Rogers, D. P., Edson, J. B., & Young, G. S. (1996). Bulk parameterization of air-sea fluxes for Tropical Ocean-Global Atmosphere Coupled-Ocean Atmosphere Response Experiment. *Journal of Geophysical Research: Oceans*, *101*(C2), 3747–3764. https://doi.org/10.1029/95JC03205

Fer, I., Peterson, A. K., Randelhoff, A., & Meyer, A. (2017). One-dimensional evolution of the upper water column in the Atlantic sector of the Arctic Ocean in winter. *Journal of Geophysical Research: Oceans*, *122*(3), 1665–1682. https://doi.org/10.1002/2016JC012431

Fetterer, F., Kerry, K., Meier, W. N., Savoie, M., & Windnagel, A. K. (2017). *Sea Ice Index (G02135, version 3)*. Boulder, CO: National Snow and Ice Data Center (NSIDC). https://doi.org/10.7265/N5K072F8

Fichefet, T., & Morales Maqueda, M. A. (1999). Modelling the influence of snow accumulation and snow-ice formation on the seasonal cycle of the Antarctic sea-ice cover. *Climate Dynamics*, *15*(4), 251–268. https://doi.org/10.1007/s003820050280

Fogt, R. L., Wovrosh, A. J., Langen, R. A., & Simmonds, I. (2012). The characteristic variability and connection to the underlying synoptic activity of the Amundsen-Bellingshausen Seas Low. *Journal of Geophysical Research: Atmospheres*, *117*, D07111. https://doi.org/10.1029/2011JD017337

Fons, S., Kurtz, N., & Bagnardi, M. (2023). A decade-plus of Antarctic sea ice thickness and volume estimates from CryoSat-2 using a physical model and waveform fitting. *The Cryosphere*, *17*(6), 2487–2508. https://doi.org/10.5194/tc-17-2487-2023

Frajka-Williams, E., Rhines, P. B., & Eriksen, C. C. (2014). Horizontal stratification during deep convection in the Labrador Sea. *Journal of Physical Oceanography*, *44*(1), 220–228. https://doi.org/10.1175/JPO-D-13-069.1

Franz, K. J., Hogue, T. S., & Sorooshian, S. (2008). Operational snow modeling: Addressing the challenges of an energy balance model for National Weather Service forecasts. *Journal of Hydrology*, *360*(1–4), 48–66. https://doi.org/10.1016/j.jhydrol.2008.07.013

Fraser, A. D., Massom, R. A., Handcock, M. S., Reid, P., Ohshima, K. I., Raphael, M. N., Cartwright, J., Klekociuk, A. R., Wang, Z., & Porter-Smith, R. (2021). Eighteen-year record of circum-Antarctic landfast-sea-ice distribution allows detailed baseline characterisation and reveals trends and variability. *The Cryosphere*, *15*(11), 5061–5077. https://doi.org/10.5194/tc-15-5061-2021

Freeman, S., Eddy, S. L., McDonough, M., Smith, M. K., Okoroafor, N., Jordt, H., & Wenderoth, M. P. (2014). Active learning increases student performance in science, engineering, and mathematics. *Proceedings of the National Academy of Sciences*, *111*(23), 8410–8415. https://doi.org/10.1073/pnas.1319030111

Fretwell, P. T., Boutet, A., & Ratcliffe, N. (2023). Record low 2022 Antarctic sea ice led to catastrophic breeding failure of emperor penguins. *Communications Earth & Environment*, *4*, 273.

https://doi.org/10.1038/s43247-023-00927-x

Furman, T., & Moldwin, M. (2021). Higher education during the pandemic: Truths and takeaways. *Eos*, *102*(9), 17–19. https://doi.org/10.1029/2021EO160171

Garnier, F., Fleury, S., Garric, G., Bouffard, J., Tsamados, M., Laforge, A., Bocquet, M., Fredensborg Hansen, R. M., & Remy, F. (2021). Advances in altimetric snow depth estimates using bi-frequency SARAL and CryoSat-2 Ka–Ku measurements. *The Cryosphere*, *15*(12), 5483–5512. https://doi.org/10.5194/tc-15-5483-2021

Garratt, J. R. (1992). *The atmospheric boundary layer*. (J. T. Houghton, M. J. Rycroft, & A. J. Dessler, Eds.). Cambridge, UK: Cambridge University Press.

Gentemann, C. L., Holdgraf, C., Abernathey, R., Crichton, D., Colliander, J., Kearns, E. J., Panda, Y., & Signell, R. P. (2021). Science storms the cloud. *AGU Advances*, *2*(2), e2020AV000354. https://doi.org/10.1029/2020AV000354

Ghosh, S., Pulford, S., & Bloom, A. J. (2022). Remote learning slightly decreased student performance in an introductory undergraduate course on climate change. *Communications Earth & Environment*, *3*, 177. https://doi.org/10.1038/s43247-022-00506-6

Gille, S. T., & Kelly, K. A. (1996). Scales of spatial and temporal variability in the Southern Ocean. *Journal of Geophysical Research: Oceans*, *101*(C4), 8759–8773. https://doi.org/10.1029/96JC00203

Girotto, M., Formetta, G., Azimi, S., Bachand, C., Cowherd, M., De Lannoy, G., Lievens, H., Modanesi, S., Raleigh, M. S., Rigon, R., & Massari, C. (2024). Identifying snowfall elevation patterns by assimilating satellite-based snow depth retrievals. *Science of The Total Environment*, *906*, 167312. https://doi.org/10.1016/j.scitotenv.2023.167312

Goosse, H., & Zunz, V. (2014). Decadal trends in the Antarctic sea ice extent ultimately controlled by ice–ocean feedback. *The Cryosphere*, *8*(2), 453–470. https://doi.org/10.5194/tc-8-453-2014

Gordon, A. L. (1978). Deep Antarctic convection west of Maud Rise. *Journal of Physical Oceanography*, *8*(4), 600–612. https://doi.org/10.1175/1520-0485(1978)008<0600:DACWOM>2.0.CO;2

Gordon, A. L. (1982). Weddell Deep Water variability. *Journal of Marine Research*, *40*, 199–217.

Gordon, A. L. (1991). Two stable modes of Southern Ocean winter stratification. In P. C. Chu & J.-C. Gascard (Eds.), *Elsevier Oceanography Series, Volume 57: Deep Convection and Deep Water Formation in the Oceans* (pp. 17–35). Elsevier. https://doi.org/10.1016/S0422-9894(08)70058-8

Gordon, A. L., & Huber, B. A. (1984). Thermohaline stratification below the Southern Ocean sea ice. *Journal of Geophysical Research*, *89*(C1), 641–648. https://doi.org/10.1029/JC089iC01p00641

Gordon, A. L., & Huber, B. A. (1990). Southern Ocean winter mixed layer. *Journal of Geophysical Research*, *95*(C7), 11655–11672. https://doi.org/10.1029/JC095iC07p11655

Gordon, A. L., Chen, C.-T. A., & Metcalf, W. G. (1984). Winter mixed layer entrainment of Weddell Deep Water. *Journal of Geophysical Research*, *89*(C1), 637–640. https://doi.org/10.1029/JC089iC01p00637

Gordon, A. L., Visbeck, M., & Comiso, J. C. (2007). A possible link between the Weddell Polynya and the Southern Annular Mode. *Journal of Climate*, *20*(11), 2558–2571. https://doi.org/10.1175/JCLI4046.1

Gouretski, V. (2018). World Ocean Circulation Experiment - Argo Global Hydrographic Climatology. *Ocean Science*, *14*(5), 1127–1146. https://doi.org/10.5194/os-14-1127-2018

Graham, R. M., Cohen, L., Ritzhaupt, N., Segger, B., Graversen, R. G., Rinke, A., Walden, V. P., Granskog, M. A., & Hudson, S. R. (2019). Evaluation of six atmospheric reanalyses over Arctic sea ice from winter to early summer. *Journal of Climate*, *32*(14), 4121–4143. https://doi.org/10.1175/JCLI-D-18-0643.1

Graham, R. M., Itkin, P., Meyer, A., Sundfjord, A., Spreen, G., Smedsrud, L. H., Liston, G. E., Cheng, B., Cohen, L., Divine, D., Fer, I., Fransson, A., Gerland, S., Haapala, J., Hudson, S. R., Johansson, A. M.,

King, J., Merkouriadi, I., Peterson, A. K., Provost, C., Randelhoff, A., Rinke, A., Rösel, A., Sennéchael, N., Walden, V. P., Duarte, P., Assmy, P., Steen, H., & Granskog, M. A. (2019). Winter storms accelerate the demise of sea ice in the Atlantic sector of the Arctic Ocean. *Scientific Reports*, *9*(1), 9222. https://doi.org/10.1038/s41598-019-45574-5

Granger, B. E., & Pérez, F. (2021). Jupyter: Thinking and storytelling with code and data. *Computing in Science & Engineering*, *23*(2), 7–14. https://doi.org/10.1109/MCSE.2021.3059263

Grapenthin, R. (2011). Computer programing for geosciences: Teach your students how to make tools. *Eos, Transactions American Geophysical Union*, *92*(50), 469–470. https://doi.org/10.1029/2011EO500010

Greengrove, C., Lichtenwalner, S., Palevsky, H., Pfeiffer-Herbert, A., Severmann, S., Soule, D., Murphy, S., Smith, L., & Yarincik, K. (2020). Using authentic data from NSF's Ocean Observatories Initiative in undergraduate teaching. *Oceanography*, *33*(1), 62–73. https://doi.org/10.5670/oceanog.2020.103

Groeskamp, S., LaCasce, J. H., McDougall, T. J., & Rogé, M. (2020). Full-depth global estimates of ocean mesoscale eddy mixing from observations and theory. *Geophysical Research Letters*, *47*(18), e2020GL089425. https://doi.org/10.1029/2020GL089425

Groot Zwaaftink, C. D., Cagnati, A., Crepaz, A., Fierz, C., Macelloni, G., Valt, M., & Lehning, M. (2013). Event-driven deposition of snow on the Antarctic Plateau: analyzing field measurements with SNOWPACK. *The Cryosphere*, *7*(1), 333–347. https://doi.org/10.5194/tc-7-333-2013

Haak, D. C., HilleRisLambers, J., Pitre, E., & Freeman, S. (2011). Increased structure and active learning reduce the achievement gap in introductory biology. *Science*, *332*(6034), 1213–1216. https://doi.org/10.1126/science.1204820

Hadjerrouit, S. (2008). Towards a blended learning model for teaching and learning computer programming: A case study. *Informatics in Education*, *7*(2), 181–210. https://doi.org/10.15388/infedu.2008.12

Haine, T. W. N., Gelderloos, R., Jimenez-Urias, M. A., Siddiqui, A. H., Lemson, G., Medvedev, D., Szalay, A., Abernathey, R. P., Almansi, M., & Hill, C. N. (2021). Is computational oceanography coming of age? *Bulletin of the American Meteorological Society*, *102*(8), E1481–E1493. https://doi.org/10.1175/BAMS-D-20-0258.1

Hanks, B. (2005). Student performance in CS1 with distributed pair programming. *ACM SIGCSE Bulletin*, *37*(3), 316–320. https://doi.org/10.1145/1067445.1067532

Harris, C. R., Millman, K. J., van der Walt, S. J., Gommers, R., Virtanen, P., Cournapeau, D., Wieser, E., Taylor, J., Berg, S., Smith, N. J., Kern, R., Picus, M., Hoyer, S., van Kerkwijk, M. H., Brett, M., Haldane, A., del Río, J. F., Wiebe, M., Peterson, P., Gérard-Marchant, P., Sheppard, K., Reddy, T., Weckesser, W., Abbasi, H., Gohlke, C., & Oliphant, T. E. (2020). Array programming with NumPy. *Nature*, *585*(7825), 357–362. https://doi.org/10.1038/s41586-020-2649-2

Haumann, F. A., Gruber, N., Münnich, M., Frenger, I., & Kern, S. (2016a). Antarctic sea-ice freshwater fluxes associated with freezing, transport, and melting. EnviDat. https://doi.org/10.16904/8

Haumann, F. A., Gruber, N., Münnich, M., Frenger, I., & Kern, S. (2016b). Sea-ice transport driving Southern Ocean salinity and its recent trends. *Nature*, *537*(7618), 89–92. https://doi.org/10.1038/nature19101

Haumann, F. A., Gruber, N., & Münnich, M. (2020). Sea-ice induced Southern Ocean subsurface warming and surface cooling in a warming climate. *AGU Advances*, *1*(2), e2019AV000132. https://doi.org/10.1029/2019AV000132

Hays, J. D., Pfirman, S., Blumenthal, B., Kastens, K. A., & Menke, W. (2000). Earth science instruction with digital data. *Computers & Geosciences*, *26*(6), 657–668. https://doi.org/10.1016/S0098-3004(99)00101-6

Hepworth, K., Ivey, C. E., Canon, C., & Holmes, H. A. (2020). Embedding online, design-focused data visualization instruction in an upper-division undergraduate atmospheric science course. *Journal of*

Geoscience Education, *68*(2), 168–183. https://doi.org/10.1080/10899995.2019.1656022

Hersbach, H., Bell, B., Berrisford, P., Hirahara, S., Horányi, A., Muñoz-Sabater, J., Nicolas, J., Peubey, C., Radu, R., Schepers, D., Simmons, A., Soci, C., Abdalla, S., Abellan, X., Balsamo, G., Bechtold, P., Biavati, G., Bidlot, J., Bonavita, M., Chiara, G., Dahlgren, P., Dee, D., Diamantakis, M., Dragani, R., Flemming, J., Forbes, R., Fuentes, M., Geer, A., Haimberger, L., Healy, S., Hogan, R. J., Hólm, E., Janisková, M., Keeley, S., Laloyaux, P., Lopez, P., Lupu, C., Radnoti, G., Rosnay, P., Rozum, I., Vamborg, F., Villaume, S., & Thépaut, J. (2020). The ERA5 global reanalysis. *Quarterly Journal of the Royal Meteorological Society*, *146*(730), 1999–2049. https://doi.org/10.1002/qj.3803

Heuzé, C., Heywood, K. J., Stevens, D. P., & Ridley, J. K. (2013). Southern Ocean bottom water characteristics in CMIP5 models. *Geophysical Research Letters*, *40*(7), 1409–1414. https://doi.org/10.1002/grl.50287

Heuzé, C., Ridley, J. K., Calvert, D., Stevens, D. P., & Heywood, K. J. (2015). Increasing vertical mixing to reduce Southern Ocean deep convection in NEMO3.4. *Geoscientific Model Development*, *8*(10), 3119–3130. https://doi.org/10.5194/gmd-8-3119-2015

Heuzé, C. H., Vivier, F., Le Sommer, J., Molines, J.-M., & Penduff, T. (2015). Can we map the interannual variability of the whole upper Southern Ocean with the current database of hydrographic observations? *Journal of Geophysical Research: Oceans*, *120*(12), 7960–7978. https://doi.org/10.1002/2015JC011115

Hodges, C. B., Moore, S., Lockee, B. B., Trust, T., & Bond, A. A. (2020, March 27). The difference between emergency remote teaching and online learning. *Educause Review*. https://er.educause.edu/articles/2020/3/the-difference-between-emergency-remote-teaching-and-online-learning

Holland, D. M. (2001). Explaining the Weddell Polynya—a large ocean eddy shed at Maud Rise. *Science*, *292*(5522), 1697–1700. https://doi.org/10.1126/science.1059322

Holland, P. R., & Kimura, N. (2016). Observed concentration budgets of Arctic and Antarctic sea ice. *Journal of Climate*, *29*(14), 5241–5249. https://doi.org/10.1175/JCLI-D-16-0121.1

Holland, P. R., & Kwok, R. (2012). Wind-driven trends in Antarctic sea-ice drift. *Nature Geoscience*, *5*(12), 872–875. https://doi.org/10.1038/ngeo1627

Holland, P. R., Bruneau, N., Enright, C., Losch, M., Kurtz, N. T., & Kwok, R. (2014). Modeled trends in Antarctic sea ice thickness. *Journal of Climate*, *27*(10), 3784–3801. https://doi.org/10.1175/JCLI-D-13-00301.1

Horvath, S., Boisvert, L., Parker, C., Webster, M., Taylor, P., Boeke, R., Fons, S., & Stewart, J. S. (2023). Database of daily Lagrangian Arctic sea ice parcel drift tracks with coincident ice and atmospheric conditions. *Scientific Data*, *10*, 73. https://doi.org/10.1038/s41597-023-01987-6

Hoyer, S., & Hamman, J. (2017). xarray: N-D labeled Arrays and Datasets in Python. *Journal of Open Research Software*, *5*(1), 10. https://doi.org/10.5334/jors.148

Huntemann, M., Heygster, G., Kaleschke, L., Krumpen, T., Mäkynen, M., & Drusch, M. (2014). Empirical sea ice thickness retrieval during the freeze-up period from SMOS high incident angle observations. *The Cryosphere*, *8*(2), 439–451. https://doi.org/10.5194/tc-8-439-2014

Hunter, J. D. (2007). Matplotlib: A 2D graphics environment. *Computing in Science & Engineering*, *9*(3), 90–95. https://doi.org/10.1109/MCSE.2007.55

Irving, D. (2019). Python for atmosphere and ocean scientists. *Journal of Open Source Education*, *2*(11), 37. https://doi.org/10.21105/jose.00037

Itkin, P., Spreen, G., Cheng, B., Doble, M., Girard-Ardhuin, F., Haapala, J., Hughes, N., Kaleschke, L., Nicolaus, M., & Wilkinson, J. (2017). Thin ice and storms: Sea ice deformation from buoy arrays deployed during N-ICE2015. *Journal of Geophysical Research: Oceans*, *122*(6), 4661–4674. https://doi.org/10.1002/2016JC012403

Itkin, P., Hendricks, S., Webster, M., von Albedyll, L., Arndt, S., Divine, D., Jaggi, M., Oggier, M.,

Raphael, I., Ricker, R., Rohde, J., Schneebeli, M., & Liston, G. E. (2023). Sea ice and snow characteristics from year-long transects at the MOSAiC Central Observatory. *Elementa: Science of the Anthropocene*, *11*(1), 00048. https://doi.org/10.1525/elementa.2022.00048

Jacobs, C. T., Gorman, G. J., Rees, H. E., & Craig, L. E. (2016). Experiences with efficient methodologies for teaching computer programming to geoscientists. *Journal of Geoscience Education*, *64*(3), 183–198. https://doi.org/10.5408/15-101.1

Jamieson, K., & Talwalkar, A. (2016). Non-stochastic best arm identification and hyperparameter optimization. In *Proceedings of the 19th International Conference on Artificial Intelligence and Statistics* (pp. 240–248).

Jenkins, J. J., Sánchez, L. A., Schraedley, M. A. K., Hannans, J., Navick, N., & Young, J. (2020). Textbook broke: Textbook affordability as a social justice issue. *Journal of Interactive Media in Education*, *2020*(1), 3. https://doi.org/10.5334/jime.549

Johnson, K. S., Plant, J. N., Coletti, L. J., Jannasch, H. W., Sakamoto, C. M., Riser, S. C., Swift, D. D., Williams, N. L., Boss, E., Haëntjens, N., Talley, L. D., & Sarmiento, J. L. (2017). Biogeochemical sensor performance in the SOCCOM profiling float array. *Journal of Geophysical Research: Oceans*, *122*(8), 6416–6436. https://doi.org/10.1002/2017JC012838

Johnson, K. S., Riser, S. C., Boss, E. S., Talley, L. D., Sarmiento, J. L., Swift, D. D., Plant, J. N., Maurer, T. L., Key, R. M., Williams, N. L., Wanninkhof, R. H., Dickson, A. G., Feely, R. A., & Russell, J. L. (2019). SOCCOM float data - Snapshot 2018-12-31. *Southern Ocean Carbon and Climate Observations and Modeling (SOCCOM) Float Data Archive*. UC San Diego Library Digital Collections. https://doi.org/10.6075/J02J6968

Jordan, R. E., Andreas, E. L., & Makshtas, A. P. (1999). Heat budget of snow-covered sea ice at North Pole 4. *Journal of Geophysical Research: Oceans*, *104*(C4), 7785–7806. https://doi.org/10.1029/1999JC900011

Jullion, L., Jones, S. C., Naveira Garabato, A. C., & Meredith, M. P. (2010). Wind-controlled export of Antarctic Bottom Water from the Weddell Sea. *Geophysical Research Letters*, *37*(9), L09609. https://doi.org/10.1029/2010GL042822

Jullion, L., Garabato, A. C. N., Bacon, S., Meredith, M. P., Brown, P. J., Torres-Valdés, S., Speer, K. G., Holland, P. R., Dong, J., Bakker, D., Hoppema, M., Loose, B., Venables, H. J., Jenkins, W. J., Messias, M.-J., & Fahrbach, E. (2014). The contribution of the Weddell Gyre to the lower limb of the Global Overturning Circulation. *Journal of Geophysical Research: Oceans*, *119*(6), 3357–3377. https://doi.org/10.1002/2013JC009725

Kacimi, S., & Kwok, R. (2020). The Antarctic sea ice cover from ICESat-2 and CryoSat-2: freeboard, snow depth, and ice thickness. *The Cryosphere*, *14*(12), 4453–4474. https://doi.org/10.5194/tc-14-4453-2020

Karnin, Z., Koren, T., & Somekh, O. (2013). Almost optimal exploration in multi-armed bandits. In *Proceedings of the 30th International Conference on Machine Learning* (Vol. 28, pp. 1238–1246).

Kastens, K. A., & Krumhansl, R. (2017). Identifying curriculum design patterns as a strategy for focusing geoscience education research: A proof of concept based on teaching and learning with geoscience data. *Journal of Geoscience Education*, *65*(4), 373–392. https://doi.org/10.5408/16-217.1

Kastens, K. A., Krumhansl, R., & Baker, I. (2015). Thinking big. *The Science Teacher*, *82*(5), 25–31.

Kastens, K. A., Zrada, M., & Turrin, M. (2020). What kinds of questions do students ask while exploring data visualizations? *Journal of Geoscience Education*, *68*(3), 199–219. https://doi.org/10.1080/10899995.2019.1675447

Keenan, E., Wever, N., Dattler, M., Lenaerts, J. T. M., Medley, B., Kuipers Munneke, P., & Reijmer, C. (2021). Physics-based SNOWPACK model improves representation of near-surface Antarctic snow and firn density. *The Cryosphere*, *15*(2), 1065–1085. https://doi.org/10.5194/tc-15-1065-2021

Kern, S., & Ozsoy-Çiçek, B. (2016). Satellite remote sensing of snow depth on Antarctic sea ice: An inter-comparison of two empirical approaches. *Remote Sensing*, *8*(6), 450.

https://doi.org/10.3390/rs8060450

Kern, S., Ozsoy-Cicek, B., Willmes, S., Nicolaus, M., Haas, C., & Ackley, S. (2011). An intercomparison between AMSR-E snow-depth and satellite C- and Ku-band radar backscatter data for Antarctic sea ice. *Annals of Glaciology*, *52*(57), 279–290. https://doi.org/10.3189/172756411795931750

Kim, T.-W., Ha, H. K., Wåhlin, A. K., Lee, S. H., Kim, C.-S., Lee, J. H., & Cho, Y.-K. (2017). Is Ekman pumping responsible for the seasonal variation of warm circumpolar deep water in the Amundsen Sea? *Continental Shelf Research*, *132*, 38–48. https://doi.org/10.1016/j.csr.2016.09.005

King, J. C., Marshall, G. J., Colwell, S., Arndt, S., Allen-Sader, C., & Phillips, T. (2022). The performance of the ERA-Interim and ERA5 atmospheric reanalyses over Weddell Sea pack ice. *Journal of Geophysical Research: Oceans*, *127*(9), e2022JC018805. https://doi.org/10.1029/2022JC018805

Kjellsson, J., Holland, P. R., Marshall, G. J., Mathiot, P., Aksenov, Y., Coward, A. C., Bacon, S., Megann, A. P., & Ridley, J. (2015). Model sensitivity of the Weddell and Ross seas, Antarctica, to vertical mixing and freshwater forcing. *Ocean Modelling*, *94*, 141–152. https://doi.org/10.1016/j.ocemod.2015.08.003

Klatt, O., Boebel, O., & Fahrbach, E. (2007). A profiling float's sense of ice. *Journal of Atmospheric and Oceanic Technology*, *24*(7), 1301–1308. https://doi.org/10.1175/JTECH2026.1

Klug, J. L., Carey, C. C., Richardson, D. C., & Darner Gougis, R. (2017). Analysis of high-frequency and long-term data in undergraduate ecology classes improves quantitative literacy. *Ecosphere*, *8*(3), e01733. https://doi.org/10.1002/ecs2.1733

Kojima, K. (1967). Densification of seasonal snow cover. *Physics of Snow and Ice: Proceedings*, *1*(2), 929–952.

Kong, F., & Yau, M.-K. (1997). An explicit approach to microphysics in MC2. *Atmosphere-Ocean*, *35*(3), 257–291. https://doi.org/10.1080/07055900.1997.9649594

Kottmeier, C., & Sellmann, L. (1996). Atmospheric and oceanic forcing of Weddell Sea ice motion. *Journal of Geophysical Research: Oceans*, *101*(C9), 20809–20824. https://doi.org/10.1029/96JC01293

Krathwohl, D. R. (2002). A revision of Bloom's taxonomy: An overview. *Theory Into Practice*, *41*(4), 212–218. https://doi.org/10.1207/s15430421tip4104_2

Kruger, J., & Dunning, D. (1999). Unskilled and unaware of it: How difficulties in recognizing one's own incompetence lead to inflated self-assessments. *Journal of Personality and Social Psychology*, *77*(6), 1121–1134. https://doi.org/10.1037/0022-3514.77.6.1121

Kuh, G., O'Donnell, K., & Schneider, C. G. (2017). HIPs at ten. *Change: The Magazine of Higher Learning*, *49*(5), 8–16. https://doi.org/10.1080/00091383.2017.1366805

Kuksenok, K., Aragon, C., Fogarty, J., Lee, C. P., & Neff, G. (2017). Deliberate individual change framework for understanding programming practices in four oceanography groups. *Computer Supported Cooperative Work*, *26*(4–6), 663–691. https://doi.org/10.1007/s10606-017-9285-x

Kurtakoti, P., Veneziani, M., Stössel, A., & Weijer, W. (2018). Preconditioning and formation of Maud Rise polynyas in a high-resolution earth system model. *Journal of Climate*, *31*(23), 9659–9678. https://doi.org/10.1175/JCLI-D-18-0392.1

Kurtz, N. T., & Markus, T. (2012). Satellite observations of Antarctic sea ice thickness and volume. *Journal of Geophysical Research: Oceans*, *117*(C8), C08025. https://doi.org/10.1029/2012JC008141

Kusahara, K., Williams, G. D., Massom, R., Reid, P., & Hasumi, H. (2019). Spatiotemporal dependence of Antarctic sea ice variability to dynamic and thermodynamic forcing: a coupled ocean-sea ice model study. *Climate Dynamics*, *52*(7–8), 3791–3807. https://doi.org/10.1007/s00382-018-4348-3

Kwok, R., & Kacimi, S. (2018). Three years of sea ice freeboard, snow depth, and ice thickness of the Weddell Sea from Operation IceBridge and CryoSat-2. *The Cryosphere*, *12*(8), 2789–2801. https://doi.org/10.5194/tc-12-2789-2018

Kwok, R., Kacimi, S., Webster, M. A., Kurtz, N. T., & Petty, A. A. (2020). Arctic snow depth and sea ice thickness from ICESat-2 and CryoSat-2 freeboards: A first examination. *Journal of Geophysical Research: Oceans*, *125*(3), 1–19. https://doi.org/10.1029/2019JC016008

Lago, V., & England, M. H. (2019). Projected slowdown of Antarctic Bottom Water formation in response to amplified meltwater contributions. *Journal of Climate*, *32*(19), 6319–6335. https://doi.org/10.1175/JCLI-D-18-0622.1

Large, W. G., & Pond, S. (1981). Open ocean momentum flux measurements in moderate to strong winds. *Journal of Physical Oceanography*, *11*(3), 324–336. https://doi.org/10.1175/1520-0485(1981)011<0324:OOMFMI>2.0.CO;2

Lasser, J., Manik, D., Silbersdorff, A., Säfken, B., & Kneib, T. (2021). Introductory data science across disciplines, using Python, case studies, and industry consulting projects. *Teaching Statistics*, *43*(S1), S190–S200. https://doi.org/10.1111/test.12243

de Lavergne, C., Palter, J. B., Galbraith, E. D., Bernardello, R., & Marinov, I. (2014). Cessation of deep convection in the open Southern Ocean under anthropogenic climate change. *Nature Climate Change*, *4*(4), 278–282. https://doi.org/10.1038/nclimate2132

Lawrence, I. R., Ridout, A. L., Shepherd, A., & Tilling, R. (2024). A simulation of snow on Antarctic sea ice based on satellite data and climate reanalyses. *Journal of Geophysical Research: Oceans*, *129*(1), e2022JC019002. https://doi.org/10.1029/2022JC019002

Lecomte, O., Fichefet, T., Vancoppenolle, M., Domine, F., Massonnet, F., Mathiot, P., Morin, S., & Barriat, P.-Y. (2013). On the formulation of snow thermal conductivity in large-scale sea ice models. *Journal of Advances in Modeling Earth Systems*, *5*(3), 542–557. https://doi.org/10.1002/jame.20039

Lecomte, O., Fichefet, T., Flocco, D., Schroeder, D., & Vancoppenolle, M. (2015). Interactions between wind-blown snow redistribution and melt ponds in a coupled ocean-sea ice model. *Ocean Modelling*, *87*, 67–80. https://doi.org/10.1016/j.ocemod.2014.12.003

Lecomte, O., Goosse, H., Fichefet, T., de Lavergne, C., Barthélemy, A., & Zunz, V. (2017). Vertical ocean heat redistribution sustaining sea-ice concentration trends in the Ross Sea. *Nature Communications*, *8*, 258. https://doi.org/10.1038/s41467-017-00347-4

Leonard, K. C., & Maksym, T. (2011). The importance of wind-blown snow redistribution to snow accumulation on Bellingshausen Sea ice. *Annals of Glaciology*, *52*(57), 271–278. https://doi.org/10.3189/172756411795931651

Lew, M. D. N., Alwis, W. A. M., & Schmidt, H. G. (2010). Accuracy of students' self-assessment and their beliefs about its utility. *Assessment & Evaluation in Higher Education*, *35*(2), 135–156. https://doi.org/10.1080/02602930802687737

Li, Liam, Jamieson, K., Rostamizadeh, A., Gonina, E., Hardt, M., Recht, B., & Talwalkar, A. (2018). A system for massively parallel hyperparameter tuning. ArXiv. https://doi.org/10.48550/arXiv.1810.05934

Li, Long, & Pomeroy, J. W. (1997). Estimates of threshold wind speeds for snow transport using meteorological data. *Journal of Applied Meteorology*, *36*(3), 205–213. https://doi.org/10.1175/1520-0450(1997)036<0205:EOTWSF>2.0.CO;2

Liggett, D., Frame, B., Convey, P., & Hughes, K. A. (2024). How the COVID-19 pandemic signaled the demise of Antarctic exceptionalism. *Science Advances*, *10*(9), eadk4424. https://doi.org/10.1126/sciadv.adk4424

Lin, J. W.-B. (2012). Why Python is the next wave in earth sciences computing. *Bulletin of the American Meteorological Society*, *93*(12), 1823–1824. https://doi.org/10.1175/BAMS-D-12-00148.1

Lindsay, R. W., Holland, D. M., & Woodgate, R. A. (2004). Halo of low ice concentration observed over the Maud Rise seamount. *Geophysical Research Letters*, *31*(13), L13302. https://doi.org/10.1029/2004GL019831

Liston, G. E., Itkin, P., Stroeve, J., Tschudi, M., Stewart, J. S., Pedersen, S. H., Reinking, A. K., & Elder, K.

(2020). A Lagrangian snow-evolution system for sea-ice applications (SnowModel-LG): Part I—Model description. *Journal of Geophysical Research: Oceans*, *125*(10), e2019JC015913. https://doi.org/10.1029/2019JC015913

Liu, J., & Curry, J. A. (2010). Accelerated warming of the Southern Ocean and its impacts on the hydrological cycle and sea ice. *Proceedings of the National Academy of Sciences*, *107*(34), 14987–14992. https://doi.org/10.1073/pnas.1003336107

Lockee, B. B. (2021). Online education in the post-COVID era. *Nature Electronics*, *4*(1), 5–6. https://doi.org/10.1038/s41928-020-00534-0

Lopatto, D. (2010). Undergraduate research as a high-impact student experience. *Peer Review*, *12*(2), 27–30.

Lynch-Stieglitz, M. (1994). The development and validation of a simple snow model for the GISS GCM. *Journal of Climate*, *7*(12), 1842–1855. https://doi.org/10.1175/1520-0442(1994)007<1842:TDAVOA>2.0.CO;2

Lytle, V. I., & Ackley, S. F. (2001). Snow-ice growth: A fresh-water flux inhibiting deep convection in the Weddell Sea, Antarctica. *Annals of Glaciology*, *33*(1), 45–50. https://doi.org/10.3189/172756401781818752

Maksym, T., & Markus, T. (2008). Antarctic sea ice thickness and snow-to-ice conversion from atmospheric reanalysis and passive microwave snow depth. *Journal of Geophysical Research: Oceans*, *113*(2), 1–18. https://doi.org/10.1029/2006JC004085

Maksym, T., Stammerjohn, S. E., Ackley, S. F., & Massom, R. (2012). Antarctic sea ice—A polar opposite? *Oceanography*, *25*(3), 140–151. https://doi.org/10.5670/oceanog.2012.88

Mantyla, A. W., & Reid, J. L. (1983). Abyssal characteristics of the World Ocean waters. *Deep Sea Research Part A, Oceanographic Research Papers*, *30*(8), 805–833. https://doi.org/10.1016/0198-0149(83)90002-X

Manucharyan, G. E., & Spall, M. A. (2016). Wind-driven freshwater buildup and release in the Beaufort Gyre constrained by mesoscale eddies. *Geophysical Research Letters*, *43*(1), 273–282. https://doi.org/10.1002/2015GL065957

Margirier, F., Bosse, A., Testor, P., L'Hévéder, B., Mortier, L., & Smeed, D. (2017). Characterization of convective plumes associated with oceanic deep convection in the northwestern Mediterranean from high-resolution in situ data collected by gliders. *Journal of Geophysical Research: Oceans*, *122*(12), 9814–9826. https://doi.org/10.1002/2016JC012633

Markus, T., & Cavalieri, D. J. (1998). Snow depth distribution over sea ice in the Southern Ocean from satellite passive microwave data. In *Antarctic sea ice: Physical processes, interactions and variability* (Vol. 74, pp. 19–39). American Geophysical Union. https://doi.org/10.1029/AR074p0019

Markus, T., & Cavalieri, D. J. (2006). Interannual and regional variability of Southern Ocean snow on sea ice. *Annals of Glaciology*, *44*, 53–57. https://doi.org/10.3189/172756406781811475

Markus, T., Massom, R., Worby, A., Lytle, V., Kurtz, N., & Maksym, T. (2011). Freeboard, snow depth and sea-ice roughness in East Antarctica from in situ and multiple satellite data. *Annals of Glaciology*, *52*(57), 242–248. https://doi.org/10.3189/172756411795931570

Marshall, G. J. (2003). Trends in the Southern Annular Mode from observations and reanalyses. *Journal of Climate*, *16*(24), 4134–4143. https://doi.org/10.1175/1520-0442(2003)016<4134:TITSAM>2.0.CO;2

Marshall, H.-P., Conway, H., & Rasmussen, L. A. (1999). Snow densification during rain. *Cold Regions Science and Technology*, *30*(1–3), 35–41. https://doi.org/10.1016/S0165-232X(99)00011-7

Marshall, J., & Schott, F. (1999). Open-ocean convection: Observations, theory, and models. *Reviews of Geophysics*, *37*(1), 1–64. https://doi.org/10.1029/98RG02739

Marshall, J., & Speer, K. (2012). Closure of the meridional overturning circulation through Southern Ocean upwelling. *Nature Geoscience*, *5*(3), 171–180. https://doi.org/10.1038/ngeo1391

Martin, T., Park, W., & Latif, M. (2013). Multi-centennial variability controlled by Southern Ocean convection in the Kiel Climate Model. *Climate Dynamics*, *40*(7–8), 2005–2022. https://doi.org/10.1007/s00382-012-1586-7

Martinson, D. G. (1990). Evolution of the Southern Ocean winter mixed layer and sea ice: Open ocean deepwater formation and ventilation. *Journal of Geophysical Research*, *95*(C7), 11641–11654. https://doi.org/10.1029/JC095iC07p11641

Martinson, D. G., & Iannuzzi, R. A. (1998). Antarctic ocean-ice interaction: Implications from ocean bulk property distributions in the Weddell gyre. In *Antarctic Sea Ice: Physical Processes, Interactions and Variability (Antarctic Research Series)* (Vol. 74, pp. 243–271). Washington, D.C.: American Geophysical Union. https://doi.org/10.1029/AR074p0243

Martinson, D. G., & Wamser, C. (1990). Ice drift and momentum exchange in winter Antarctic pack ice. *Journal of Geophysical Research*, *95*(C2), 1741–1755. https://doi.org/10.1029/JC095iC02p01741

Martinson, D. G., Killworth, P. D., & Gordon, A. L. (1981). A convective model for the Weddell Polynya. *Journal of Physical Oceanography*, *11*(4), 466–488. https://doi.org/10.1175/1520-0485(1981)011<0466:ACMFTW>2.0.CO;2

Massom, R. A., Drinkwater, M. R., & Haas, C. (1997). Winter snow cover on sea ice in the Weddell Sea. *Journal of Geophysical Research: Oceans*, *102*(C1), 1101–1117. https://doi.org/10.1029/96JC02992

Massom, R. A., Lytle, V. I., Worby, A. P., & Allison, I. (1998). Winter snow cover variability on East Antarctic sea ice. *Journal of Geophysical Research: Oceans*, *103*(C11), 24837–24855. https://doi.org/10.1029/98JC01617

Massom, R. A., Eicken, H., Hass, C., Jeffries, M. O., Drinkwater, M. R., Sturm, M., Worby, A. P., Wu, X., Lytle, V. I., Ushio, S., Morris, K., Reid, P. A., Warren, S. G., & Allison, I. (2001). Snow on Antarctic sea ice. *Reviews of Geophysics*, *39*(3), 413–445. https://doi.org/10.1029/2000RG000085

Massom, R. A., Scambos, T. A., Bennetts, L. G., Reid, P., Squire, V. A., & Stammerjohn, S. E. (2018). Antarctic ice shelf disintegration triggered by sea ice loss and ocean swell. *Nature*, *558*(7710), 383–389. https://doi.org/10.1038/s41586-018-0212-1

Massonnet, F., Mathiot, P., Fichefet, T., Goosse, H., König Beatty, C., Vancoppenolle, M., & Lavergne, T. (2013). A model reconstruction of the Antarctic sea ice thickness and volume changes over 1980-2008 using data assimilation. *Ocean Modelling*, *64*, 67–75. https://doi.org/10.1016/j.ocemod.2013.01.003

Maykut, G. A. (1986). The surface heat and mass balance. In N. Untersteiner (Ed.), *The Geophysics of Sea Ice (NATO ASI Series, Series B: Physics, Vol. 146)* (pp. 395–463). London: Plenum Press. https://doi.org/10.1007/978-1-4899-5352-0_6

Maykut, G. A., & Untersteiner, N. (1971). Some results from a time-dependent thermodynamic model of sea ice. *Journal of Geophysical Research*, *76*(6), 1550–1575. https://doi.org/10.1029/JC076i006p01550

Mazloff, M. R., Heimbach, P., & Wunsch, C. (2010). An eddy-permitting Southern Ocean state estimate. *Journal of Physical Oceanography*, *40*(5), 880–899. https://doi.org/10.1175/2009JPO4236.1

McCallum, S., Schultz, J., Sellke, K., & Spartz, J. (2015). An examination of the flipped classroom approach on college student academic involvement. *International Journal of Teaching and Learning in Higher Education*, *27*(1), 42–55.

McConnell, D. A., Chapman, L., Czajka, C. D., Jones, J. P., Ryker, K. D., & Wiggen, J. (2017). Instructional utility and learning efficacy of common active learning strategies. *Journal of Geoscience Education*, *65*(4), 604–625. https://doi.org/10.5408/17-249.1

McDonnell, J., Lichtenwalner, S., Glenn, S., Ferraro, C., Hunter-Thomson, K., & Hewlett, J. (2015). The challenges and opportunities of using data in teaching from the perspective of undergraduate

oceanography professors. *Marine Technology Society Journal*, *49*(4), 76–85. https://doi.org/10.4031/MTSJ.49.4.9

McDowell, C., Werner, L., Bullock, H., & Fernald, J. (2002). The effects of pair-programming on performance in an introductory programming course. *ACM SIGCSE Bulletin*, *34*(1), 38–42. https://doi.org/10.1145/563340.563353

McKinney, W. (2010). Data structures for statistical computing in Python. In *Proceedings of the 9th Python in Science Conference* (pp. 56–61). https://doi.org/10.25080/Majora-92bf1922-00a

McPhee, M. G. (2000). Marginal thermobaric stability in the ice-covered upper ocean over Maud Rise. *Journal of Physical Oceanography*, *30*(11), 2710–2722. https://doi.org/10.1175/1520-0485(2000)030<2710:MTSITI>2.0.CO;2

McPhee, M. G. (2017). The sea ice–ocean boundary layer. In D. N. Thomas (Ed.), *Sea ice* (pp. 138–159). Chichester, UK: John Wiley & Sons, Ltd. https://doi.org/10.1002/9781118778371.ch5

McPhee, M. G., Ackley, S. F., Guest, P., Stanton, T. P., Huber, B. A., Martinson, D. G., Morison, J. H., Muench, R. D., & Padman, L. (1996). The Antarctic Zone Flux Experiment. *Bulletin of the American Meteorological Society*, *77*(6), 1221–1232. https://doi.org/10.1175/1520-0477(1996)077<1221:TAZFE>2.0.CO;2

McPhee, M. G., Kottmeier, C., & Morison, J. H. (1999). Ocean heat flux in the central Weddell Sea during winter. *Journal of Physical Oceanography*, *29*(6), 1166–1179. https://doi.org/10.1175/1520-0485(1999)029<1166:OHFITC>2.0.CO;2

Meehl, G. A., Arblaster, J. M., Chung, C. T. Y., Holland, M. M., DuVivier, A., Thompson, L., Yang, D., & Bitz, C. M. (2019). Sustained ocean changes contributed to sudden Antarctic sea ice retreat in late 2016. *Nature Communications*, *10*, 14. https://doi.org/10.1038/s41467-018-07865-9

Meier, W. N., Gallaher, D., & Campbell, G. G. (2013). New estimates of Arctic and Antarctic sea ice extent during September 1964 from recovered Nimbus I satellite imagery. *The Cryosphere*, *7*(2), 699–705. https://doi.org/10.5194/tc-7-699-2013

Meier, W. N., Peng, G., Scott, D. J., & Savoie, M. H. (2014). Verification of a new NOAA/NSIDC passive microwave sea-ice concentration climate record. *Polar Research*, *33*(1), 21004. https://doi.org/10.3402/polar.v33.21004

Meier, W. N., Fetterer, F., & Windnagel, A. K. (2017). *Near-Real-Time NOAA/NSIDC Climate Data Record of passive microwave sea ice concentration, version 1*. Boulder, CO: NASA National Snow and Ice Data Center (NSIDC). https://doi.org/10.7265/N5FF3QJ6

Meier, W. N., Fetterer, F., Savoie, M., Mallory, S., Duerr, R., & Stroeve, J. (2017). *NOAA/NSIDC Climate Data Record of passive microwave sea ice concentration, version 3*. Boulder, CO: NASA National Snow and Ice Data Center (NSIDC). https://doi.org/10.7265/N59P2ZTG

Meier, W. N., Markus, T., & Comiso, J. C. (2018). *AMSR-E/AMSR2 Unified L3 Daily 12.5 km Brightness Temperatures, Sea Ice Concentration, Motion & Snow Depth Polar Grids (AU_SI12, version 1)*. Boulder, CO: NASA National Snow and Ice Data Center (NSIDC) Distributed Active Archive Center (DAAC). https://doi.org/10.5067/RA1MIJOYPK3P

Meier, W. N., Fetterer, F., Windnagel, A. K., & Stewart, J. S. (2021a). *Near-Real-Time NOAA/NSIDC Climate Data Record of Passive Microwave Sea Ice Concentration (G10016, version 2)*. Boulder, CO: National Snow and Ice Data Center (NSIDC). https://doi.org/10.7265/tgam-yv28

Meier, W. N., Fetterer, F., Windnagel, A. K., & Stewart, J. S. (2021b). *NOAA/NSIDC Climate Data Record of Passive Microwave Sea Ice Concentration (G02202, version 4)*. Boulder, CO: National Snow and Ice Data Center (NSIDC). https://doi.org/10.7265/efmz-2t65

Meijers, A. J. S., Meredith, M. P., Abrahamsen, E. P., Morales Maqueda, M. A., Jones, D. C., & Naveira Garabato, A. C. (2016). Wind-driven export of Weddell Sea slope water. *Journal of Geophysical Research: Oceans*, *121*(10), 7530–7546. https://doi.org/10.1002/2016JC011757

Melsheimer, C., Spreen, G., Ye, Y., & Shokr, M. (2023). First results of Antarctic sea ice type retrieval from

active and passive microwave remote sensing data. *The Cryosphere*, *17*(1), 105–126. https://doi.org/10.5194/tc-17-105-2023

Mensa, J. A., & Timmermans, M.-L. (2017). Characterizing the seasonal cycle of upper-ocean flows under multi-year sea ice. *Ocean Modelling*, *113*, 115–130. https://doi.org/10.1016/j.ocemod.2017.03.009

Meredith, M. P., Nicholls, K. W., Renfrew, I. A., Boehme, L., Biuw, M., & Fedak, M. (2011). Seasonal evolution of the upper-ocean adjacent to the South Orkney Islands, Southern Ocean: Results from a "lazy biological mooring." *Deep Sea Research Part II: Topical Studies in Oceanography*, *58*(13–16), 1569–1579. https://doi.org/10.1016/j.dsr2.2009.07.008

Meredith, M. P., Meijers, A. S., Naveira Garabato, A. C., Brown, P. J., Venables, H. J., Abrahamsen, E. P., Jullion, L., & Messias, M.-J. (2015). Circulation, retention, and mixing of waters within the Weddell-Scotia Confluence, Southern Ocean: The role of stratified Taylor columns. *Journal of Geophysical Research: Oceans*, *120*(1), 547–562. https://doi.org/10.1002/2014JC010462

Merkouriadi, I., Cheng, B., Graham, R. M., Rösel, A., & Granskog, M. A. (2017). Critical role of snow on sea ice growth in the Atlantic sector of the Arctic Ocean. *Geophysical Research Letters*, *44*(20), 10479–10485. https://doi.org/10.1002/2017GL075494

Met Office. (2022). Cartopy: a cartographic Python library with a Matplotlib interface [Computer software]. https://scitools.org.uk/cartopy

Meyer, A., Rose, D. H., & Gordon, D. (2014). *Universal design for learning: theory and practice*. CAST. https://www.cast.org/news/2022/read-universal-design-learning-udl-theory-practice-free-clusive

Middendorf, J., & Kalish, A. (1996). The "change-up" in lectures. *The National Teaching and Learning Forum*, *5*(2), 1–5.

Moore, G. W. K., Alverson, K., & Renfrew, I. A. (2002). A reconstruction of the air–sea interaction associated with the Weddell Polynya. *Journal of Physical Oceanography*, *32*(6), 1685–1698. https://doi.org/10.1175/1520-0485(2002)032<1685:AROTAS>2.0.CO;2

Motoi, T., Ono, N., & Wakatsuchi, M. (1987). A mechanism for the formation of the Weddell Polynya in 1974. *Journal of Physical Oceanography*, *17*(12), 2241–2247. https://doi.org/10.1175/1520-0485(1987)017<2241:AMFTFO>2.0.CO;2

Muench, R. D., Morison, J. H., Padman, L., Martinson, D. G., Schlosser, P., Huber, B. A., & Hohmann, R. (2001). Maud Rise revisited. *Journal of Geophysical Research*, *106*(C2), 2423–2440. https://doi.org/10.1029/2000JC000531

Mundy, C. J., Barber, D. G., & Michel, C. (2005). Variability of snow and ice thermal, physical and optical properties pertinent to sea ice algae biomass during spring. *Journal of Marine Systems*, *58*(3–4), 107–120. https://doi.org/10.1016/j.jmarsys.2005.07.003

National Academies of Sciences, Engineering, and Medicine. (2018). *Open science by design: Realizing a vision for 21st century research*. Washington, D.C.: The National Academies Press. https://doi.org/10.17226/25116

Nicolaus, M., Haas, C., & Bareiss, J. (2003). Observations of superimposed ice formation at melt-onset on fast ice on Kongsfjorden, Svalbard. *Physics and Chemistry of the Earth, Parts A/B/C*, *28*(28–32), 1241–1248. https://doi.org/10.1016/j.pce.2003.08.048

Nicolaus, M., Hoppmann, M., Arndt, S., Hendricks, S., Katlein, C., König-Langlo, G., Nicolaus, A., Rossmann, L., Schiller, M., Schwegmann, S., Langevin, D., & Bartsch, A. (2017). *Snow height and air temperature on sea ice from Snow Buoy measurements*. Bremerhaven, Germany: Alfred Wegener Institute, Helmholtz Center for Polar and Marine Research. https://doi.org/10.1594/PANGAEA.875638

Nicolaus, M., Hoppmann, M., Arndt, S., Hendricks, S., Katlein, C., Nicolaus, A., Rossmann, L., Schiller, M., & Schwegmann, S. (2021). Snow depth and air temperature seasonality on sea ice derived from snow buoy measurements. *Frontiers in Marine Science*, *8*, 655446. https://doi.org/10.3389/fmars.2021.655446

Nissen, C., Timmermann, R., Hoppema, M., Gürses, Ö., & Hauck, J. (2022). Abruptly attenuated carbon sequestration with Weddell Sea dense waters by 2100. *Nature Communications*, *13*, 3402. https://doi.org/10.1038/s41467-022-30671-3

O'Reilly, C. M., Josek, T., Darner, R. D., & Fortner, S. K. (2022). Pedagogy of teaching with large datasets: Designing and implementing effective data-based activities. *Biochemistry and Molecular Biology Education*, *50*(5), 466–472. https://doi.org/10.1002/bmb.21663

Ohshima, K. I., Fukamachi, Y., Williams, G. D., Nihashi, S., Roquet, F., Kitade, Y., Tamura, T., Hirano, D., Herraiz-Borreguero, L., Field, I., Hindell, M., Aoki, S., & Wakatsuchi, M. (2013). Antarctic Bottom Water production by intense sea-ice formation in the Cape Darnley polynya. *Nature Geoscience*, *6*(3), 235–240. https://doi.org/10.1038/ngeo1738

Old, P. L. (2019). *Bridging the gap in oceanographic data science curriculum: prototyping experiential learning materials in Python* [Undergraduate thesis, University of Washington]. ResearchWorks Archive. https://hdl.handle.net/1773/45628

Orsi, A. H., Johnson, G. C., & Bullister, J. L. (1999). Circulation, mixing, and production of Antarctic Bottom Water. *Progress in Oceanography*, *43*(1), 55–109. https://doi.org/10.1016/S0079-6611(99)00004-X

Orsi, A. H., Jacobs, S. S., Gordon, A. L., & Visbeck, M. (2001). Cooling and ventilating the abyssal ocean. *Geophysical Research Letters*, *28*(15), 2923–2926. https://doi.org/10.1029/2001GL012830

Palomino, J., Wasser, L., & Joseph, M. (2021). *Introduction to earth data science textbook* (Version 1.5). Earth Lab CU Boulder. https://doi.org/10.5281/zenodo.3382162

Parkinson, C. L. (2019). A 40-y record reveals gradual Antarctic sea ice increases followed by decreases at rates far exceeding the rates seen in the Arctic. *Proceedings of the National Academy of Sciences*, *116*(29), 14414–14423. https://doi.org/10.1073/pnas.1906556116

Parkinson, C. L., Comiso, J. C., & Zwally, H. J. (2004). *Nimbus-5 ESMR polar gridded sea ice concentrations, version 1*. Boulder, CO: NASA National Snow and Ice Data Center (NSIDC). https://doi.org/10.5067/W2PKTWMTY0TP

Patoux, J., Yuan, X., & Li, C. (2009). Satellite-based midlatitude cyclone statistics over the Southern Ocean: 1. Scatterometer-derived pressure fields and storm tracking. *Journal of Geophysical Research*, *114*, D04105. https://doi.org/10.1029/2008JD010873

Pears, A., Seidman, S., Malmi, L., Mannila, L., Adams, E., Bennedsen, J., Devlin, M., & Paterson, J. (2007). A survey of literature on the teaching of introductory programming. *ACM SIGCSE Bulletin*, *39*(4), 204–223. https://doi.org/10.1145/1345375.1345441

Pedro, J. B., Martin, T., Steig, E. J., Jochum, M., Park, W., & Rasmussen, S. O. (2016). Southern Ocean deep convection as a driver of Antarctic warming events. *Geophysical Research Letters*, *43*(5), 2192–2199. https://doi.org/10.1002/2016GL067861

Pellichero, V., Sallée, J.-B., Schmidtko, S., Roquet, F., & Charrassin, J.-B. (2017). The ocean mixed layer under Southern Ocean sea-ice: Seasonal cycle and forcing. *Journal of Geophysical Research: Oceans*, *122*, 1063–1084. https://doi.org/10.1002/2016JC011970

Pellichero, V., Sallée, J.-B., Chapman, C. C., & Downes, S. M. (2018). The Southern Ocean meridional overturning in the sea-ice sector is driven by freshwater fluxes. *Nature Communications*, *9*, 1789. https://doi.org/10.1038/s41467-018-04101-2

Perkel, J. M. (2021). Ten computer codes that transformed science. *Nature*, *589*(7842), 344–348. https://doi.org/10.1038/d41586-021-00075-2

Petty, A. A., Webster, M., Boisvert, L., & Markus, T. (2018). The NASA Eulerian Snow on Sea Ice Model (NESOSIM) v1.0: initial model development and analysis. *Geoscientific Model Development*, *11*(11), 4577–4602. https://doi.org/10.5194/gmd-11-4577-2018

Petty, A. A., Bagnardi, M., Kurtz, N. T., Tilling, R., Fons, S., Armitage, T., Horvat, C., & Kwok, R. (2021). Assessment of ICESat-2 sea ice surface classification with Sentinel-2 imagery: implications for

freeboard and new estimates of lead and floe geometry. *Earth and Space Science*, *8*(3), e2020EA001491. https://doi.org/10.1029/2020EA001491

Pichette, J., Brumwell, S., & Rizk, J. (2020). *Improving the accessibility of remote higher education: Lessons from the pandemic and recommendations*. Higher Education Quality Council of Ontario. https://heqco.ca/pub/improving-the-accessibility-of-remote-higher-education-lessons-from-the-pandemic-and-recommendations/

Pitman, A. J., Yang, Z.-L., Cogley, J. G., & Henderson-Sellers, A. (1991). *Description of Bare Essentials of Surface Transfer for the Bureau of Meteorology Research Centre AGCM*.

Pond, S., & Pickard, G. L. (1983). *Introductory dynamic oceanography* (2nd ed.). Oxford: Butterworth-Heinemann.

Porter, D. F., Springer, S. R., Padman, L., Fricker, H. A., Tinto, K. J., Riser, S. C., Bell, R. E., & ROSETTA-Ice Team. (2019). Evolution of the seasonal surface mixed layer of the Ross Sea, Antarctica, observed with autonomous profiling floats. *Journal of Geophysical Research: Oceans*, *124*(7), 4934–4953. https://doi.org/10.1029/2018JC014683

Prince, M. (2004). Does active learning work? A review of the research. *Journal of Engineering Education*, *93*(3), 223–231. https://doi.org/10.1002/j.2168-9830.2004.tb00809.x

Prince, M., Felder, R., & Brent, R. (2020). Active student engagement in online STEM classes: Approaches and recommendations. *Advances in Engineering Education*, *8*(4), 1–25.

Purich, A., & Doddridge, E. W. (2023). Record low Antarctic sea ice coverage indicates a new sea ice state. *Communications Earth & Environment*, *4*, 314. https://doi.org/10.1038/s43247-023-00961-9

Ramachandran, R., Bugbee, K., & Murphy, K. (2021). From open data to open science. *Earth and Space Science*, *8*(5), e2020EA001562. https://doi.org/10.1029/2020EA001562

Ramirez, S., Teten, S., Mamo, M., Speth, C., Kettler, T., & Sindelar, M. (2022). Student perceptions and performance in a traditional, flipped classroom, and online introductory soil science course. *Journal of Geoscience Education*, *70*(1), 130–141. https://doi.org/10.1080/10899995.2021.1965419

Raphael, M. N., & Handcock, M. S. (2022). A new record minimum for Antarctic sea ice. *Nature Reviews Earth & Environment*, *3*(4), 215–216. https://doi.org/10.1038/s43017-022-00281-0

Reeve, K. A., Boebel, O., Strass, V., Kanzow, T., & Gerdes, R. (2019). Horizontal circulation and volume transports in the Weddell Gyre derived from Argo float data. *Progress in Oceanography*, *175*, 263–283. https://doi.org/10.1016/j.pocean.2019.04.006

Reintges, A., Martin, T., Latif, M., & Park, W. (2017). Physical controls of Southern Ocean deep-convection variability in CMIP5 models and the Kiel Climate Model. *Geophysical Research Letters*, *44*(13), 6951–6958. https://doi.org/10.1002/2017GL074087

Reiser, F., Willmes, S., Hausmann, U., & Heinemann, G. (2019). Predominant sea ice fracture zones around Antarctica and their relation to bathymetric features. *Geophysical Research Letters*, *46*(21), 12117–12124. https://doi.org/10.1029/2019GL084624

Reiser, F., Willmes, S., & Heinemann, G. (2020). A new algorithm for daily sea ice lead identification in the Arctic and Antarctic winter from thermal-infrared satellite imagery. *Remote Sensing*, *12*(12), 1957. https://doi.org/10.3390/rs12121957

Ren, L., Speer, K., & Chassignet, E. P. (2011). The mixed layer salinity budget and sea ice in the Southern Ocean. *Journal of Geophysical Research*, *116*(C8), C08031, 1–17. https://doi.org/10.1029/2010JC006634

Renfrew, I. A., Moore, G. W. K., Guest, P. S., & Bumke, K. (2002). A comparison of surface layer and surface turbulent flux observations over the Labrador Sea with ECMWF analyses and NCEP reanalyses. *Journal of Physical Oceanography*, *32*(2), 383–400. https://doi.org/10.1175/1520-0485(2002)032<0383:ACOSLA>2.0.CO;2

Resplandy, L., Séférian, R., & Bopp, L. (2015). Natural variability of CO2 and O2 fluxes: What can we learn from centuries-long climate models simulations? *Journal of Geophysical Research: Oceans*,

120(1), 384–404. https://doi.org/10.1002/2014JC010463

Ricker, R., Hendricks, S., Helm, V., Skourup, H., & Davidson, M. (2014). Sensitivity of CryoSat-2 Arctic sea-ice freeboard and thickness on radar-waveform interpretation. *The Cryosphere*, *8*(4), 1607–1622. https://doi.org/10.5194/tc-8-1607-2014

Riihelä, A., Bright, R. M., & Anttila, K. (2021). Recent strengthening of snow and ice albedo feedback driven by Antarctic sea-ice loss. *Nature Geoscience*, *14*(11), 832–836. https://doi.org/10.1038/s41561-021-00841-x

Rintoul, S. R., Chown, S. L., DeConto, R. M., England, M. H., Fricker, H. A., Masson-Delmotte, V., Naish, T. R., Siegert, M. J., & Xavier, J. C. (2018). Choosing the future of Antarctica. *Nature*, *558*(7709), 233–241. https://doi.org/10.1038/s41586-018-0173-4

Riser, S. C., Freeland, H. J., Roemmich, D., Wijffels, S., Troisi, A., Belbéoch, M., Gilbert, D., Xu, J., Pouliquen, S., Thresher, A., Le Traon, P.-Y., Maze, G., Klein, B., Ravichandran, M., Grant, F., Poulain, P.-M., Suga, T., Lim, B., Sterl, A., Sutton, P., Mork, K.-A., Vélez-Belchí, P. J., Ansorge, I. J., King, B., Turton, J., Baringer, M., & Jayne, S. R. (2016). Fifteen years of ocean observations with the global Argo array. *Nature Climate Change*, *6*(2), 145–153. https://doi.org/10.1038/nclimate2872

Riser, S. C., Swift, D., & Drucker, R. (2018). Profiling floats in SOCCOM: Technical capabilities for studying the Southern Ocean. *Journal of Geophysical Research: Oceans*, *123*, 4055–4073. https://doi.org/10.1002/2017JC013419

Roach, L. A., & Meier, W. N. (2024). Sea ice in 2023. *Nature Reviews Earth & Environment*, *5*(4), 235–237. https://doi.org/10.1038/s43017-024-00542-0

Roach, L. A., Eisenman, I., Wagner, T. J. W., Blanchard-Wrigglesworth, E., & Bitz, C. M. (2022). Asymmetry in the seasonal cycle of Antarctic sea ice driven by insolation. *Nature Geoscience*, *15*(4), 277–281. https://doi.org/10.1038/s41561-022-00913-6

Rogers, R. R., & Yau, M.-K. (1989). *A short course in cloud physics*. Burlington, MA: Butterworth-Heinemann.

Roquet, F., Williams, G., Hindell, M. A., Harcourt, R., McMahon, C., Guinet, C., Charrassin, J.-B., Reverdin, G., Boehme, L., Lovell, P., & Fedak, M. (2014). A Southern Indian Ocean database of hydrographic profiles obtained with instrumented elephant seals. *Scientific Data*, *1*, 140028. https://doi.org/10.1038/sdata.2014.28

Rostosky, P., Spreen, G., Gerland, S., Huntemann, M., & Mech, M. (2020). Modeling the microwave emission of snow on Arctic sea ice for estimating the uncertainty of satellite retrievals. *Journal of Geophysical Research: Oceans*, *125*(3), e2019JC015465. https://doi.org/10.1029/2019JC015465

Rowe, P. M., Fortmann, L., Guasco, T. L., Wright, A., Ryken, A., Sevier, E., Stokes, G., Mifflin, A., Wade, R., Cheng, H., Pfalzgraff, W., Beaudoin, J., Rajbhandari, I., Fox-Dobbs, K., & Neshyba, S. (2021). Integrating polar research into undergraduate curricula using computational guided inquiry. *Journal of Geoscience Education*, *69*(2), 178–191. https://doi.org/10.1080/10899995.2020.1768004

Ryan, S., Schröder, M., Huhn, O., & Timmermann, R. (2016). On the warm inflow at the eastern boundary of the Weddell Gyre. *Deep-Sea Research Part I: Oceanographic Research Papers*, *107*, 70–81. https://doi.org/10.1016/j.dsr.2015.11.002

Rye, C. D., Marshall, J., Kelley, M., Russell, G., Nazarenko, L. S., Kostov, Y., Schmidt, G. A., & Hansen, J. (2020). Antarctic glacial melt as a driver of recent Southern Ocean climate trends. *Geophysical Research Letters*, *47*(11), e2019GL086892. https://doi.org/10.1029/2019GL086892

Saenko, O. A., Schmittner, A., & Weaver, A. J. (2002). On the role of wind-driven sea ice motion on ocean ventilation. *Journal of Physical Oceanography*, *32*(12), 3376–3395. https://doi.org/10.1175/1520-0485(2002)032<3376:OTROWD>2.0.CO;2

Sarmiento, J. L., Johnson, K. S., Arteaga, L. A., Bushinsky, S. M., Cullen, H. M., Gray, A. R., Hotinski, R. M., Maurer, T. L., Mazloff, M. R., Riser, S. C., Russell, J. L., Schofield, O. M., & Talley, L. D. (2023). The Southern Ocean carbon and climate observations and modeling (SOCCOM) project: A review.

Progress in Oceanography, *219*, 103130. https://doi.org/10.1016/j.pocean.2023.103130

Scheick, J., Leong, W. J., Bisson, K., Arendt, A., Bhushan, S., Fair, Z., Hagen, N. R., Henderson, S., Knuth, F., Li, T., Liu, Z., Piunno, R., Ravinder, N., Setiawan, L. D., Sutterley, T., Swinski, J. P., & Anubhav. (2023). icepyx: querying, obtaining, analyzing, and manipulating ICESat-2 datasets. *Journal of Open Source Software*, *8*(84), 4912. https://doi.org/10.21105/joss.04912

Schwegmann, S., Haas, C., Fowler, C., & Gerdes, R. (2011). A comparison of satellite-derived sea-ice motion with drifting-buoy data in the Weddell Sea, Antarctica. *Annals of Glaciology*, *52*(57), 103–110. https://doi.org/10.3189/172756411795931813

Semtner, A. J. (1976). A model for the thermodynamic growth of sea ice in numerical investigations of climate. *Journal of Physical Oceanography*, *6*(3), 379–389. https://doi.org/10.1175/1520-0485(1976)006<0379:AMFTTG>2.0.CO;2

Shay, J. E., & Pohan, C. (2021). Resilient instructional strategies: Helping students cope and thrive in crisis. *Journal of Microbiology & Biology Education*, *22*(1), 1–8. https://doi.org/10.1128/jmbe.v22i1.2405

Shen, X., Ke, C.-Q., & Li, H. (2022). Snow depth product over Antarctic sea ice from 2002 to 2020 using multisource passive microwave radiometers. *Earth System Science Data*, *14*(2), 619–636. https://doi.org/10.5194/essd-14-619-2022

Shi, Q., Yang, Q., Mu, L., Wang, J., Massonnet, F., & Mazloff, M. R. (2021). Evaluation of sea-ice thickness from four reanalyses in the Antarctic Weddell Sea. *The Cryosphere*, *15*(1), 31–47. https://doi.org/10.5194/tc-15-31-2021

Siegelman, L., Roquet, F., Mensah, V., Rivière, P., Pauthenet, E., Picard, B., & Guinet, C. (2019). Correction and accuracy of high- and low-resolution CTD data from animal-borne instruments. *Journal of Atmospheric and Oceanic Technology*, *36*(5), 745–760. https://doi.org/10.1175/JTECH-D-18-0170.1

Sigman, D. M., Hain, M. P., & Haug, G. H. (2010). The polar ocean and glacial cycles in atmospheric CO2 concentration. *Nature*, *466*(7302), 47–55. https://doi.org/10.1038/nature09149

Silvano, A., Foppert, A., Rintoul, S. R., Holland, P. R., Tamura, T., Kimura, N., Castagno, P., Falco, P., Budillon, G., Haumann, F. A., Naveira Garabato, A. C., & Macdonald, A. M. (2020). Recent recovery of Antarctic Bottom Water formation in the Ross Sea driven by climate anomalies. *Nature Geoscience*, *13*(12), 780–786. https://doi.org/10.1038/s41561-020-00655-3

Singh, H. K. A., Landrum, L., Holland, M. M., Bailey, D. A., & DuVivier, A. K. (2021). An overview of Antarctic sea ice in the Community Earth System Model version 2, part I: Analysis of the seasonal cycle in the context of sea ice thermodynamics and coupled atmosphere-ocean-ice processes. *Journal of Advances in Modeling Earth Systems*, *13*(3), e2020MS002143. https://doi.org/10.1029/2020MS002143

Slater, A. G., Pitman, A. J., & Desborough, C. E. (1998). The validation of a snow parameterization designed for use in general circulation models. *International Journal of Climatology*, *18*(6), 595–617. https://doi.org/10.1002/(SICI)1097-0088(199805)18:6<595::AID-JOC275>3.0.CO;2-O

Smedsrud, L. H. (2005). Warming of the deep water in the Weddell Sea along the Greenwich meridian: 1977–2001. *Deep Sea Research Part I: Oceanographic Research Papers*, *52*(2), 241–258. https://doi.org/10.1016/j.dsr.2004.10.004

Smith, A., Lott, N., & Vose, R. (2011). The Integrated Surface Database: Recent developments and partnerships. *Bulletin of the American Meteorological Society*, *92*(6), 704–708. https://doi.org/10.1175/2011BAMS3015.1

Smith, J. A., Hillenbrand, C.-D., Pudsey, C. J., Allen, C. S., & Graham, A. G. C. (2010). The presence of polynyas in the Weddell Sea during the Last Glacial Period with implications for the reconstruction of sea-ice limits and ice sheet history. *Earth and Planetary Science Letters*, *296*(3–4), 287–298. https://doi.org/10.1016/j.epsl.2010.05.008

Song, Y., Behrangi, A., & Blanchard-Wrigglesworth, E. (2020). Assessment of satellite and reanalysis cold

season snowfall estimates over Arctic sea ice. *Geophysical Research Letters*, *47*(16), e2020GL088970. https://doi.org/10.1029/2020GL088970

Spreen, G., Kaleschke, L., & Heygster, G. (2008). Sea ice remote sensing using AMSR-E 89-GHz channels. *Journal of Geophysical Research: Oceans*, *113*(2), C02S03. https://doi.org/10.1029/2005JC003384

Srinath, K. R. (2017). Python–the fastest growing programming language. *International Research Journal of Engineering and Technology*, *4*(12), 354–357.

Stains, M., Harshman, J., Barker, M. K., Chasteen, S. V., Cole, R., DeChenne-Peters, S. E., Eagan, M. K., Esson, J. M., Knight, J. K., Laski, F. A., Levis-Fitzgerald, M., Lee, C. J., Lo, S. M., McDonnell, L., McKay, T. A., Michelotti, N., Musgrove, A., Palmer, M. S., Plank, K. M., Rodela, T. M., Sanders, E. R., Schimpf, N. G., Schulte, P. M., Smith, M. K., Stetzer, M. R., Van Valkenburgh, B., Vinson, E., Weir, L. K., Wendel, P. J., Wheeler, L. B., & Young, A. M. (2018). Anatomy of STEM teaching in North American universities. *Science*, *359*(6383), 1468–1470. https://doi.org/10.1126/science.aap8892

Stephens, B. B. ., & Keeling, R. F. (2000). The influence of Antarctic sea ice on glacial-interglacial CO2 variations. *Nature*, *404*(3), 171–174. https://doi.org/10.1038/35004556

de Steur, L., Holland, D. M., Muench, R. D., & McPhee, M. G. (2007). The warm-water "halo" around Maud Rise: Properties, dynamics and impact. *Deep Sea Research Part I: Oceanographic Research Papers*, *54*(6), 871–896. https://doi.org/10.1016/j.dsr.2007.03.009

Stroeve, J., Liston, G. E., Buzzard, S., Zhou, L., Mallett, R., Barrett, A., Tschudi, M., Tsamados, M., Itkin, P., & Stewart, J. S. (2020). A Lagrangian snow evolution system for sea ice applications (SnowModel-LG): Part II—Analyses. *Journal of Geophysical Research: Oceans*, *125*(10), e2019JC015900. https://doi.org/10.1029/2019JC015900

Stroeve, J., Nandan, V., Willatt, R., Dadic, R., Rostosky, P., Gallagher, M., Mallett, R., Barrett, A., Hendricks, S., Tonboe, R., McCrystall, M., Serreze, M., Thielke, L., Spreen, G., Newman, T., Yackel, J., Ricker, R., Tsamados, M., Macfarlane, A., Hannula, H.-R., & Schneebeli, M. (2022). Rain on snow (ROS) understudied in sea ice remote sensing: a multi-sensor analysis of ROS during MOSAiC (Multidisciplinary drifting Observatory for the Study of Arctic Climate). *The Cryosphere*, *16*(10), 4223–4250. https://doi.org/10.5194/tc-16-4223-2022

Stull, R. B. (2000). *Meteorology for scientists and engineers* (2nd ed.). Belmont, CA: Brooks/Cole.

Sturm, M., & Massom, R. A. (2017). Snow in the sea ice system: friend or foe? In D. N. Thomas (Ed.), *Sea ice* (pp. 65–109). Chichester, UK: John Wiley & Sons, Ltd. https://doi.org/10.1002/9781118778371.ch3

Sturm, M., Morris, K., & Massom, R. A. (1998). The winter snow cover of the West Antarctic pack ice: Its spatial and temporal variability. In *Antarctic sea ice: Physical processes, interactions and variability* (Vol. 74, pp. 1–18). American Geophysical Union. https://doi.org/10.1029/AR074p0001

Sumata, H., Lavergne, T., Girard-Ardhuin, F., Kimura, N., Tschudi, M. A., Kauker, F., Karcher, M., & Gerdes, R. (2014). An intercomparison of Arctic ice drift products to deduce uncertainty estimates. *Journal of Geophysical Research: Oceans*, *119*(8), 4887–4921. https://doi.org/10.1002/2013JC009724

Swadling, K. M., Constable, A. J., Fraser, A. D., Massom, R. A., Borup, M. D., Ghigliotti, L., Granata, A., Guglielmo, L., Johnston, N. M., Kawaguchi, S., Kennedy, F., Kiko, R., Koubbi, P., Makabe, R., Martin, A., McMinn, A., Moteki, M., Pakhomov, E. A., Peeken, I., Reimer, J., Reid, P., Ryan, K. G., Vacchi, M., Virtue, P., Weldrick, C. K., Wongpan, P., & Wotherspoon, S. J. (2023). Biological responses to change in Antarctic sea ice habitats. *Frontiers in Ecology and Evolution*, *10*, 1073823. https://doi.org/10.3389/fevo.2022.1073823

Swart, S., Campbell, E. C., Heuzé, C. H., Johnson, K. S., Lieser, J. L., Massom, R. A., Mazloff, M. R., Meredith, M. P., Reid, P. A., Sallée, J.-B., & Stammerjohn, S. E. (2018). Return of the Maud Rise polynya: Climate litmus or sea ice anomaly? [in "State of the Climate in 2017"]. *Bulletin of the American Meteorological Society*, *99*(8), S188–S189.

https://doi.org/10.1175/2018BAMSStateoftheClimate.1

Szanyi, S., Lukovich, J. V., Barber, D. G., & Haller, G. (2016). Persistent artifacts in the NSIDC ice motion data set and their implications for analysis. *Geophysical Research Letters*, *43*(20), 10800–10807. https://doi.org/10.1002/2016GL069799

Talley, L. D. (2008). Freshwater transport estimates and the global overturning circulation: Shallow, deep and throughflow components. *Progress in Oceanography*, *78*(4), 257–303. https://doi.org/10.1016/j.pocean.2008.05.001

Talley, L. D. (2011). Dynamical processes for descriptive ocean circulation. In *Descriptive Physical Oceanography: An Introduction* (6th ed., pp. 187–222). London: Elsevier. https://doi.org/10.2307/20206579

Talley, L. D., Rosso, I., Kamenkovich, I., Mazloff, M. R., Wang, J., Boss, E., Gray, A. R., Johnson, K. S., Key, R. M., Riser, S. C., Williams, N. L., & Sarmiento, J. L. (2019). Southern Ocean biogeochemical float deployment strategy, with example from the Greenwich Meridian line (GO-SHIP A12). *Journal of Geophysical Research: Oceans*, *124*(1), 403–431. https://doi.org/10.1029/2018JC014059

Tamura, T., Ohshima, K. I., & Nihashi, S. (2008). Mapping of sea ice production for Antarctic coastal polynyas. *Geophysical Research Letters*, *35*(7), L07606. https://doi.org/10.1029/2007GL032903

Tamura, T., Ohshima, K. I., Nihashi, S., & Hasumi, H. (2011). Estimation of surface heat/salt fluxes associated with sea ice growth/melt in the Southern Ocean. *Scientific Online Letters on the Atmosphere*, *7*(1), 17–20. https://doi.org/10.2151/sola.2011-005

Tamura, T., Ohshima, K. I., Fraser, A. D., & Williams, G. D. (2016). Sea ice production variability in Antarctic coastal polynyas. *Journal of Geophysical Research: Oceans*, *121*(5), 2967–2979. https://doi.org/10.1002/2015JC011537

Testor, P., Bosse, A., Houpert, L., Margirier, F., Mortier, L., Legoff, H., Dausse, D., Labaste, M., Karstensen, J., Hayes, D., Olita, A., Ribotti, A., Schroeder, K., Chiggiato, J., Onken, R., Heslop, E., Mourre, B., D'ortenzio, F., Mayot, N., Lavigne, H., de Fommervault, O., Coppola, L., Prieur, L., Taillandier, V., Durrieu de Madron, X., Bourrin, F., Many, G., Damien, P., Estournel, C., Marsaleix, P., Taupier-Letage, I., Raimbault, P., Waldman, R., Bouin, M.-N., Giordani, H., Caniaux, G., Somot, S., Ducrocq, V., & Conan, P. (2018). Multiscale observations of deep convection in the northwestern Mediterranean Sea during winter 2012-2013 using multiple platforms. *Journal of Geophysical Research: Oceans*, *123*(3), 1745–1776. https://doi.org/10.1002/2016JC012671

Teusner, R., Matthies, C., & Staubitz, T. (2018). What stays in mind? - Retention rates in programming MOOCs. *2018 IEEE Frontiers in Education Conference*. https://doi.org/10.1109/FIE.2018.8658890

Theobald, E. J., Hill, M. J., Tran, E., Agrawal, S., Arroyo, E. N., Behling, S., Chambwe, N., Cintrón, D. L., Cooper, J. D., Dunster, G., Grummer, J. A., Hennessey, K., Hsiao, J., Iranon, N., Jones, L., Jordt, H., Keller, M., Lacey, M. E., Littlefield, C. E., Lowe, A., Newman, S., Okolo, V., Olroyd, S., Peecook, B. R., Pickett, S. B., Slager, D. L., Caviedes-Solis, I. W., Stanchak, K. E., Sundaravardan, V., Valdebenito, C., Williams, C. R., Zinsli, K., & Freeman, S. (2020). Active learning narrows achievement gaps for underrepresented students in undergraduate science, technology, engineering, and math. *Proceedings of the National Academy of Sciences*, *117*(12), 6476–6483. https://doi.org/10.1073/pnas.1916903117

Thompson, D. W. J., Solomon, S., Kushner, P. J., England, M. H., Grise, K. M., & Karoly, D. J. (2011). Signatures of the Antarctic ozone hole in Southern Hemisphere surface climate change. *Nature Geoscience*, *4*(11), 741–749. https://doi.org/10.1038/ngeo1296

Thyng, K. M., Greene, C. A., Hetland, R. D., Zimmerle, H. M., & DiMarco, S. F. (2016). True colors of oceanography: Guidelines for effective and accurate colormap selection. *Oceanography*, *29*(3), 9–13. https://doi.org/10.5670/oceanog.2016.66

Timmermann, R., Lemke, P., & Kottmeier, C. (1999). Formation and maintenance of a polynya in the Weddell Sea. *Journal of Physical Oceanography*, *29*(6), 1251–1264. https://doi.org/10.1175/1520-0485(1999)029<1251:FAMOAP>2.0.CO;2

Timmermann, R., Beckmann, A., & Hellmer, H. H. (2001). The role of sea ice in the fresh-water budget of the Weddell Sea, Antarctica. *Annals of Glaciology*, *33*(1997), 419–424. https://doi.org/10.3189/172756401781818121

Timms, G. P., & Guyon, J. R. (2023). From zero to Python in 10.5 hours: Building foundational programming skills with marine biology graduate students and researchers in an introductory workshop series. *Science & Technology Libraries*, *42*(3), 371–390. https://doi.org/10.1080/0194262X.2022.2116143

Toyota, T., Massom, R., Lecomte, O., Nomura, D., Heil, P., Tamura, T., & Fraser, A. D. (2016). On the extraordinary snow on the sea ice off East Antarctica in late winter, 2012. *Deep Sea Research Part II: Topical Studies in Oceanography*, *131*, 53–67. https://doi.org/10.1016/j.dsr2.2016.02.003

Treasure, A., Roquet, F., Ansorge, I. J., Bester, M., Boehme, L., Bornemann, H., Charrassin, J.-B., Chevallier, D., Costa, D., Fedak, M., Guinet, C., Hammill, M., Harcourt, R., Hindell, M., Kovacs, K., Lea, M.-A., Lovell, P., Lowther, A., Lydersen, C., McIntyre, T., McMahon, C., Muelbert, M., Nicholls, K., Picard, B., Reverdin, G., Trites, A., Williams, G. D., & de Bruyn, P. J. N. (2017). Marine mammals exploring the oceans pole to pole: A review of the MEOP Consortium. *Oceanography*, *30*(2), 132–138. https://doi.org/10.5670/oceanog.2017.234

Tschudi, M. A., Meier, W. N., Stewart, J. S., Fowler, C., & Maslanik, J. (2019). *Polar Pathfinder Daily 25 km EASE-Grid Sea Ice Motion Vectors (NSIDC-0116, version 4)*. Boulder, CO: NASA National Snow and Ice Data Center (NSIDC) Distributed Active Archive Center (DAAC). https://doi.org/10.5067/INAWUWO7QH7B

Tschudi, M. A., Meier, W. N., & Stewart, J. S. (2019). *Quicklook Arctic Weekly EASE-Grid Sea Ice Motion Vectors (NSIDC-0748, version 1)*. Boulder, CO: NASA National Snow and Ice Data Center (NSIDC) Distributed Active Archive Center (DAAC). https://doi.org/10.5067/O0XI8PPYEZJ6

Tschudi, M. A., Meier, W. N., & Stewart, J. S. (2020). An enhancement to sea ice motion and age products at the National Snow and Ice Data Center (NSIDC). *The Cryosphere*, *14*(5), 1519–1536. https://doi.org/10.5194/tc-14-1519-2020

Turner, J., Colwell, S. R., Marshall, G. J., Lachlan-Cope, T. A., Carleton, A. M., Jones, P. D., Lagun, V., Reid, P. A., & Iagovkina, S. (2004). The SCAR READER project: toward a high-quality database of mean Antarctic meteorological observations. *Journal of Climate*, *17*(14), 2890–2898. https://doi.org/10.1175/1520-0442(2004)017<2890:TSRPTA>2.0.CO;2

Turner, J., Holmes, C., Caton Harrison, T., Phillips, T., Jena, B., Reeves-Francois, T., Fogt, R., Thomas, E. R., & Bajish, C. C. (2022). Record low Antarctic sea ice cover in February 2022. *Geophysical Research Letters*, *49*(12), e2022GL098904. https://doi.org/10.1029/2022GL098904

Våge, K., Pickart, R. S., Thierry, V., Reverdin, G., Lee, C. M., Petrie, B., Agnew, T. A., Wong, A., & Ribergaard, M. H. (2009). Surprising return of deep convection to the subpolar North Atlantic Ocean in winter 2007–2008. *Nature Geoscience*, *2*(1), 67–72. https://doi.org/10.1038/ngeo382

Vancoppenolle, M., Fichefet, T., & Goosse, H. (2009). Simulating the mass balance and salinity of Arctic and Antarctic sea ice. 2. Importance of sea ice salinity variations. *Ocean Modelling*, *27*(1–2), 54–69. https://doi.org/10.1016/j.ocemod.2008.11.003

Vellukunnel, M., Buffum, P., Boyer, K. E., Forbes, J., Heckman, S., & Mayer-Patel, K. (2017). Deconstructing the discussion forum: Student questions and computer science learning. In *Proceedings of the 2017 ACM SIGCSE Technical Symposium on Computer Science Education* (pp. 603–608). ACM. https://doi.org/10.1145/3017680.3017745

Venegas, S. A., & Drinkwater, M. R. (2001). Sea ice, atmosphere and upper ocean variability in the Weddell Sea, Antarctica. *Journal of Geophysical Research*, *106*(C8), 16747–16765. https://doi.org/10.1029/2000JC000594

Verdy, A., & Mazloff, M. R. (2017). A data assimilating model for estimating Southern Ocean biogeochemistry. *Journal of Geophysical Research: Oceans*, *122*(9), 6968–6988. https://doi.org/10.1002/2016JC012650

Virtanen, P., Gommers, R., Oliphant, T. E., Haberland, M., Reddy, T., Cournapeau, D., Burovski, E., Peterson, P., Weckesser, W., Bright, J., van der Walt, S. J., Brett, M., Wilson, J., Millman, K. J., Mayorov, N., Nelson, A. R. J., Jones, E., Kern, R., Larson, E., Carey, C. J., Polat, İ., Feng, Y., Moore, E. W., VanderPlas, J., Laxalde, D., Perktold, J., Cimrman, R., Henriksen, I., Quintero, E. A., Harris, C. R., Archibald, A. M., Ribeiro, A. H., Pedregosa, F., van Mulbregt, P., Vijaykumar, A., Bardelli, A. Pietro, Rothberg, A., Hilboll, A., Kloeckner, A., Scopatz, A., Lee, A., Rokem, A., Woods, C. N., Fulton, C., Masson, C., Häggström, C., Fitzgerald, C., Nicholson, D. A., Hagen, D. R., Pasechnik, D. V., Olivetti, E., Martin, E., Wieser, E., Silva, F., Lenders, F., Wilhelm, F., Young, G., Price, G. A., Ingold, G.-L., Allen, G. E., Lee, G. R., Audren, H., Probst, I., Dietrich, J. P., Silterra, J., Webber, J. T., Slavič, J., Nothman, J., Buchner, J., Kulick, J., Schönberger, J. L., de Miranda Cardoso, J. V., Reimer, J., Harrington, J., Rodríguez, J. L. C., Nunez-Iglesias, J., Kuczynski, J., Tritz, K., Thoma, M., Newville, M., Kümmerer, M., Bolingbroke, M., Tartre, M., Pak, M., Smith, N. J., Nowaczyk, N., Shebanov, N., Pavlyk, O., Brodtkorb, P. A., Lee, P., McGibbon, R. T., Feldbauer, R., Lewis, S., Tygier, S., Sievert, S., Vigna, S., Peterson, S., More, S., Pudlik, T., Oshima, T., Pingel, T. J., Robitaille, T. P., Spura, T., Jones, T. R., Cera, T., Leslie, T., Zito, T., Krauss, T., Upadhyay, U., Halchenko, Y. O., & Vázquez-Baeza, Y. (2020). SciPy 1.0: fundamental algorithms for scientific computing in Python. *Nature Methods*, *17*(3), 261–272. https://doi.org/10.1038/s41592-019-0686-2

Walter, B., Weigel, H., Wahl, S., & Löwe, H. (2024). Wind tunnel experiments to quantify the effect of aeolian snow transport on the surface snow microstructure. *The Cryosphere*, *18*(8), 3633–3652. https://doi.org/10.5194/tc-18-3633-2024

Wang, C., Graham, R. M., Wang, K., Gerland, S., & Granskog, M. A. (2019). Comparison of ERA5 and ERA-Interim near-surface air temperature, snowfall and precipitation over Arctic sea ice: effects on sea ice thermodynamics and evolution. *The Cryosphere*, *13*(6), 1661–1679. https://doi.org/10.5194/tc-13-1661-2019

Wang, G., Hendon, H. H., Arblaster, J. M., Lim, E.-P., Abhik, S., & van Rensch, P. (2019). Compounding tropical and stratospheric forcing of the record low Antarctic sea-ice in 2016. *Nature Communications*, *10*, 13. https://doi.org/10.1038/s41467-018-07689-7

Wang, J., Massonnet, F., Goosse, H., Luo, H., Barthélemy, A., & Yang, Q. (2024). Synergistic atmosphere-ocean-ice influences have driven the 2023 all-time Antarctic sea-ice record low. *Communications Earth & Environment*, *5*, 415. https://doi.org/10.1038/s43247-024-01523-3

Wang, Y., Chassignet, E. P., & Speer, K. (2024). On the dynamics of the Ross Gyre: the relative importance of wind, buoyancy, eddies, and the Antarctic Circumpolar Current. *Frontiers in Marine Science*, *11*, 1465808. https://doi.org/10.3389/fmars.2024.1465808

Wang, Zhaohui, Fraser, A. D., Reid, P., O'Farrell, S., & Coleman, R. (2024). Antarctic sea ice surface temperature bias in atmospheric reanalyses induced by the combined effects of sea ice and clouds. *Communications Earth & Environment*, *5*, 552. https://doi.org/10.1038/s43247-024-01692-1

Wang, Zhaomin, Turner, J., Sun, B., Li, B., & Liu, C. (2015). Cyclone-induced rapid creation of extreme Antarctic sea ice conditions. *Scientific Reports*, *4*(1), 5317. https://doi.org/10.1038/srep05317

Ward, J. L., Payne, A. E., & Pettersen, C. (2023). Present-day regional Antarctic sea ice response to extratropical cyclones. *Journal of Geophysical Research: Atmospheres*, *128*(23), e2023JD038914. https://doi.org/10.1029/2023JD038914

Webster, M. A., Gerland, S., Holland, M., Hunke, E. C., Kwok, R., Lecomte, O., Massom, R. A., Perovich, D. K., & Sturm, M. (2018). Snow in the changing sea-ice systems. *Nature Climate Change*, *8*(11), 946–953. https://doi.org/10.1038/s41558-018-0286-7

Wei-Bing Lin, J., Aizenman, H., Manette Cartas Espinel, E., Gunnerson, K., & Liu, J. (2022). *An introduction to Python programming for scientists and engineers*. Cambridge University Press. https://doi.org/10.1017/9781108571531

Weijer, W., Veneziani, M., Stössel, A., Hecht, M. W., Jeffery, N., Jonko, A., Hodos, T., & Wang, H. (2017). Local atmospheric response to an open-ocean polynya in a high-resolution climate model. *Journal of Climate*, *30*(5), 1629–1641. https://doi.org/10.1175/JCLI-D-16-0120.1

Williams, L., & Upchurch, R. L. (2001). In support of student pair-programming. *ACM SIGCSE Bulletin*, *33*(1), 327–331. https://doi.org/10.1145/366413.364614

Wilson, E. A., Riser, S. C., Campbell, E. C., & Wong, A. P. S. (2019). Winter upper-ocean stability and ice-ocean feedbacks in the sea ice-covered Southern Ocean. *Journal of Physical Oceanography*, *49*(4), 1099–1117. https://doi.org/10.1175/JPO-D-18-0184.1

Wilson, G. (2016). Software Carpentry: lessons learned. *F1000Research*, *3*, 62. https://doi.org/10.12688/f1000research.3-62.v2

Wilson, G., Aruliah, D. A., Brown, C. T., Chue Hong, N. P., Davis, M., Guy, R. T., Haddock, S. H. D., Huff, K. D., Mitchell, I. M., Plumbley, M. D., Waugh, B., White, E. P., & Wilson, P. (2014). Best practices for scientific computing. *PLoS Biology*, *12*(1), e1001745. https://doi.org/10.1371/journal.pbio.1001745

Wong, A. P. S., & Riser, S. C. (2011). Profiling float observations of the upper ocean under sea ice off the Wilkes Land coast of Antarctica. *Journal of Physical Oceanography*, *41*(6), 1102–1115. https://doi.org/10.1175/2011JPO4516.1

Wong, A. P. S., Wijffels, S. E., Riser, S. C., Pouliquen, S., Hosoda, S., Roemmich, D., Gilson, J., Johnson, G. C., Martini, K., Murphy, D. J., Scanderbeg, M., Bhaskar, T. V. S. U., Buck, J. J. H., Merceur, F., Carval, T., Maze, G., Cabanes, C., André, X., Poffa, N., Yashayaev, I., Barker, P. M., Guinehut, S., Belbéoch, M., Ignaszewski, M., Baringer, M. O., Schmid, C., Lyman, J. M., McTaggart, K. E., Purkey, S. G., Zilberman, N., Alkire, M. B., Swift, D., Owens, W. B., Jayne, S. R., Hersh, C., Robbins, P., West-Mack, D., Bahr, F., Yoshida, S., Sutton, P. J. H., Cancouët, R., Coatanoan, C., Dobbler, D., Juan, A. G., Gourrion, J., Kolodziejczyk, N., Bernard, V., Bourlès, B., Claustre, H., D'Ortenzio, F., Le Reste, S., Le Traon, P.-Y., Rannou, J.-P., Saout-Grit, C., Speich, S., Thierry, V., Verbrugge, N., Angel-Benavides, I. M., Klein, B., Notarstefano, G., Poulain, P.-M., Vélez-Belchí, P., Suga, T., Ando, K., Iwasaska, N., Kobayashi, T., Masuda, S., Oka, E., Sato, K., Nakamura, T., Sato, K., Takatsuki, Y., Yoshida, T., Cowley, R., Lovell, J. L., Oke, P. R., van Wijk, E. M., Carse, F., Donnelly, M., Gould, W. J., Gowers, K., King, B. A., Loch, S. G., Mowat, M., Turton, J., Rama Rao, E. P., Ravichandran, M., Freeland, H. J., Gaboury, I., Gilbert, D., Greenan, B. J. W., Ouellet, M., Ross, T., Tran, A., Dong, M., Liu, Z., Xu, J., Kang, K., Jo, H., Kim, S.-D., & Park, H.-M. (2020). Argo data 1999–2019: Two million temperature-salinity profiles and subsurface velocity observations from a global array of profiling floats. *Frontiers in Marine Science*, *7*, 700. https://doi.org/10.3389/fmars.2020.00700

Worby, A. P., Markus, T., Steer, A. D., Lytle, V. I., & Massom, R. A. (2008). Evaluation of AMSR-E snow depth product over East Antarctic sea ice using in situ measurements and aerial photography. *Journal of Geophysical Research*, *113*(C5), C05S94. https://doi.org/10.1029/2007JC004181

Worby, A. P., Geiger, C. A., Paget, M. J., Van Woert, M. L., Ackley, S. F., & DeLiberty, T. L. (2008). Thickness distribution of Antarctic sea ice. *Journal of Geophysical Research*, *113*(C5), C05S92. https://doi.org/10.1029/2007JC004254

World Meteorological Organization. (2014). *Sea-ice nomenclature*. WMO No. 259.

Yamazaki, K., Aoki, S., Shimada, K., Kobayashi, T., & Kitade, Y. (2020). Structure of the subpolar gyre in the Australian-Antarctic Basin derived from Argo floats. *Journal of Geophysical Research: Oceans*, *125*(8), e2019JC015406. https://doi.org/10.1029/2019JC015406

Yamazaki, T., Kondo, J., Sakuraoka, T., & Nakamura, T. (1993). A one-dimensional model of the evolution of snow-cover characteristics. *Annals of Glaciology*, *18*(3), 22–26. https://doi.org/10.1017/S0260305500011204

Yan, Z., Pang, X., Ji, Q., Chen, Y., Luo, C., Fan, P., & Liang, Z. (2023). Retrieval of snow depth on Antarctic sea ice from the FY-3D MWRI data. *Acta Oceanologica Sinica*, *42*(12), 105–117. https://doi.org/10.1007/s13131-023-2179-5

Yan, Z., Ji, Q., He, B., Chen, Y., Wang, Y., & Pang, X. (2024). A combined multi-source data and deep learning approach for retrieving snow depth on Antarctic sea ice during the melting season. *International Journal of Digital Earth*, *17*(1), 2376260. https://doi.org/10.1080/17538947.2024.2376260

Yu, Z., & Gao, M. (2022). Effects of video length on a flipped English classroom. *SAGE Open*, *12*(1), 215824402110684. https://doi.org/10.1177/21582440211068474

Yuan, X., Patoux, J., & Li, C. (2009). Satellite-based midlatitude cyclone statistics over the Southern Ocean: 2. Tracks and surface fluxes. *Journal of Geophysical Research*, *114*(D4), D04106. https://doi.org/10.1029/2008JD010874

Yuretich, R. F., Khan, S. A., Leckie, R. M., & Clement, J. J. (2001). Active-learning methods to improve student performance and scientific interest in a large introductory oceanography course. *Journal of Geoscience Education*, *49*(2), 111–119. https://doi.org/10.5408/1089-9995-49.2.111

Zanowski, H., & Hallberg, R. (2017). Weddell Polynya transport mechanisms in the abyssal ocean. *Journal of Physical Oceanography*, *47*(12), 2907–2925. https://doi.org/10.1175/JPO-D-17-0091.1

Zanowski, H., Hallberg, R., & Sarmiento, J. L. (2015). Abyssal ocean warming and salinification after Weddell Polynyas in the GFDL CM2G coupled climate model. *Journal of Physical Oceanography*, *45*(11), 2755–2772. https://doi.org/10.1175/JPO-D-15-0109.1

Zhang, J. (2014). Modeling the impact of wind intensification on Antarctic sea ice volume. *Journal of Climate*, *27*(1), 202–214. https://doi.org/10.1175/JCLI-D-12-00139.1

Zhang, J., Lindsay, R., Schweiger, A., & Steele, M. (2013). The impact of an intense summer cyclone on 2012 Arctic sea ice retreat. *Geophysical Research Letters*, *40*(4), 720–726. https://doi.org/10.1002/grl.50190

Zhang, L., Delworth, T. L., Cooke, W., & Yang, X. (2019). Natural variability of Southern Ocean convection as a driver of observed climate trends. *Nature Climate Change*, *9*(1), 59–65. https://doi.org/10.1038/s41558-018-0350-3

Zhang, L., Delworth, T. L., Yang, X., Zeng, F., Lu, F., Morioka, Y., & Bushuk, M. (2022). The relative role of the subsurface Southern Ocean in driving negative Antarctic Sea ice extent anomalies in 2016–2021. *Communications Earth & Environment*, *3*, 302. https://doi.org/10.1038/s43247-022-00624-1

Zhou, L., Xu, S., Liu, J., & Wang, B. (2018). On the retrieval of sea ice thickness and snow depth using concurrent laser altimetry and L-band remote sensing data. *The Cryosphere*, *12*(3), 993–1012. https://doi.org/10.5194/tc-12-993-2018

Zwally, H. J., Yi, D., Kwok, R., & Zhao, Y. (2008). ICESat measurements of sea ice freeboard and estimates of sea ice thickness in the Weddell Sea. *Journal of Geophysical Research: Oceans*, *113*(2), C02S15. https://doi.org/10.1029/2007JC004284

VITA

Ethan Chen Campbell grew up in Park Ridge, Illinois. During college at Princeton University, he fell in love with oceanography, including through a research cruise to the Southern Ocean. He graduated *magna cum laude* with an A.B. degree in Geosciences in 2016 and moved to Seattle to pursue a Ph.D. degree in physical oceanography at the University of Washington. The submission of this dissertation marks the close of that journey—one under the mentorship of his graduate advisor, Stephen Riser, with whom he first collaborated during a college summer research internship—and the beginning of a new chapter.